Characterization of the Oxygen Binding Sites in Stearoyl-ACP Desaturase and Hemerythrin by Resonance Raman Spectroscopy

Jingyuan Ai

B.S., Zhengzhou University, China, 1989

M.S., University of Science and Technology of China, 1992

A dissertation submitted to the faculty of the

Oregon Graduate Institute of Science and Technology

in partial fulfillment of the

requirements for the degree

Doctor of Philosophy

in

Biochemistry and Molecular Biology

February, 1998

The dissertation "Characterization of the Oxygen Binding Sites in Stearoyl-ACP Desaturase and Hemerythrin by Resonance Raman Spectroscopy" by Jingyuan Ai has been examined and approved by the following examination committee:

Joann Sanders-Loehr
Professor and Dissertation Advisor

Thomas M. Loehr
Professor

Ninjan J. Blackburn
Professor

David R. Boone
Professor

This dissertation is dedicated to

my parents,

my wife,

and my daughter.

ACKNOWLEDGMENTS

First, I want to express my deepest thanks to my research advisors, Professor Joann Sanders-Loehr and Professor Thomas Loehr, who not only spent infinite time and energy in training me to be a scientist and providing me many learning opportunities, but also gave me so much help in my life during the last five years. I would like to thank Professor Ninian Blackburn and Professor David Boone for the time they spent carefully reviewing my dissertation. I am also grateful to our collaborators: Dr. Brian Fox for providing stearoyl-ACP Δ^9 desaturase, Dr. Walther Ellis for providing the myohemerythrin L103N mutant, and Dr. Donald Kurtz for providing the hemerythrin mutants. I would like to thank Dr. Pierre Moënne-Loccoz, Dr. Jinshu Ling, Dr. Nobuhumi Nakamura, and Dr. Jonathan Cohen, all of the metalloprotein group, and my many friends at OGI for their help and friendship during my Ph.D. studies. Special appreciation to my grandparents, my parents, my uncles, my aunts, and many former teachers in China for providing me with love, support, encouragement, and hope during my long period of my studies. Finally, I want to thank my wife Hu Bin and my daughter Ai Karen for providing me with a joyful life, and for their patience during the last two years.

TABLE OF CONTENTS

LIST OF TABLES

LIST OF FIGURES

ABSTRACT

Characterization of the Oxygen Binding Sites in Stearoyl-ACP Desaturase and Hemerythrin by Resonance Raman Spectroscopy

Jingyuan Ai

Oregon Graduate Institute of Science and Technology

Supervising Professor: Joann Sanders-Loehr

Resonance Raman (RR) spectroscopy has been used to study the diiron-oxo proteins including stearoyl-ACP Δ^9 Desaturase (Δ9D), L103N mutant of myohemerythrin (Mhr), L28Y and L98Y mutants of hemerythrin (Hr).
Δ9D inserts a 9,10 *cis* double bond into the hydrocarbon chain of stearoyl-ACP. This reaction involves the activation of a diiron site. Δ9D displays a ν_s(Fe-O-Fe) peak at 519 cm^{-1} and a ν_{as}(Fe-O-Fe) peak at 747 cm^{-1}, which have 18 and 34 cm^{-1} downshifts respectively in $H_2{}^{18}O$. This proves that Δ9D contains an oxo-bridged diiron cluster. In order to investigate the coordination geometry of the diferric-peroxo intermediate, we studied the binding of azide to the diiron center of Δ9D. RR experiments demonstrated the existence of a symmetrically coordinated azide with a $\nu_{as}(N_3)$ mode at 2100 cm^{-1} which shifted to 2089 cm^{-1} as a single band with $^{15}N^{14}N_2^-$. The most probable structure is a μ-1,3 bridging azide. This finding supports the likelihood of a μ-1,2 bridging peroxide as a catalytic intermediate in the Δ9D reaction cycle.

Hr and Mhr function as oxygen transport and storage proteins, respectively, in some marine invertebrate species. The Leu103 residue of Mhr, and the Leu98 and Leu28 residues of Hr form a hydrophobic pocket around O_2 binding sites. The Leu103 of Mhr was mutated to a hydrophilic residue of similar size: Asn. Our Raman data, combined with the X-ray structure, indicate that the L103N mutant has a

firmly bound hydroxide ligand held by H-bonding to a water molecule that is in turn H-bonded to Asn-103. This H-bonding network could be responsible for the faster rate of autooxidation of bound O_2 in the oxy complex of the L103N mutant.

The L98Y mutant of Hr exhibits vibrational peaks at 573, 1167, 1297, 1502, and 1603 cm^{-1}, which are characteristic of ferric phenolate complex. In contrast, the L28Y mutant of Hr displays an antiferromagnetically coupled $Fe^{II}Fe^{III}$ EPR signal and an inter-valence charge transfer band at 657 nm. With 647 nm excitation, it exhibits two $\nu_s(Fe^{II}\text{-}O\text{-}Fe^{III})$ and $\nu_{as}(Fe^{II}\text{-}O\text{-}Fe^{III})$ peaks at 479 and 694 cm^{-1} respectively. This spectral evidence suggests that L28Y Hr contains an oxo-bridged mixed-valence species ($Fe^{II}\text{-}O\text{-}Fe^{III}$). Thus, the introduction of more hydrophobic residues near the O_2 binding site of Hr can result either in iron ligation (L98Y) or in the stabilization of a mixed-valence intermediate (L28Y). This indicates that a variation in hydrophobic residues could be responsible for the formation of different catalytic intermediates in different diiron-oxo enzymes.

CHAPTER I

O_2 BINDING SITES IN DIIRON-OXO PROTEINS

Plant and animal life on earth depends upon reactions of the O_2 molecule with organic compounds, and these are quite exothermic. Since oxygen is inactive toward most organic substrates, organisms have evolved many protein systems containing metal ions to transport and activate oxygen (Lippard & Berg, 1994). There are three O_2 transport proteins: hemoglobin (Hb), hemocyanin (Hc), and hemerythrin (Hr), all of which are metalloproteins. Hemoglobin is the most common and occurs in all vertebrates and many invertebrates; it uses an iron-porphyrin (heme) group as its active site. Hemocyanin has two copper atoms at the O_2 binding site and occurs among arthropods and mollusks. The third, hemerythrin is found in several phyla of marine invertebrates and utilizes two non-heme iron atoms to bind O_2. The O_2 molecule is also stored in muscle tissue by the proteins myoglobin (Mb) and myohemerythrin (Mhr) which have metal core structures analogous to those of the transport proteins. Interestingly, each of the specific functional centers employed in the reversible binding of O_2 also participates in O_2 activation reactions. Dinuclear centers similar to the O_2-binding sites of Hr and Hc are used to activate O_2 in methane monooxygenase and tyrosinase, respectively, and the iron-porphyrin centers in Hb bear a similar relationship to those in cytochromes P-450, catalases, and peroxidases.

Resonance Raman spectroscopy is a powerful tool for studying the active sites of metalloproteins (Spiro, 1988). In this thesis, this vibrational technique was used to study the diiron proteins stearoyl-ACP Δ^9 desaturase (Δ9D), Hr, and Mhr. Other diiron proteins that interact with O_2 as part of their biological function also include the R2 subunit of ribonucleotide reductase (R2), the hydroxylase component of methane monooxygenase (MMOH). In this chapter, I will first briefly review the

diiron site structures, spectroscopic properties, and catalytic mechanisms of these enzymes. Next, I will discuss how small molecules such as azide (N_3^-) can be used to probe the O_2 binding site in diiron proteins. Finally, I will outline the main research in this thesis.

Overview of Diiron-oxo Proteins

Hemerythrin

Hemerythrin functions as an oxygen transport protein in several phyla of marine invertebrates. In most species, the protein is an octamer, although monomeric and other oligomeric forms are found. Each subunit ranges in molecular weight from 13.5–13.9 kDa and contains two ligand-bridged iron atoms. Myohemerythrin (Mhr) is a monomeric protein usually isolated from the muscles of sipunculids, and is very similar to the Hr subunit both in structure and function (Stenkamp, 1994). Hr and Mhr function in a manner comparable to the mammalian proteins Hb and Mb.

Structure. The crystal structures of oxy- and deoxy-Hr (Stenkamp et al., 1985; Holmes et al., 1991), met-Hr (Stenkamp et al., 1984), azidomet-Hr (Holmes & Stenkamp, 1991), and azidomet-Mhr (Sheriff et al., 1987) have been solved. The structural details, together with the extensive spectroscopic studies (Sanders-Loehr, 1989a; Vincent et al., 1990), make Hr and Mhr the best understood diiron proteins.

The polypeptide chain in Mhr or the subunit of Hr folds into four α-helices that pack roughly parallel to one another (Figure 1.1). The four α-helices bundle forms an effective metal ion binding motif in many natural proteins (Presnell & Cohen, 1989). One characteristic of this packing is that there is one close-contact region, and the helices slightly diverge away from this contact region (Stenkamp, 1994). This generates a cleft or cavity between the helices that can be filled with a dinuclear iron center. In addition to the amino acids bound to the iron atoms, the cleft is lined with hydrophobic amino acids making a suitable binding environment for exogenous ligands such as O_2.

The active site structures of deoxy- and oxy-Hr from *Themiste dyscrita* are shown in Figure 1.2. The two iron atoms are bound to five histidine and two

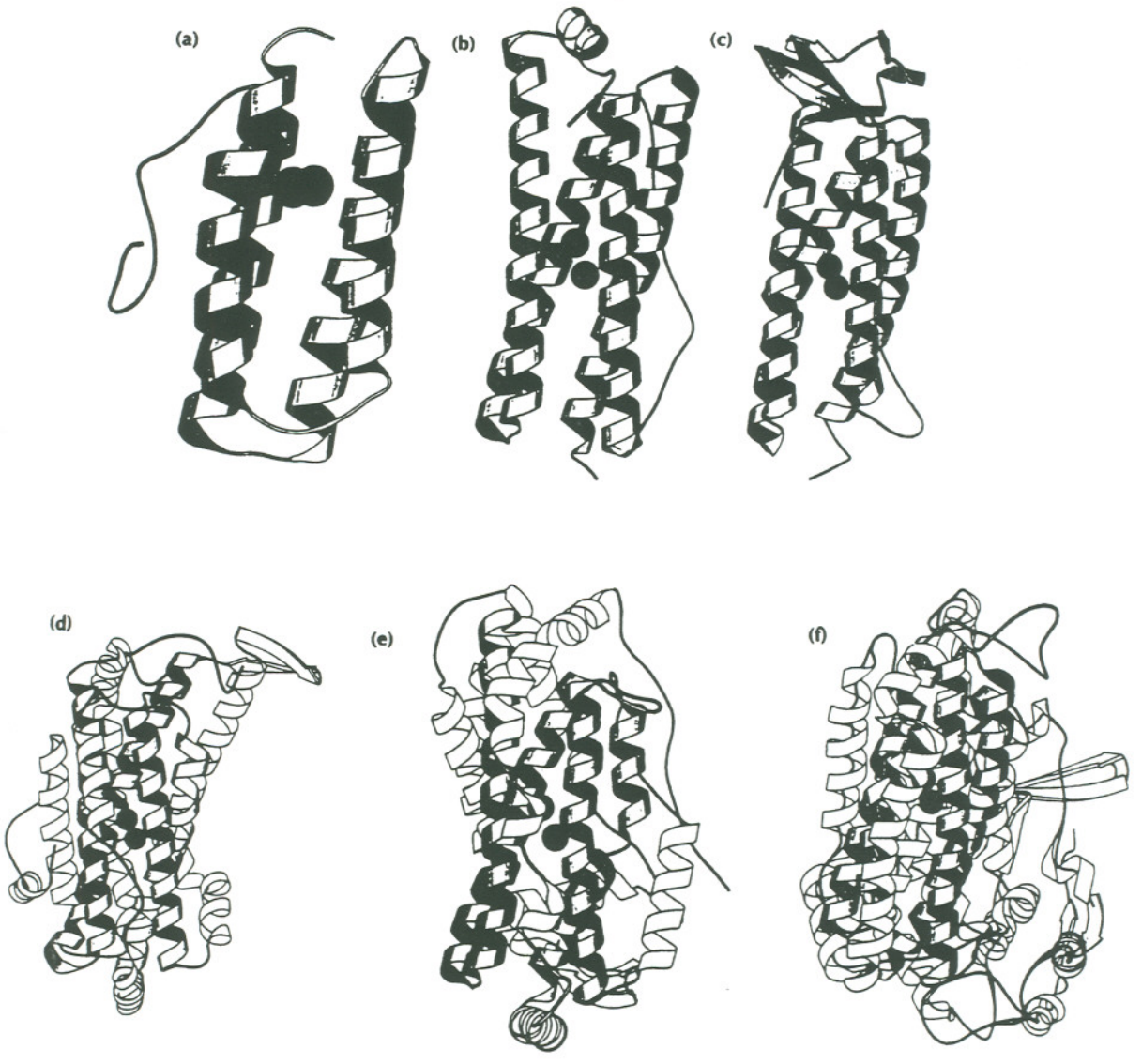

Figure 1.1 Three-dimensional structures of diiron proteins. (a) Hemerythrin. (b) Bacterioferritin. (c) Rubrerythrin. (d) Ribonucleotide reductase R2. (e) Stearoyl-ACP Δ^9 desaturase. (f) Methane monooxygenase hydroxylase. All helical proteins contain two metal-binding helix pairs (darkly shaded). Adapted From Nordlund & Eklund, 1995.

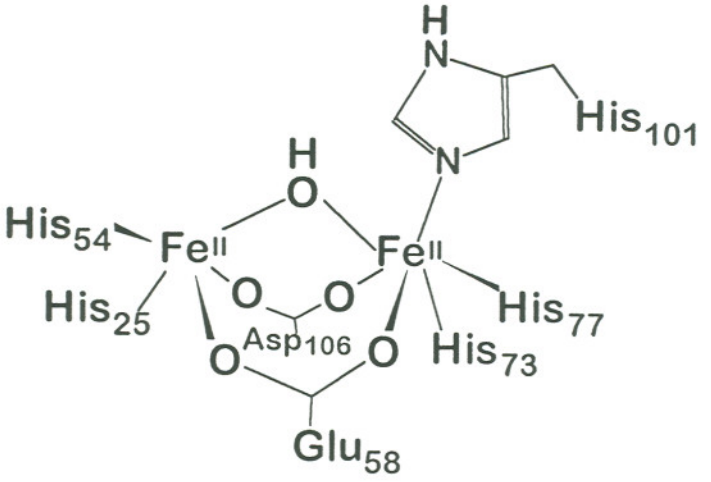

A. Deoxy-Hr

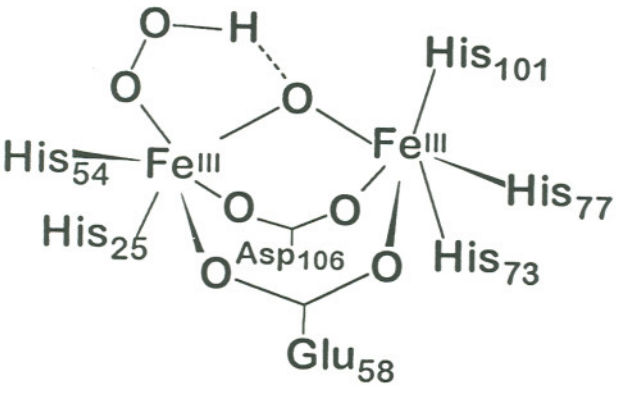

B. Oxy-Hr

Figure 1.2 Schematic diagram of diiron site of deoxy-Hr and oxy-Hr. Adapted from Holmes et al., 1991.

carboxylic acid residues. Two helices furnish ligands to one iron, while the other two α-helices provide ligands to the another iron. All of the histidine residues bind through the ϵ nitrogen atoms from their imidazole side chains. Three of the histidines residues (His-73, 77, and 101) bind to one iron atom (Fe1), and two (His-25 and 54) bind to the other iron atom (Fe2). The Glu-58 and Asp-106 residues bridge between two metals using each oxygen atom of their carboxylates to bind to separate iron atoms. In deoxy-Hr, the diiron core is asymmetric, with Fe1 being 6-coordinate and Fe2 being 5-coordinate. The Fe2 site presents the only open coordination position for binding exogenous ligands such as dioxygen. This is consistent with the structure of oxy-Hr, in which O_2 is coordinated to only one of the iron atoms. Deoxy-Hr has one solvent-derived hydroxide bridge linking the two iron atoms. In the met and oxy forms, the bridge becomes deprotonated to form the very stable oxo-bridged structure. The Fe-O-Fe unit is described as a μ-oxo-bridged binuclear iron center. Key distances and angles are presented in Table 1.1. The Fe-μO bond distances observed in deoxy-Hr are slightly longer than those in met-, azidomet-, or oxy-Hr. This elongation is consistent with the increase in Fe-O distances on going from μ-oxo- to μ-hydroxo-bridged complexes (Stenkamp, 1994).

The amino acid residues surrounding the dioxygen binding site that are not bound to the iron atoms are all hydrophobic (Stenkamp, 1994). There are five residues with atoms within 4 Å of the dioxygen molecule in oxy-Hr from *T. dyscrita*: Leu-28, Leu-98, Phe-55, Trp-97 and Ile-102 (Holmes et al., 1991). These five residues are invariant across the sequences reported except that Leu-28 is replaced by an isoleucine in *N. diversicolor* Mhr (Stenkamp, 1994). In chapter IV and V, mutations done on Leu-28 and Leu-98 are described that were made to study the functions of these hydrophobic residues.

Mechanism. The functional mechanism of Hr has been demonstrated by X-ray crystallography and spectroscopy. The most important findings on the structural studies is that in oxy-Hr, hydroperoxide coordinates in a bent, end-on fashion to the Fe2 site. The Mössbauer spectrum of oxy-Hr has two distinct doublets with similar isomer shifts (δ = 0.51, 0.52 mm s^{-1}) but different quadrupole splitting parameters (ΔE_Q = 0.91, 1.93 mm s^{-1}), consistent with an asymmetric, antiferromagnetically

Table 1.1

Average Bond Distances (Å) and Angles (Deg)
in the Different Forms of Hr (Resolution at 2.0 Å).[a]

	Deoxy-Hr	Oxy-Hr	Met-Hr	Azidomet-Hr
Fe1-Glu58	2.33	2.20	2.26	2.17
Fe1-His73	2.23	2.22	2.22	2.24
Fe1-His77	2.21	2.18	2.15	2.20
Fe1-His101	2.24	2.21	2.15	2.22
Fe1-Asp106	2.17	2.13	2.08	2.15
Fe1-μO	2.15	1.88	1.92	1.80
Fe2-His25	2.15	2.14	2.07	2.21
Fe2-His54	2.28	2.25	2.23	2.24
Fe2-Glu58	2.14	2.20	2.04	2.25
Fe2-Asp106	2.14	2.15	2.08	2.09
Fe2-μO	1.88	1.79	1.66	1.79
Fe1-Fe2	3.32	3.27	3.25	3.23
Fe1-O-Fe2	111°	125°	127°	135°
μO-peroxo O2		2.80		
Fe2-peroxo O1		2.15		
Fe2-N1				2.34

[a] Data are from Stenkamp, 1994.

coupled diferric site (Clark & Webb, 1981). On the basis of ν(O-O) at 844 cm^{-1}, resonance Raman spectroscopy established that the oxidation level in oxy-Hr is peroxide (O_2^{2-}) (Dunn et al., 1973). In D_2O, the 4-cm^{-1} upshift of the ν(O-O) peak to 848 cm^{-1} indicated that the bound peroxide is protonated (Shiemke et al., 1984). Using ^{16}O-^{18}O as substrate, the ν(O-O) peak split into two peaks at 825 and 818 cm^{-1} (Kurtz et al., 1976). Thus, consistent with the crystal structure, resonance Raman data clearly showed that the peroxide was bound in an end-on mode.

The crystal structure of oxy-Hr revealed that peroxide binds to Fe2 site in *syn* orientation which allows the hydrogen bonding between hydroperoxide and the oxo bridge (Figure 1.2) (Holmes et al., 1991). The distance between the oxo bridge and the outer peroxo oxygen atom is 2.8 Å, well within the range of hydrogen bonding interaction (Table 1.1). In D_2O, the 4-cm^{-1} upshift of the ν_s(Fe-O-Fe) peak at 486 cm^{-1} also demonstrated that the bound hydroperoxide has a H-bond to the oxo bridge (Figure 1.3) (Shiemke et al., 1986). Hydroxomet-Hr is the only other protein that can use a proton to form a hydrogen bond with the oxo bridge and has such a deuterium isotope effect (Shiemke et al., 1986).

Overall, binding of O_2 to deoxy-Hr is a two-electron transfer reaction, with the oxidation of both iron atoms from ferrous to ferric and the reduction of O_2 to O_2^{2-}; this is accompanied by transfer of a proton from the hydroxo bridge to the peroxide to give a hydroperoxide ion. The resulting hydroperoxide is stabilized in part by the hydrogen bonding to the oxide bridge, and by the hydrophobic nature of O_2-binding pocket.

Spectroscopy. Spectroscopic work further characterized the structure of deoxy-Hr, oxy-Hr and met-Hr proteins (Table 1.2). These studies established a basis for all diiron proteins. The oxo bridge in the diferric form defines many of its distinctive properties. In oxy and met-Hr, the iron atoms are antiferromagnetically coupled with coupling constants of $J = -90$ cm^{-1} and $J = -130$ cm^{-1}, respectively (Dawson et al., 1972). In deoxy-Hr, the magnetic coupling constant is much smaller ($J = -15$ cm^{-1}) due to the μ-hydroxo bridge (Maroney et al., 1986). In addition, diferric Hr proteins have short Fe-μO distances (~ 1.8 Å) (Table 1.1), and large Mössbauer quadrupole splittings ($\Delta E_Q \geq 1.3$ mm/s) (Clark & Webb, 1981).

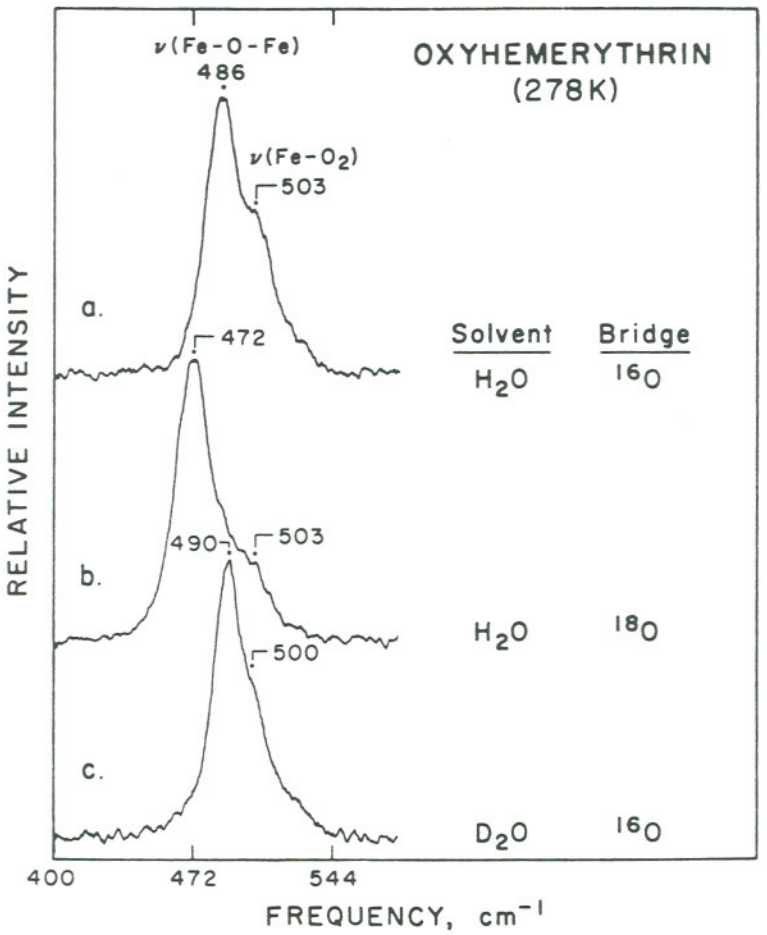

Figure 1.3 Resonance Raman spectra of oxy-Hr. Adapted from Shiemke et al., 1986.

Table 1.2

Spectroscopic Properties of Different Forms of Hr

	Properties	Deoxy-Hr	Oxy-Hr	Met-Hr	Azidomet-Hr
Raman[b]	ν_s(Fe-O-Fe)		486	510	507
	ν_{as}(Fe-O-Fe)		753	750	768
	ν(O-O)		844		2050[a]
	ν(Fe-L)		503		369
Electronic[c]	O^{2-}→Fe(III) CT. λ, nm (ϵ, $M^{-1}cm^{-1}$)		360 (5400) 330 (6900)	355 (5400)	370 (4800) 327 (7200)
	L→Fe(III) CT λ, nm (ϵ, $M^{-1}cm^{-1}$)		500 (2200)		445 (3700)
Magnetic[c]	J, cm^{-1} [e]	−15	−90	−130	
Mössbauer[d]	Fe1 δ, mm/s	1.14	0.51	0.46	0.51
	Fe1 ΔE_Q, mm/s	2.76	0.91	1.57	1.96
	Fe2 δ, mm/s		0.52		0.51
	Fe2 ΔE_Q, mm/s		1.93		1.47

[a] $\nu(N_3)$. [b] Shiemke et al., 1984. [c] Sanders-Loehr, 1989. [d] Vincent et al., 1990. [e] These values are reported using the convention $\mathbf{H} = -2J\mathbf{S}_1 \cdot \mathbf{S}_2$.

The carboxylate bridges bend the Fe-O-Fe unit to an angle of 120–130°, resulting in an Fe-Fe separation of 3.2 Å and giving rise to a series of characteristic visible features and Raman vibrations. First, the absorption spectra of diferric Hr proteins contain two $O^{2-} \rightarrow$ Fe(III) charge transfer bands at $\sim$330 nm (ϵ = 6800 $M^{-1}cm^{-1}$) and $\sim$360 nm (ϵ = 5500 $M^{-1}cm^{-1}$) (Garbett et al., 1969; Reem et al., 1989). In addition, oxy-Hr is characterized by an intense visible band near 500 nm, which is associated with a peroxide $\rightarrow$ Fe(III) charge transfer (Shiemke et al., 1986). Second, resonance Raman studies have assigned the peaks at $\sim$510 cm^{-1} and 750–785 cm^{-1} of diferric Hr proteins to ν_s(Fe-O-Fe) and ν_{as}(Fe-O-Fe) respectively, based on their isotope shifts after the oxo bridge is replaced by ^{18}O (Loehr & Shiemke, 1988). For oxy-Hr, the ν_s(Fe-O-Fe) and ν_{as}(Fe-O-Fe) occur at lower frequencies, 486 and 753 cm^{-1}, respectively. This has been attributed to the presence of the hydrogen bond to the oxo bridge (Shiemke et al., 1984).

Ribonucleotide reductase

Ribonucleotide reductase plays a crucial role in DNA synthesis by catalyzing the direct reduction of all ribonucleotides to the corresponding deoxyribonucleotides (Reichard, 1988). Ribonucleotide reductase from *E. coli* has an $\alpha_2\beta_2$ holoenzyme composition where the two homodimers are denoted R1 and R2. The R1 protein has a molecular mass (M_r) of 171 kD (2×761 residues) and R2 has a M_r of 87 kD (2×375 residues). The R1 protein contains allosteric binding sites and the active site, whereas each subunit of the R2 protein contains a dinuclear iron center and the critical Tyr-122 radical, which initializes the catalytic reaction through electron transfer.

Diiron site structure. The crystal structure of the R2 protein has been determined in both reduced and oxidized (met) forms (Nordlund et al., 1990; Åberg, 1993; Nordlund & Eklund, 1993). The overall structure of the R2 homodimer is heart shaped and in which the two diiron clusters are 25 Å apart. The structure is composed of 70% α helical bundles. Four of them provide the ligands for the diiron cluster (Figure 1.1). The Fe-O-Fe axis is parallel relative to the long axis of the helices. A similar case has been found for MMOH (Rosenzweig et al., 1993). In

contrast, the structure of Hr shows that the Fe-O-Fe axis of its diiron cluster is approximately perpendicular to the long axis of a four helix bundle (Stenkamp, 1994). Moreover, the diiron sites of R2 is bound by two Glu-X-X-His motifs. The diiron sites in Hr do not contain this sequence motif. As discussed in Chapter II, these structural differences and others prove that R2 and the other diiron-oxo enzymes (e.g., MMOH and Δ9D) form a separate class with no evolutionarily relationship to Hr.

The active site structure and coordination geometry are shown in Figure 1.4. Oxidized R2 has an oxo (O^{2-}) bridge between two Fe(III) atoms which is confirmed by spectroscopic results (Table 1.3). The two iron atoms are also bridged by a single carboxylate (Glu-115), which bends the Fe-O-Fe unit to an angle of 130° and affords an Fe-Fe separation of 3.2 Å. Glu-238 is bound to one iron (Fe2) and points to the second iron (Fe1). Fe1 is also ligated to the Nδ atom of His-118 and two oxygen atoms of Asp-84 (bidentate), and Fe2 to the Nδ atom of His-241 and one oxygen atom of Glu-204. In addition, each iron atom has one water molecule as ligand. Like those in Hr and MMOH, the R2 diiron center is surrounded by a hydrophobic patch, composed of residues Phe-208, Phe-212, and Ile-234. Tyr-122 is located 5.3 Å from Fe1 and is buried $\sim$10 Å under the surface of the protein.

The diiron site structure of reduced R2 has important changes from oxidized R2. It lacks oxy, hydroxo or water bridges between the two iron centers. Instead, there are distinct carboxylate shifts between reduced and oxidized R2 proteins. Monodentate ligand Glu-238 in $R2_{ox}$ becomes a bridge between two iron atoms. Bidentate Asp-84 becomes a monodentate ligand to Fe2. The Fe-Fe distance has increased to 3.8 Å.

An interesting comparison among the diiron site structures in R2, MMOH, and Hr has been made by Kurtz (1997). In this respect, the active site in R2 is more similar to that in MMOH (Figure 1.5). First, the diiron site in Hr has only one open position for binding O_2. However, the diiron sites in R2 and MMOH have open or labile coordination positions on both irons. The obvious inference is that the Hr diiron site allows only terminal O_2 binding, whereas the O_2-activating diiron sites permit O_2 bridging of the irons. This is demonstrated by the experiment that NO can

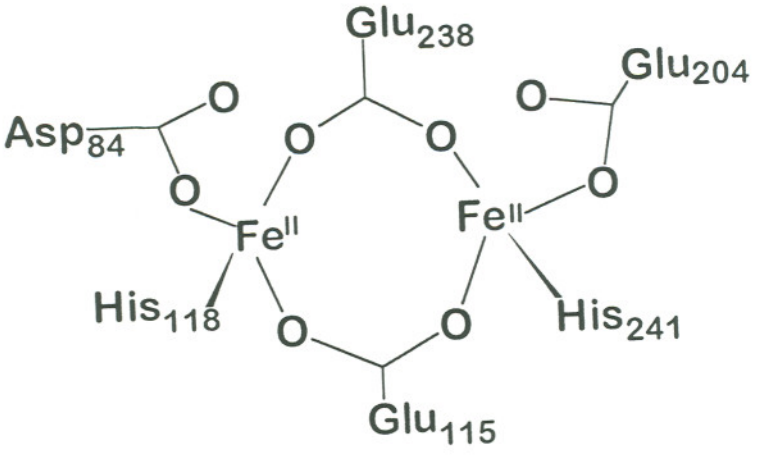

A. R2red

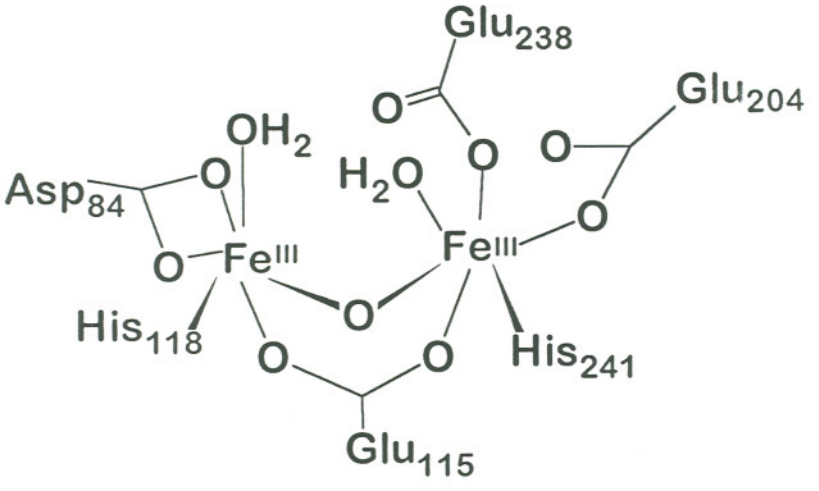

B. R2ox

Figure 1.4 Schematic diagram of diiron site of reduced and oxidized R2. Adapted from Nordlund et al., 1990 and Åberg, 1993.

Table 1.3

Spectroscopic Properties of Different Forms of R2[a]

Properties	$R2_{red}$	$R2_{ox}$
Raman Scattering		
ν_s(Fe-O-Fe), cm^{-1}		496
ν_{as}(Fe-O-Fe) cm^{-1}		756
Electronic Absorption		325 (9400)
λ, nm		370 (7200)
(ϵ, $M^{-1}cm^{-1}$)		500 (800)
		600 (300)
Magnetic Susceptibility		
-J, cm^{-1}	10	110
Mössbauer Spectroscopy		
Fe1 δ, mm/s	1.26	0.53
Fe1 ΔE_Q, mm/s	3.13	1.66
Fe2 δ, mm/s	1.26	0.44
Fe2 ΔE_Q, mm/s	3.13	2.45

[a] Data are from Sanders-Loehr, 1989.

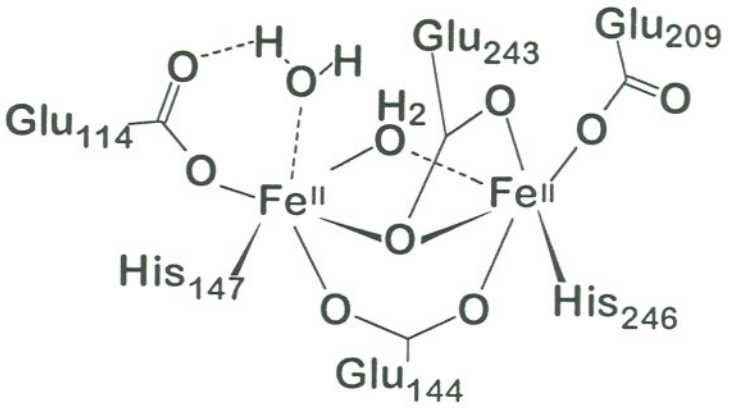

A. $MMOH_{red}$

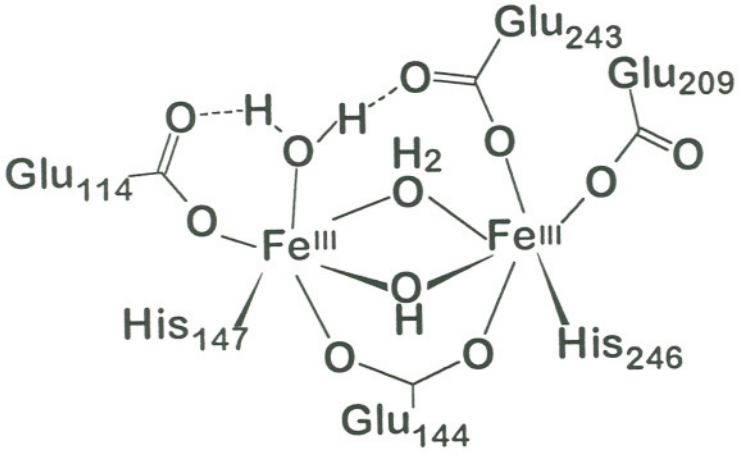

B. $MMOH_{ox}$

Figure 1.5 Schematic diagram of diiron site of reduced and oxidized MMOH. Adapted from Rosenzweig et al., 1993 and Rosenzweig et al., 1995.

bind with both iron sites in diferrous R2 to form N_2O (Haskin et al., 1995). Second, the diiron site in R2 is more flexible than that in Hr upon changes in diiron oxidation state. In the conversion from oxidized R2 to reduced R2, carboxylate shifts are apparent, and Fe1-Fe2 distance increases 0.5 Å. However, there is little rearrangement of the diiron coordination geometry during interconversions of deoxy-Hr, oxy-Hr, and met-Hr. The Fe1-Fe2 distances change very little: 3.32 Å (deoxy), 3.27 Å (oxy) and 3.25 Å (met) (Table 1.1) (Stenkamp, 1994). Third, the diiron centers in R2 and MMOH have a predominate oxygen ligand environment, whereas Hr has a predominate nitrogen ligand environment. R2 only provides two His-based nitrogen ligands: one to each iron. Oxygen from carboxylates and solvent comprise the remainder of the coordination of the diiron cluster in R2. In contrast, Hr provides five histidine residues to the diiron cluster. Also, unlike Hr, both R2 and MMOH exhibit the conserved EXXH motif. In the model studies, the electron density contributed by the ligands can modulate the reactivity of the O_2 adduct (Dong et al., 1996). It is likely that the histidine-rich active site of Hr helps to maintain the O-O bond, thereby contributing to the reversibility of O_2 binding; the anionic carboxylate-rich diiron sites of MMOH and R2 activate the O-O bond and promote O-O bond scission and reactivity.

Spectroscopy. The main spectroscopic properties of R2 are shown in Table 1.3 (Sanders-Loehr, 1989). Oxidized R2 exhibits two oxo → Fe(III) charge transfer bands at 325 and 370 nm. Resonance Raman studies assign the vibrations at 496 and 756

cm^{-1} to the symmetric and asymmetric stretching modes of the Fe-O-Fe core. Mössbauer data show that both irons are coupled high-spin ferric atoms in slightly different environments. Overall, the spectroscopic studies clearly demonstrate that oxidized R2 contains an oxo bridge between two magnetically coupled irons.

O_2 activation. The biological function of the diiron center in R2 is to generate a tyrosyl radical through a redox cycle. The net reaction is described by equation 1. Three electrons come from tyrosine and two ferrous ions, and the fourth from another

$$Y122\text{-}H + 2Fe(II) + O_2 + e^- + H^+ \rightarrow Y122\bullet + F(III)\text{-}O\text{-}Fe(III) + H_2O \quad (1)$$

source perhaps another Fe(II). The reaction of the reduced R2 mutant, F208Y, with O_2 provides additional information on O_2 activation by this site (Ormö et al., 1992; Åberg et al., 1993). In this mutant, a tyrosine replaces Phe-208 in the hydrophobic pocket surrounding the diiron site. Crystallography and resonance Raman spectroscopy proved that Tyr-208 is oxidized to 3,4-dihydroxyphenylalanine (DOPA) and then undergoes bidentate coordination to one iron site. This tyrosine hydroxylase activity of F208Y R2 mutant suggests that R2, MMOH and Δ9D may share a common mechanism for the O_2 activation.

A common mechanism for O_2 activation by R2 and MMOH has been proposed, as shown in Figure 1.6 (Que & Dong, 1996). The diferrous unit provides two electrons to reduce dioxygen, yielding a diferric-peroxide complex. Recent Mössbauer analysis has detected a potential diferric-peroxide intermediate for R2 that has properties similar to compound **P** of MMOH ($\delta \cong 0.66$ mm/s, $\Delta E_Q \cong 1.5$ mm/s) (Tong et al., 1996). Support for the existence of a diferric-peroxide intermediate comes from another reaction. The diferric R2 can react with hydrogen peroxide to generate the tyrosyl radical (Sahlin et al., 1990).

The diferric-peroxide intermediates then undergoes homolytic cleavage to yield high-valent species called **Q** and **X** that are diiron analogs of heme peroxidase compounds **I** and **II** (Dawson, 1988). In the reaction of apo R2 with Fe^{2+}, O_2, and excess reductant, intermediate **X** accumulates with k_1 of 8 s^{-1}, and decays slowly with k_2 of 0.8 s^{-1}, which is the same rate constant observed for the formation of Tyr-122 radical and diferric cluster (Bollinger et al., 1994). This kinetics analysis strongly suggest that intermediate **X** is the diiron species that directly oxidizes Tyr-122 to the radical (Tong et al., 1996).

Intermediate X. The intermediate **X** of R2 is the first high valent (ferryl) intermediate found in non-heme systems. **X** has an electronic absorption feature at 365 nm and a free radical like X-band EPR signal with *g* value at 2.00 (Ravi et al., 1994). The EPR signal is hyperfine broadened by ^{57}Fe incorporation into the cluster or when the formation reaction was carried out with $^{17}O_2$ or in $H_2{}^{17}O$. This indicates that **X** is associated with the iron and oxygen cluster. The formal oxidation state of **X** is at the Fe^{III}/Fe^{IV} level, which is one electron more oxidized than the diferric R2 and

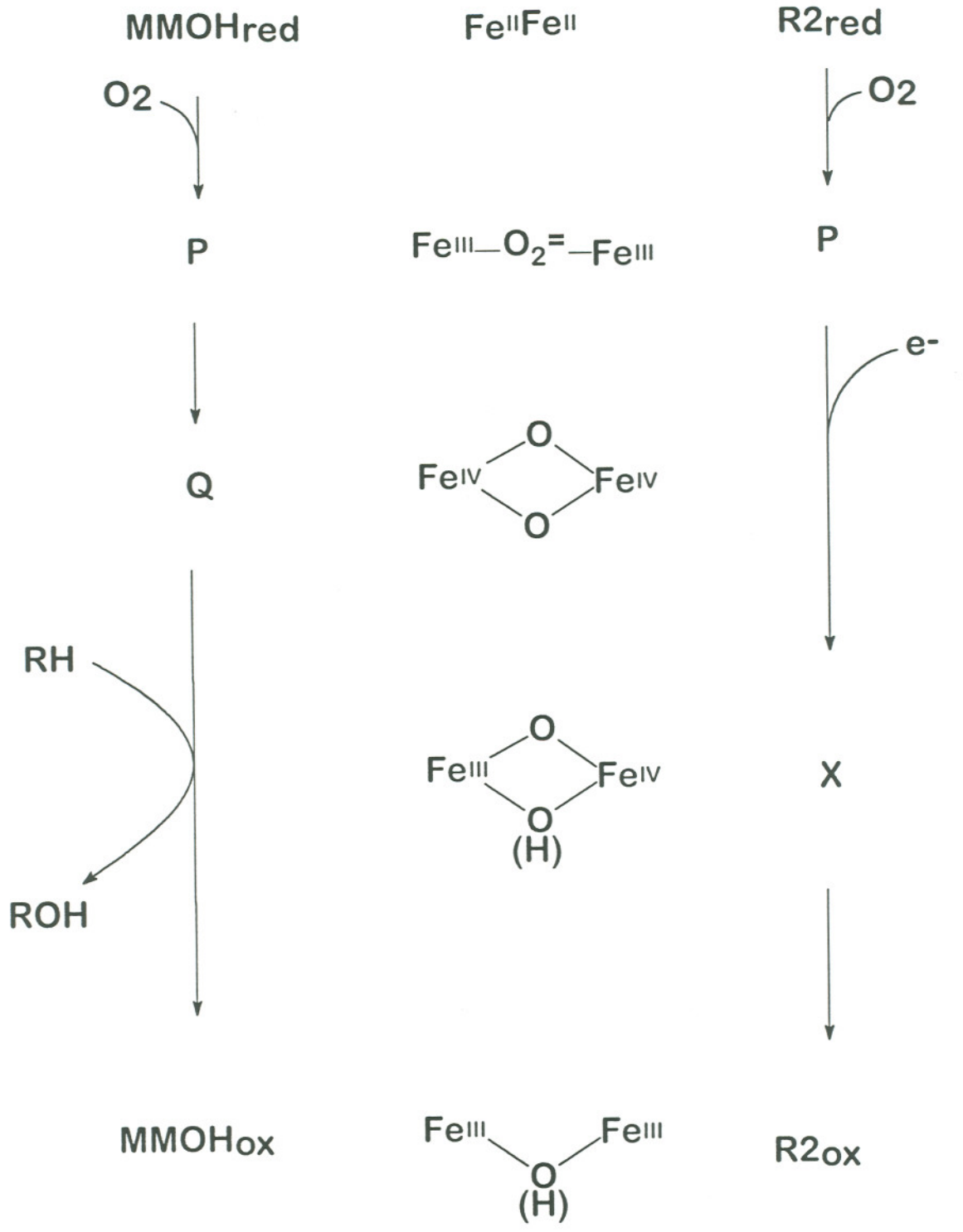

Figure 1.6 Proposed common mechanistic framework for R2 and MMOH. Adapted from Que & Dong, 1996.

one electron reduced from the compound **Q** state of MMOH. Mössbauer measurements and analysis assuming isotropic hyperfine coupling tensors for both iron sites, established that **X** contains two antiferromagnetically coupled iron ions, with isomer shifts at 0.55 and 0.36 mm/s. These studies led to a proposal that **X** is composed of two high spin coupled ferric ions and a ligand radical, which are mutually spin coupled to give an S = ½ ground state (Ravi et al., 1994). Recently, an extension of rapid freeze-quench methodology to Q-band ENDOR spectroscopy using ^{57}Fe has shown that one of the irons has a very nearly isotropic hyperfine tensor ($\mathbf{A}(Fe_A)$ = -[74.2(2), 72.2(2), 73.2(2)] MHz), as expected for Fe^{III}, but the other iron site displays considerable anisotropy ($\mathbf{A}(Fe_B)$ = +[27.5(2), 36.8(2), 36.8(2)] MHz), indicative of substantial Fe^{IV} character (Sturgeon et al., 1996). Reanalysis of the Mössbauer data using these results leads to isomer shifts of $\delta(Fe_A)$ = 0.56 mm/s and $\delta(Fe_B)$ = 0.26 mm/s. Based on the hyperfine anisotropy of Fe_B plus the reduced isomer shift, intermediate **X** is best described as a spin-coupled Fe(III)/Fe(IV) center with significant spin delocalization onto the oxygen ligands (Sturgeon et al., 1996).

^{17}O-ENDOR studies further demonstrated that **X** has three exogenous O atoms, two of which derive from O_2 and the third from water (Burdi et al., 1996). Resonance Raman with $^{18}O_2$ on the Y122F R2 demonstrated that the O_2 is the source of the oxo bridge in oxidized R2 (Ling et al., 1994). Recently, a high valent Fe^{III}/Fe^{IV} compound that contains $[Fe_2(\mu\text{-}O)_2]^{3+}$ diamond core complex has been synthesized from the reaction of a diiron(III) compound with hydrogen peroxide (Dong et al., 1995a,b). This $Fe_2(\mu\text{-}O)_2$ species also can carry out the reactions corresponding to those associated with R2, MMOH, and Δ9D (Kim et al., 1997). EXAFS characterization of **X** from the wild type protein revealed that **X** contains a very short Fe-Fe separation of 2.5 Å, which is similar to the $Fe_2(\mu\text{-}O)_2$ species in the model compound (Riggs-Gelasco et al., 1996). This led to a proposal that **X** may have an $[Fe_2(\mu\text{-}O)_2]$ structure.

Q-band ^{1}H ENDOR revealed the presence of strongly coupled, exchangeable proton(s) associated with one or more of the sites (Burdi et al., 1996). In another X-band ^{1}H ENDOR study on the R2-Y122F/Y356F mutant, it was concluded that a large hyperfine coupling in the 18–23 MHz range probably ruled out **X** containing a

terminally bound water, and suggested the presence of a bridging hydroxide or a strongly bound terminal hydroxide (Veselov & Scholes, 1996). The resonance Raman study with $^{18}O_2$ and $H_2{}^{18}O$ on the F208Y R2 showed that the source of the new oxygen in the DOPA-208 was from water rather than molecular oxygen (Ling et al., 1994). It is possible that the iron close to the Tyr-122 may contain a terminal hydroxide ligand. The detailed structure on **X** still is not clear, and needs more evidence.

Methane monooxygenase

Methane monooxygenase (MMO) is found in both a soluble and a membrane-bound form. The soluble MMO catalyzes the oxidation of methane to methanol, as depicted in equation 2.

$$CH_4 + O_2 + H^+ + NADH \rightarrow CH_3OH + H_2O + NAD^+ \qquad (2)$$

Most studies have focused on MMO isolated from *Methylococcus capsulatus* (Bath) (*MC*) (Feig & Lippard, 1994) or *Methylosinus trichosporium* (OB3b) (*MT)* (Lipscomb, 1994; Wallar & Lipscomb, 1996). The MMO has an $\alpha_2\beta_2\gamma_2$ composition with a molecular weight of 251 kDa (Fox et al., 1989). The MMO enzyme system contains three proteins, a hydroxylase housing two diiron centers, a reductase containing one FAD and one [2Fe-2S] cluster, and protein B, a coupling unit that facilitates electron transfer from the reductase to the hydroxylase (MMOH) and modulates the properties of the hydroxylase (Feig & Lippard, 1994; Lipscomb, 1994).

Diiron site Structure. Both oxidized and reduced MMOH from *MC* have been solved at 1.7-Å resolution in flash frozen crystals at -160°C (Figure 1.5) (Rosenzweig et al., 1995). Similar to R2, the diiron cluster resides in the center of a four-helix bundle (Figure 1.1), and two Glu-X-X-His motifs serve as ligands to the irons. In the oxidized form, there are three bridges between two irons: Glu-144, a hydroxide, and a water molecule. The absence of visible absorption, short Fe-O distance, and large antiferromagnetic exchange coupling excludes the possibility of an oxo bridge between the two irons (Feig & Lippard, 1994). The terminal ligands include two histidines (147 and 246), three glutamates (114, 243 and 209), and a

water molecule. A similar diiron site, but with a di-μ-OH diamond core, has been observed in the crystal structure of oxidized MMOH from *MT* (Wallar & Lipscomb, 1996). Upon reduction of the diiron cluster to the diferrous form, one specific ligand, Glu-243, undergoes a carboxylate shift. This carboxylate ligand shifts being from a terminal, monodentate ligand to Fe2 to a monodentate, bridging ligand between two irons. The second oxygen of this Glu-243 still coordinates to Fe2. In addition, the hydroxide bridge is lost, and the other water bridge shifts from serving as a bridge to being terminally bound to Fe1. Also, the terminal water bound to Fe1 in the oxidized form of MMOH seems to move out of bonding distance (2.63 Å) upon reduction of the cluster. Thus, the irons in reduced MMOH are five coordinate which is reasonable for their reaction with O_2. Conversion from oxidized MMOH to reduced MMOH increases the Fe-Fe distance from 3.1 Å to 3.28 Å. The crystal structure of the $MMOH_{ox}$ at room temperature shows a acetate bridge between the two irons, replacing the water bridge and increasing the Fe-Fe distance from 3.1 Å to 3.4 Å (Rosenzweig et al., 1993). This anion arises from the crystallization buffer and is not part of the native structure. Nonetheless, like R2, the coordination site of the diiron cluster in MMOH appears more flexible than in Hr.

The hydrophobic pocket adjacent to the active site in MMO is larger than the one found in R2. This is consistent with their different functions. MMOH can catalyze the oxidation of many hydrocarbon substrates (Lipscomb, 1994), including small molecules like methane as well as bulky compounds such as 2,2-diphenylmethylcyclopropane (Feig & Lippard, 1994). R2 does not bind exogenous substrate, but, instead catalyzes the oxidation of Tyr-122 within the protein. The diiron site in MMOH is accessible to large molecules. Resonance Raman spectra and a phenolate → Fe^{III} charge transfer transition in the electronic spectrum have demonstrated that phenol can bind directly to the iron atoms (Andersson et al., 1991).

Intermediate P. After the reaction of diferrous MMOH with O_2, an intermediate (called **P** or **L**) has formed and has been studied by spectroscopy (Lee et al., 1993a; Liu et al., 1995a). **P** has an absorption band near 600 nm (λ_{max} 625 nm, ϵ 1500 $M^{-1}cm^{-1}$) which can be assigned to peroxide → Fe(III) charge transfer (Lee et al., 1993a). **P** exhibits a symmetric Mössbauer doublet (δ = 0.66 mm/s, ΔE_Q =

1.51 mm/s) which indicates that both irons are in ferric states and the two iron sites in this intermediate are equivalent (Table 1.4) (Liu et al., 1994, 1995a). The Mössbauer data strongly support that peroxide binds with diferric center in a symmetric mode.

By comparison to copper-dioxygen systems, which have been more thoroughly investigated (Kitajima & Moro-oka, 1994), possible binding modes for O_2 to dinuclear metal centers have been proposed as in Figure 1.7 (Feig & Lippard, 1994). The terminal peroxo modes (e) and (f) are asymmetric, and thus cannot serve as binding modes for **P** with equivalent iron sites. The side-on bridging (c) mode has not been found in diiron systems. The O-O stretch of a model complex in which peroxide binds side-on (as in f) with mononuclear iron is at 815 cm^{-1} (Ahmad et al., 1988). The O-O stretch of hemocyanin in which the peroxo group is side-on ligated to dinuclear copper as in (c) is at 749 cm^{-1} (Ling et al., 1994b; Magnus et al., 1994). Recently, the crystal structures of one *trans*-μ-1,2-peroxo diferric complex (a) (Kim & Lippard, 1996) and two *cis*-μ-1,2-peroxo diferric complexes (b) (Dong et al., 1996; Ookubo et al., 1996) have been reported. These peroxide complexes exhibit a peroxide → Fe(III) charge transfer, a resonance Raman ν(O-O) near 900 cm^{-1} and diamagnetic Mössbauer parameters which are similar to that of intermediate **P** (Table 1.4). Thus, this strongly suggests that **P** has a μ-1,2-peroxo diferric structure.

Such a μ-1,2-peroxo diferric model is also consistent with the coordination of the diiron cluster in reduced MMOH in that both iron atoms have accessible positions for dioxygen binding. In chapter III, the binding of azide to the diiron site of Δ9D suggests that Δ9D may also have a μ-1,2-peroxo diferric intermediate. However, it is possible that the μ-1,2-peroxo diferric mode may convert to side-on bridging peroxo diferric mode (μ-η^2: η^2, as in Figure 1.7c) through ligand rearrangement in the diiron clusters. The interconversions between μ-1,2-peroxo and μ-η^2: η^2-peroxo binding modes have been detected in a peroxo dicopper(II) model complex for hemocyanin (Jung et al., 1996).

Intermediate Q. Intermediate **P** converts to a yellow (λ_{max} = 330, 430 nm) species named intermediate **Q** (Lee et al., 1993b; Liu et al., 1995a). The formation rate of **Q** is independent of substrate. In contrast, its decay rate is linearly dependent

Table 1.4

Spectroscopic Properties of Diferric Peroxide Compounds

Compounds	Electronic γ_{max} (ϵ) nm ($cm^{-1}M^{-1}$)	Raman ν(O-O) cm^{-1}	Mössbauer		Binding mode
			ΔE_Q mm/s	δ mm/s	
Intermediate P[a]	$\approx$ 600-650 (ϵ_{625} = 1500)	n.d.	1.51	0.66	*trans* μ-1,2?
$[Fe_2(\mu\text{-}O_2)(\mu\text{-}O_2CCH_2Ph)_2\{HB(pz')_3\}_2]$[b]	694 (2650)	888	1.40	0.66	*trans* μ-1,2
$[Fe_2(\mu\text{-}O_2)$(N-Et-HPTB)$(OPPh_3)_2](BF_4)_3$[c]	588 (1500)	900	0.72	0.52	*cis* μ-1,2
$[Fe_2(\mu\text{-}O_2)$(Ph-bimp)$(C_6H_5COO)](BF_4)_2$[d]	500-800 (1700)	n.d.	0.74 1.70	0.58 0.65	*cis* μ-1,2
Oxy-Hr[e]	500 (2200)	844	0.91 1.93	0.51 0.52	*syn* end-on

[a] Liu et al., 1995. [b] Kim & Lippard, 1996. [c] Dong et al., 1996; Menage et al., 1990.
[d] Ookubo et al., 1996. [e] Vincent et al., 1990.

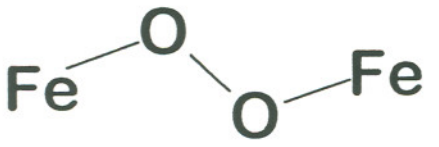

a) *trans* 1,2-bridge

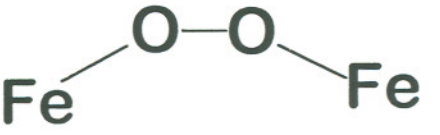

b) *cis* 1,2-bridge

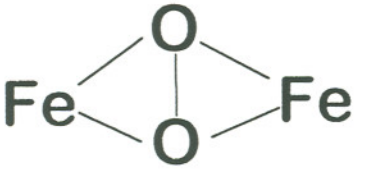

c) side-on bridge

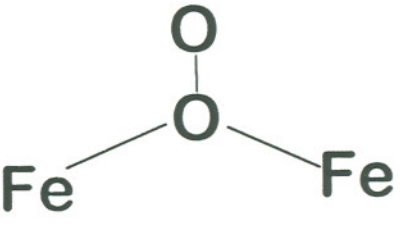

d) 1,1-bridge

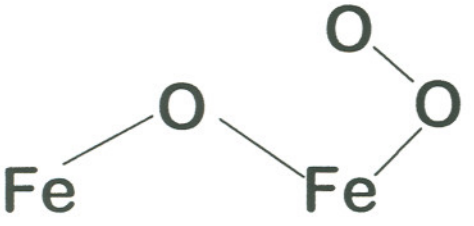

e) *syn* end-on

f) mono-iron end-on

Figure 1.7 Potential dioxygen binding modes for diiron compounds.

on substrate concentration (Lee et al., 1993a). Also, the product is formed at the same rate as **Q** decays. Thus, **Q** reacts directly with substrate to form product. The Mössbauer spectrum of **Q** from *MC* gives parameters δ = 0.21 mm/s, ΔE_Q = 0.68 mm/s and δ = 0.14 mm/s, ΔE_Q = 0.55 mm/s (Liu et al., 1994, 1995a) and from *MT*, parameters δ = 0.17 mm/s, ΔE_Q = 0.53 mm/s (Lee et al., 1993b), indicating that **Q** is a diferryl intermediate. In high applied field, it has a diamagnetic ground state. This suggests that **Q** contains an antiferromagnetically coupled diiron(IV) species. This is the first biological system shown to contain dinuclear Fe(IV) species.

EXAFS combined with Mössbauer analysis show that Q has a single Fe-O bond (1.77 Å) per iron atom and an Fe-Fe distance of 2.46 Å (Shu et al., 1997). By comparison with other synthesized $Fe_2(\mu\text{-}O)_2$ diamond core complexes (Que & Dong, 1996), **Q** has been proposed as a di-μ-oxo diiron(IV) diamond core structure (Figure 1.6). However, this diamond core structure of **Q** still remains controversial and needs more supporting evidence such as resonance Raman spectroscopy; thus far, the latter experiments have proven to be elusive.

Catalytic mechanism. Since the crystal structures of MMOH in both oxidized and reduced forms are known and the existence of **Q** and other intermediates have been demonstrated, it is of great interest to elucidate the substrate hydroxylation mechanism. During the hydroxylation reaction, one atom of O_2 is incorporated into methane to form CH_3OH and the other forms water (Fox et al., 1989). Several catalytic mechanisms for the oxygen insertion have been proposed (Feig & Lippard, 1994; Wallar & Lipscomb, 1996). Similar to P-450, the "rebound" mechanism was regarded as one of the favored mechanisms for this reaction (Wallar & Lipscomb, 1996). Intermediate **Q** abstracts a hydrogen atom from the substrate to yield a substrate radical intermediate and a metal-bound hydroxyl moiety. Radical recombination of the substrate and the hydroxyl radicals would yield oxygenated product. One supporting line of evidence comes from the experiment that (R)- or (S)-[$^2H_1$,$^3H_1$]ethane undergoes partial inversion of configuration during oxidation to ethanol, implying the formation of an unbound substrate-derived intermediate (Prestley et al., 1992). Another evidence is from the large deuterium kinetic isotope

effect of 50–100 for the reaction of compound **Q** with CH_4, implying that C-H bond breaking is a rate-limiting step in the oxygenation reaction (Nesheim et al., 1996).

Other diiron-oxo proteins

Stearoyl-acyl carrier protein Δ^9 desaturase (Δ9D). Another diiron containing enzyme that activates oxygen as a part of its catalytic cycle is Δ9D. Isolated from *Ricinus communis* (castor bean), this soluble enzyme inserts a 9,10 *cis* double bond into the bound fatty acid of stearoyl-acyl carrier protein (ACP) to convert it to oleoyl-ACP in the presence of O_2, NAD(P)H, NAD(P)H ferredoxin oxidoreductase, and ferredoxin (Nagai & Bloch, 1968). Despite the requirement of O_2, no oxygen atom is incorporated into the product. Nevertheless, the active site structure and general characteristics of the reaction appear to be similar to those of MMO. Thus, it is possible that this enzyme catalyzes the first half of an MMO-like reaction to generate a radical intermediate of the substrate, but does not complete the OH rebound step to yield an alcohol. Instead, a second electron is apparently abstracted to yield a desaturated bond and a second water.

Δ9D has been purified from a variety of species. The soluble desaturase protein has been shown to be a homodimer with a molecular weight near 70 kDa (McKeon & Stumpf, 1982; Shanklin & Somerville, 1991). Past studies have demonstrated that Δ9D contained iron (Strittmatter et al., 1974). More recent electronic, Mössbauer, and resonance Raman studies with the castor bean desaturase have shown that each monomer of the homodimer contains an oxo-bridged diiron core (Fox et al., 1993, 1994). More specifically, the Mössbauer results indicated that Δ9D contained mostly antiferromagnetically spin-coupled high-spin Fe(III) sites (~80%), manifested in a single quadrupole doublet (ΔE_Q = 1.54 mm/s and δ = 0.53 mm/s), with the minority of the iron (~20%) existing in the high-spin diferrous form (Fox et al., 1993). The strong coupling that was observed ($J > 60$ cm^{-1}) is in accord with the existence of an oxo bridge. The isomer shift of the quadrupole doublet is at the high range of values for diferric clusters, which suggested that the coordination environment of the irons is rich in oxygenous ligands, such as water and carboxylates. As presented in chapter II, resonance Raman studies reveal symmetric and

asymmetric vibrational modes (519 and 747 cm^{-1}) that are typical of oxo-bridged diiron clusters (Fox et al., 1994).

Even though Δ9D does not have the same substrate specificity or catalytic outcome as MMOH and R2, it does seem to have the same active site residues, which include two Glu-X-X-His motifs as the ligands to the irons, and the residues involved in a hydrogen bonding network to the iron cluster (Asp, Glu, Arg), and a threonine that may play a part role in O_2 binding or proton transport (Fox et al., 1994). The crystal structure of reduced Δ9D has been determined to a resolution of 2.4 Å (Lindqvist et al., 1996). The 363 amino acid monomer consists of a single domain of 11 α-helices. Nine of these form an antiparallel helix bundle. The enzyme subunit contains a diiron cluster, with ligands from four of the α-helices in the helix bundle (Figure 1.1). The structure of the diiron cluster is shown in Figure 1.8. The distance between the iron atoms is 4.2 Å, and the coordination geometry of each iron is a distorted octahedron where one of ligand position is unoccupied. The structure of the cluster is highly symmetric. Both Glu-143 and Glu-229 act as bridging ligands. Glu-105 is a bidentate ligand to one iron ion and, correspondingly, Glu-196 is a bidentate ligand to the second iron ion. Each iron ion is also ligated by a nitrogen atom, δN in His-146 and His-232 respectively. The orientation of the iron ligands is maintained by side chain hydrogen bonds. A water molecule is 3.2 and 3.4 Å to the iron ions respectively, and thus within the second coordination sphere from the iron atoms. This water molecule is located in a small hydrophobic pocket composed of Thr-199 and Trp-139 residues.

A superposition of the structure of Δ9D on the three-dimensional structures of two other diiron proteins, the R2 subunit of ribonucleotide reductase from *E. coli* (Nordlund et al., 1990) and the α subunit of MMO from *M. capsulatus* (Rosenzweig et al., 1993) shows that their overall structures are similar. With the conserved amino acid residues, there is little doubt that these enzymes are evolutionary related. Therefore, they may also share the similar oxygen activation mechanism with the common intermediates such as diferric peroxide and diferryl intermediates.

Rubrerythrin. Rubrerythrin (Rr) from anaerobic sulfate-reducing bacteria *Desulfovibrio vulgaris* contains two types of iron sites: one rubredoxin-like $Fe(SCys)_4$

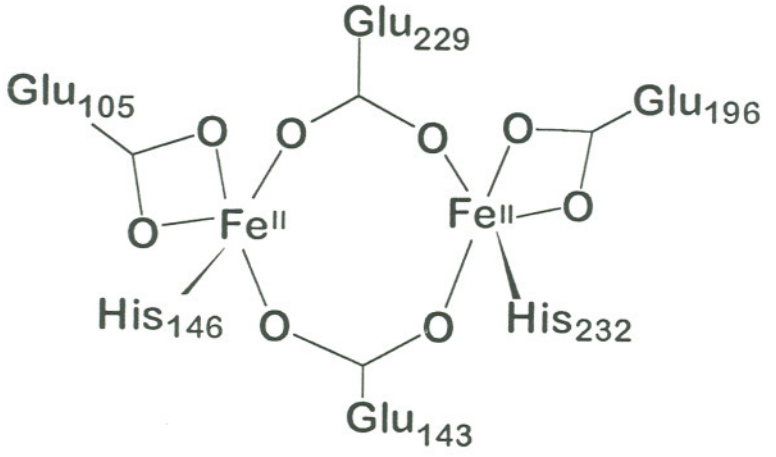

Figure 1.8 Schematic diagram of diiron site of reduced Δ9D. Adapted from Lindqvist et al., 1996.

site and one oxo-bridged diiron site (Ravi et al., 1993; Dave et al., 1994). The four-helix bundle structure of Rr shows a particularly striking similarity to those of bacterioferritin and the H-chain ferritin subunits (Figure 1.1) (DeMaré et al., 1996). Together with its ferroxidase activity (Bonomi et al., 1996), Rr is likely involved in the iron metabolism. Comparing with R2 and MMOH, the crystal structure of Rr shows that the His residue in the first EXXH motif (His-56) is not coordinated to the iron in the oxidized form, instead, an additional glutamate (Glu-97) coordinates with iron. The diiron site in Rr is located close to the protein surface, and the ligands Glu-94, Glu-97 and the oxo bridge are solvent accessible (DeMaré et al., 1996). The whole structure of Rr is significantly smaller, and lacks many of the connecting helices present in R2 and MMOH (Nordlund & Eklund, 1995). Therefore, the diiron site of Rr may well have a different function from those of R2 and MMOH. Rr may serve as another example of a protein similar to bacterioferritin and the H-chain subunit of ferritin with ferroxidase activity (Bonomi et al., 1996).

Small Molecules as Probes for O_2 Binding

The diiron proteins discussed above utilize O_2 as substrate to transport or they activate O_2 during their reactions. The intermediates **X** from R2, and **P** and **Q** from MMOH have been identified. However, the exact structures of these intermediates remain a challenging topic for the biochemist and spectroscopist because of the limited stability and the concentration of these intermediates. Therefore, it is helpful to use other small molecules having a similar structure to oxygen to mimic the structures of these intermediates. In this section, I will briefly review how azide and NO have been used to probe O_2 binding in dinuclear systems such as Hr and R2.

Azide with met-Hr

Since the highest occupied orbitals of azide are a set of filled degenerate nonbonding π orbitals analogous to the set of degenerate nonbonding π^* in peroxide, azide is a spectroscopic analogue for peroxide (Pate et al., 1989). Azide is a strong π donor ligand, so it can form a stable complex with both ferrous or ferric ions.

In addition to binding oxygen reversibly, Hr can form complexes with a wide range of anionic ligands, such as azide and chloride (Garbett et al., 1969). Azidomet-Hr has an absorption band at 490 nm (ϵ = 2000 $M^{-1}cm^{-1}$) assigned to $N_3^- \rightarrow$Fe(III) charge transfer (Reem et al., 1989). The resonance Raman spectrum of azidomet-Hr exhibits a ν_s(Fe-O-Fe) peak at 507 cm^{-1}, indicating it contains a normal diiron-oxo structure as in met-Hr (Dunn et al., 1975). By the way, azidomet-Hr also has a ν(Fe-N_3) peak at 376 cm^{-1} and a ν(N-N-N) peak at 2049 cm^{-1}. With mixed isotopically labeled azide ($^{15}N^{14}N^{14}N$), the ν(N-N-N) peak split into two peaks, suggesting that azide binds to the diiron-oxo cluster in an end-on mode (Kurtz et al., 1976). The crystal structures of azidomet-Hr solved at 2.0 Å resolution showed that azide indeed binds the Fe2 site in an end-on binding mode (Stenkamp et al., 1984), consistent with the results from the resonance Raman studies. As a result of these azidomet-Hr studies, a similar end-on binding for O_2 was proposed in oxy-Hr. Later, the crystal structure of oxy-Hr confirmed that peroxide and azide are bound in an analogous geometric disposition (Holmes et al., 1991).

Azide with deoxy-Hr and reduced R2

Studies of the binding reactivities of azide with deoxy-Hr and reduced R2 has led to structural information about the coordination environment of the diferrous active site in these proteins. As discussed earlier in this chapter, the crystal structures show that the diferrous site in Hr, R2, and MMOH are all coordinatively unsaturated. Azide binds to the open coordination position on the five-coordinate Fe(II) of deoxy-Hr (K_B = 70 M^{-1}), resulting in two six-coordinate Fe(II) ions (Reem & Solomon, 1987). Azide titration studies on fully reduced R2 indicate that azide can bind to both ferrous sites with reduced affinities at K_B = 21 and 3 M^{-1}, respectively (Pulver et al., 1995). In contrast, azide does not bind to the diferrous site in MMOH (Pulver et al., 1993). In deoxy-Hr, the diferrous center has five histidine ligands and two carboxylate ligands. Since histidines are neutral ligands, the $Fe^{II}Fe^{II}$ center has an overall positive charge. Hence, azide can interact well with this active site on the basis of electrostatics. In contrast, the diferrous sites in R2 and MMOH have two histidine ligands and four carboxylate ligands. The abundance of carboxylate ligands

leads to a neutral diferrous center, which is reflected in decreased azide binding. The reason for the difference of azide binding between reduced R2 and MMOH is not clear, however, it suggests that the diiron site in MMOH is more negative. This can explain why MMOH has a comparatively long-lived [$Fe^{IV}Fe^{IV}$] intermediate **Q**, while R2 has a relatively stable [$Fe^{III}Fe^{IV}$] intermediate **X**, which is one electron reduced from **Q**. The abundance of histidine ligands in Hr stabilizes oxy-Hr toward further activation of the peroxide, a reaction that must be prevented in this respiratory protein.

NO as probe for O_2 binding

Nitric oxide (NO) has a similar structure and electronic properties to O_2, and can be used as an O_2 analog to study the O_2 binding. NO can reversibly form adducts with the diiron site of deoxy-Hr (Nocek et al., 1988). It directly coordinates to the Fe2 site in a bent end-on fashion, with a H-bond to the proton of the μ-hydroxo bridge in the Fe-(OH)-Fe unit. This binding mode is very close to that of O_2 in oxy-Hr (Figure 1.2).

The reaction of NO with the diiron(II) center of R2 has also been investigated by spectroscopic methods (Haskin et al., 1995). The reduced R2 reacts with NO to form an adduct with visible absorption features at 450 and 620 nm and Mössbauer parameters of δ = 0.75 mm/s, ΔE_Q = -2.13 and -1.73 mm/s (Haskin et al., 1995), which are typical characteristics of those complexes with high-spin iron(III) antiferromagnetically coupled to NO^- (Brown et al., 1995). However, unlike other non-heme Fe^{III}-NO^- complexes, this product is EPR silent. Mössbauer studies showed that each iron site of reduced R2 binds one NO to form local Fe^{III}-NO^- centers which then couple antiferromagnetically with $J \approx -5\ cm^{-1}$ to afford an $\{FeNO\}_2$ center. This center then decomposes to form oxidized R2 accompanied by the release of N_2O. These observations suggest that both iron(II) ions of the diferrous center of reduced R2 have available sites for NO binding, in agreement with the crystal structure of reduced R2 (Figure 1.4). Furthermore, the bound NO molecules are sufficiently close to each other to permit N-N bond formation to produce N_2O in a reaction analogous to that catalyzed by NO reductase (Girsch & de Vries, 1997). These

observations support the proposal that O_2 binding may involve both Fe(II) centers to form a μ-1,2-peroxo diferric center.

Scope of This Thesis

In this thesis, resonance Raman spectroscopy was used to study several diiron-oxo proteins including Δ9D, Mhr, the L103N mutant of Mhr, and the L28Y mutant of Hr. Our goals were to obtain structural information about the diiron-oxo sites, and to try to understand the nature of the reactions at these active sites. In Chapter II, resonance Raman was used to identify the Fe-O-Fe center in Δ9D. The angle of the Fe-O-Fe bridge and the source of the oxo-bridge were also characterized. The comparison of the active site amino acid sequence with those of Mhr, Hr, R2, and MMOH were used to classify Δ9D, R2 and MMOH as Class II diiron proteins, whereas Mhr and Hr were classified as Class I diiron proteins.

In Chapter III, we used azide to react with diferric Δ9D as a model for the O_2 binding. A μ-1,2 mode for O_2 binding was proposed.

In Chapter IV, we used resonance Raman spectroscopy to study Mhr and its L103N mutant. It was found that the mutation of L103N introduced a hydroxide ligand into the Fe2 site, and weakened the binding of azide.

In Chapter V, we combined electronic, resonance Raman, and EPR spectroscopy to characterize a novel Fe^{II}-O-Fe^{III} cluster in the L28Y mutant of Hr, in which the hydrophobic environment around the diiron-oxo site increased. In addition, we found that the L98Y and the L98A mutant with added phenol can form ferric-phenolate complexes, whereas L98A mutant with catechol formed a monodentate ferric-catecholate complex.

Chapter VI presents conclusions on the significance of the findings in this thesis and directions for future research.

CHAPTER II

RESONANCE RAMAN EVIDENCE FOR AN FE-O-FE CENTER IN STEAROYL-ACP DESATURASE. PRIMARY SEQUENCE IDENTITY WITH OTHER DIIRON-OXO PROTEINS[1]

Abstract

The stearoyl-ACP Δ9 desaturase from plants is a new example of a growing number of proteins that contain oxo or hydroxo-bridged diiron clusters. Based upon differences in primary sequence motifs providing the cluster ligands and upon structural differences elucidated by X-ray crystallography, we now propose that the presently known, soluble diiron-oxo proteins can be grouped into two classes, I and II. Class I contains hemerythrin, myohemerythrin and, possibly, purple acid phosphatase. Class II contains ribonucleotide reductases, bacterial hydrocarbon hydroxylases (methane monooxygenase, toluene-4-monooxygenase and phenol hydroxylase), rubrerythrin, and stearoyl-ACP desaturases. Through the use of resonance Raman spectroscopy, we have detected symmetric (ν_s = 519 cm^{-1}) and asymmetric (ν_{as} = 747 cm^{-1}) vibrational modes in the castor stearoyl-ACP Δ^9 desaturase, which are typical of oxo-bridged diiron clusters. These frequencies shift by −18 and −34 cm^{-1}, respectively, in $H_2{}^{18}O$, proving that the bridging ligand is readily exchangeable with solvent ($t_{1/2}$ = 7 min). Calculation of an ~123° Fe-O-Fe angle from the position of ν_s and ν_{as} and from the ^{18}O-dependent shift in these frequencies suggests that the diiron-oxo cluster in the desaturase is triply bridged in the diferric state. In the diferrous state, the two iron sites of the cluster are structurally inequivalent, as shown by differential temperature dependence of the

[1] As published in *Biochemistry* **1994**, *33*, 12776–12786. Reprinted with permission.

Mössbauer quadrupole splittings. For the class II diiron-oxo proteins, primary sequence alignments reveal conserved amino acid residues which act as iron cluster ligands, participate in a H-bonding network, and are potentially involved in O_2-binding and activation. Based on this conservation, a structural model for the stearoyl-ACP Δ^9 desaturase active site is proposed that has strong similarity to both ribonucleotide reductase and methane monooxygenase. However, after single turnover of the diferrous state with $^{18}O_2$, ^{18}O is not detected in the oxo bridge of the castor desaturase. This is in contrast to the outcome observed for ribonucleotide reductase, suggesting the desaturase and ribonucleotide reductase differ in certain aspects of their respective O_2-activation reactions.

Introduction

Diiron-oxo clusters have now been identified in the proteins of a wide variety of organisms (Sanders-Loehr, 1989; Que & True, 1990; Vincent et al., 1990). These clusters contain two iron atoms connected by either an oxo or a hydroxo bridging ligand. At least one other bridging ligand is a carboxylate group provided by Asp or Glu. The remaining protein-derived iron ligands are N-atoms from His and O-atoms from either Asp or Glu. For hemerythrin (Hr), ribonucleotide reductase (R2) and methane monooxygenase (MMOH), the diiron-oxo proteins whose X-ray structures have been solved, all protein-derived cluster ligands are provided by a protein secondary structural motif consisting of four a helices (Holmes et al., 1991; Nordlund & Eklund, 1993; Rosenzweig et al., 1993). The primary ligation spheres of Hr and R2 are shown in Figure 2.1, while the primary sequence motifs and the connectivities of the alpha helices are shown in Figure 2.2. Based upon differences in the primary sequence motif providing these ligands and upon structural differences elucidated by X-ray crystallography, we now propose that the above proteins can be grouped into two classes, I and II. A third category, class III, for membrane-associated diiron enzymes, is described in a companion paper (Shanklin et al., 1994).

The best characterized class I diiron-oxo protein is Hr, an O_2-transport protein from marine worms (Loehr & Shiemke, 1988). The X-ray structure of Hr (Holmes et

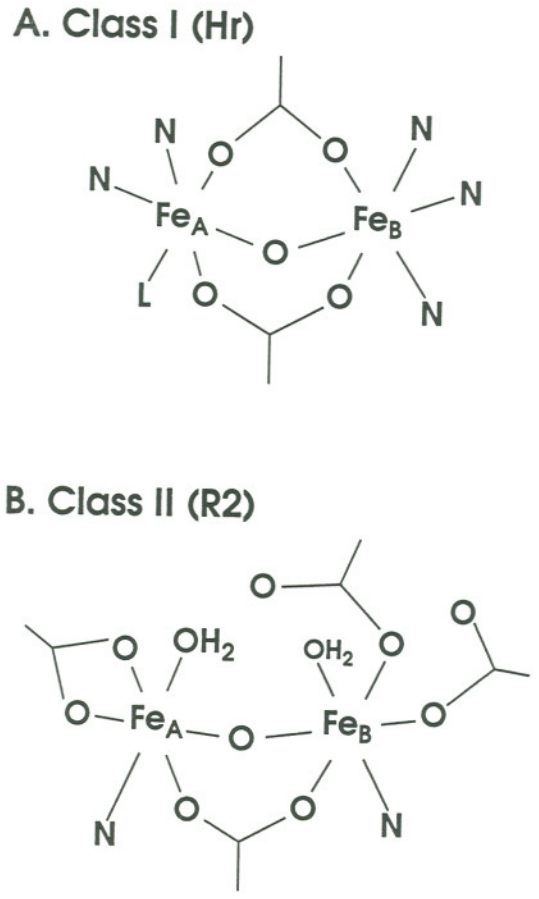

Figure 2.1 Structures of the oxo bridged diferric clusters found in two classes of diiron-oxo proteins. (A) Class I, as exemplified by Hr (Holmes et al., 1991). (B) Class II, as exemplified by R2 (Nordlund & Eklund, 1993).

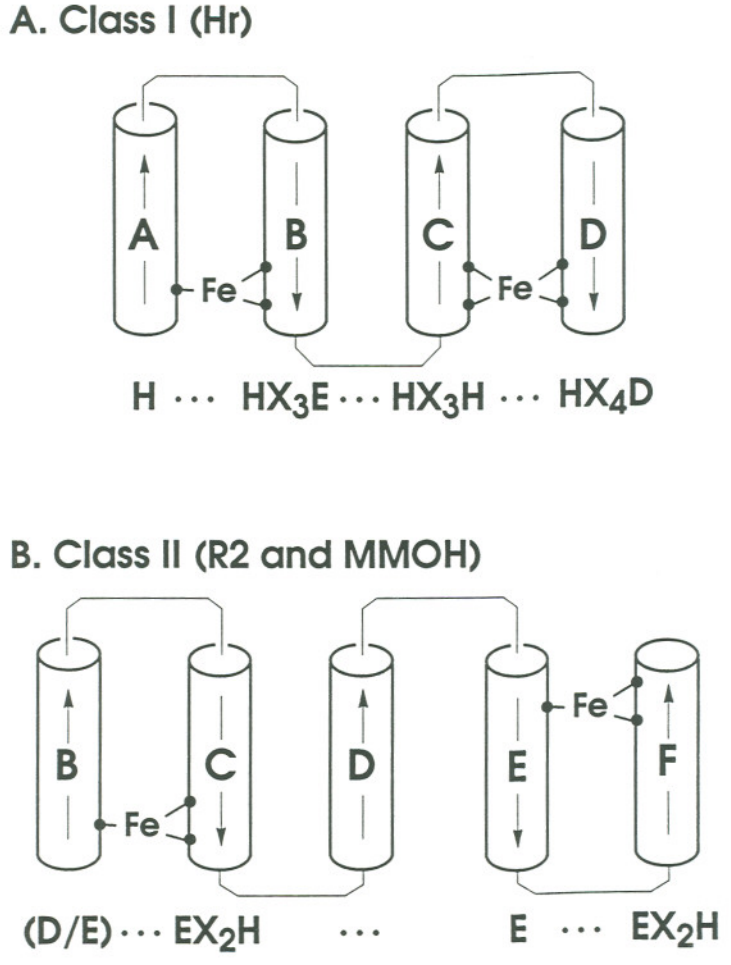

Figure 2.2 Connectivity of the four helix bundles providing the iron-binding ligands in the class I and class II diiron-oxo proteins. The helices are labeled using the nomenclature developed for Hr (Sheriff et al., 1987) and R2 (Nordlund et al., 1990), respectively. The primary sequence motifs present in these two classes are as indicated. For the class II, helices B and C contribute ligands to the Fe_A site, while helices E and F contribute ligands to the Fe_B site.

al., 1991) and myoHr (Sheriff et al., 1987) shows that the diiron axis is oriented *perpendicular* relative to the long axis of the four helix bundle, with ligands arising from four contiguous helices, A, B, C and D (Figure 2.2A). In the diferric state, Hr contains an oxo bridge and two carboxylate bridges, one each from Asp and Glu residues (Figure 2.1A). One iron atom, Fe^A, is coordinated by two His residues and has a coordination site where O_2 binds to the diferrous state (L in Figure 2.1A). The other iron atom, Fe_B, is coordinated by three His residues. The only ligand change upon deoxygenation is the protonation of the oxo bridge (Holmes et al., 1991). For Hr, six of the protein ligands of the cluster are provided by an HX_3E, HX_3H and HX_4D primary sequence motif (Sanders-Loehr & Loehr, 1979).

The best characterized class II diiron-oxo proteins are the R2 component of ribonucleotide reductase (Fontecave et al., 1992), the hydroxylase component of methane monooxygenase (MMOH) (Froland et al., 1991), and rubrerythrin (RBR) (Ravi et al., 1993). The X-ray structures of R2 and MMOH show that the class II proteins have the diiron axis oriented *parallel* to the long axis of the four-helix bundle with ligands arising from four non-contiguous helices, B, C, E and F (see Figure 2.2B) (Nordlund & Eklund, 1993; Rosenzweig et al., 1993). Since both the diiron moieties and the helical pairs have opposite orientations in the class I and class II proteins, it is unlikely that these two classes are evolutionarily related (Nordlund et al., 1990b). R2, MMOH, and RBR contain two copies of the primary sequence motif EX_2H that are separated by an intervening sequence containing helix D and other secondary structural elements. The His residues in each of these sequences act as a ligand for one iron atom (see Figure 2.1B). In the diferric state of R2, one Glu residue (E115) is a bridging ligand (Nordlund & Eklund, 1993), while a "semi-bridging" Glu residue (E144) and an exogenous bridging ligand, most likely acetate, are observed in the diferric state of MMOH (Rosenzweig et al., 1993). The remaining coordination sites are occupied by oxygen-containing ligands: protein carboxylates or solvent water. Resonance Raman studies have shown that both R2 (Sjšberg et al., 1982) and RBR (Dave et al., 1994) contain oxo bridged clusters in the diferric state while Mössbauer, integer-spin EPR (Fox et al., 1993) and EXAFS

(DeWitt et al., 1991) studies indicate MMOH has a hydroxo bridged cluster in the diferric state.

Our recent studies indicate that the stearoyl-acyl carrier protein Δ^9 desaturase (Δ9D) from castor plant is a new example of a diiron-oxo enzyme (Fox et al., 1993). In the present work, primary sequence alignments place Δ9D in class II, while optical and Mössbauer studies are consistent with a diiron-oxo cluster structure similar to that of R2 and RBR. Through the use of resonance Raman (RR) spectroscopy, we have now identified Fe-O-Fe vibrational modes which confirm that diferric Δ9D has an oxo bridge and that this oxo bridge is readily exchangeable with solvent water.

The class II diiron-oxo proteins can also be grouped into three different catalytic subclasses based on their known O_2-utilizing reactions: tyrosine radical formation by R2 (Bollinger et al., 1991; Ling et al., 1994); hydrocarbon hydroxylation by MMOH (Froland et al., 1992); and the insertion of a 9,10 *cis* double bond by Δ9D, converting stearoyl-ACP to oleyl-ACP (Nagai & Bloch, 1968). Despite these differences in substrate specificity and catalytic outcome, Δ9D appears to have the same active site residues as the other class II diiron-oxo enzymes. This includes Glu and His residues that are ligands to the iron atoms, Asp, Glu and Arg residues that are involved in a hydrogen bonding network to the cluster and a Thr residue that may be part of the O_2-binding site. However, ^{18}O is not detected in the oxo bridge following single turnover of the diferrous Δ9D with $^{18}O_2$, which is in contrast to the result observed for R2 (Ling et al., 1994). Thus, the stearoyl-ACP desaturases likely use a pathway of O_2-activation differing from that proposed for R2.

Materials and Methods

Bacterial expression vector, protein purification, and reagents

An expression vector for the Δ9D from castor (*Ricinus communis*) was constructed as previously described (Shanklin & Somerville, 1991; Fox et al., 1993b). Expression of the Δ9D in *Escherichia coli* BL21(DE3) was as previously described except that the ampicillin concentration was increased to 0.1 g/liter and the concentration of isopropyl-thio-galactopyranoside was increased to 0.5 mM. Induced

cells were collected after 5 h by centrifugation, washed in 25 mM HEPES, pH 8, and stored at -80°C. The Δ9D was purified as previously reported and the concentration of clusters was determined from the absorbance at 340 nm (ϵ_{340} = 4200 cm^{-1} M^{-1} per cluster) (Fox et al., 1993b).

Solvent isotope exchange

Samples of the Δ9D (1.2 mM) in 50 mM HEPES (pH 7.8) containing 50 mM NaCl and 5% (v/v) glycerol were diluted four-fold into the same buffer (pH reading 7.8) prepared in $H_2{}^{18}O$ (97 atom %, ICON) or D_2O (99.7 atom %, Merck, Sharp, and Dohme) without glycerol and concentrated six-fold using a Microcon-30 device (Amicon). The samples were then diluted five-fold with the same buffer and reconcentrated ten-fold to give final Δ9D samples that were ~3.5 mM in cluster with an $H_2{}^{18}O$ or D_2O enrichment of 90%. The samples were incubated overnight at 4°C prior to use in Raman experiments. A control sample of the Δ9D was prepared in $H_2{}^{16}O$ using the same procedures.

The rate of isotope exchange with solvent was measured by mixing a Δ9D sample in $H_2{}^{16}O$ with an equal volume of buffer in $H_2{}^{18}O$, incubating for a certain length of time, and then allowing the sample to freeze on the cold head of the Displex closed-cycle helium refrigerator (Air Products). For reaction times of less than 9 minutes, the sample was instead frozen by ejecting a 20 mL droplet into isopentane chilled with liquid nitrogen. The latter sample was transferred to the cold head of the Displex prechilled to 180 K, evacuated 2 hours at 180 K to remove isopentane, and then cooled to 15 K.

Gaseous isotope incorporation

Concentrated Δ9D (~3.5 mM cluster) in $H_2{}^{16}O$ buffer, prepared as above, was mixed with ~3.5 mM ACP (*E. coli*, Sigma) and 10 mM methyl viologen and flushed with argon gas. The clusters were reduced by the anaerobic addition of ~5 mM sodium dithionite. Reoxidation was accomplished by the addition of $^{16}O_2$ (1 mL air) or $^{18}O_2$ (0.5 mL of 98.7 atom %, YEDA, Rehovot, Israel) with the greenish

yellow color of the diferric cluster reappearing in ~2 min. The samples were then transferred to capillary tubes and frozen in liquid nitrogen.

Resonance Raman spectroscopy

Raman spectra were recorded on a computerized Jarrell-Ash spectrophotometer using an RCA C31034 photomultiplier tube and an ORTEC model 9302 amplifier-discriminator. The excitation source was a Spectra-Physics 2025-11 (Kr) or Spectra-Physics 164 (Ar) laser. Spectra were obtained in a 150°-backscattering geometry from samples cooled to 15 K on the cold head of a Displex or to 90 K in capillaries inserted into a copper rod in a Dewar flask filled with liquid nitrogen (Loehr & Sanders-Loehr, 1993). The Raman spectrometer was calibrated by scattering from CCl_4 and peak positions are estimated to be accurate to ± 1 cm^{-1}. Raman data were processed by use of LabCalc (Galactic Industries). For the RR excitation profile, all spectra were recorded on the same sample under the same instrumental conditions. Enhancement was measured as the area of the protein peak relative to the area of the ice peak at 230 cm^{-1}.

Mössbauer spectroscopy

Mössbauer samples of the diferrous Δ9D were prepared and spectra were obtained as previously described (Fox et al., 1993b). Least-squares fitting was used to determine the splittings of the two partially resolved quadrupole doublets in the diferrous Δ9D using WMOSS (WEB Research Co.). A Fourier filtering procedure was used to enhance spectral resolution by removing the contribution of the source linewidth from the experimental spectra (Dibar Ure & Flinn, 1971; Filter et al., 1978). The individual areas of the two doublets were constrained to equal contributions during these fitting procedures. No significant improvement in the quality of the fits was obtained by allowing the areas to be parameters in the fitting procedure.

Primary sequence analysis

Portions of the following amino acid sequences were obtained from nucleotide sequences (GenBank, release 79.0, October, 1993; EMBL, release 36.0, September, 1993; Accession numbers and abbreviations used in Figures 2.8 and 2.9 are indicated). Ribonucleotide reductases: *E. coli* (K02672, Eco) (Carlson et al., 1984); Epstein-Barr virus (V01555, EBV). Methane monooxygenase hydroxylases: *Methylococcus capsulatus* (Bath) (M58499, Mc) (Stainthorpe et al., 1990); *Methylosinus trichosporium* OB3b (X55394, Mt) (Cardy et al., 1991). Toluene-4-monooxygenase *tmoA* polypeptide, *Pseudomonas mendocina* KR1 (M65106, Pm) (Yen et al., 1991). Phenol hydroxylase *dmpN* polypeptide, *Pseudomonas* sp. CF600 (M60276, Ps) (Nordlund et al., 1990a). Stearoyl-ACP desaturases: castor (M59857, cas) (Shanklin & Somerville, 1991); safflower (M61109, saf) (Thompson et al., 1991); cucumber (M59858, cuc) (Shanklin & Somerville, 1991); spinach (X62898, spn) (Nishida et al., 1992); *Brassica* (X60978, brs) (Knutzon et al., 1992); *Simmondsia* (M83119, smm); potato (M91238, pot); linseed (X70962, lns); Δ^4 desaturase, coriander (M93115, cor) (Cahoon et al., 1992). BESTFIT is part of the Genetics Computer Group software package.

Results

Electronic spectrum of Δ9D

Proteins and model complexes containing oxo-bridged diiron clusters exhibit intense absorption bands in the UV region (300–370 nm, ϵ_{max} = 4,000–9,000 M^{-1} cm^{-1} per cluster). These transitions have been assigned as oxo → Fe^{3+} charge transfer (CT) (Reem et al., 1989; Sanders-Loehr et al., 1989). The absorption spectrum of Δ9D is typical of an Fe-O-Fe system with two intense bands at 325 and 355 nm and a series of weaker bands at 470 and 570 nm (Figure 2.3). The weaker bands may include contributions from both CT and ligand field transitions. The intensity and shape of the absorption spectrum is unchanged in the pH range from 6 to 9. Since conversion of an oxo bridge to a hydroxo species would lead to altered

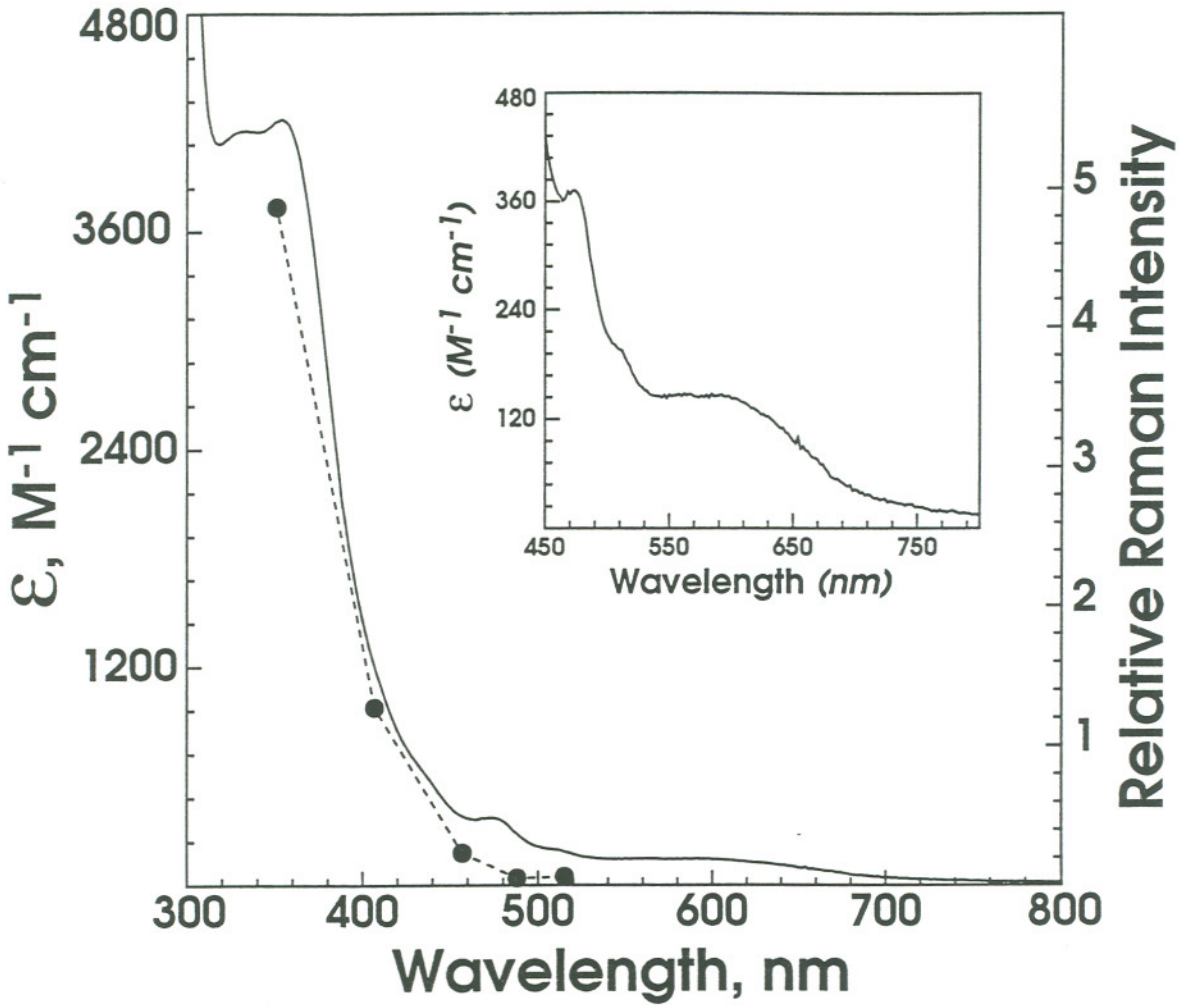

Figure 2.3 Absorption spectrum (____) and RR excitation profile (-----) for the Fe-O-Fe moiety of Δ9D. Raman intensity at 519 cm^{-1} was measured relative to the 230-cm^{-1} ice peak using conditions as in Figure 2.4, but with additional excitations at 406.7 nm (20 mW), 457.9 nm (30 mW), 488.0 nm (30 mW), and 514.5 nm (40 mW). The inset shows an expanded scale of the low intensity absorption features in the 450–800 nm region. Samples in 50 mM HEPES, pH 7.8 and 50 mM NaCl.

spectral frequencies and diminished intensities (Turowski et al., 1994), it is unlikely that a change in the protonation state of the Δ9D cluster core occurs in this pH range.

Resonance Raman spectrum of Δ9D

Three vibrational modes are expected for an oxo-bridged diiron center: a symmetric stretch, ν_s(Fe-O-Fe), an asymmetric stretch, ν_{as}(Fe-O-Fe), and an Fe-O-Fe bend, with the symmetric stretch being the major contributor in a resonance Raman spectrum (Sanders-Loehr et al., 1989). Excitation of Δ9D within the oxo → Fe CT band leads to the appearance of two resonance-enhanced Raman features at 519 and 747 cm^{-1} (Figure 2.4A), which are at the correct energies and relative intensities for ν_s(Fe-O-Fe) and ν_{as}(Fe-O-Fe), respectively. These assignments have been verified by observing that the two peaks shift by −18 and −34 cm^{-1}, respectively, when Δ9D is equilibrated in $H_2{}^{18}O$ (Figure 2.4C). The Fe-O-Fe frequencies for Δ9D are similar to those observed for other diiron-oxo proteins, particularly Hr and RBR (Table 2.1). The excitation profile for the ν_s(Fe-O-Fe) mode of Δ9D shows that the Raman intensity maximizes within the 350-nm absorption band (Figure 2.3), thereby providing definitive evidence for the oxo → Fe(III) CT assignment. The excitation profile for Δ9D is similar to that of oxyHr whose Raman intensity also tracks its 360-nm absorption (Sanders-Loehr et al., 1989).

Vibrational frequencies for ν_s(M-O-M) and ν_{as}(M-O-M) are known to be sensitive to the M-O-M angle (Wing & Callahan, 1969) and, thus, can serve as useful indicators of metal cluster geometry. A survey of oxo-bridged diiron model compounds reveals that Fe-O-Fe angles range from 180–150° for monobridged μ-oxo complexes, to 138–129° for dibridged μ-oxo, μ-carboxylato complexes, and to 124–119° for tribridged m-oxo, di-m-carboxylato complexes (Sanders-Loehr et al., 1989). The ν_s(Fe-O-Fe) values are *inversely proportional* to the Fe-O-Fe angle ($\nu_s^2 \propto \cos\theta$) and range from 381–458 cm^{-1} for monobridged, to 454–499 cm^{-1} for dibridged, and to 525–540 cm^{-1} for tribridged complexes. In contrast, the ν_{as}(Fe-O-Fe) values are *directly proportional* to the Fe-O-Fe angle ($\nu_{as}^2 \propto 1-\cos\theta$) and range from 885–795 cm^{-1} for monobridged, to 778–763 cm^{-1} for dibridged, and to 751–725 cm^{-1} for tribridged complexes. The Δ9D values of 518 cm^{-1} for ν_s(Fe-O-Fe) and 747 cm^{-1}

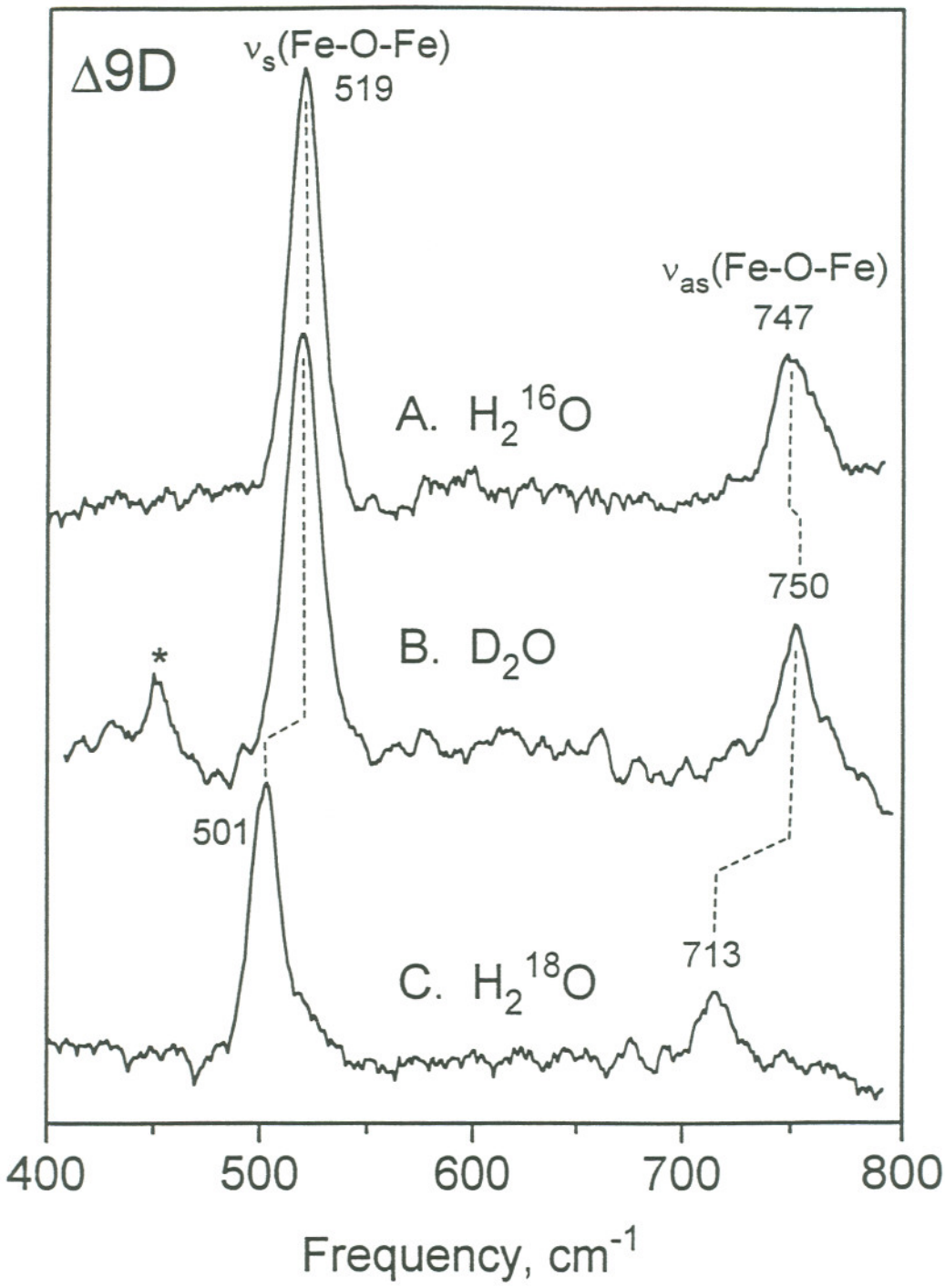

Figure 2.4 RR spectrum of Δ9D in (A) H_2O, (B) D_2O, and (C) $H_2{}^{18}O$. Spectra obtained on Δ9D samples (~4.5 mM in iron-oxo cluster) at 15 K using 350.7-nm excitation (20 mW), 12-cm^{-1} spectral resolution, 1-cm^{-1}/s scan rate and an accumulation of 9 (A), 16 (B), and 9 (C) scans. A plasma line is indicated by *.

Table 2.1

Resonance Raman Parameters for Diiron-Oxo Proteins

Diiron-oxo protein	Subunit MW[a]	ν_s(Fe-O-Fe)[b]			ν_{as}(Fe-O-Fe)[b]				Fe-X-Fe angle	
		ν	$\Delta^{18}O$	ΔD	ν	$\Delta^{18}O$	ΔD	I_{as}/I_s[c]	calc[d]	obs[e]
Class I										
HE (oxy)	13,500	486	−14	+4	756	−37	n.d.	0.18	134	125
Hr ($metN_3$)	13,500	507	−14	0	768	−35	n.d.	0.27	136	128
PAP	38,500	n.o.[f]								
Class II										
Δ9D	41,800	519	−18	0	747	−34	+3	0.29	123	
RBR	21,900	514	−18	+2	n.o.				122	
R2	43,500	493	−13	+3	756	−25	n.d.	0.20	138	130
MMOH	53,000	n.o.[f]								

[a] Sources of subunit molecular weights are: Hr and PAP (Sanders-Loehr et al., 1989); Δ9D (Fox et al., 1993b); R2 (Carlson et al., 1984); RBR (Dave et al., 1994); MMOH (Cardy et al., 1991). [b] Vibrational frequencies in cm^{-1} in $H_2{}^{16}O$. Isotopic shifts in cm^{-1} are for $H_2{}^{18}O$-$H_2{}^{16}O$ ($\Delta^{18}O$) or D_2O-$H_2{}^{16}O$ (ΔD). The sources of Raman data are: Hr and R2 (Sjšberg et al., 1987; Sanders-Loehr et al., 1989); RBR (Dave et al., 1994); Δ9D, PAP and MMOH (this laboratory). n.d., not determined. n.o., not observed. [c] Intensity (peak area) of ν_{as}(Fe-O-Fe) relative to that of ν_s(Fe-O-Fe). [d] Fe-O-Fe angle calculated from 18O isotopic shifts according to (Wing & Callahan, 1969). Given the ± 1 cm^{-1} error in Δ18O, the error in the calculation is $\pm$ 4°. [e] Observed Fe-O-Fe angle for Hr from X-ray crystallography (Holmes et al., 1991) and for R2 from EXAFS (Scarrow et al., 1987). [f] The bridging ligand in the diferric state of PAP and MMOH has been proposed to be a hydroxo species (DeWitt et al., 1991; Wang et al., 1991; Fox et al., 1993a).

for ν_{as}(Fe-O-Fe) are both closest to those of the tribridged classification. The 18-cm^{-1} oxygen isotope shift and calculated Fe-O-Fe angle of 123° (Table 2.1) are also most consistent with a tribridged structure for Δ9D. RBR has similar ν_s(Fe-O-Fe) and $\Delta^{18}O$ values of 514 and −18 cm^{-1}, respectively, and a calculated Fe-O-Fe angle of 122° (Table 2.1).

A surprising difference between Δ9D and RBR relates to the fact that ν_{as}(Fe-O-Fe) is quite intense in the RR spectrum of Δ9D (Figure 2.4), but too weak to be observed in RBR (Dave et al., 1994). The asymmetric stretch is forbidden according to the selection rules for Raman spectroscopy, and in symmetrical tribridged model compounds, ν_{as}(Fe-O-Fe) is typically less than 10% as intense as ν_s(Fe-O-Fe) or it is not observed at all (Sanders-Loehr et al., 1989). The large I_{as}/I_s value of 0.29 for Δ9D is similar to the values of 0.27 for azidometHr and 0.20 for R2 (Table 2.1). In the latter two cases, the enhanced intensity for ν_{as}(Fe-O-Fe) can be correlated with the presence of different terminal ligands to Fe_A and Fe_B (Figure 2.1). It is possible that Δ9D also has different terminal ligands to the two Fe atoms, whereas the terminal ligand distribution in RBR is more symmetrical. Although the Mössbauer spectra of the diferric forms of Δ9D and RBR indicate fairly equivalent iron atoms in both proteins (Fox et al., 1993b; Ravi et al., 1993), this may not be as reliable an indicator of structural inequivalence as the intensity of ν_{as}(Fe-O-Fe). Two quadrupole doublets are clearly observed in the Mössbauer spectrum of R2, but azidometHr exhibits only one quadrupole doublet despite its known asymmetry in terminal ligands (Sanders-Loehr et al., 1989).

For oxyHr, R2, and RBR, incubation in D_2O results in 2–4 cm^{-1} upshifts in ν_s(Fe-O-Fe) (Table 2.1). Such upshifts indicate that the oxo bridge is serving as a H-bond acceptor and that the H-bond strength is weaker with D in place of H. The observation of a D-isotope effect in oxyHr but not in azidometHr (Table 2.1) is consistent with the crystallographic data showing that the hydroxoperoxide ligand in oxyHr is H-bonded to the oxo bridge whereas the azide ligand in azidometHr is not (Loehr & Shiemke, 1988; Holmes et al., 1991). The D-isotope effect in R2 and RBR is most likely due to a H-bond from one of the terminally ligated water molecules (Figure 2.1B). Although Δ9D shows no D-isotope dependence for ν_s(Fe-O-Fe), the

ν_{as}(Fe-O-Fe) mode does undergo a 3-cm_{-1} upshift in D_2O (Figure 2.4B). This again is indicative of an aqua ligand being H-bonded to the oxo bridge. The greater sensitivity of ν_{as} than ν_s to D substitution may be due to a greater distortion of the H-bond in the asymmetric stretching motion of the Fe-O-Fe group.

Source of the oxo bridge in Δ9D

The spectrum in Figure 2.4C shows that the m-oxo groups of Δ9D can undergo complete exchange with solvent $H_2{}^{18}O$. The rate of exchange with solvent was investigated by mixing $H_2{}^{18}O$-equilibrated Δ9D with an equal volume of $H_2{}^{16}O$ and freezing the sample after various incubation times. From the rate of reappearance of the ν_s(Fe-O-Fe) mode at 519 cm^{-1}, we calculated a pseudo first-order rate constant of 6.3 h^{-1} and a $t_{1/2}$ of 7 min for oxo bridge exchange (data not shown). Similar exchange rates have been noted for RBR (Ravi et al., 1993) and R2, the latter having a $t_{1/2}$ of 15 min (Sjšberg et al., 1982).

The fact that the oxo bridge exchanges with solvent oxygen on the minutes time scale makes it facile to trap intermediates. In the case of R2, reaction of the diferrous protein with $^{18}O_2$ and freeze-trapping of the diferric product revealed that $^{18}O_2$ was the initial source of oxygen in the oxo bridge (Ling et al., 1994). To perform a similar experiment with Δ9D, it was necessary to add acyl carrier protein (ACP). The reaction of diferrous Δ9D with O_2 takes several hours in the absence of ACP, but is complete in ~2 min in the presence of ACP. Despite this marked effect on the reactivity of the diiron site in the reduced enzyme, ACP does not seem to affect the structure or reactivity of the diiron site in the oxidized enzyme. Thus, in the RR spectrum of diferric Δ9D, neither ν_s(Fe-O-Fe) (Figure 2.5) nor ν_{as}(Fe-O-Fe) is affected by the addition of equimolar ACP. The rate of oxo-bridge exchange is also unaffected by ACP. Approximately 30% exchange is observed (based on the appearance of RR intensity at 501 cm^{-1}) for $H_2{}^{16}O$ samples frozen 3 min after addition of an equal volume of $H_2{}^{18}O$ (Figure 2.5A). When diferrous Δ9D in $H_2{}^{16}O$ is oxidized in the presence of ACP and frozen 3 min after the addition of $^{16}O_2$ or $^{18}O_2$, only an Fe-^{16}O-Fe species is observed (Figure 2.5B,C). If $^{18}O_2$ had been the initial source of the oxo bridge, then ~70% of the Fe-O-Fe symmetric stretch should have

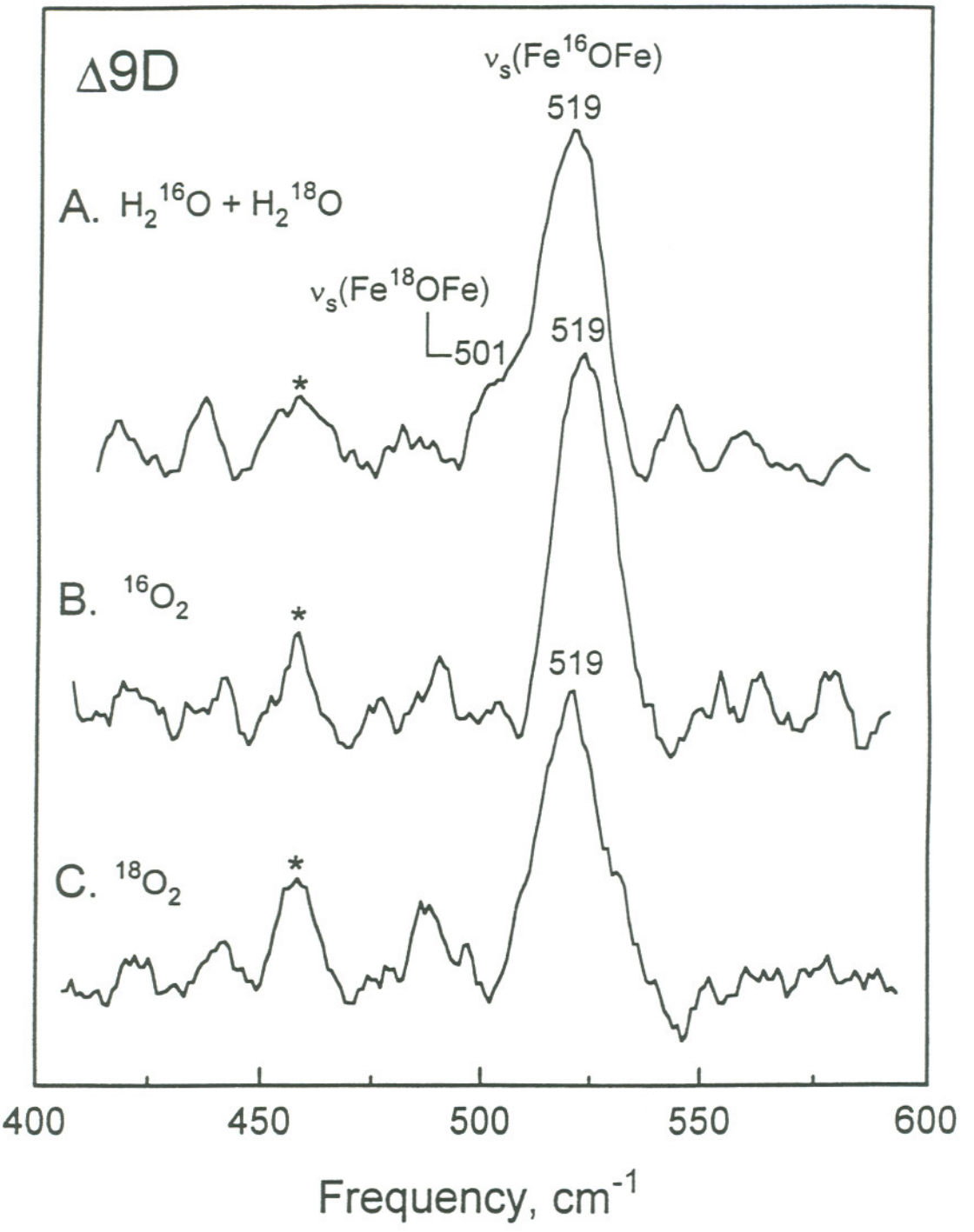

Figure 2.5 RR spectrum of Δ9D reacted with equimolar ACP and frozen 3 minutes after the addition of isotope. (A) Oxidized Δ9D in $H_2{}^{16}O$ mixed with an equal volume of $H_2{}^{18}O$. Spectral conditions as in Figure 2.4, but 2.4 mM in iron-oxo cluster and 18 scans. (B) Reduced Δ9D mixed with $^{16}O_2$. (C) Reduced Δ9D mixed with $^{18}O_2$. Spectra in (B) and (C) obtained on 2.8 mM samples at 90 K using 350.7-nm excitation (20 mW), 15-cm^{-1} spectral resolution, 0.5-cm^{-1}/s scan rate, and an accumulation of 12 and 16 scans, respectively.

been observed at 501 cm^{-1}. Since there is no indication of any Fe-^{18}O-Fe component at 501 cm^{-1} (Figure 2.5C), O_2 is unlikely to react with diferrous Δ9D in the μ-1,1 binding mode that was proposed for R2 (Ling et al., 1994).

Structural differentiation of iron sites in Δ9D

We have previously shown by using Mössbauer spectroscopy that the iron atoms of the diferric Δ9D are in essentially equivalent structural environments with δ = 0.53 mm/s and ΔE_Q = 1.54 mm/s (Fox et al., 1993). In contrast, Figure 2.6 shows that the iron sites of the diferrous Δ9D cluster are structurally distinct. Above 90 K, a temperature-dependent decrease in quadrupole splitting is observed for only one doublet, while the other doublet maintains an essentially temperature independent quadrupole splitting. The two doublets contribute equal fractions to the total spectral area and maintain a constant Lorentzian line width. The isomeric shifts of both doublets exhibit a similar 2nd order Doppler shift. Temperature dependence in the quadrupole splittings generally arises from thermal population of low-lying orbital states. Thus, the two doublets most likely represent two iron sites within the Δ9D cluster which are structurally distinct because of differences in ligand field properties.

Circular dichroism

Circular dichroism measurements previously indicated that R2 contains ~60% a helical content (Sjšberg et al., 1982), which is consistent with the ~70% a helical content determined by X-ray crystallography (Nordlund & Eklund, 1993). Figure 2.7 shows the circular dichroism spectrum of Δ9D. The positive maximum at 192 nm, negative peaks at 210 and 221 nm, the amplitude of these bands, as well as the peak to peak ratio ($\Delta\epsilon_{192}$:$\Delta\epsilon_{221}$ ≈ 2) are all characteristic of proteins with an α-helical content in the 75 to 80% range (Manavalan & Johnson, 1987). This percentage is close to that of R2, which has a similar subunit size and dimeric structure (Table 2.1).

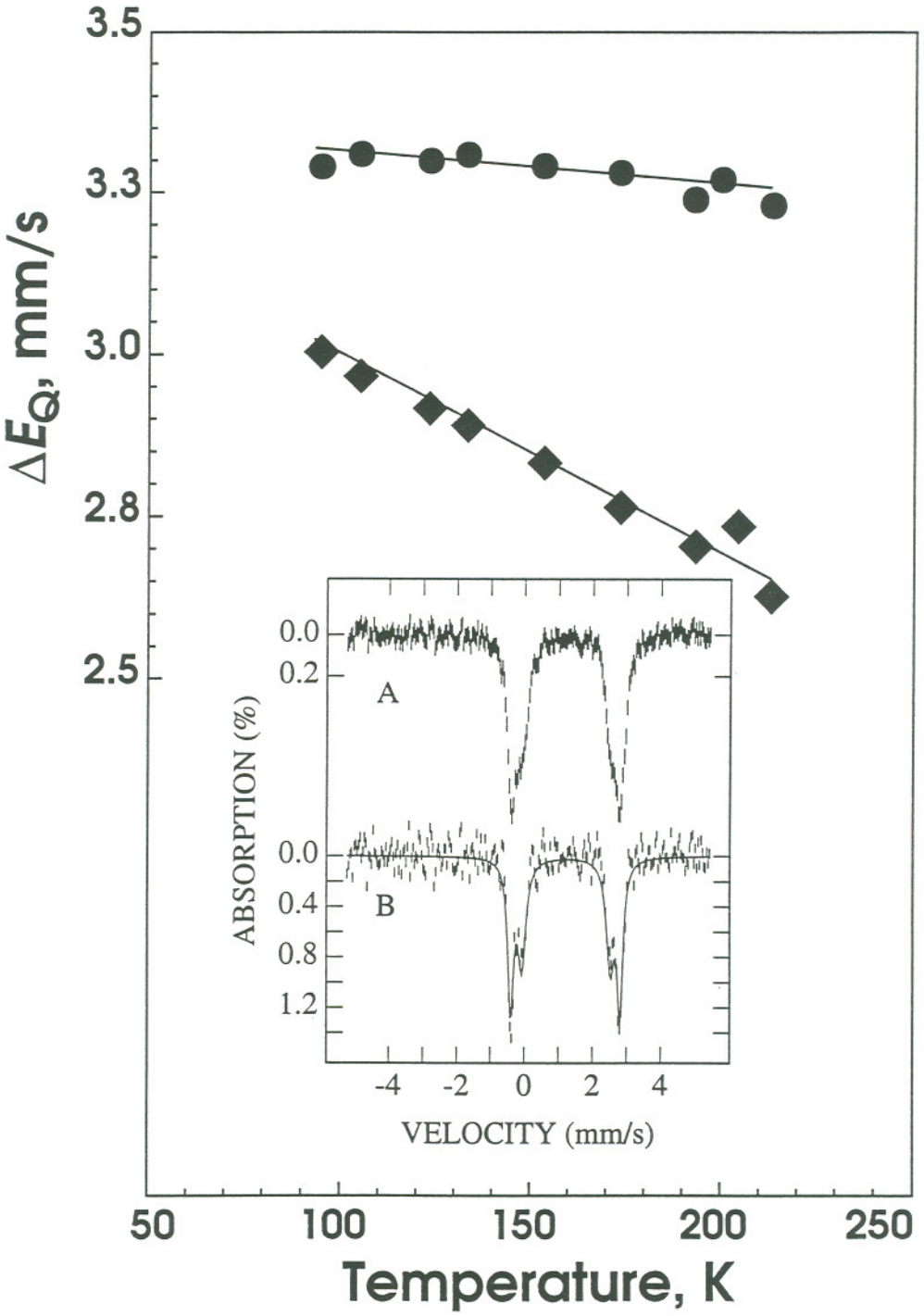

Figure 2.6 Temperature dependence of the two quadrupole doublets observed in the diferrous state of Δ9D. The inset shows (A) the Mössbauer spectrum obtained at 213 K and (B) a Fourier-filtered spectrum removing the contribution of source linewidth and a least-squares fit assuming two doublets of equal area contribution.

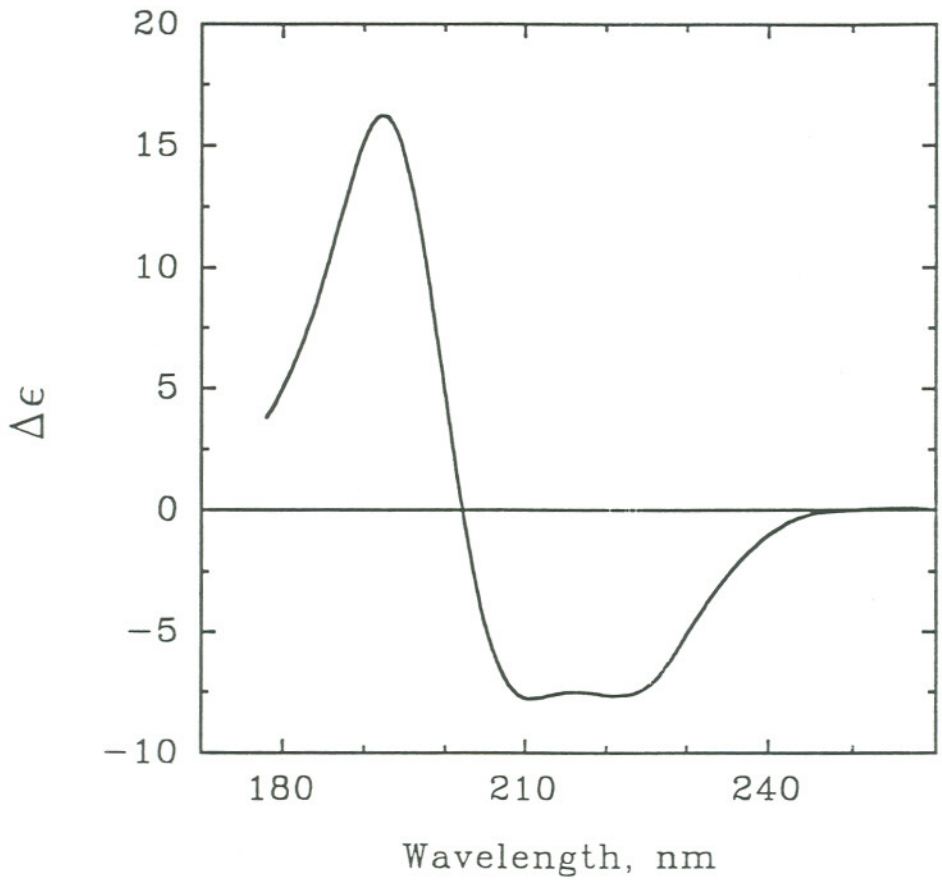

Figure 2.7 Circular dichroism spectrum of 14.3 μM Δ9D in 10 mM phosphate buffer, pH 7.8. Spectral analysis using VARSELEC (Manavalan & Johnson, 1987) gave the following secondary structural parameters: a-helix, 76%; parallel b-sheet, 3%; b-turn, 10%; other, 12%. Similar values were obtained at 7.1 μM Δ9D.

Structural relationships among the class II diiron-oxo proteins

Four of the cluster ligands in R2 and MMOH are provided by two copies of the primary sequence motif EX_2H. Two other ligands are provided by Asp or Glu residues preceding the EX_2H sequence by approximately 35 residues. Nordlund et al. have proposed that these ligands have arisen from a duplication of the genetic element providing the (D/E) ··· EX_2H motif (Nordlund et al., 1990). Computer searches reveal that a large number of proteins contain a single copy of the EX_2H motif (~10% of the 33,369 total entries in SWISS-PROT, release 27.0, October, 1993). However, by restricting the search to provide only proteins which contain two copies of this motif separated by between 60 to 180 amino acids, a considerably smaller number of proteins are identified (0.3% of total entries). As indicated by Figures 2.8 and 2.9, the proteins in the class II can be divided into three catalytic subclasses: the ribonucleotide reductases (Fontecave et al., 1992), the bacterial hydrocarbon hydroxylases (Fox et al., 1993b) the plant stearoyl-acyl carrier protein desaturases (Fox et al., 1993), and RBR (Ravi et al., 1993). Primary sequence alignments for the hydroxylases and the desaturases corresponding to the helix B and C regions of R2 and MMOH are shown in Figure 2.8, while the helix E and F regions are shown in Figure 2.9.

The R2 proteins have diverged extensively at the primary sequence level, with only 16 residues conserved among all species thus far examined. Many of these conserved residues appear to be involved in iron binding and O_2-activation (Nordlund & Eklund, 1993). The bacterial hydroxylase MMOH is highly conserved in two species of methanotrophic bacteria at the primary sequence level (89% similarity and 80% identity as estimated by BESTFIT) (Cardy et al., 1991). We have identified two other non-heme iron hydroxylases containing the double EX_2H motif. These are toluene-4-monooxygenase (T4MOH) (Yen et al., 1991) and phenol hydroxylase (PH) (Nordlund et al., 1990a; Powlowski & Shingler, 1990). These two enzymes from soil pseudomonads (Pm and Ps, respectively, in Figure 2.8 and 2.9) exhibit ~20% primary sequence identity with MMOH. However, since T4MOH and PH are non-heme iron proteins that have an oligomeric structure, electron transfer chain, and

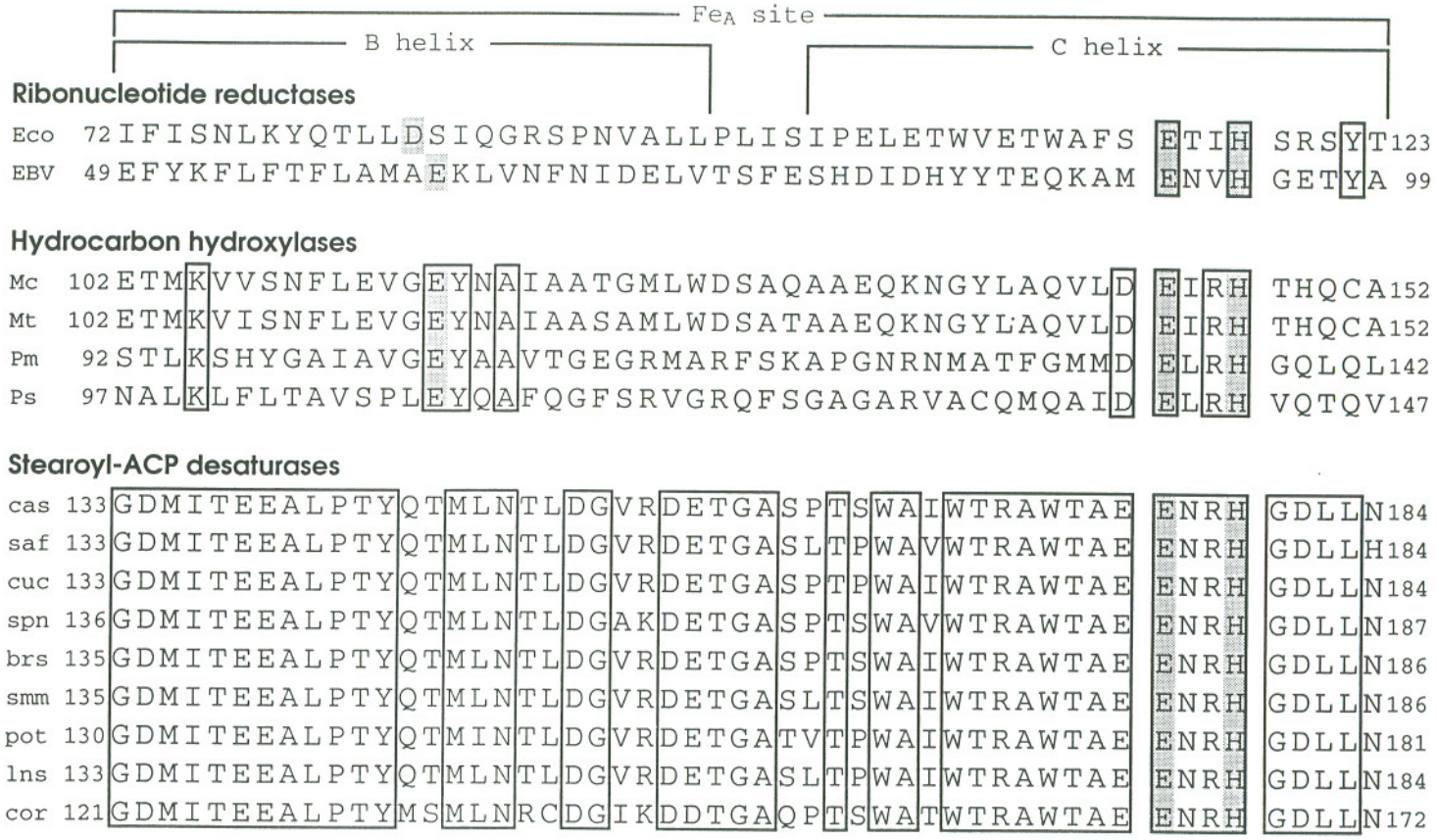

Figure 2.8 Primary sequence identities within the Fe_A site of class II diiron-oxo proteins. All sequences are aligned relative to the conserved His residue in helix C (H118) of *E. coli* R2. Shaded residues indicate cluster ligands identified in the X-ray structures of R2 and MMOH (Nordlund & Eklund, 1993; Rosenzweig et al., 1993) and probable iron ligands in Δ9D. Sequence sources are described in Experimental Procedures.

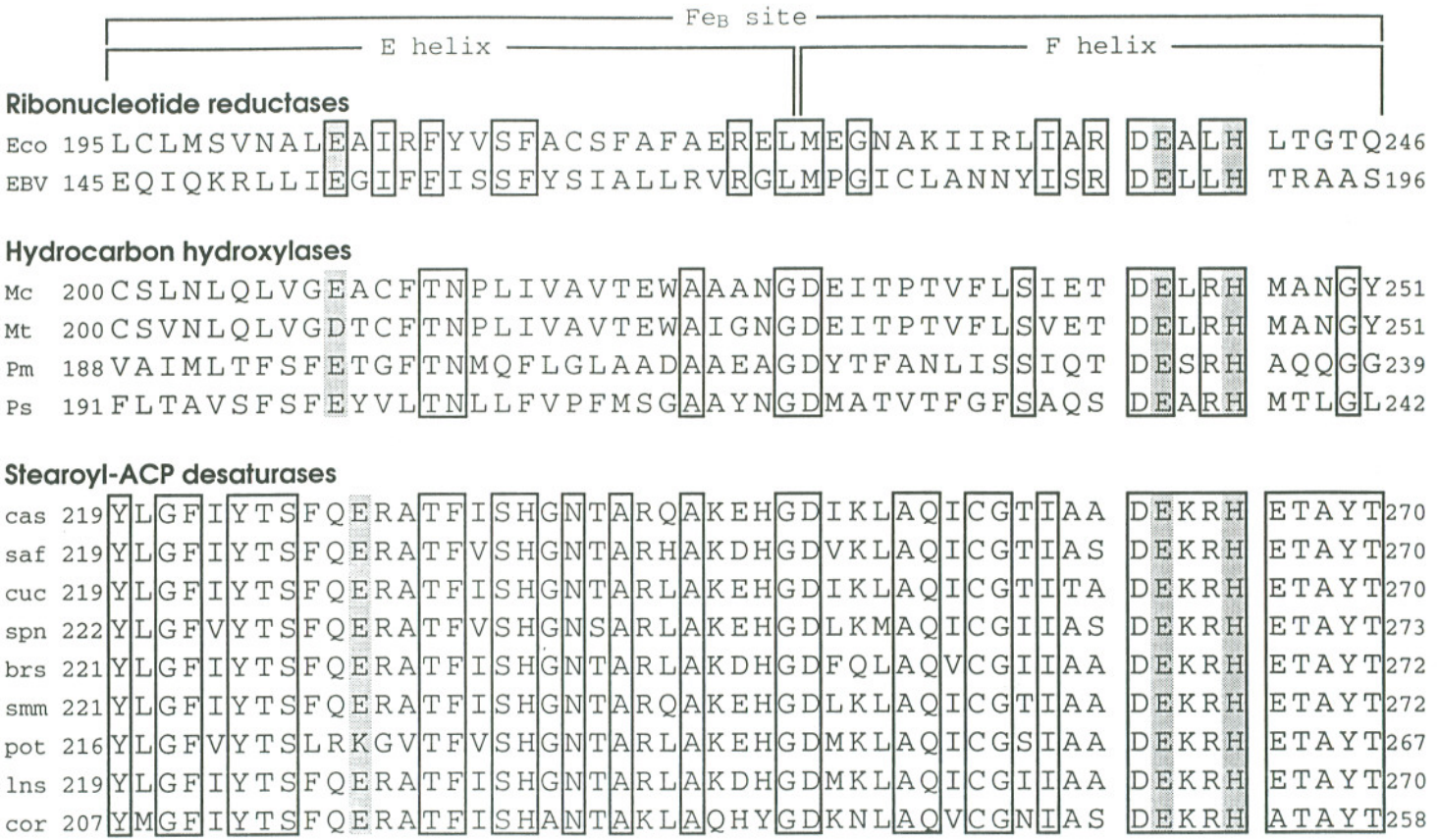

Figure 2.9 Primary sequence identities within the Fe_B site of class II diiron-oxo proteins. All sequences are aligned relative to the conserved His residue in the helix F (H241) of *E. coli* R2. Other terminology is as in Figure 2.8.

spectroscopic properties similar to MMOH, it is highly likely that they also use diiron clusters to catalyze hydroxylation reactions.

The stearoyl-ACP desaturases are highly conserved among higher plants, exhibiting greater that 85% identity at the primary sequence level (Figures 2.8 and 2.9). The Δ^4-desaturase from coriander (Cahoon et al., 1992) shows a similar degree of identity, and, thus has also been included in this catalytic subclass. Examination of the primary sequences for the ribonucleotide reductases, the hydroxylases and the desaturases reveals there is little overall identity between these three catalytic subclasses. In fact, pairwise comparisons using algorithms such as BESTFIT suggest no significant sequence identity. Nevertheless, their homology is clearly indicated from the conservation of a number of key residues which serve as (*i*) the iron ligands, (*ii*) hydrogen bonding partners to the cluster and (*iii*) residues in the proposed O_2-binding region.

i. Diiron-oxo cluster ligands. The EX_2H sequences which can be identified as iron ligands in the castor Δ9D are residues E176 and H179 from helix C (Figure 2.8) and E262 and H265 from helix F (Figure 2.9). These numbers are 33 higher than in Figure 2.8 because they include a 33-residue amino-terminal transit peptide that is present in the initial transcript but not in the mature protein (Lindqvist et al., 1996). A fifth potential iron ligand is found in the E helix region in all of the desaturases (E229 in castor Δ9D, see Figure 2.9) except for that from potato, and it closely matches the monodentate Glu ligand in the E helix region of R2 and MMOH. The B helix region of R2 and MMOH is more variable, with either Asp or Glu residues acting as bidentate or monodentate iron ligands, respectively. No suitable ligating amino acid is found at this location in Δ9D. Although the desaturases do contain six conserved Asp and Glu residues in the B helix region, the assignment of any one of these residues as a cluster ligand would likely require a substantial deviation from the a-helical secondary structure observed in both R2 and MMOH. Therefore, a cluster ligand from the B helix region of the desaturases can not be assigned at this time.

ii. Hydrogen Bonding to the Diiron-Oxo Cluster. The conserved residue Asp 237 from helix F of *E. coli* R2 (Figure 2.9) forms a hydrogen bond to the iron ligand H118 (Nordlund & Eklund, 1993). An identically conserved Asp residue is observed

in all of the bacterial hydroxylases and all of the desaturases, indicating a similar hydrogen bonding pattern to one iron of the cluster. MMOH contains an additional symmetry-conserved Asp 143 residue from helix C (Figure 2.8) which is hydrogen bonded to the iron ligand H246 (Rosenzweig et al., 1993). T4MOH and PH also contain this additional Asp residue. Likewise, a conserved Glu residue is found at this position in all desaturases, suggesting the presence of a related hydrogen bonding network. The desaturases and hydroxylases also contain a conserved Arg residue within each of the EX_2H motifs, yielding (D/E)EXRH as the conserved sequence for these proteins (Fox et al., 1993b). Computer searches for proteins containing two copies of this motif have identified only the desaturases and hydroxylases. The X-ray structure of MMOH reveals that these Arg residues expand the H-bonding network by interacting with the conserved Asp residues that are H-bonded to the two His ligands (A. C. Rosenzweig & S. J. Lippard, personal communication).

iii. Formation of the proposed O_2-binding site. For R2, the conserved residue F208, in helix E (Figure 2.9), resides in a hydrophobic pocket that is proposed to form part of the O_2-binding site (Nordlund & Eklund, 1993). Corresponding to the position of F208, both the desaturases and hydroxylases have a conserved Thr residue (Thr 232 in the castor Δ9D). In MMOH, this Thr residue is present in the π-turn of helix E. A conserved Thr residue is also found in the ^{1}-turn of a helix in the cytochrome P450 family, and is believed to participate in O_2-activation chemistry (Martinis et al., 1989).

The conserved residue Ile 234 in helix F is also found in the hydrophobic pocket of R2. For the desaturases, a conserved Ile residue is present in the corresponding position (Ile 258 in the castor Δ9D), while Ile or chemically conservative substitutions of Val or Ala residues are observed at the corresponding position for the bacterial hydroxylases.

Helix C of R2 contains the catalytically essential residue Tyr 122 (Figure 2.8), which is oxidized during a single turnover of the diferrous cluster with O_2 to yield a stable free radical, Tyr 122$\cdot$. This residue is not conserved in the other class II iron-oxo enzymes. All desaturases have a Leu residue (Leu 183 in the castor Δ9D), while T4MOH and PH have Gln residues and MMOH has a Cys residue. Although the Cys

residue has been suggested to play a role in O_2-activation by MMOH (Nordlund et al., 1992, Rosenzweig et al., 1993), the lack of conservation in the other enzymes makes this suggestion less plausible.

Discussion

The presently known proteins containing Fe-O-Fe or Fe-OH-Fe clusters can be separated into two *unrelated classes* based on examination of primary sequences and available X-ray structures (Figures 2.1 and 2.2). The class I diiron-oxo proteins are distinguished by pairs of His/His or His/-CO_2 ligands separated by 3–4 intervening residues and an Fe-O-Fe axis perpendicular to the four-helix bundle from which the ligands originate. Members of class I include Hr and myoHr. Two parts of the Hr motif appear to align with conserved sequences in the mammalian purple acid phosphatases including uteroferrin, suggesting that these latter proteins may also contain a protein fold related to class I (Vincent et al., 1990). In addition, the copper-containing respiratory protein hemocyanin appears to be related to Hr, with each Cu of the binuclear cluster ligated by a HX_3H primary sequence contained in a helix-turn-helix secondary structure (Volbeda & Hol, 1989).

The class II diiron-oxo proteins have pairs of -CO_2/His ligands separated by 2 intervening residues and an Fe-O-Fe axis parallel to the four-helix bundle from which the ligands originate. Members of class II include R2, MMOH and other hydrocarbon hydroxylases, RBR, and the soluble stearoyl-ACP desaturases. The spectroscopic and primary sequence information from the present work allows us to make predictions about the active site structure (Figure 2.10) and reaction mechanism (Figure 2.11) of the class II stearoyl-ACP desaturases. Another class of diiron proteins described below and in a companion paper (Shanklin et al., 1994), include both hydrocarbon hydroxylases and fatty acid desaturases that are membrane-bound.

Structure of the diiron-oxo site in diferric Δ9D

From the amino acid sequence identities in the class II proteins (Figures 2.8 and 2.9), it is likely that the two conserved His and three conserved Glu serve as iron

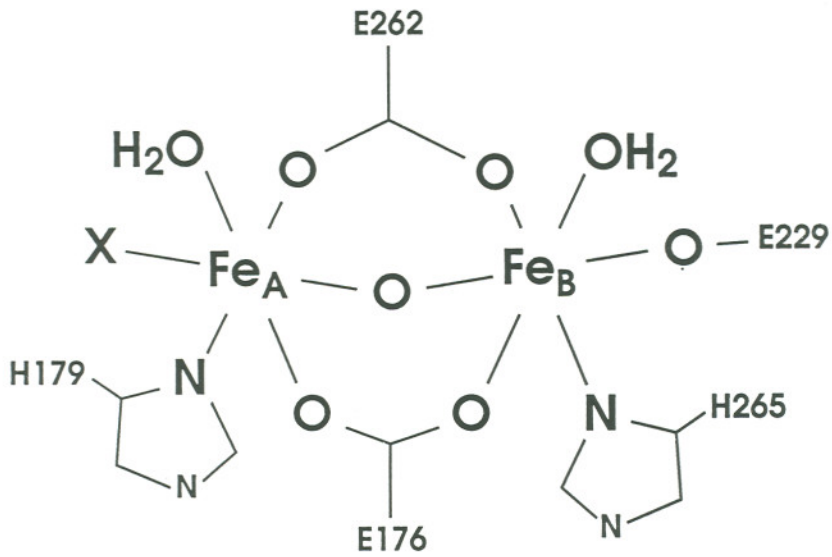

Figure 2.10 Proposed structure for the primary ligation sphere of the diiron-oxo cluster in Δ9D. Numbered residues are assigned by homology to R2 and MMOH. The numbering used here includes a 33-residue transit peptide that is cleaved off to yield a mature desaturase. Thus, all amino acid numbers are higher by 33 than in Figure 1.8 and 3.1 (Lindqvist et al., 1996).

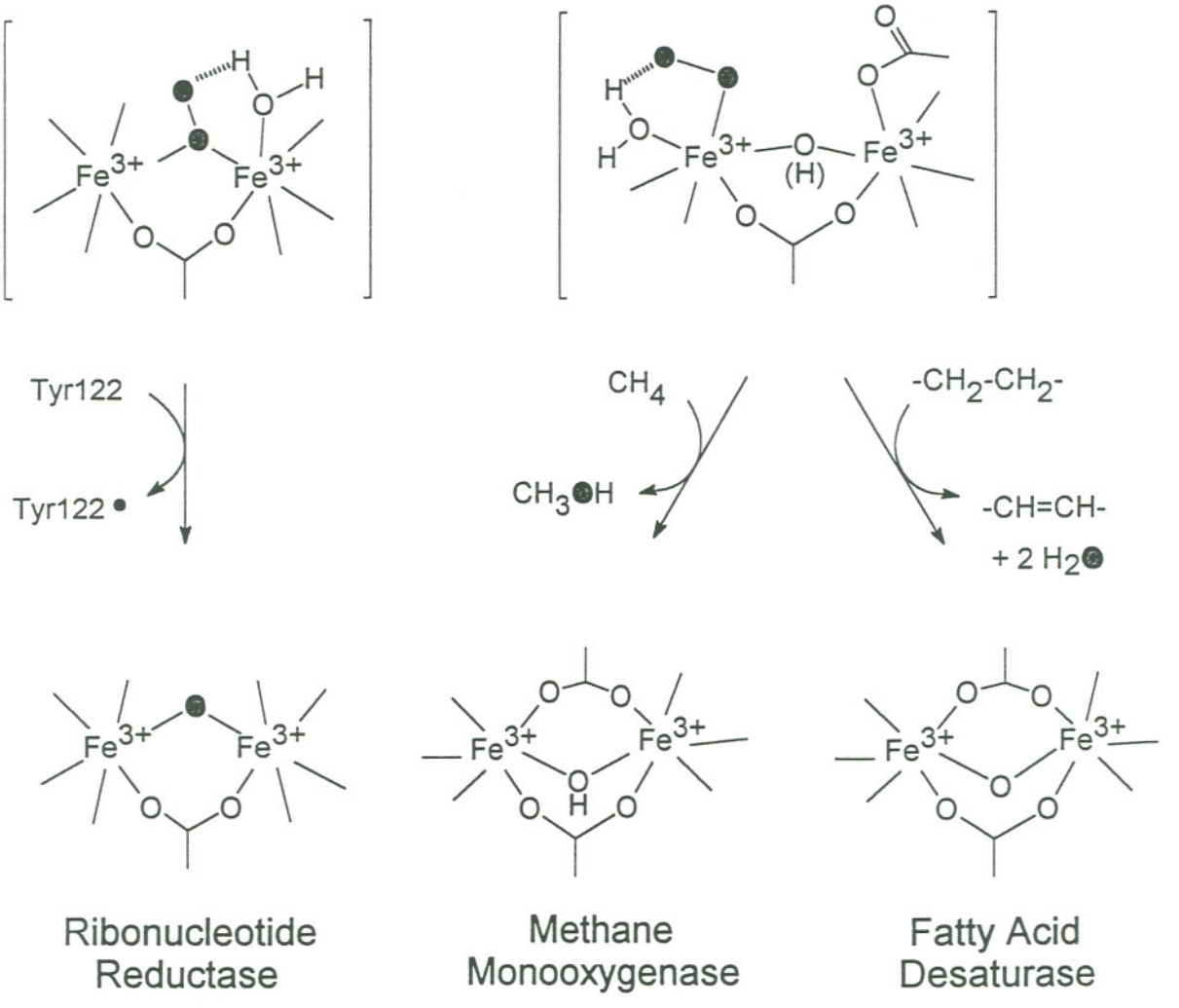

Figure 2.11 Differences in O_2-activation chemistry of the class II diiron-oxo enzymes. The structures of the diferric resting states of R2 and MMOH are known from X-ray crystallography (Nordlund & Eklund; 1993, Rosenzweig et al., 1993). The structures of the peroxo intermediates of ribonucleotide reductase (R2), methane monooxygenase (MMOH), and fatty acid desaturases (Δ9D) are shown in brackets to indicate that no such intermediate has yet been isolated. *Stippled* oxygens are derived from $^{18}O_2$.

ligands in Δ9D (Figure 2.10). By analogy with the known structures of R2 and MMOH (Figure 2.1B), the first EX_2H motif (E176 and H179 in castor Δ9D) is proposed to ligate Fe_A and to bridge to Fe_B. The second EX_2H motif (E262 and H265 in castor Δ9D) and the third conserved Glu (E229 in castor Δ9D) are proposed to bind to Fe_B, as is observed in R2 and MMOH.

The oxo bridge shown in Figure 2.10 has been definitively identified by RR spectroscopy through the observation of ^{18}O-dependent Fe-O-Fe vibrations (Figure 2.4). The RR work on Δ9D further suggests a tribridged structure with an Fe-O-Fe angle of $\sim 123°$ and an asymmetric distribution of terminal ligands to the two iron atoms. A notable feature of the X-ray structures of R2 and MMOH is the flexibility of the carboxylate ligands, a feature in keeping with the carboxylate shift behavior observed in model compounds (Rardin et al., 1991). Thus, the glutamate in R2 (which corresponds to E262 in Δ9D) varies from a bridging ligand in diferrous R2 (Åberg, 1993) to a terminal Fe_B ligand in diferric R2. For this reason, we have chosen E262 as the most probable third bridging group in Δ9D. The terminal carboxylate on Fe_A is also variable, being monodentate in diferrous R2 and diferric MMOH, but bidentate in diferric R2 (Figure 2.1A). It is possible that one of the terminal carboxylates in Δ9D (Figure 2.10) is also bidentate. This disposition could account for the site asymmetry of both diferric R2 and Δ9D, as indicated by the high intensity of their ν_{as}(Fe-O-Fe) vibrations (Table 2.1).

Structure of the diiron site in diferrous Δ9D

In the case of Hr, conversion of the oxy to the diferrous deoxy form is accompanied by protonation of the oxo bridge to yield a μ-hydroxo group, with no change in the protein ligands (Holmes et al., 1991). In contrast, reduction of the diferric site in R2 results in marked ligand rearrangement. Diferrous R2 has a bridging carboxylate in place of the bridging oxygen and an iron coordination number of 4 instead of 6, due to the loss of the terminal aqua ligands (Åberg, 1993). The reaction of O_2 with diferrous R2 appears to occur by displacement of a bridging carboxylate, resulting in a μ-1,1 bridging peroxide (Figure 2.11) which converts to a μ-oxo group following O-O bond cleavage (Ling et al., 1994). The failure to observe

any incorporation of label in the μ-oxo position of Δ9D upon reaction of the diferrous form with $^{18}O_2$ (Figure 2.5) suggests that its mode of initially binding O_2 may be unlike that of R2. Thus, one possibility is that diferrous Δ9D contains a protonated oxo bridge and that O_2 binds as a terminal ligand to only one Fe (Figure 2.11). The fact that the Mössbauer spectra of Δ9D show a marked difference between Fe_A and Fe_B in the diferrous but not the diferric state (Figure 2.6) suggests that some additional ligand rearrangement has occurred in diferrous Δ9D. For example, one of the bridging carboxylates may have dissociated from one Fe in the reduced form, thereby making the two iron atoms less equivalent and also providing a vacant coordination site for O_2 binding.

Comparison of class II diiron-oxo enzymes

Each of the class II enzymes (R2, MMOH, and Δ9D) has a diferric resting state. A common feature of the catalytic cycle appears to be a thermodynamically favored reduction directly to the diferrous state (Paulsen et al., 1994). For the three catalytic subclasses described here, O_2-activation chemistry is a major consequence of enzymatic turnover. It is likely that all of these reactions proceed via reduction of O_2 to generate a bound hydroperoxide intermediate (Lee et al., 1993a,b; Ling et al., 1994). Our present results indicate that there may already be a divergence of pathways even at the O_2-binding stage. Thus, R2 appears to form a μ-1,1 bridging peroxo intermediate leading to incorporation of $^{18}O^-$ into a bridging position. In contrast, no $^{18}O^-$ incorporation is observed for Δ9D under similar conditions, suggesting a different structure for the peroxo intermediate (Figure 2.11). The pathways leading to reactive species may also diverge, with the activated intermediate(s) generating (i) a tyrosyl radical in R2, (ii) a hydroxylated methane in MMOH, and (iii) an abstraction of electrons from stearoyl-ACP in Δ9D (Figure 2.11). In the case of the Tyr 208 mutant of R2, the pathway probably involves a high-valent iron intermediate (generated by O-O bond cleavage) since no oxygen from O_2 is incorporated into the hydroxylated DOPA 208 product (Ling et al., 1994). For MMOH, compound Q has Mössbauer parameters consistent with a strongly antiferromagnetically coupled cluster containing either intermediate-spin ($S = 1$) or

high-spin ($S = 2$) Fe^{IV} (Lee et al., 1993a). Compound Q is kinetically competent to hydroxylate methane (Lee et al., 1993b).

There are several lines of evidence that Δ9D is more similar to MMOH than R2. The primary sequence alignment reveals that the desaturases and hydroxylases have an additional 2 residues conserved in the Fe_A site and an additional 5 residues conserved in the Fe_B site that are not Fe ligands; these residues are not conserved in R2 (Figures 2.8 and 2.9). Three of these additionally conserved residues (a carboxylate and two Arg residues) form an extended H-bonding network to the two His ligands in MMOH (A. C. Rosenzweig & S. J. Lippard, personal communication). Our proposed structure for the diferric Δ9D cluster is similar to the tribridged structure of diferric MMOH determined by X-ray crystallography, except for the presence of an additional, exogenous carboxylate and a μ-oxo instead of μ-hydroxo bridge (Figure 2.11). It is possible that the presence of an oxo bridge in the Δ9D is related to the potential presence of 4 endogenous carboxylate ligands versus the presence of 5 carboxylate ligands in MMOH (4 endogenous plus one exogenous).

Mössbauer spectra of MMOH (Fox et al., 1993a) reveal that the two iron atoms in the diferrous form are inequivalent, similar to our findings for Δ9D (Figure 2.6). Investigation of MMOH by MCD spectroscopy (Pulver et al., 1993) has led to the proposal that the diferrous form has a 5-coordinate Fe where O_2 may bind in a terminal fashion, similar to our proposed structure for Δ9D (Figure 2.11). The closer similarity between the desaturases and the hydroxylases is logical since both of these enzymes must break inactivated C-H bonds as part of their respective catalytic cycles. The least similarity between MMOH and Δ9D occurs in the B helix region associated with the Fe_A site (Figure 2.8). This may be a consequence of the difference between binding a small substrate like methane as compared to an enormous substrate like stearate covalently bound to acyl carrier protein.

Relationship between soluble and membrane fatty acid desaturases

The plant Δ^9 and coriander Δ^4 desaturases are the only fatty acid desaturases presently known to be soluble enzymes. In contrast, all other fatty acid desaturases are integral membrane proteins (Fulco, 1974). Despite this structural difference, the

soluble and membrane desaturases have several important similarities including the catalytic requirement for iron (Nagai & Bloch, 1968), the inhibition by metal chelators (Jaworski & Stumpf, 1974), the stereospecificity of the desaturation reaction, and the kinetic isotope effects observed for C-H bond cleavage (Morris, 1970). These similarities suggest that a common mechanism is used for the desaturation reaction, which may include the requirement for a structurally related catalytic active site. The EX_2H iron binding motif characteristic of the soluble desaturase has not been found in any of the membrane desaturases sequenced to date. However, all membrane desaturases do contain *three* copies of potential iron-binding motifs: $HX_{(3\text{ or }4)}H$, $HX_{(2\text{ or }3)}HH$ and $HX_{(2\text{ or }3)}HH$. Surprisingly, the iron-containing membrane enzymes alkane hydroxylase (van Beilen et al., 1992) and xylene monooxygenase (Suzuki et al., 1991) exhibit similar primary sequence motifs. In an accompanying paper (Shanklin et al., 1994), we report site-directed mutagenic studies on the stearoyl-CoA Δ^9 desaturase from rat liver that indicate these conserved His residues are essential for catalytic function. In addition, other conserved structural features and the presently available spectroscopic properties of these membrane-associated proteins are reported. These observations suggest that the membrane associated desaturases, alkane hydroxylase, and xylene monooxygenase collectively comprise a class III category of diiron proteins.

CHAPTER III

AZIDE ADDUCTS OF STEAROYL-ACP DESATURASE. A MODEL FOR μ-1,2 BRIDGING BY DIOXYGEN IN THE DINUCLEAR IRON ACTIVE SITE[1]

Abstract

The stearoyl-acyl carrier protein Δ^9 desaturase (Δ9D) uses an oxo-bridged diiron center to catalyze the NAD(P)H- and O_2-dependent desaturation of stearoyl-ACP. The diferric center in Δ9D has substantial similarities in amino acid sequence and physical properties to those of ribonucleotide reductase and methane monooxygenase. These three enzymes also appear to share common features of their reaction cycles, including the binding of O_2 to the diferrous state and the subsequent generation of transient diferric-peroxo and diferryl species. In order to investigate the coordination environment of the proposed diferric-peroxo intermediate, we have studied the binding of azide to the diiron center of Δ9D using optical, resonance Raman (RR), and transient kinetic spectroscopic methods. The addition of azide results in the appearance of new absorption bands at 325 nm and 440 nm ($K_{app} \sim 3.5$ s^{-1} in 0.7 M NaN_3, pH 7.8). RR experiments demonstrate the existence of two different adducts: an η^1-terminal structure at pH 7–8 ($^{14}N_3^-$ asymmetric stretch at 2073 cm^{-1}, resolved into *two* bands with $^{15}N^{14}N_2^-$) and a μ-1,3 bridging structure at pH < 7 ($^{14}N_3^-$ asymmetric stretch at 2100 cm^{-1}, shifted as a *single* band with $^{15}N^{14}N_2^-$). Both adducts also exhibit an Fe-N_3 stretching mode at $\sim$380 cm^{-1}, but no accompanying Fe-O-Fe stretching mode, presumably due to either protonation or loss of the oxo bridge.

---

[1] As published in *J. Biol. Inorg. Chem.* **1997**, 2, 37-45. Reprinted with permission.

The ability to form a μ-1,3 bridging azide supports the likelihood of a μ-1,2 bridging peroxide as a catalytic intermediate in the Δ9D reaction cycle and underscore the adaptability of diiron sites to different bridging geometry. Moreover, the protonation and loss of the oxo bridge proposed to be required in the formation of the μ-1,3 azide bridge may also occur during enzyme catalysis to optimally position the diferrous site for O_2 binding.

Introduction

The plant fatty acid desaturases catalyze the O_2- and NAD(P)H dependent insertion of a *cis*-double bond into fatty acyl chains (Holloway, 1983). For the soluble forms of these enzymes, the substrate is covalently attached to acyl carrier protein (ACP) via a phosphopantetheine thioester linkage (Jaworski & Stumpf, 1974). The best characterized acyl-ACP desaturase is the recombinant stearoyl-ACP Δ^9-desaturase (Δ9D) from castor-oil plant, *Ricinus communis* (Shanklin & Somerville, 1991; Fox et al., 1993). This enzyme is a homodimer of 40-kDa subunits, and it catalyzes the conversion of stearoyl-ACP to oleyl-ACP (Nagai & Bloch, 1966).

Mössbauer studies have demonstrated that diferric Δ9D contains an antiferromagnetically coupled diiron center (Fox et al., 1993), and resonance Raman (RR) studies have shown that the two iron atoms are bridged by an oxo group that is exchangeable with solvent (Fox et al., 1994). These spectroscopic properties are consistent with the assignment of Δ9D to a group of structurally related enzymes containing oxo or hydroxo-bridged diiron centers that have been designed as class II to distinguish them from the unrelated class I respiratory protein, hemerythrin (Fox et al., 1994; Nordlund & Eklund, 1995). Other members of the class II are R2 component of the aerobic ribonucleotide reductase (Nordlund & Eklund, 1993); a ferroxidase enzyme, rubrerythrin (Bonomi et al., 1996), and the soluble bacterial hydrocarbon hydroxylases (Nordlund et al., 1993): methane monooxygenase (MMO) (Lipscomb, 1994; Rosenzweig et al., 1995), toluene monooxygenase (Olsen et al., 1994; Newman & Wackett, 1995; Pikus et al., 1996), phenol hydroxylase (Nordlund et al., 1993), and alkane epoxidase (Miura & Dalton, 1995). Based upon the

similarities in spectroscopic properties and amino acid sequences observed for Δ9D and the crystallographically characterized diiron proteins R2 (Nordlund & Eklund, 1993) and MMO (Rosenzweig et al., 1995), we proposed a structural model for the diferric coordination environment of Δ9D (Fox et al., 1994). In this model, the two iron atoms have an oxo bridge, as well as Glu and His ligation from the two copies of the conserved EXXH motif in all class II diiron-oxo proteins (Shanklin & Somerville, 1991), with the remaining ligands being protein-derived carboxylates and water (Figure 3.1).

Each of the class II diiron enzymes catalyzes the reductive activation of O_2 as an integral part of its reaction cycle. This sequence is believed to be initiated by the formation of a diferric-peroxo intermediate (Feig & Lippard, 1994; Lipscomb, 1994; Que & Dong, 1996), and a number of protein bound and synthetic complexes that delineate the structural possibilities for this intermediate have been characterized (Murch et al., 1986; Jocobsen et al., 1988; Kitajima et al., 1992, 1994; Lee et al., 1993; Magnus et al., 1994; Dong & Que, 1996; Kim & Lippard, 1996). Since azide can substitute for peroxide in many metalloenzyme active sites, notably the diiron site of hemerythrin (Freier et al., 1980; Sheriff et al., 1987; Hilmes et al., 1991) and the dicopper site of hemocyanin (Pate et al., 1989; Kitajima et al., 1992, 1993; Magnus et al., 1994), azide complexes provide an experimentally defined basis for probing O_2 coordination. Here we report studies of azide binding to Δ9D and provide evidence for both η^1-terminal and μ-1,3 bridging coordination of azide to the diferric protein. The ability of Δ9D to form a μ-1,3 azide adduct suggests that a μ-1,2 bridging peroxo intermediate can form upon reaction with O_2. In both azido-Δ9D adducts, the oxo bridge is either protonated or lost, with the latter possibility corresponding to the absence of hydroxo or water bridges in the diferrous forms of MMO (Rosenzweig et al., 1995), R2 (Åberg, 1993), and Δ9D (Lindqvist et al., 1996). The loss of the catalytic cycle that optimally positions the iron atoms for O_2-binding.

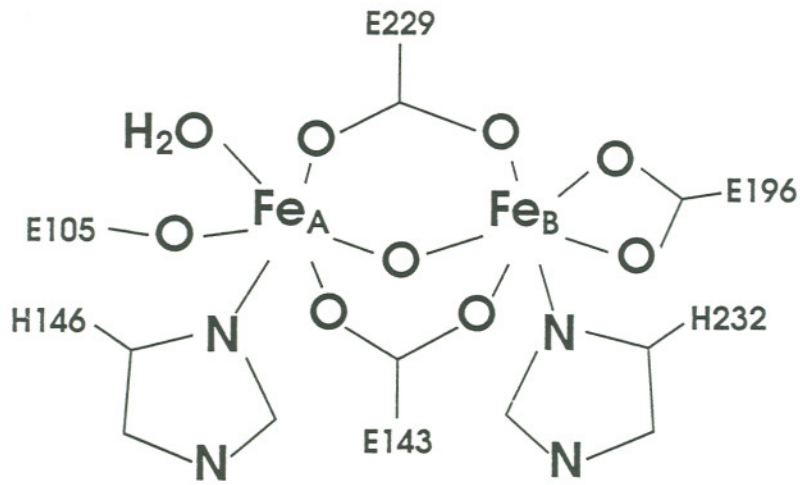

Figure 3.1 Proposed structure for the oxo-bridged binuclear iron center in diferric Δ9D. Ligands were assigned by the spectroscopic similarities and amino acid primary sequence alignments with R2 and MMOH (Fox et al., 1994). The numbering of the ligands and the identification of Glu105 as a ligand to Fe_A are from the Δ9D crystal structure Lindqvist et al., 1996).

Materials and Methods

Protein samples

The expression of Δ9D in *Escherichia coli* BL21(DE3), its purification, and quantitation of the diiron center content were as previously described (Hoffman et al., 1995), with the exception that the purification buffer was 25 mM HEPES, 50 mM NaCl, 5% (v/v) glycerol (pH 7.8). Optical spectra of Δ9D adducts were obtained on a Hewlett Packard 8452 diode array spectrometer at room temperature. The samples used for RR experiment were 2–3.5 mM in diiron centers (ϵ_{340} = 4200 $M^{-1}cm^{-1}$ per diiron center). The azide adducts of diferric Δ9D were produced in the following buffers: 50 mM MES (pH 6.2); 50 mM MOPS (pH 6.8); 50 mM HEPES (pH 7.8); 50 mM CAPS (pH 8.5). Sodium azide was prepared as a 4.2 M solution in the appropriate buffer and added to the enzyme to give a final concentration of 100 to 700 mM. Azide-containing samples were frozen immediately after preparation.

Myohemerythrin (MHr) from *Themiste zostericola* was prepared from a recombinant wild-type expressed in *Escherichia coli* (Lloyd et al., 1995) and was generously provided by Dr. Walter R. Ellis, Jr. RR samples contained 4–8 mM diferric protein (metMHr) and 200–400 mM sodium azide in 50 mM Tris-sulfate (pH 8.0).

Stopped-flow absorption spectroscopy

The rate of complexatiom of azide with Δ9D was determined using an OLIS stopped-flow device attached to a rapid scanning monochromator. Reaction were initiated by rapid mixing of equal volumes of azide (typically 1.4 M NaN_3 in 25 mM HEPES, pH 7.8) and Δ9D (68 μM Δ9D in 25 mM HEPES, pH 7.8) solutions.

Optical spectra were recorded from 300 to 600 nm at a sampling rate of 32 scans/s. No significant change in the optical spectrum occurred after 10 s, indicating that the complexation reaction was complete. Kinetic data were reduced by factor analysis using singular value decomposition, and then globally fit using nonlinear least squares fitting algorithms provide by OLIS (Hoffman et al., 1995; Lloyd et al.,

1995). The absorption data were best fit by a single exponential with correction for initial absorbance background, $a_t = a_0 \exp(k_{obs}t) + c$.

Resonance Raman spectroscopy

Unless otherwise stated, Raman spectra were obtained using a custom McPherson 2061/207 spectrograph (0.67 m) with a Princeton Instruments (LN-1100PB) liquid N_2-cooled CCD detector, and Rayleigh scatting was attenuated with a Kaiser Optical holographic super-notch filter. Alternatively, Raman spectra were recorded on a computerized Jarrell-Ash spectrophotometer using a cooled RCA C31034A photomultiplier tube and ORTEC model 9302 amplifier-discriminator, especially for 350-nm excitation. All spectra were collected in an $\sim$ 150° backscattering geometry from samples maintained at 15 K by use of a closed cycle helium refrigerator (Air Products, Displex) (Loehr & Sanders-Loehr, 1993). The desired excitation wavelengths were provided by Coherent Innova 90-6 Ar and Innova 302 Kr lasers. Absolute frequencies were obtained by calibration with aspirin ($<$ 1000 cm^{-1}) or acetonitrile and DMSO-d_6 ($>$ 2000 cm^{-1}) and are accurate to ± 1 cm^{-1}. Isotope shifts, obtained from spectra recorded under identical experimental conditions, have been evaluated by abscissa and curve resolution of overlapping bands and are accurate to ± 0.5 cm^{-1}.

Results

Electronic spectrum of azide adduct

The absorption spectrum of Δ9D is typical of an Fe-O-Fe system with two intense at 325 and 355 nm and a series of weaker bands from 470 to 570 nm (*solid* line of Figure 3.2). These bands have been assigned as oxo→Fe(III) charge transfer (Reem et al., 1989; Sanders-Loehr et al., 1989). We have previously reported that azide can form an adduct with the diferric enzyme, giving rise to new absorption bands (Fox et al., 1993). In the presence of 700 mM azide at pH 7.8, the absorbance increased at $\sim$325 nm and $\sim$440 nm (*dotted* line of Figure 3.2) in a single exponential phase with a rate constant of 3.5 s^{-1}. Several lines of evidence indicate

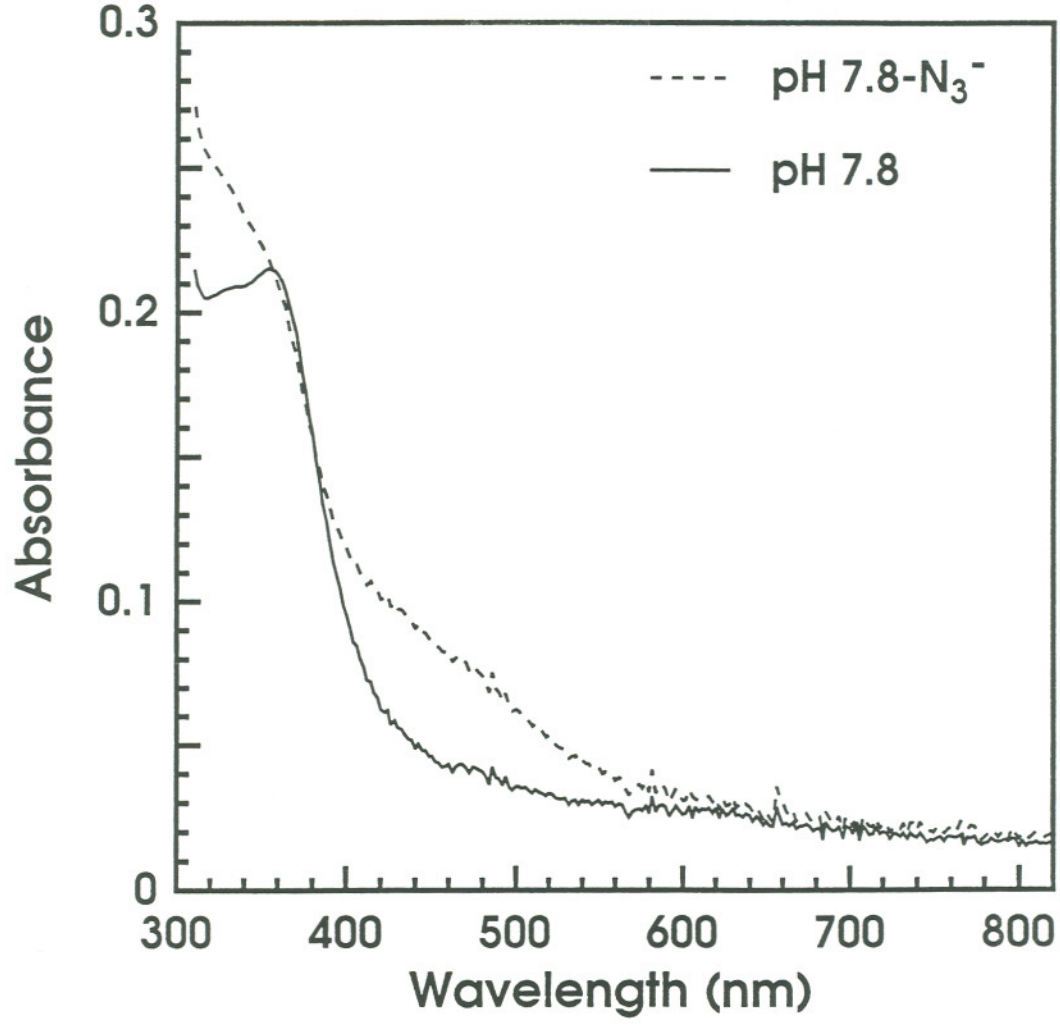

Figure 3.2 Electronic spectra of diferric Δ9D (*solid* line) and azido-Δ9D (*dashed* line). Samples contained ~40 μM Δ9D and, as indicated, 700 mM azide in 50 mM HEPES (pH 7.8).

that this absorption spectrum corresponds to an enzyme-bound complex. When the complex formed in 700 mM azide at pH 7.8 is concentrated by ultrafiltration (Centricon 50, Amicon), the retentate exhibits the expected absorption increase whereas the eluate shows no absorption from free ferric azide. Furthermore, a 10-fold dilution of the above reaction mixture into azide-free buffer results in the reappearance of the absorption spectrum (> 90%) of the original Fe-O-Fe system, with only a slight residual absorbance at 325 nm attributable to the remaining azide complex. This measurement demonstrates the reversible dissociation of the azide complex.

The broad, new absorbance that appears at ~440 nm upon azide binding to Δ9D is reminiscent of the absorbance features of other ferric azide adducts. For example, azide complexes of the class I diferric proteins, hemerythrin (Hr) and myohemerythrin (MHr), exhibit a similarly broad absorption at 445 nm that has been assigned as azide → Fe(III) charge transfer from its ability to yield resonance-enhanced azide vibrations in RR spectra (Kurtz et al., 1977). The X-ray structures of these two proteins reveal that the azide is bound asymmetrically as an η^1-terminal complex with one end of the azide coordinated to only one of the two iron atoms (Sheriff et al., 1987; Holmes et al., 1991). Azide complexes of class II iron-oxo enzymes also show new absorption bands at 425 nm in methane monooxygenase (Atta et al., 1993) and 453 nm in rubrerythrin (Gupta et al., 1995). The coordination mode(s) in these latter complexes have not been assigned, however.

ν_{as}(NNN) reveals bridging and terminal azide in azide-Δ9D

Excitation within the 440-nm absorption band of azido-Δ9D results in the appearance of two resonance-enhanced vibrations at 2073 and 2100 cm^{-1} (Figure 3.3). These are in the expected range for the asymmetric stretch of azide, which occurs at 2041 cm^{-1} in the free azide anion (Nakamoto, 1986) and at 2050 cm^{-1} in hydrazoic acid (**7**, Table 3.1). The two peaks in the Δ9D spectrum can be assigned to two different azide adducts on the basis that the 2100-cm^{-1} species predominates at pH 6.2, whereas the 2073-cm^{-1} species predominates at pH 7.8.

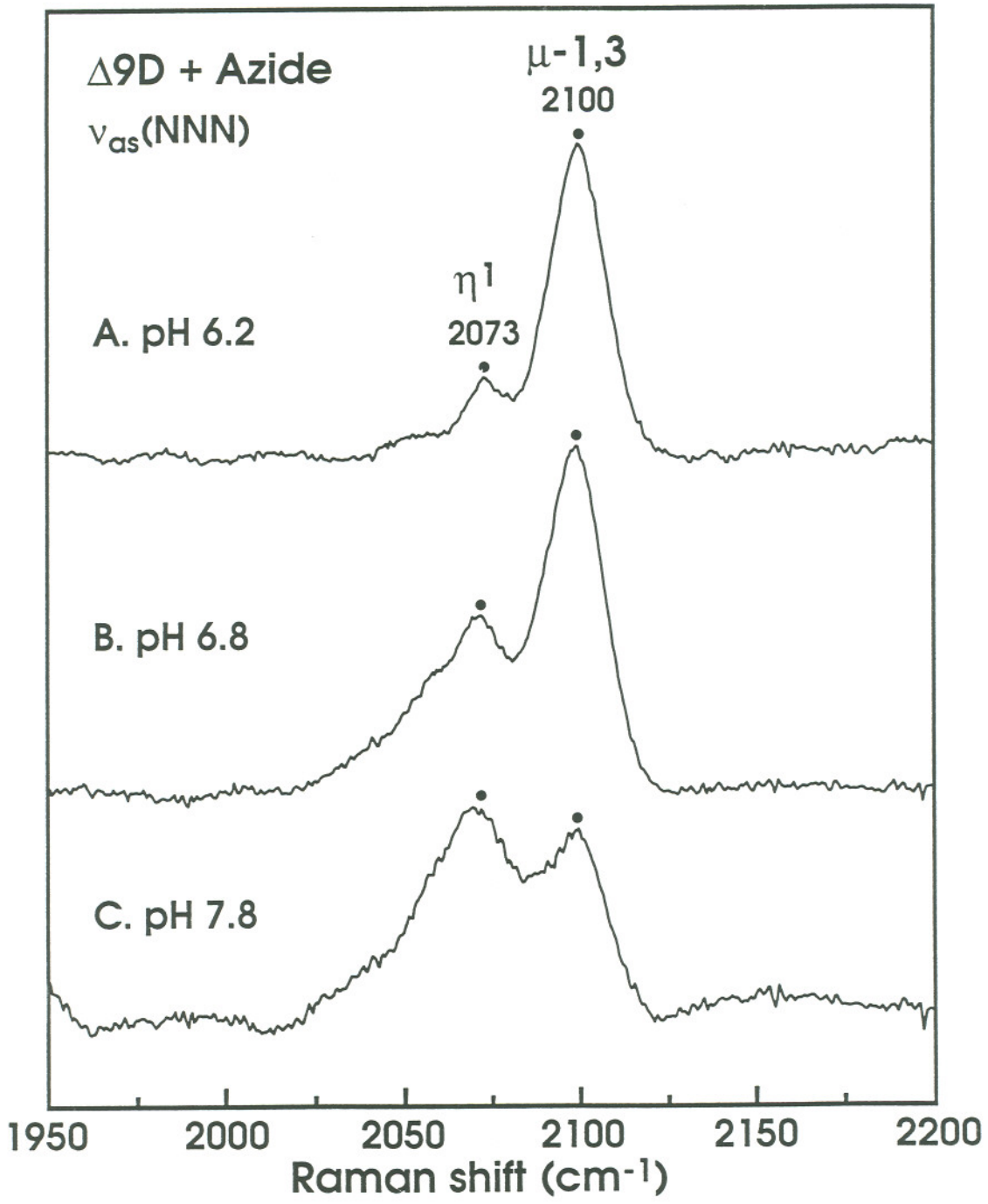

Figure 3.3 Effect of pH on the intra-azide stretching modes of azido-Δ9D. Samples contained 2.0 mM Δ9D and 700 mM azide. **A** In 50 mM MES (pH 6.2). **B** In 50 mM MOPS (pH 6.8). **C** In 50 mM HEPES (pH 7.8). Raman spectra were obtained with 488-nm excitation (60 mW), 1200-groove grating, spectral resolution of 6 cm^{-1}, and 20-min accumulation. The terms μ-1,3 and η^1 identify the asymmetric intra-azide stretches, ν_{as}(NNN), of the bridging and terminal complex, respectively.

Table 3.1. Vibrational frequencies of ferric and cupric azide complexes[a]

		ν_{as}(NNN) (cm^{-1})				ν_s(Fe-N_3) (cm^{-1})	
		ν	$\Delta^{14}N_2{}^{15}N$	$\Delta^{15}N^{14}N_2$	$(\Delta\Delta)$	ν	$\Delta\nu_{av}$[b]
η^1-*terminal (M-NNN)*							
1	Δ9D at pH 7.8 (Fe-N_3)	2073	-2	-14	(12)	378	-4
2	Myohemerythrin (Fe-N_3)	2048	-5	-17	(12)	369	-3
3	Hemerythrin (Fe-N_3)	2048	-6	-17	(11)	375	
4	[Cu(Et_4dien)(N_3)Br]	2062	-8	-14	(6)		
5	[py_2-Cu(NO_3)(N_3)]	2041	-8	-16	(8)		
6	[Cu(L'-O-)(N_3)]	2039	-6	-17	(11)		
7	H-N_3	2150	-5	-23	(18)		
μ-*1,3 bridging (M-NNN-M)*							
8	Δ9D at pH 6.2 (Fe-N_3-Fe)	2100	-11	-11	(0)	380	-4
9	[Cu_2(L-Et)(N_3)]$^{2+}$	2025	-12	-12	(0)	358	-5
10	[Cu_2(bpeac)(N_3)]$^{2+}$	2038[c]	<-14	-12	<(2)	358	-5
11	[Cu(HB(pz')$_3$]$_2$(OH)(N_3)	2028					
μ-*1,1 bridging (M_2-NNN)*							
12	[Cu_2(N_6O)(N_3)]$^{2+}$	2065	-3	-20	(17)		
13	[Cu_2(L-O-)(N_3)]$^{2+}$	2075	-2	-20	(18)		

[a] RR frequencies in cm^{-1}. $\Delta^{14}N_2{}^{15}N$ and $\Delta^{15}N^{14}N_2$ refer to frequency shifts for M-$^{14}N_2{}^{15}N$ and M-$^{15}N^{14}N_2$ relative to M-$^{14}N_3$. ΔΔ is the difference between $\Delta^{14}N_2{}^{15}N$ and $D^{15}N^{14}N_2$. Data from the following sources: **1, 8** (this work); **2** (Atta et al., 1993); **3** (Kurtz et al., 1977); **4-6, 9, 10, 12, 13** (Pate et al., 1989); **7** (McKee et al., 1984); **11** (Kitajima et al., 1993). [b] Average shift with $^{14}N_2{}^{15}N$. [c] Data from FTIR spectroscopy.

Further information about the nature of these two adducts comes from the use of the mixed isotope of azide, $^{15}N^{14}N_2^-$. The 2100-cm^{-1} peak (Figure 3.4A), which is the dominant mode in azido-Δ9D at pH 6.2, shifts uniformly by 11 cm^{-1} to lower energy (Figure 3.4B). The observation of only a *single* peak in the mixed isotope measurement suggests that this band must arise from a *symmetric* coordination of azide, such that the two ends of the azide molecule are equivalent. The only known symmetric coordination for metalloazide complexes occurs when azide forms a bridge between two metals ions in a μ-1,3 geometry. The −11 cm^{-1} shift observed from $^{15}N^{14}N_2$ substitution in azide-Δ9D is most similar to the −12 cm^{-1} shift observed for several copper model complexes known to have bridging μ-1,3 azides (**9**, **10**, Table 3.1). These model complexes also exhibit only a single vibrational mode with mixed-isotope azide. Therefore, we can assign the 2100-cm^{-1} peak in the azide-Δ9D to a μ-1,3 azide adduct.

Significantly different mixed-isotope behavior is observed for the η^1-terminal azide complexes of diferric Hr and MHr (Figure 3.4C). The azide complex of MHr shows a single ν_{as}(NNN) vibrational mode at 2048 cm^{-1} when prepared from $^{14}N_3^-$. In the presence of $^{15}N^{14}N_2$-azide, this ν_{as} band splits into two peaks of equal area at 2043 and 2031 cm^{-1} (Figure 3.4D), corresponding to the Fe-$^{14}N^{14}N^{15}N$ and Fe-$^{15}N^{14}N^{14}N$ orientations, respectively, with isotope shifts of −5 and −16 cm^{-1} relatively to Fe-$^{14}N_3$ (**2**, Table 3.1). The mixed-isotope azide complex of Hr reveals a similar splitting of ν_{as}(NNN) into two modes with downshifts of −6 and −17 cm^{-1} (**3**, Table 3.1). This same type of splitting is observed for the 2073-cm^{-1} azide species of Δ9D (Figure 3.5) at pH 7.8, where the contribution of the terminal adduct is maximized. With $^{14}N_3^-$ at pH 7.8, the peaks at 2100 and 2073 cm^{-1} can each be fit by a single band with the same width at half-height (Figure 3.5A). With $^{15}N^{14}N_2$-azide, spectral deconvolution reveals that the 2100-cm^{-1} mode from the μ-1,3 bridging azide shifts 11 cm^{-1} to lower energy as a single peak (Figure 3.5B), just as it did at pH 6.2 (Figure 3.4B). The remaining RR intensity in the mixed-isotope complex at pH 7.8 (Figure 3.5B) is much broad to be due to a single species. Instead, it is best modeled as the overlapping contributions of two vibrational modes at 2059 and 2071 cm^{-1} with equal areas and

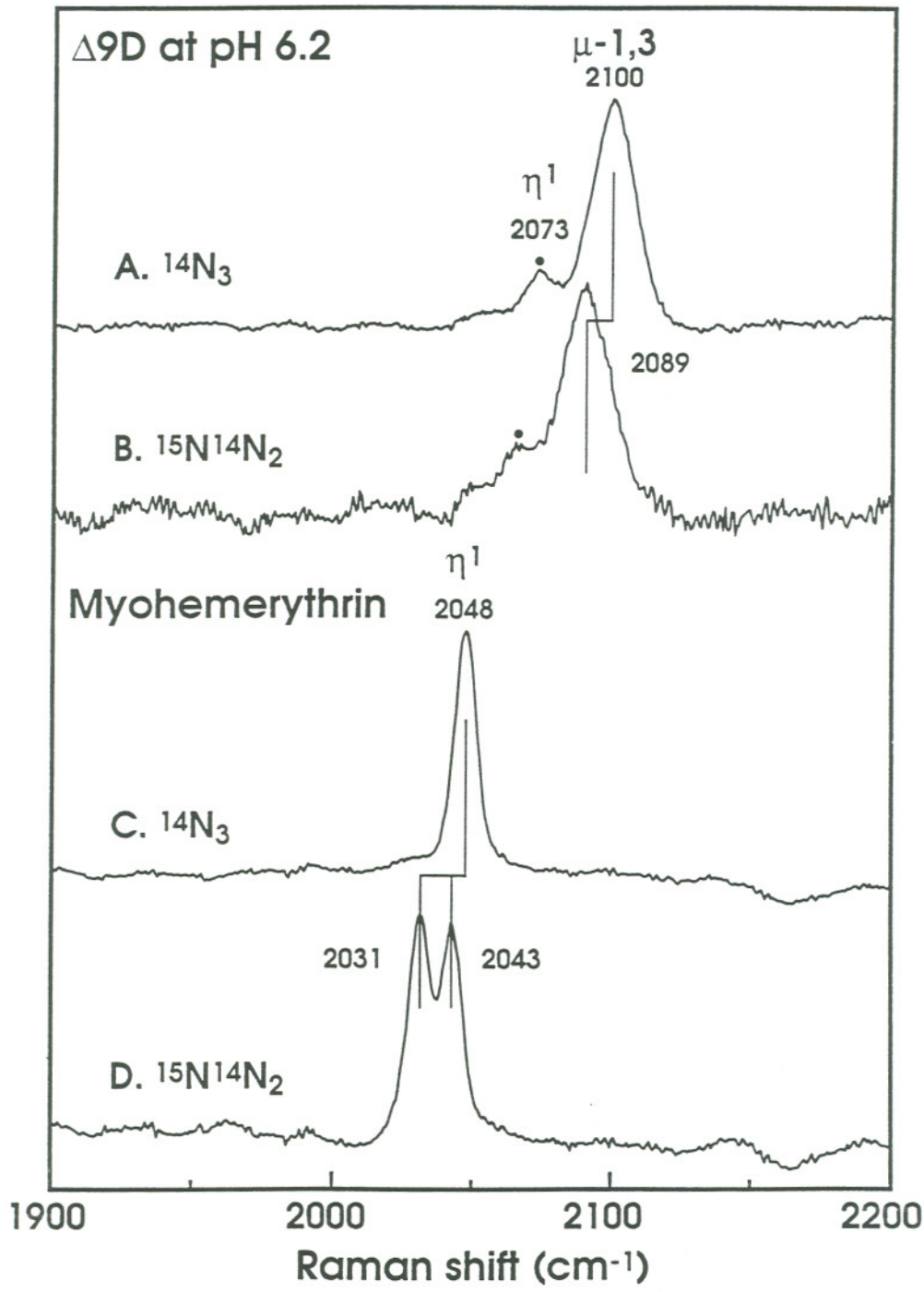

Figure 3.4 Effect of ^{15}N-azide on the intra-azide stretches of azido-Δ9D at pH 6.2. **A** Adduct of 700 mM $^{14}N_3^-$ with 2.0 mM Δ9D at pH 6.2. **B** Adduct of 700 mM $^{15}N^{14}N_2^-$ with Δ9D at pH 6.2. **C** Adduct of 200 mM $^{14}N_3^-$ with 4 mM MHr in 0.5 M Tris-sulfate (pH 8.0). **D** Adduct of 200 mM $^{15}N^{14}N_2$ with MHr. The Raman spectra were collected as in Figure 3.3.

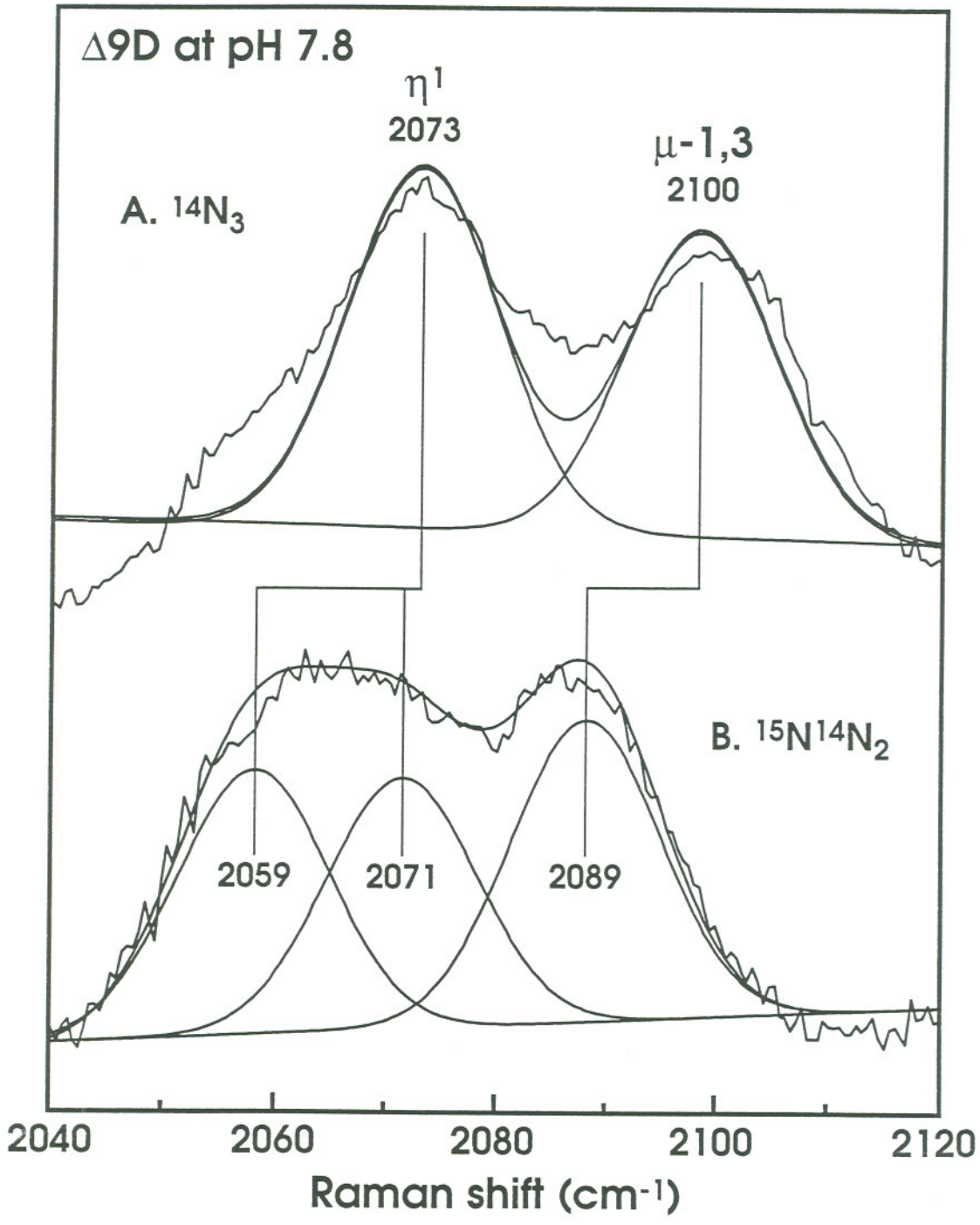

Figure 3.5 Effect of ^{15}N-azide on the intra-azide stretches of azido-Δ9D at pH 7.8. **A** Complex of Δ9D with $^{14}N_3^-$ at pH 7.8, as in Fig. 3C. **B** Complex of Δ9D with $^{15}N^{14}N_2^-$ at pH 7.8. The RR spectra were collected as in Figure 3.3. Each spectral envelope was fitted with a set of Gaussian curves using a constant width at half-height of 16 cm^{-1}, and the resulting sums are superimposed on the spectral envelope.

widths at half-height that have clearly arisen from the 2073-cm^{-1} mode of the $^{14}N_3$-azide complex (Figure 3.5A).

The appearance if two bands at 2059 and 2071 cm^{-1} in the mixed azide complexes of Δ9D (Figure 3.5B) indicates that the azide is bound *asymmetrically*. These bands could represent either an η^1-terminal configuration or a μ-1,1 bridging (μ-η^1:η^1) azide. However, the former seems more likely, as the respective isotope shifts of –2 cm^{-1} for Fe-$^{14}N^{14}N^{15}N$ and –14 cm^{-1} for Fe-$^{15}N^{14}N^{14}N$, as well as their 12 cm^{-1} differential (ΔΔ), are most similar to the values for the η^1-terminal complexes of Hr and MHr (**2**, **3**, Table 3.1). The Δ9D splitting are also close to the 6–11 cm^{-1} differentials observed for inorganic copper complexes containing η^1-terminal azide ligands (**4–6**, Table 3.1). In contrast, copper complexes with μ-1,1 bridging azide have significantly larger isotope shifts of –20 cm^{-1} for Cu-$^{15}N^{14}N^{14}N$ and larger differential (ΔΔ) values of 17–18 cm^{-1} (**12**, **13**, Table 3.1). Therefore, we have assigned the 2073 cm^{-1} band in azido-Δ9D to an η^1-terminal azide adduct.

Fe-N_3 and Fe-O-Fe vibrational modes

Excitation of Δ9D within its 440-nm absorption band results in the appearance of an additional peak in the RR spectrum at 378 cm^{-1} (Figure 3.6A). This peak is identified as the Fe-N_3 stretch by its 4-cm^{-1} shift to lower energy with $^{15}N^{14}N_2^-$ (Figure 3.6B). The frequency and isotope dependence of azido-Δ9D are similar to azido-MHr, whose ν(Fe-N_3) at 369 cm^{-1} undergoes a 3-cm^{-1} shift to lower energy with $^{15}N^{14}N_2^-$ (Figure 3.6C,D), and azido-Hr, which exhibits its corresponding ν(Fe-N_3) mode at 375 cm^{-1} (**3**, Table 3.1). Mixed-isotope substitution of an η^1-terminal azide is expected to result in two ν(Fe-N_3) vibrational modes, as was observed for the ν_{as}(NNN) modes of MHr (Figure 3.4D) and Δ9D (Figure 3.5B). However, since the isotope effect at 369 cm^{-1} is expected to be far less than the 12-cm^{-1} difference at 2050 cm^{-1}, the mixed-isotope splitting was not resolved in either MHr or Hr. In contrast, the 27 cm^{-1} difference in the ν_{as}(NNN) frequencies of the bridging and terminal azides in Δ9D (**1**, **8**, Table 3.1) does yield an observable effect on the ν(Fe-N_3) mode of Δ9D. Thus, the ν(Fe-N_3) peak, which is at 378 cm^{-1} in Δ9D at pH 7.8, where the terminal species predominates (60%), shifts 2 cm^{-1} to higher energy at pH

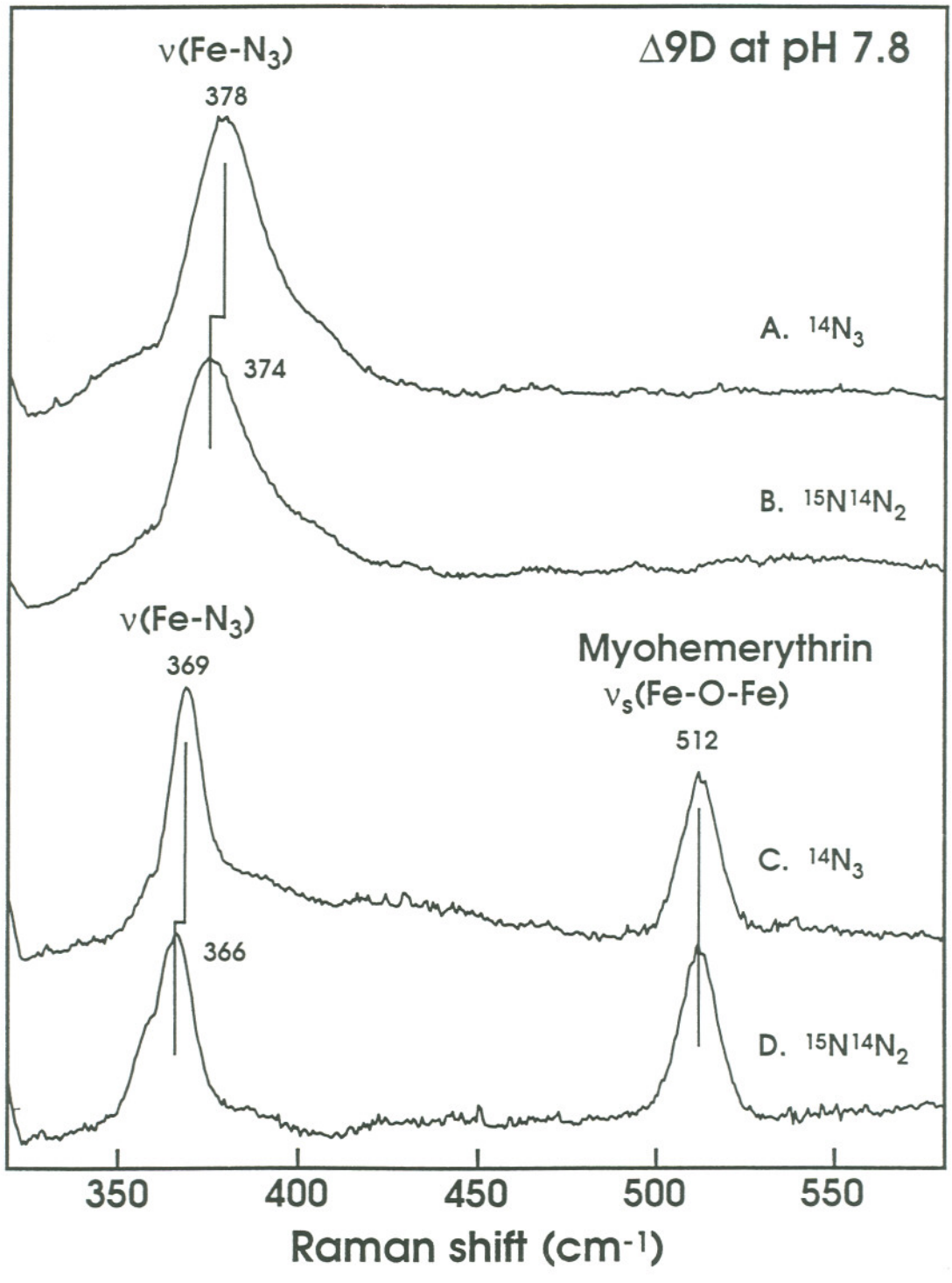

Figure 3.6 Fe-N_3 stretching modes in azido-Δ9D and azido-MHr. **A** and **B.** Samples of Δ9D at pH 7.8, as in Figure 3.5. **C.** Adduct of 400 mM $^{14}N_3^-$ with 1 mM MHr at pH 8.0. **D.** Adduct of 400 mM $^{15}N^{14}N_2^-$ with 1 mM MHr.

6.2 (Table 3.1) where the bridging species predominates (90%). The presence of two species (bridging and terminal) at pH 7.8 is also suggested by the observation that the ν(Fe-N_3) peak in Δ9D (Figure 3.6A) is significantly broader than in MHr (Figure 3.6C).

A further significant difference between azido-Δ9D and azido-MHr relates to the occurrence of the Fe-O-Fe symmetric stretch. Azide binding causes the ν_s(Fe-O-Fe) in Hr to shift from 512 to 507 cm^{-1} and the enhancement maximum to shift from 400 to 520 nm (Sanders-Loehr et al., 1989). This vibration is observed at 512 cm^{-1} in azido-MHr (Figure 3.6C) upon 488-nm excitation into the azide$\hat{E}\rightarrow\hat{E}Fe^{3+}$ charge transfer band, and was previously identified by its 18-cm^{-1} shift to lower energy in $H_2{}^{18}O$ (Duff et al., 1981). While the Fe-O-Fe symmetric stretch is not observed in azido-Δ9D with 488-nm excitation (Figure 3.6A), a residual Fe-O-Fe peak can be observed at 519 cm^{-1} with 350-nm excitation of azido-Δ9D. This peak has the same frequency and excitation maximum as the Fe-O-Fe stretch of the azide-free protein (Fox et al., 1994), suggesting that it represents a fraction of uncomplexed Δ9D in the azide-treated sample. This suggestion is supported by the observation that the ν_s(Fe-O-Fe) mode in Δ9D shows an inverse intensity relationship with the ν(Fe-N_3) mode (Figure 3.7). Thus, the increase in the amount of the various azide adducts upon going from pH 8 to pH 6 appears to correlate with the disappearance of the Fe-O-Fe moiety. Since Fe-OH vibrational modes are rarely observed in RR spectra (Ling et al., 1992), this could imply that the oxo bridge has become protonated. Alternatively, the loss of the Fe-O-Fe vibrational mode could mean that the oxo bridge has been lost upon formation of the N_3-adduct.

Effect of pH on azide complexes

The Raman intensity at 380 cm^{-1} (I_{380}) has contributions from the symmetric Fe-N vibration of both the μ-1,3-bridging and η^1-terminal azide adducts of Δ9D. Based on the I_{380}, azide complex formation is maximal at pH 6.2 (Figure 3.7). Quantitation of the behavior of the individual species is complicated by the tendency of azide to remove Fe from the protein at lower pH values. A comparison of the optical spectra of the eluate and retentate from a microconcentrator reveals that about

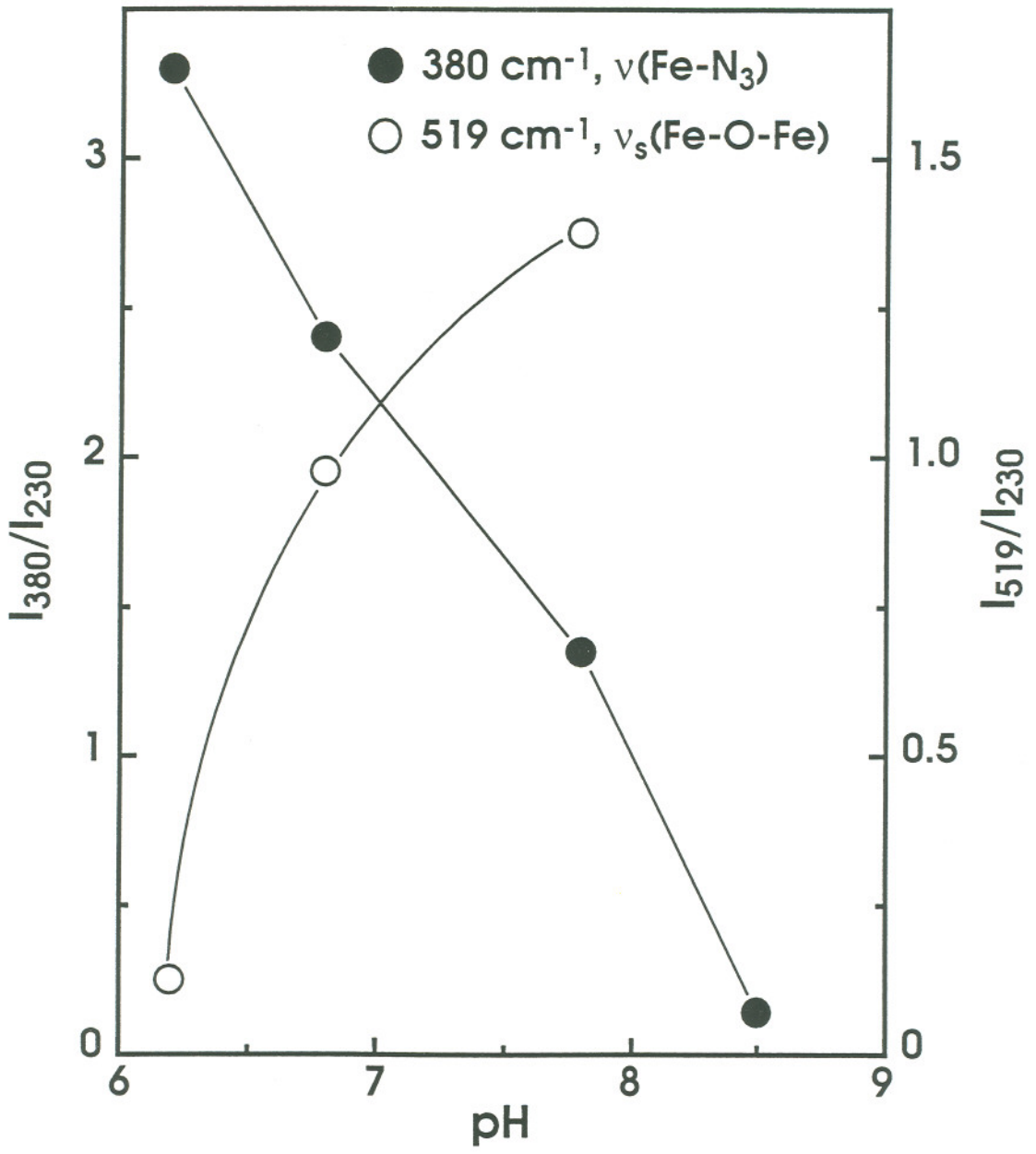

Figure 3.7 Intensity of Fe-N_3 and Fe-O-Fe vibrations as a function of pH. Intensities of Raman peaks measured as peak heights relative to the height of the ice mode at 230 cm^{-1}. The azide adducts of Δ9D were prepared as in Figure 3.3. Raman spectra containing ν(Fe-N_3) at 380 cm^{-1} (●) were obtained with 488-nm excitation (60 mW). Raman spectra containing ν_s(Fe-O-Fe) at 519 cm^{-1} (○) were obtained with 350-nm excitation (20 mW) on a Jarrell-Ash spectrophotometer.

20% of the ferric azide is no longer protein-bound at pH 6.8 and that considerably more iron is lost from the protein when the pH drops below 6.0. Freezing within 5 minutes of azide addition helps to minimize the amount of iron loss. Although the Fe-N_3 eluates produced at pH 6.8 and below have an intense orange color and significant optical absorbance at 340 and 460 nm, they do not yield any resonance-enhanced Raman vibrations. Thus, all of the RR features observed for azido-Δ9D can be attributed to azide adducts of the active site diiron centers. Analysis of the intra-azide stretching vibrations shows that the μ-1,3-bridging adduct accounts for $\sim$90% of the protein-bound azide at pH 6.2 and that the η^1-terminal adduct accounts for $\sim$60% of the protein-bound azide at pH 7.8 (Figure 3.3). However, at pH 8.5 and higher, the Fe-O-Fe species predominates and neither the terminal nor the bridging azide adducts are found (Figure 3.7).

The reactions between pH 7.5 and 8.5 are relatively reversible, primarily because there is less removal of Fe from the enzyme. Based on the changes in RR intensity of the Fe-N_3 symmetric stretch as a function of azide concentration, we estimate a K_D of $\sim$500 mM^{-1} for azido-Δ9D at pH 7.8. Azide appears to bind with similar affinity to the bridging and terminal positions because the relative Raman peak intensities for the two intra-azide stretch (Figure 3.3C) do not change when the azide concentration is lowered. Similarly, stopped flow experiments performed at pH 7.8 show that adduct formation (as monitored by either 325-nm or 440-nm absorbance) occurs in a single exponential phase implying that the two species form at the same rate, with a rate constant of 3.5 s^{-1}.

Discussion

Azide reactions with Δ9D

A mechanism accounting for the formation of both η^1-terminal and μ-1,3-bridging azide adducts is shown in Figure 3.8. At high pH, azide binding to form the η^1-terminal adduct is accompanied by the release of a metal-bound hydroxide or water or by rearrangement of a bidentate carboxylate ligand to provide an open coordination site. The increase in the Raman intensity of the η^1-terminal adduct at 2073 cm^{-1} as

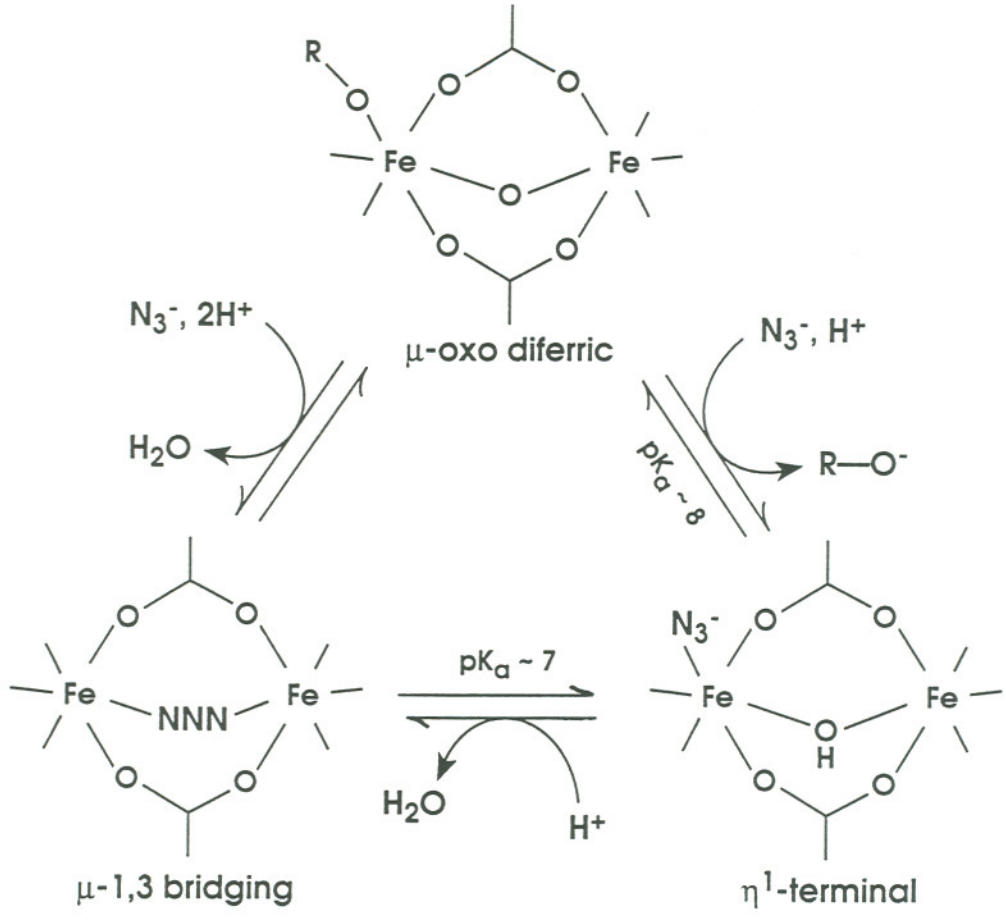

Figure 3.8 Proposed mechanism for the formation of the η^1-terminal and μ-1,3 bridging azide adducts from the diferric resting state of Δ9D. R—O^- indicates either hydroxo, water, or carboxylate.

the pH is lowered from 8.5 to 7.5 suggests a pK_a value of ~ 8. This protonation equilibrium most likely involves conversion of the oxo bridge to a hydroxo bridge, thereby explaining the failure to observe an Fe-O-Fe stretching mode with visible excitation (Figure 3.6). Similarly, the formation of a terminal azide complex in deoxyHr appears to be accompanied by protonation of the bridging oxygen (Reem & Solomon, 1987). Although it is possible for Δ9D to have two terminal azide ligands, the observation of only one ν_{as}(NNN) mode at 2073 cm^{-1} makes it likely that only one azide is bound in Δ9D. This is in contrast to MMO where the diiron center in the oxidized enzyme has been shown to bind two exogenous molecules of phenol, with two distinct Fe-O modes being detected by RR spectroscopy (Andersson et al., 1992).

Bridging azide becomes favored in Δ9D (Figure 3.8) as the pH is lowered from 7.8 to 6.2, with an apparent pK_a of ~ 7 for the conversion from the η^1-terminal to the μ-1,3 complex (Figure 3.3). Further protonation of the bridging oxygen is proposed, converting the hydroxo bridge to an aqua bridge which then dissociates to permit formation of μ-1,3 azide bridge. Alternatively, azide could replace a carboxylate bridge, as has been observed during the chemical synthesis of **11** and related complexes (Wieghardt et al., 1985; Kitajima et al., 1993). However, this seems less likely since carboxylate dissociation would not explain the observed pH dependence of the reaction and two carboxylate bridges are observed in the crystal structure of diferrous Δ9D (Lindqvist et al., 1996). A μ-1,3 bridging azide has also been proposed for the azide adduct of hemocyanin in its oxidized, dicupric state (Pate et al., 1989).

Metal-metal distances in bridged complexes

A number of μ-azido, μ-peroxo, and μ-oxo complexes of iron and copper have been characterized by X-ray crystallography (Figure 3.9). When the two metals are bridged by a single azide ion (as in 21), they have fairly long metal-metal distances of 4.8–5.1 Å and M-N-N angles of 123–132° (Chaudhuri et al., 1986). However, the presence of an additional bridging ligand as in **9**, **10**, and **11** constrains the metal-metal separation to a shorter distance of 3.6–3.7 Å, with a narrower M-N-N angle of 110–115°. A similar trend is observed for the peroxo complexes, where the singly

azides

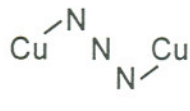

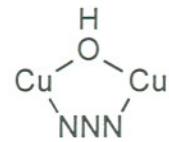

	21	**9**	**10**	**11**
M ···· M (Å)	4.80	3.61	3.68	3.71
∠M–O–M (deg)	—	137	138	148
∠M–NN (deg)	123	106	115	110

peroxides

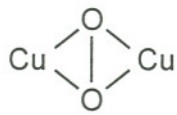

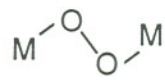

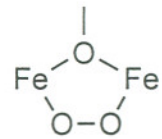

	14	**15, Cu**	**16, Fe**	**17**	**18**
M ···· M (Å)	3.56	4.36	4.00	3.46	3.33
M–O (Å)	1.92	1.85	1.89	1.90	1.93
∠M–O–M (deg)	135	—	—	121	112

bis-μ-oxo

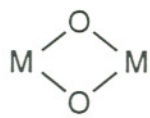

	19, Cu	**20, Fe**
M ···· M (Å)	2.79	2.71
M–O (Å)	1.81	1.84,1.92
∠M–O–M (deg)	101	93

Figure 3.9 Structures and metrical parameters of azide and peroxide complexes of binuclear metal sites. The metal oxidation states are Cu(II) or Fe(III), except for **19**, which is $Cu(III)_2$. Data from the following sources: **9** (McKee et al., 1981; McKee et al., 1984); **10** (Sorrell et al., 1985); **11** (Kitajima et al., 1993); **14** (Kitajima et al., 1992); **15** (Jacobsen et al., 1988); **16** (Kim & Lippard, 1996); **17** (Dong & Que, 1996); **18** (Ookubo et al., 1996); **19** (Halfen et al., 1996); **20** (Zang et al., 1995).

bridged structure **15** has a metal-metal distance of 4.36 Å, while the bis-μ-carboxylato complex **16**, and complexes **14**, **17**, and **18** containing monoatomic bridges have shorter metal-metal distances of 4.0 and 3.33–3.56 Å, respectively. A further contraction of metal-metal distance occurs in the di-μ-oxo complexes **19** and **20** which have values of 2.71–2.79 Å. The enzymes containing binuclear metal clusters appear to have a similar flexibility in metal-metal distances, thereby allowing them to adopt all of these bridging ligands. Thus, the Cu-Cu distance in hemocyanin varies from 4.6 Å in the dicuprous state (Magnus et al., 1994) to 3.66 Å for the μ-1,3-azide complex (Woolery et al., 1984), and 3.6 Å for the μ-η^2:η^2dicupric peroxide (Magnus et al., 1994), whose structure is similar to **14**. Similarly, the Fe-Fe distance in diferric MMO ranges from 3.1 Å with hydroxo to 3.4 Å with carboxylato as the third bridging ligand (Rosenzweig et al., 1995). Such changes in metal-metal distance are important in allowing the diiron enzymes to accommodate different catalytic intermediate with different bridging geometries.

In the crystal structure of the Δ9D, each iron is 5-coordinate with a His-nitrogen, a bidentate carboxylate, and two bridging carboxylates as ligands (Figure 3.10) and an iron-iron distance of 4.2 Å (Lindqvist et al., 1996). Since these properties are more characteristic of a diferrous state, it is likely that the diiron center was reduced in the X-ray beam. Furthermore, there is no evidence for the bridging oxygen which is known to be present in oxidized Δ9D (Fox et al., 1994) and the observed Fe-Fe distance is considerably, longer than the ~3.2 Å EXAFS value for diferric Δ9D (L. Shu, J. A. Broaderwater, B. G. Fox, L. Que, Jr., unpublished results). The substantial increase in iron-iron distance upon conversion of Δ9D from the diferric to the diferrous state emphasizes the conformational flexibility of the class II diiron enzymes relative to the class I O_2-carrier, hemerythrin, where the structure of the diferric and diferrous states are essentially super-imposable (Sheriff et al., 1987; Holmes et al., 1991). Similarly, the diferrous forms of R2 (Åberg, 1993) and MMO (Rosenzweig et al., 1995) have also undergone loss of a bridging oxo or hydroxo group, with a concomitant increase in iron-iron distance.

The presence of open coordination sites in the diiron enzymes appears to have functional significance. Thus, diferrous R2 is capable of binding two molecules of

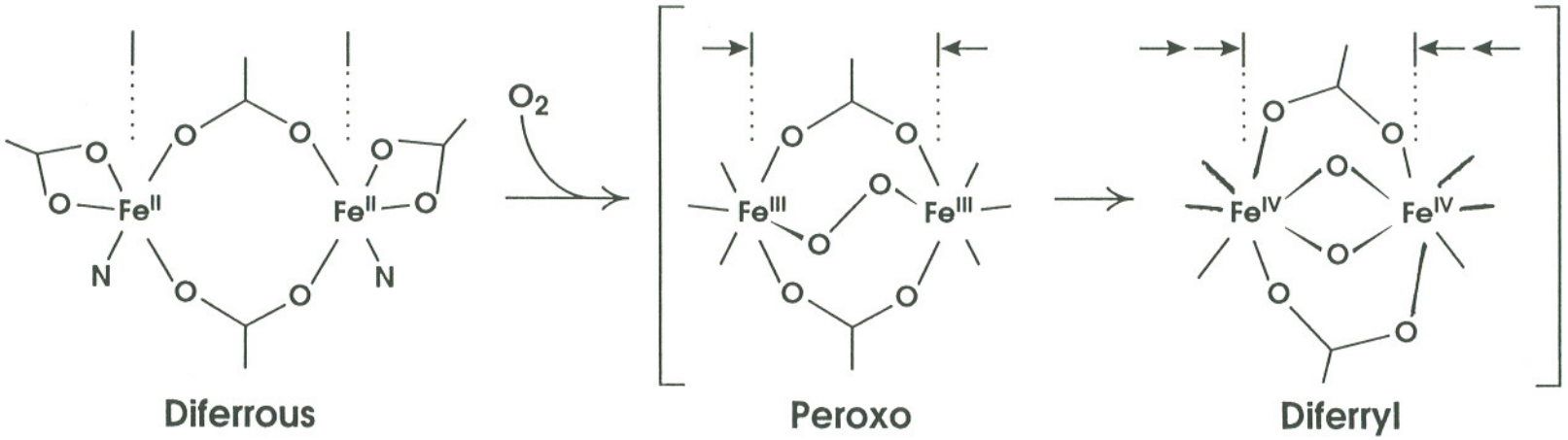

Figure 3.10 Proposed structures of key diiron center intermediates in the reaction cycle of the acyl ACP desaturases. The structure of the diferrous form has been determined by X-ray crystallography (Lindqvist et al., 1996). Arrows and dotted lines indicate the probable changes in iron-iron spacing upon reaction with O_2 to generate diferric-peroxo and bis-μ-oxo diferryl intermediates.

azide (Elgren et al., 1993; Pulver et al., 1995) or NO (Haskin et al., 1995). These molecules are presumably occupying coordination sites that would otherwise be filled by a bridging peroxide (Ling et al., 1994) in the normal reaction cycle of R2. Although the diferric forms of the iron-oxo enzymes are coordinatively saturated, they are capable of undergoing ligand exchange, particularly in the bridging position. For example, in one of the crystal structure of diferric MMO, an endogenous OH bridge has been replaced by an exogenous acetate bridge which binds as a bidentate carboxylate (Rosenzweig et al., 1995). The μ-1,3 bridging azide in diferric Δ9D provides another example of an endogenous oxo bridge being replaced by an exogenous anion (Figure 3.8). Given that the metal-metal spacing can range from 4.2 Å to 3.2 Å in going from diferrous to diferric Δ9D, there should be adequate flexibility to accommodate a bridging azide, particularly if the multiply bridged site could adopt a metal-metal distance to the 3.7 Å value for **11** or the 4.0 Å value for the diferric peroxo complex **16** (Figure 3.9). It is likely that this conformational flexibility also plays a role in the catalytic cycle of this enzyme.

Relevance to O_2-reactivation in the catalytic cycle

Structures for three key intermediates in the Δ9D reaction cycle are shown in Figure 3.10 that are similar to intermediate previously proposed for MMO and R2 (Feig & Lippard, 1994; Lipscomb, 1994; Burdi et al., 1996; Que & Dong, 1996). The formation of a μ-1,3 azide complex described here suggests the potential for a related μ-1,2 diferric-peroxo intermediate in Δ9D. Addition of O_2 to the pentacoordinate diferrous center and formation of the μ-1,2 peroxide could proceed spontaneously without a need for the release of previously bound ligands or changes in protonation state. This reaction also provides a rationalization for the ability H_2O_2 to support catalytic turnover of the diferric MMO, whereas peracids and iodosylbenzene do not (Andersson et al., 1991). Furthermore, the 4.2 Å iron-iron distance in diferrous (Lindqvist et al., 1996) would have to decrease only slightly to match the 4.0 Å distance observed in the *trans*-diferric peroxo complex **16** (Figure 3.9) which also has two carboxylate bridges. Although a μ-1,2peroxide intermediate could have either a *cis* or *trans* geometry, a *trans* configuration is supported by the

close match in the Mössbauer and RR parameters of **16** and compound **P**, the proposed diferric peroxo intermediate of MMO (Liu et al., 1995; Kim & Lippard, 1996).

Homolysis of the O-O bond in the μ-1,2 bridged peroxo species (Que & Dong, 1996) could produce a di-μ-oxo diferryl intermediate (Figure 3.10), possessing the two oxidizing equivalents required for the O_2-dependent desaturation stoichiometry (van de Loo et al., 1993). Steric considerations would favor a *trans* over a *cis* configuration for the conversion of the peroxide to a di-μ-oxo species. Rearrangements of the carboxylate ligands could permit the decrease in the metal-metal distance needed for a di-μ-oxo intermediate (Figure 3.9), as well as allowing the hexacoordinate geometry of the iron sites to be maintained. This mechanism demands that both atoms from O_2 be incorporated into the di-μ-oxo intermediate, and suggests that one atom of O_2 may remain as the oxo bridge after catalytic turnover to the diferric state. Indeed, this result has been observed for single turnover oxidation of R2 in the presence of $^{18}O_2$ by use of RR spectroscopy (Ling et al., 1994). While comparable ^{18}O incorporation was not observed during single turnover of Δ9D (Fox et al., 1994), it is possible that the μ-oxo species in Δ9D may undergo more rapid exchange with solvent in the diferryl than the diferric state. The faster oxo-bridge exchange in Δ9D could be due to the presence of a solvent molecule located in a small hydrophobic pocket near the iron center, as well as to the presence of T199 in the active site (Lindqvist et al., 1996).

How the individual diiron enzymes R2, MMO, and Δ9D mediate the fate of a common diferryl oxidizing intermediate to provide Tyr-122 radical formation, hydrocarbon hydroxylation, and acyl chain desaturation remains to be elucidated. In the case of Δ9D, the crystal structure (Lindqvist et al., 1996) shows that tight binding contacts position the fatty acid near to the diiron center in a manner that enforces the exclusive formation of *cis*-double bonds.

CHAPTER IV

EFFECTS OF THE Leu 103Asn MUTATION ON LIGAND BINDING TO THE DIIRON SITE IN MYOHEMERYTHRIN[1]

Abstract

Resonance Raman spectroscopy has been used to identify exogenous ligands at the O_2 binding site in myohemerythrin (Mhr) from *Themiste zostericola* and its L103N mutant. The Fe^{III}-O-Fe^{III} moiety of Mhr exhibits an oxo → Fe CT band at 369 nm and a ν_s(Fe-O-Fe) vibration at 506 cm^{-1} that are typical of an OH-coordinated species. Addition of 1 M LiCl results in the displacement of hydroxide by chloride, as judged by the appearance of a new absorption maximum at 381 nm and ν_s(Fe-O-Fe) at 511 cm^{-1}. This verifies the finding of a chloride ligand in the X-ray structure of Mhr crystallized from 1M LiCl (Martins et al., 1997). Interestingly, the L103N mutant crystallized under the same conditions gives no indication of a chloride ligand. Its X-ray structure has been interpreted as having a more firmly bound hydroxide ligand held in place by H-bonding to a water molecule that is in turn H-bonded to Asn-103. This interpretation is supported by the observation of a ν_s(Fe-O-Fe) peak at 516 cm^{-1} that is unaffected by the addition of chloride, but splits into two peaks at 506 and 526 cm^{-1} in D_2O. This splitting is ascribed to Fermi resonance coupling of ν_s(Fe-O-Fe) with δ(Fe-O-D) and, thus, provides strong evidence for a coordinated hydroxide in the L103N mutant. Addition of azide to the L103N mutant results in the appearance of two ν(Fe-N_3) modes at 337 and 366 cm^{-1}, corresponding to two different azide complexes. One of these frequencies is considerably lower than that in wild-type Mhr, which exhibits a single ν(Fe-N_3) mode at 369 cm^{-1}. The low frequency of the

---

[1] This work was performed in collaboration with Professor Walther R. Ellis Jr. and Dr. Laura J. Martins, Department of Chemistry, University of Utah.

337-cm^{-1} Fe-N stretch in the L103N mutant is proposed to be due to H-bonding of the coordinated azide nitrogen by the H_2O-Asn 103 network. This H-bonding network could be responsible for the faster rate of autooxidation of bound O_2 in the oxy complex of the L103N mutant. Thus, these RR studies provide direct evidence that the Leu 103 residue plays a functional role in determining the bond strength and orientation of exogenous ligands at the diiron site of Mhr.

Introduction

Hemerythrin (Hr) functions as an oxygen transport protein in four phyla of marine invertebrates. Hr is usually found as a homooctamer, although dimers, trimers and tetramers are also known (Stenkamp, 1994). A monomeric analogue of Hr, myohemerythrin (Mhr), was isolated from the muscles of the sipunculid worm, *Themiste zostericola* (Klippenstein et al., 1972). Mhr is very similar to a Hr monomer in both structure and function (Stenkamp, 1994). In both cases, the monomer is a single polypeptide chain with a molecular weight of $\sim$13.9 kD and a diiron center which is responsible for the reversible binding of one molecule of O_2. The diferrous cluster of deoxyMhr reacts with dioxygen to form the diferric cluster of oxyMhr, accompanied by the two-electron reduction of dioxygen to peroxide which is protonated (Dunn et al., 1973; Shiemke et al., 1984). The binding of hydroperoxide is stabilized by a hydrogen bond between the hydroperoxide and the oxo bridge (Shiemke et al., 1986, Stemkamp, 1994). OxyMhr can release O_2 by reverting to deoxyMhr or it can decay by an autooxidation process whereby H_2O_2 dissociates from the diiron center with the concomitant formation of diferric (met) Mhr. In their met states, Hr and Mhr can form complexes with a wide range of anionic ligands, such as azide and chloride, which serve as hydroperoxide analogs (Freier et al., 1980; Duff et al., 1981).

The crystal structure of azidoMhr from *T. zostericola* has been solved at 1.7-Å resolution (Sheriff et al., 1987). Mhr possesses a four-helix bundle that surrounds the diiron site. The two iron atoms are linked by two carboxylates from Asp-111 and Glu-58 and one oxo bridging atom. One iron atom (Fe1) is coordinated to three His

ligands (His-73, His-77, and His-106); the other iron atom (Fe2) is coordinated to two His ligands (His-25 and His-54) and the exogenous ligand, azide. The crystal structures of azidometHr (Holmes & Stenkamp, 1991) and oxyHr (Holmes et al., 1991) from *Themiste dyscrita* have shown that azide and peroxide bind to the Fe2 site in an analogous fashion. The exogenous ligand site is located in a cleft surrounded by hydrophobic amino acids which help to stabilize the iron-ligand complex (Yamashita, et al., 1990). The Leu 103 residue in the hydrophobic pocket of Mhr (Figure 4.1A), which corresponds to Leu 98 in octameric Hr, is totally conserved in the sequences of all Hrs and Mhrs (Takashi & Cox, 1991; Stenkamp, 1994). More importantly, in oxyHr and azidometHr from *T. descrita,* and azidometMhr from *T. zostericola*, the methyl groups of this Leu residue are in van der Waals contact with the bound exogenous ligand (ca. 4 Å from the active site).

In order to further understand the structural and functional role of the hydrophobic pocket, Leu 103 of Mhr has been mutated to Asn, a residue of equivalent size but increased polarity, and the resultant protein has been expressed in *E. coli* (Raner et al., 1994). The L103N mutant exhibits little O_2 transport capability due to the rapid autooxidation of its oxy adduct to diferric protein and hydrogen peroxide (Raner et al., 1997). In addition, the met form of the L103N mutant has a greatly reduced affinity for azide with a binding constant that is 460-fold less than in wild-type Mhr (Raner et al., 1997). The crystal structure of the L103N mutant in the absence of added exogenous ligands has been solved at 1.8-Å resolution (Martin et al., 1997). This structure revealed a coordinated solvent molecule at the exogenous-ligand site on Fe2 that appeared to interact with Asn 103 via an intervening water molecule (Figure 4.1B). Our resonance Raman (RR) spectroscopic studies have provided direct evidence that the exogenous ligand of the L103N mutant is a hydroxide ion.

The diferric clusters in Hr and Mhr have been extensively studied by RR spectroscopy (Kurtz et al., 1977; Sanders-Loehr, 1989). The RR spectra of Hr, Mhr and their complexes exhibit Fe-O-Fe vibrational modes at $\sim$510 cm^{-1} and $\sim$760 cm^{-1} that have been assigned to the symmetric stretch, ν_s(Fe-O-Fe), and asymmetric stretch, ν_{as}(Fe-O-Fe), respectively (Freier et al., 1980; Duff et al., 1981; Sanders-

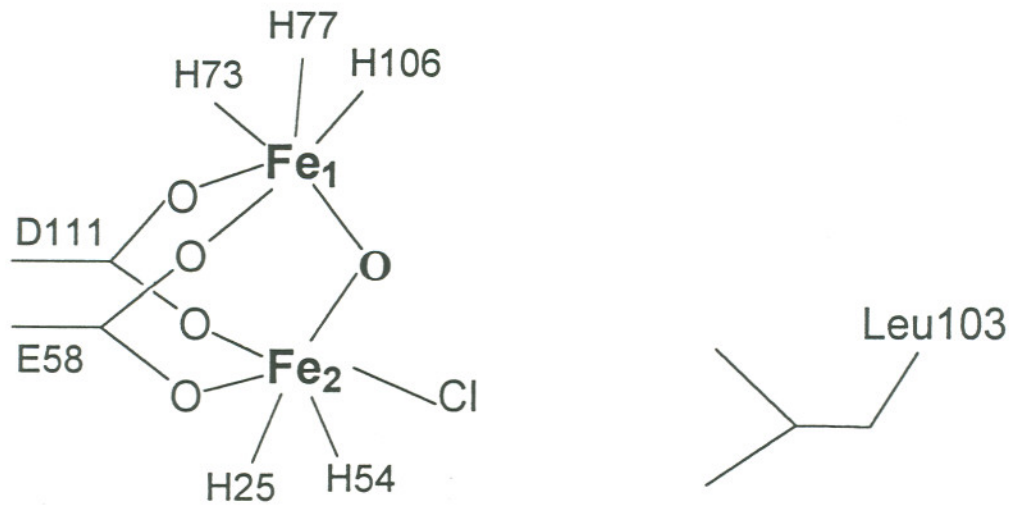

A. MHr(Cl)

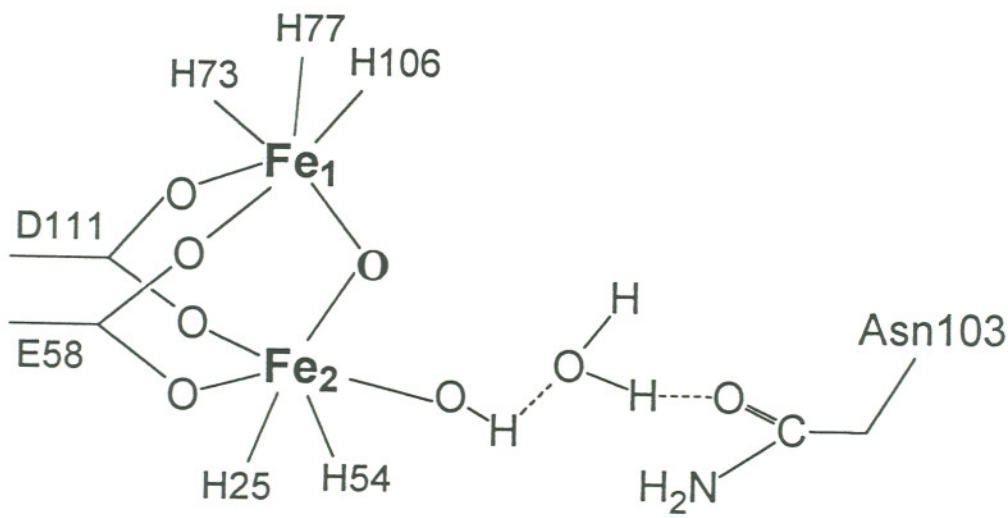

B. L103N mutant

Figure 4.1 Diiron sites in the met forms of (A) Mhr and (B) L103N mutant. The structures were determined by X-ray crystallography (Martins et al., 1997). The presence of a chloro ligand in Mhr and a hydroxo ligand in L103N was verified by RR spectroscopy (present work).

Loehr et al., 1989). Comparison of RR and crystallographic data from a large number of diiron-oxo model compounds has revealed that the frequencies of ν_s(Fe-O-Fe) and ν_{as}(Fe-O-Fe) are related to the angle of the Fe-O-Fe moiety and, hence, are sensitive to the number of bridging groups between the two iron atoms (Sanders-Loehr et al., 1989). The RR spectra also reveal vibrations of exogenous ligands. Thus, oxyHr exhibits ν(Fe-O_2) at 503 cm^{-1} and ν(O-O) at 844 cm^{-1}, whereas azidometHr exhibits ν(Fe-N_3) at 375 cm^{-1} and ν_{as}(N_3) at 2048 cm^{-1}. Consistent with the crystal structures, RR experiments with mixed isotopes demonstrated that both the peroxide and the azide were bound in an end-on fashion (Kurtz et al., 1976). We have used RR spectroscopy to probe the diiron site structure of the L103N mutant and discovered that it forms two different complexes with added azide.

Materials and Methods

Overexpression and purification of Mhrs

The recombinant Mhrs used in this study were expressed in *Escherichia coli* BL-21 (DE3) cells possessing either the pMHR plasmid (carrying the gene for wild-type *Themiste zostericola* Mhr) or the pL103N plasmid (carrying the L103N mutation in *T. zostericola* Mhr) and purified as previously described (Raner et al., 1997).

Raman samples

All studies were performed on the met forms of wild-type Mhr and its L103N mutant at a protein concentration of ~4 mM. For deuterium isotope exchange, the protein samples (~4.0 mM) were diluted 10-fold in 50 mM Tris-SO_4 in D_2O. The buffer was prepared by dilution of 1.5 M Tris-SO_4 into 99.9 atom % D_2O (Aldrich) to yield 96.5 atom % D. The samples were reconcentrated 10-fold in a Microcon 10 ultrafiltration device (Amicon) to give Raman samples with a D_2O enrichment of 87% (pH reading 8.3). A control sample was prepared in 50 mM Tris-SO_4 in H_2O (pH 8.0) using the same procedures. The samples were incubated overnight at 4°C prior to use in Raman experiments. Azide complexes of Mhr or the L103N mutant were

prepared by adding solid $Na^{14}N_3$ or $Na^{15}N_3$ (ICN, 99 atom % ^{15}N, uniformly labeled) to the ~4.0 mM protein sample to give a final azide concentration of 100 mM.

Resonance Raman spectroscopy

Unless otherwise stated, Raman spectra were recorded on a custom McPherson 2061/207 spectrograph with a Princeton Instruments liquid-N_2-cooled (LN-1100PB) CCD detector, and Rayleigh scattering was attenuated with a Kaiser Optical holographic super-notch filter. Alternatively, Raman spectra were recorded on a computerized Jarrell-Ash spectrophotometer using a cooled RCA C31034A photomultiplier and an ORTEC model 9302 amplifier-discriminator. The desired excitation wavelengths were provided by Spectra-Physics 164 Ar, Coherent Innova 90 Ar, and Coherent Innova 302 Kr lasers. The spectra were obtained in a 90°-scattering geometry from the samples at 278 K in glass capillaries cooled by a copper rod immersed in an ice bath, or in a 150° backscattering geometry from the samples cooled to ~15 K on the cold head of a helium refrigerator (Displex, Air Products) or from the samples at 90 K in capillaries cooled by a copper rod in a Dewar flask filled with liquid nitrogen (Loehr & Sanders-Loehr, 1993). Peak frequencies were calibrated relative to an indene standard and are accurate to $\pm$ 1 cm^{-1}. Spectra of isotopically substituted samples were obtained under identical instrumental conditions such that frequency shifts are accurate to $\pm$ 0.5 cm^{-1}.

Results and Discussion

Identification of chloride ligand in Mhr

The crystal structure of recombinant Mhr from *T. zostericola* (Martins et al., 1997) revealed a single-atom substituent on Fe2 that was tentatively identified as a chloride adduct (Figure 4.1A). This assignment was based on the fact that the crystals had been soaked in 1 M LiCl and that satisfactory B values were obtained when this site was refined as a chloride. Further evidence for chloride as the exogenous ligand in Mhr in the presence of 1 M LiCl comes from the electronic and RR spectroscopic properties of this system.

The electronic spectra of oxo-bridged diiron proteins and model complexes exhibit two intense absorption bands between 300 and 400 nm that have been assigned to oxo →Fe(III) charge transfer (CT) (Garbett et al., 1969; Reem et al., 1989; Sanders-Loehr et al., 1989). In the case of metHr, the energies of these two absorption bands are sensitive to the nature of the exogenous ligand (Garbett et al., 1969; Reem et al., 1989). In the chloride complex of octameric Hr, both of these bands occur at longer wavelength than in the hydroxide complex (Table 4.1). A similar spectral shift to longer wavelength is observed for Mhr in the presence of 1 M chloride (Figure 4.2A), with the resulting maxima at 329 and 381 nm being essentially identical to the values observed in the chloride complex of Hr. Excitation within an oxo → Fe(III) CT band causes enhancement of the Fe-O-Fe symmetric stretch in the RR spectrum. The frequency of the ν_s(Fe-O-Fe) mode in Hr has been found to vary from 506 to 514 cm^{-1}, depending on the nature of the exogenous ligand (Freier et al., 1980; Shiemke et al., 1986). Mhr exhibits the same ν_s(Fe-O-Fe) frequencies as Hr (within $\pm$ 1 cm^{-1}) with azide, cyanide, and thiocyanate as exogenous ligands (Duff et al., 1981). In the presence of 1 M chloride, the ν_s(Fe-O-Fe) mode in Mhr occurs at 511 cm^{-1} (Table 4.1) which is essentially the same as the 510-cm^{-1} value for Hr(Cl) and significantly different from the 506-cm^{-1} value for MHr(OH). These Raman results provide additional support for the formation of a chloride adduct in Mhr.

Identification of hydroxide ligand in Mhr

In the absence of added anions, metHr exhibits two different diiron site structures that are dependent on the pH. The low-pH form has been characterized by X-ray crystallography and shown to have an unusual 5-coordinate Fe2 that is lacking an exogenous ligand (Holmes et al., 1991). Hydroxide ion binding is associated with a pK_a of 7.4–8.4 and results in a shift of the major absorption band from ~355 nm to ~362 nm (Bradic & Wilkins, 1981; McCallum et al., 1984). The met form of Mhr exhibits no spectral change between pH 8 and 9, and its 369-nm absorption maximum is more characteristic of a hydroxide adduct (Table 4.1). Further evidence for a hydroxo ligand comes from studies of the autooxidation of oxyMhr, where the

Table 4.1

Absorbance and Raman Spectroscopic Properties
of Met Forms of Hemerythrin and Myohemerythrin

Sample	Conditions	Oxo→Fe^{III} CT Bands nm		ν_s(Fe-O-Fe) cm^{-1}
Octameric Hr[a]				
Hr	pH 7.0	335	355	512
Hr(OH)	pH 9.0	320	362	506[b]
Hr(Cl)	1 M NaCl	329	380	510
Myohemerythrin[c]				
Mhr(OH)	pH 8–9	324	369	506
Mhr(Cl)	1 M LiCl	329	381	511
L103N(OH)	pH 8–9	334	372	516
L103N(OH)	1 M LiCl	334	372	516

[a] Octameric hemerythrin from *Phascolopsis gouldii*. Electronic spectra from Garbett et al. (1969) and McCallum et al. (1984). Raman spectra at 278 K from Shiemke et al. (1986). [b] Non-H-bonded *trans* species. [c] Raman spectra at 15 K, except Mhr(OH) at 278 K.

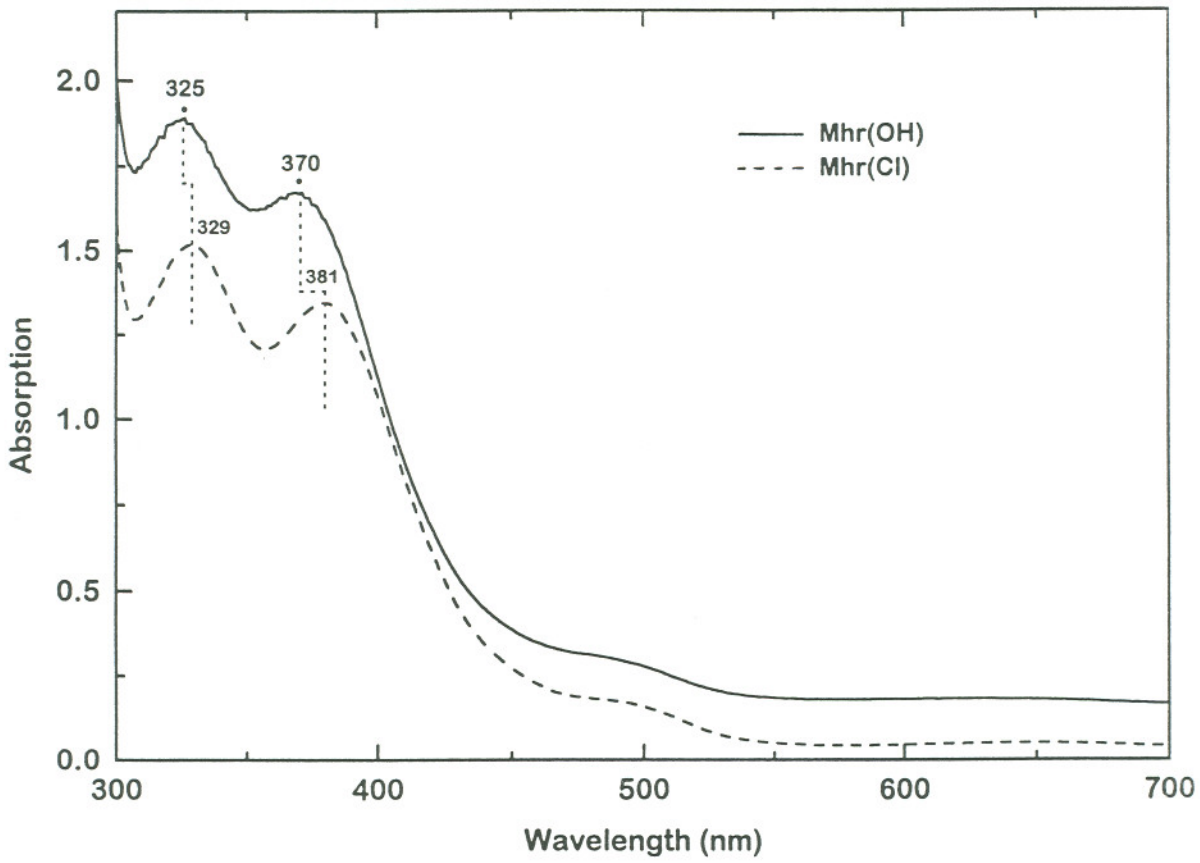

Figure 4.2 Effect of chloride on the absorption spectrum of Mhr. Protein in 50 mM Tris-SO_4 (pH 8.0) in the absence (___) and presence (------) of 1 M LiCl.

displacement of peroxide from Fe2 appears to be solvent-assisted and occurs more readily at higher pH, leading to a Mhr(OH) product (Lloyd et al., 1998). Since the absorption spectrum of Mhr(OH) is unaltered between pH 8 and 9, Mhr(OH) must have a lower pKa (~7.0) for conversion to the acid form.

The RR spectrum of the Mhr(OH) reveals a ν_s(Fe-O-Fe) mode at 506 cm^{-1} that is unaffected by D_2O (Figure 4.3A). The lack of a D-isotope dependence for ν_s(Fe-O-Fe) is similar to the behavior of other anion adducts of Hr (Shiemke et al., 1986) and indicates that this is a pure Fe-O-Fe stretching mode that is not coupled to any Fe-OH vibrations or affected by hydrogen bonding. The RR behavior of Hr(OH) is considerably more complex with two ν_s(Fe-O-Fe) modes at 492 and 506 cm^{-1}, an ν(Fe-OH) mode at 565 cm^{-1}, and extensive shifts in D_2O indicative of Fermi-resonance coupling of ν_s(Fe-O-Fe) with δ(Fe-O-D) (Shiemke et al., 1986). The 492-cm^{-1} mode has been attributed to a *cis* complex in which the coordinated hydroxide is H-bonded to the oxo bridge, and the 506-cm^{-1} mode has been attributed to a *trans* complex in which the hydroxide is not H-bonded to the oxo bridge. The 506-cm^{-1} frequency and lack of a deuterium effect for ν_s(Fe-O-Fe) in Mhr(OH) suggest the presence of a hydroxide ligand that is not involved in hydrogen bonding.

Identification of hydroxide ligand in L103N mutant

The crystal structure of the L103N mutant of Mhr (Martins et al., 1997) revealed that the exogenous ligand at the Fe2 site is H-bonded to a water molecule which in turn is H-bonded to the carbonyl of Asn 103 (Figure 4.1B). Although the crystals were prepared from 1 M LiCl (pH 7.0), satisfactory B values could only be obtained when the exogenous ligand was refined as hydroxide rather than chloride. Furthermore, the energy of the oxo ® Fe(III) CT band of the L103N mutant at 372 nm (Figure 4.4A) is closer to that of Mhr(OH) at 369 nm than of Mhr(Cl) at 381 nm (Table 4.1). Raman spectroscopy provides additional evidence for a hydroxide ligand in the L013N mutant.

The L103N mutant reveals a ν_s(Fe-O-Fe) mode at 514 cm^{-1} when the RR spectrum is obtained at ice temperature (Figure 4.3B) and at 516 cm^{-1} when the RR spectrum is obtained at 90 K (Figure 4.5A). Incubation in D_2O results in a 12-cm^{-1}

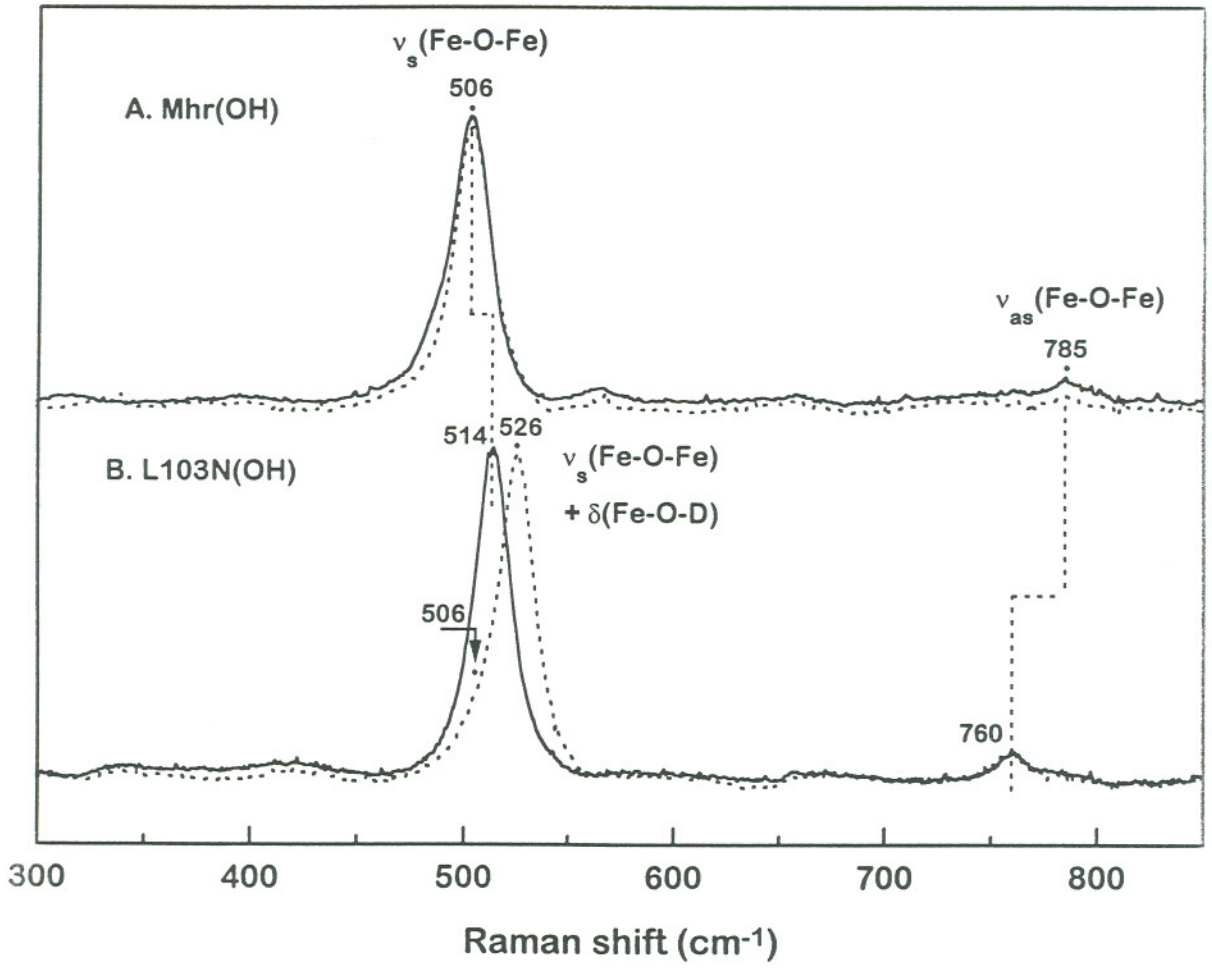

Figure 4.3 Raman spectra of Mhr and L103N mutant. (A) Mhr at pH 8.0 in H_2O (____) or at pH reading 8.3 in D_2O (-----). (B) L103N mutant at pH 8.0 in H_2O (____) or at pH reading 8.3 in D_2O (-----). The spectra were obtained at 278 K using 413-nm excitation (20 mW), 1800-groove grating, 6-cm^{-1} resolution, and 6-min accumulation.

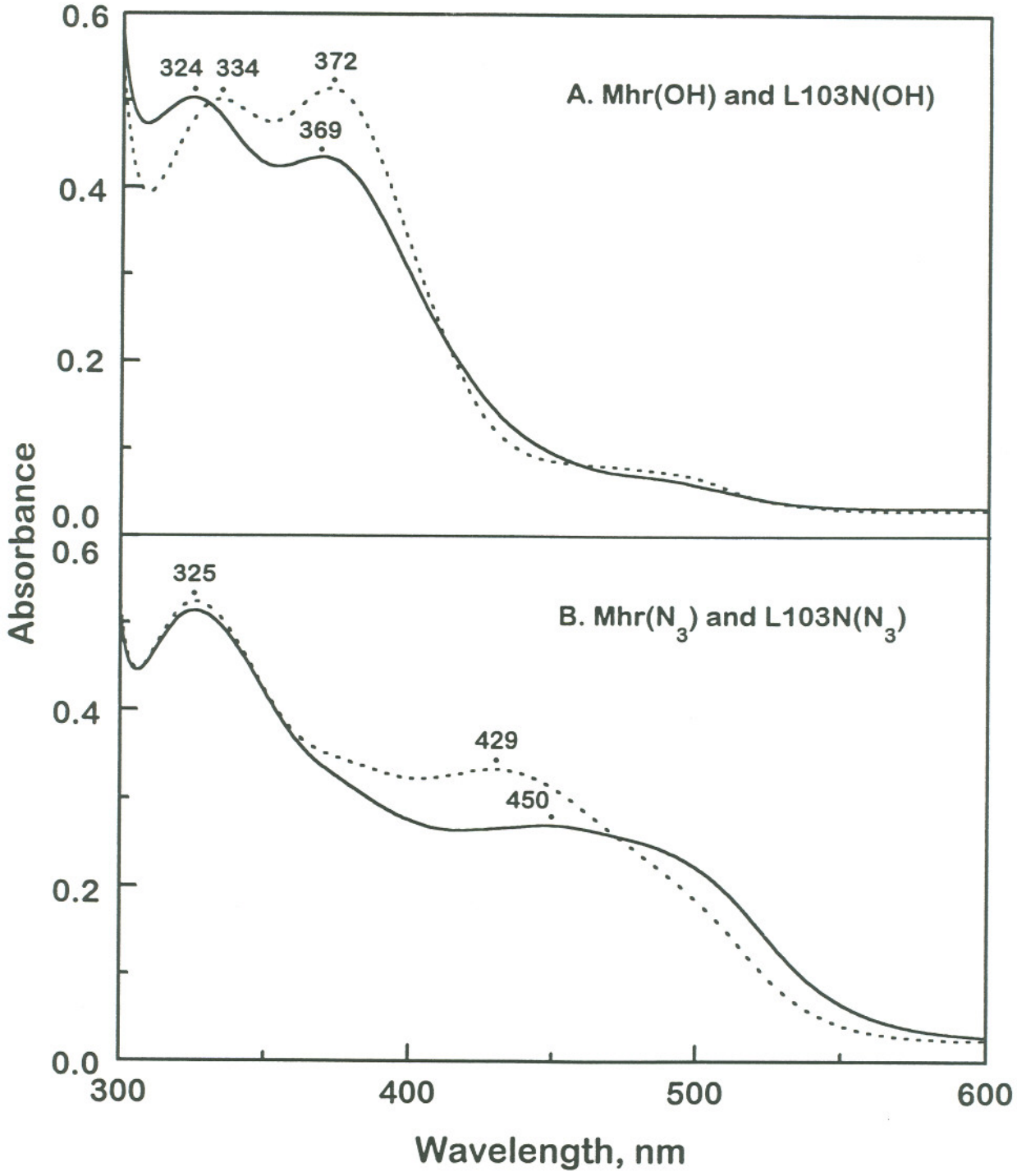

Figure 4.4 Absorption spectra of Mhr (___) and L103N mutant (-----). (A) Protein (~0.08 mM) in 50 mM Tris-SO_4 (pH 8.0). (B) Protein in same buffer plus 100 mM azide.

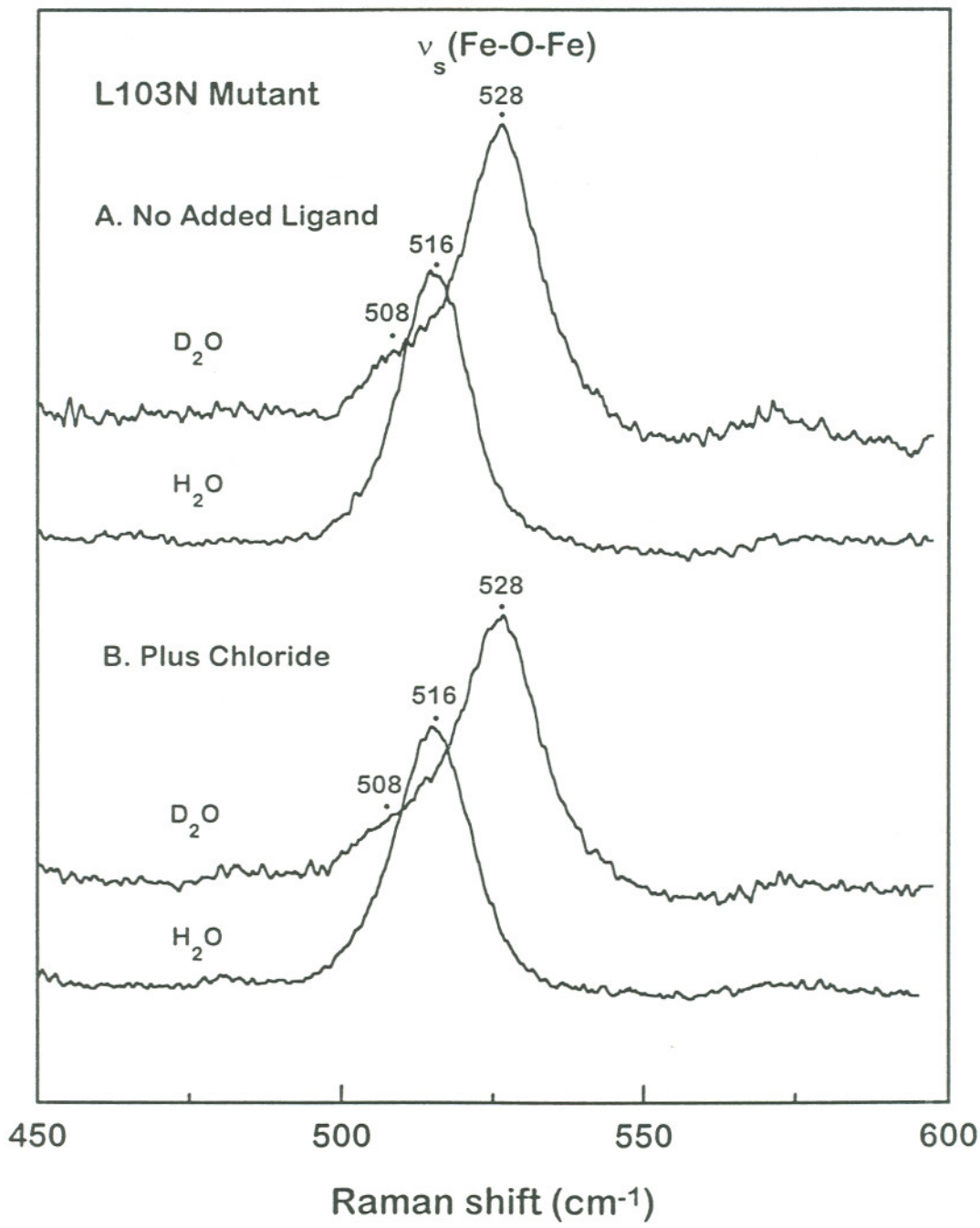

Figure 4.5 Chloride-independence of Raman spectra of L103N mutant. (A) Samples (~4 mM) in H_2O (___) or D_2O (-----). (B) Samples (~4 mM) plus 1 M LiCl in H_2O (___) of D_2O (-----). The spectra were obtained at 90 K using 413-nm excitation (20 mW), 3600-groove grating, 6-cm^{-1} resolution, and 15-min accumulation.

upshift to 528 cm^{-1} with a shoulder appearing at 508 cm^{-1} (Figure 4.5A). The D-dependence of ν_s(Fe-O-Fe) in the L103N mutant is reminiscent of the *cis* form of Hr(OH) in which the ν_s(Fe-O-Fe) peak at 490 cm^{-1} splits into two peaks at 518 cm^{-1} and 463 cm^{-1} in D_2O, presumably due to vibrational coupling between ν_s(Fe-O-Fe) and δ(Fe-O-D) (Shiemke et al., 1986). Typically, the M-O-H bend in metal hydroxide complexes occurs at 900 ($\pm$ 300) cm^{-1} and shifts several hundred cm^{-1} to lower energy upon deuteration (Nakamoto, 1986). Thus, in the L103N mutant, the ν_s(Fe-O-Fe) mode at 516 cm^{-1} could undergo a similar Fermi resonance coupling with an Fe-O-D bend near 516 cm^{-1} to produce two new peaks at 528 and 508 cm^{-1}.

The addition of 1 M LiCl, as was used in the preparation of the L103N crystals (Martin et al., 1997), has no effect on the ν_s(Fe-O-Fe) modes of the L103N mutant in either H_2O or D_2O (Figure 4.5B). This demonstrates that chloride is not a ligand and that the hydroxide in L103N(OH) is more strongly coordinated than in Mhr(OH), since the latter is converted to Mhr(Cl) in the presence of 1 M LiCl (Table 4.1). It is likely that the the H-bonding network involving an intervening water molecule and the amide side chain of Asn 103 helps to anchor the hydroxide ligand in the L103N mutant (Figure 4.1B).

The L103N mutant exhibits a ν_{as}(Fe-O-Fe) mode at 760 cm^{-1} which, in contrast to the ν_s(Fe-O-Fe) mode, is unaffected by D_2O (Figure 4.3B). The lack of a D-isotope dependence is indicative of a lack of H-bonding to the oxo bridge and, thus, supports the crystallographic model for the L103N mutant. A comparison of the Fe-O-Fe vibrational modes in Mhr(OH) and L103N(OH) shows an 8-cm^{-1} increase in ν_s(Fe-O-Fe) and a 25-cm^{-1} decrease in ν_{as}(Fe-O-Fe) in the L103N mutant (Figure 4.3). Based on RR studies of diiron-oxo model compounds (Sanders-Loehr et al., 1989), the concomitant increase of ν_s(Fe-O-Fe) and decrease of ν_{as}(Fe-O-Fe) are indicative of a narrower Fe-O-Fe angle. This result is consistent with the X-ray crystal structures of Mhr(Cl) and L103N(OH) which have Fe-O-Fe angles of 129° and 126°, respectively (Martins et al., 1997).

Azide adducts of Mhr and L103N

Azide serves as a reporter for O_2 binding to the diiron center in Hr and Mhr. The crystal structures of oxyHr and metHr(N_3) reveal that peroxide and azide are both coordinated in an end-on fashion to the Fe2 site with their two oxygen and three nitrogen atoms, respectively, directed into the hydrophobic pocket (Stenkamp, 1994). The structure of the peroxy complex is depicted in Figure 5.1 (Chapter 5). The major difference between peroxide and azide binding is that the peroxide is protonated and H-bonded to the oxo bridge, whereas the azide is not protonated or H- bonded and its central and terminal atoms are slightly farther away from the oxo bridge. A similar azide coordination geometry has been observed in the crystal structure of Mhr(N_3) (Sheriff et al., 1987). Although no crystal structure has been determined for the azide adduct of the L103N mutant, its electronic and RR spectroscopic properties indicate significant differences in azide binding. The structure of the azide adduct is of particular interest because substitution of polar Asn 103 for nonpolar Leu 103 results in a 10^3-fold increase in the rate of autooxidation of the oxy complex (Lloyd et al., 1998).

The electronic spectrum of Mhr(N_3) has an oxo → Fe(III) CT band at 325 nm and a broad N_3^- → Fe(III) CT band centered at 450 nm (Figure 4.4B). These electronic assignments have been verified by RR spectroscopy for both Hr(N_3) (Shiemke et al., 1984) and Mhr(N_3) (Duff et al., 1981). In the case of Mhr(N_3), excitation within the 325-nm band results in resonance enhancement of the ν_s(Fe-O-Fe) mode at 514 cm^{-1}, whereas excitation within the 450-nm band results in resonance enhancement of ν(Fe-N_3) at 369 cm^{-1} as well as the ν_s(Fe-O-Fe) mode (Figure 4.6A). In the electronic spectrum of L103N with azide, the N_3^- → Fe(III) CT band is blue-shifted to 429 nm (Figure 4.4B). This indicates that the L103N mutant binds azide differently from wild-type Mhr.

The Raman spectrum of L103N with ^{14}N-azide differs from Mhr(N_3) in that it exhibits two modes at 337 and 366 cm^{-1} (Figure 4.6B). When the adducts are prepared with uniformly labelled ^{15}N-azide, the Mhr mode undergoes a 9-cm^{-1} downshift to 360 cm^{-1} (Figure 4.6A), and the L103N modes undergo 8- and 9-cm^{-1} downshifts to 329 and 357 cm^{-1}, respectively (Figure 4.6C). Thus, the L103N mutant

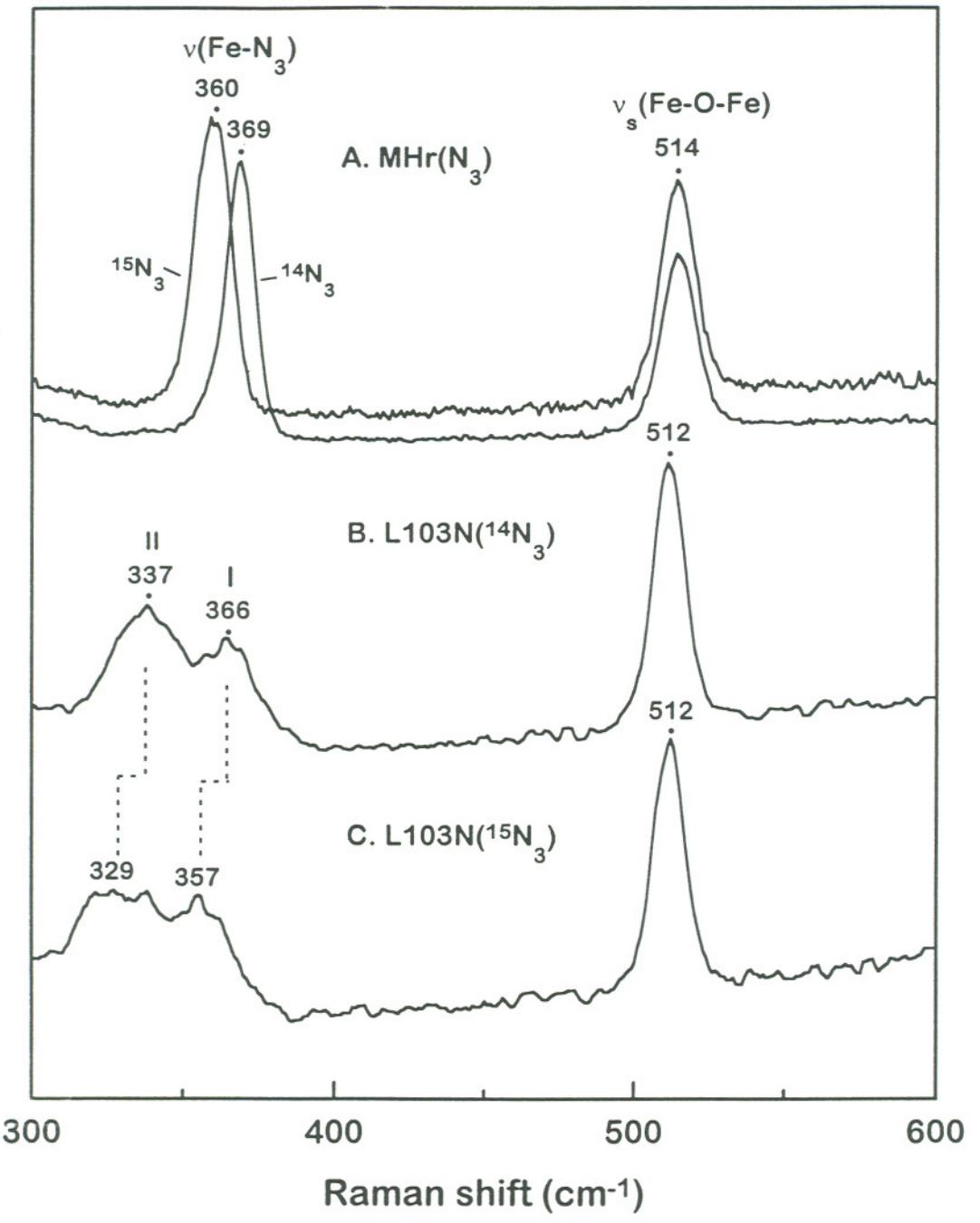

Figure 4.6 Effect of azide on low-frequency Raman spectra of Mhr and L103N mutant. (A) Mhr in 100 mM $Na^{14}N_3$ (___) of $Na^{15}N_3$ (-----) at pH 8.0. (B) L103N mutant in 100 mM $Na^{14}N_3$ in H_2O, pH 8.0 (___) or D_2O, pH reading 8.3 (-----). (C) L103N mutant in 100 mM $Na^{15}N_3$ in H_2O, pH 8.0 (___) or D_2O, pH reading 89.3 (-----). Spectra were obtained on samples at 15 K using a Jarrell-Ash spectrometer with a 1-cm^{-1}/s scan rate and an accumulation of 3 scans. Excitation in (A) was 514 nm (45 mW) with 8-cm^{-1} resolution. Excitation in (B) and (C) was 488 nm (50 mW) with 6-cm^{-1} resolution.

is capable of binding azide in two different conformations, henceforth referred to as mode I and mode II. Mode I has a ν(Fe-N_3) frequency of 366 cm^{-1}, close to the 369-cm^{-1} value for wild-type and indicative of a similar Fe-N bond strength. Mode II with its ν(Fe-N_3) frequency of 337 cm^{-1} must have a weaker Fe-N bond than in Mhr(N_3). Interestingly, only a single peak due to ν_s(Fe-O-Fe) is observed at 512 cm^{-1} in the azide adduct of L103N, with a peak width similar to that of the 514-cm^{-1} ν_s(Fe-O-Fe) in Mhr(N_3). Thus, the variable modes of azide binding in the L103N mutant apparently have no effect on the strength or angle of the Fe-O-Fe bond.

The two different azide-binding geometries (modes I and II) in the L103N mutant are strongly dependent on temperature. In the frozen state at 15 K, the 337-cm^{-1} mode II is the dominant species (as in Figure 4.6B). However, in solution at ice temperature, the 366-cm^{-1} mode I predominates (Figure 4.7A). The temperature dependence indicates that the two azide-binding geometries are in equilibrium in a single protein molecule. Azide mode I with its more normal Fe-N bond would be the major species present in solution studies of the L103N mutant, such as the absorption spectrum (Figure 4.4B). The Raman spectra showed very little dependence of species distribution on excitation wavelength between 406 and 514 nm. Previous studies of azide binding kinetics and thermodynamics for the L103N mutant were measured at 444 nm and were fit with a single azide adduct (Raner et al., 1997). Thus, it appears that the two azide binding modes cannot be distinguished by either absorption properties or azide-binding kinetics.

In addition to the Fe-N_3 stretch, the Raman spectrum of Mhr(N_3) has a resonance-enhanced azide vibration, ν_{as}(NNN), at 2050 cm^{-1} which undergoes a 66-cm^{-1} downshift with $^{15}N_3$ (Figure 4.8A). With the L103N mutant, the predominant ν_{as}(NNN) occurs at 2063 cm^{-1} and undergoes a 67-cm^{-1} downshift with $^{15}N_3$ (Figure 4.8B,C). The 2063-cm^{-1} peak is most likely associated with mode II, the species that dominates the low-temperature spectrum. The L103N spectra appear to have a lower energy shoulder at $\sim$2051 cm^{-1} with $^{14}N_3$ (Figure 4.8B) and at $\sim$1987 cm^{-1} with $^{15}N_3$ (Figure 4.8C) that are similar to the frequencies in Mhr(N_3) (Figure 4.8A) and could be due to the contribution of mode I. The increased energy of the 2063-cm^{-1} mode II peak compared to the 2050-cm^{-1} peak in Mhr(N_3) is indicative of a change in azide

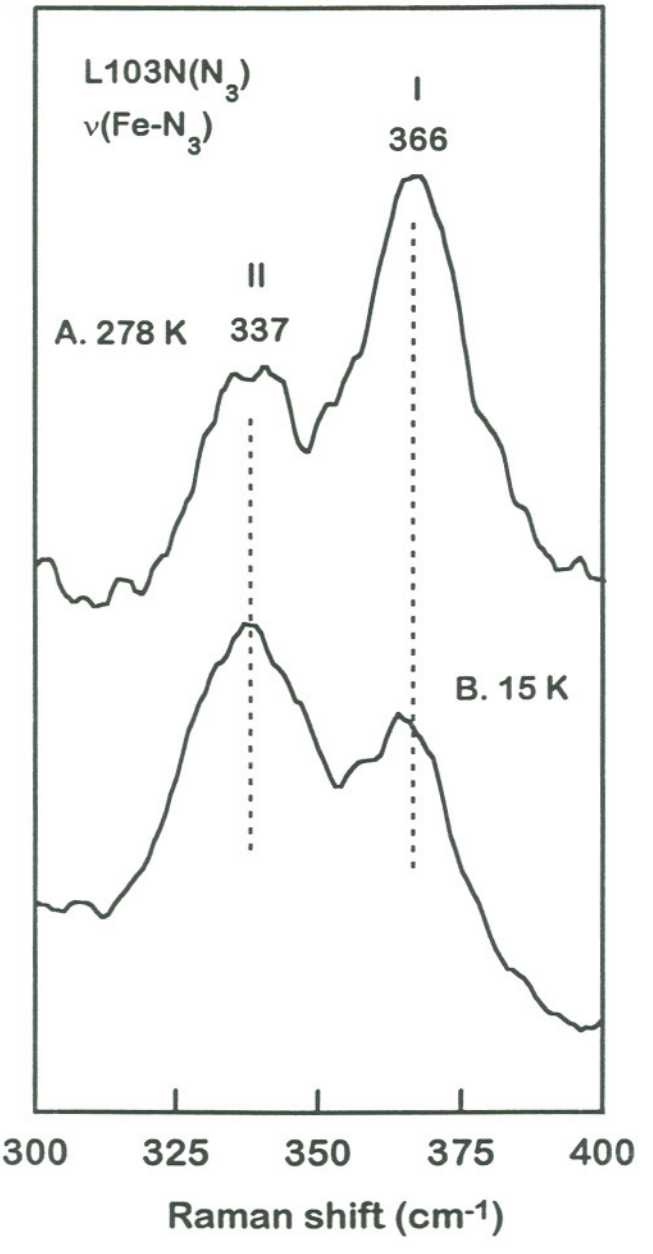

Figure 4.7 Temperature-dependence of ν(Fe-N_3) modes of L103N mutant. (A) Spectrum at 278 K for sample in 100 mM NaN_3 was obtained with 488-nm (10 mW) excitation, 1800-groove grating, and 25-min accumulation. (B) Spectrum at 15 K for sample in 100 mM NaN_3 was obtained as in Figure 4.6B.

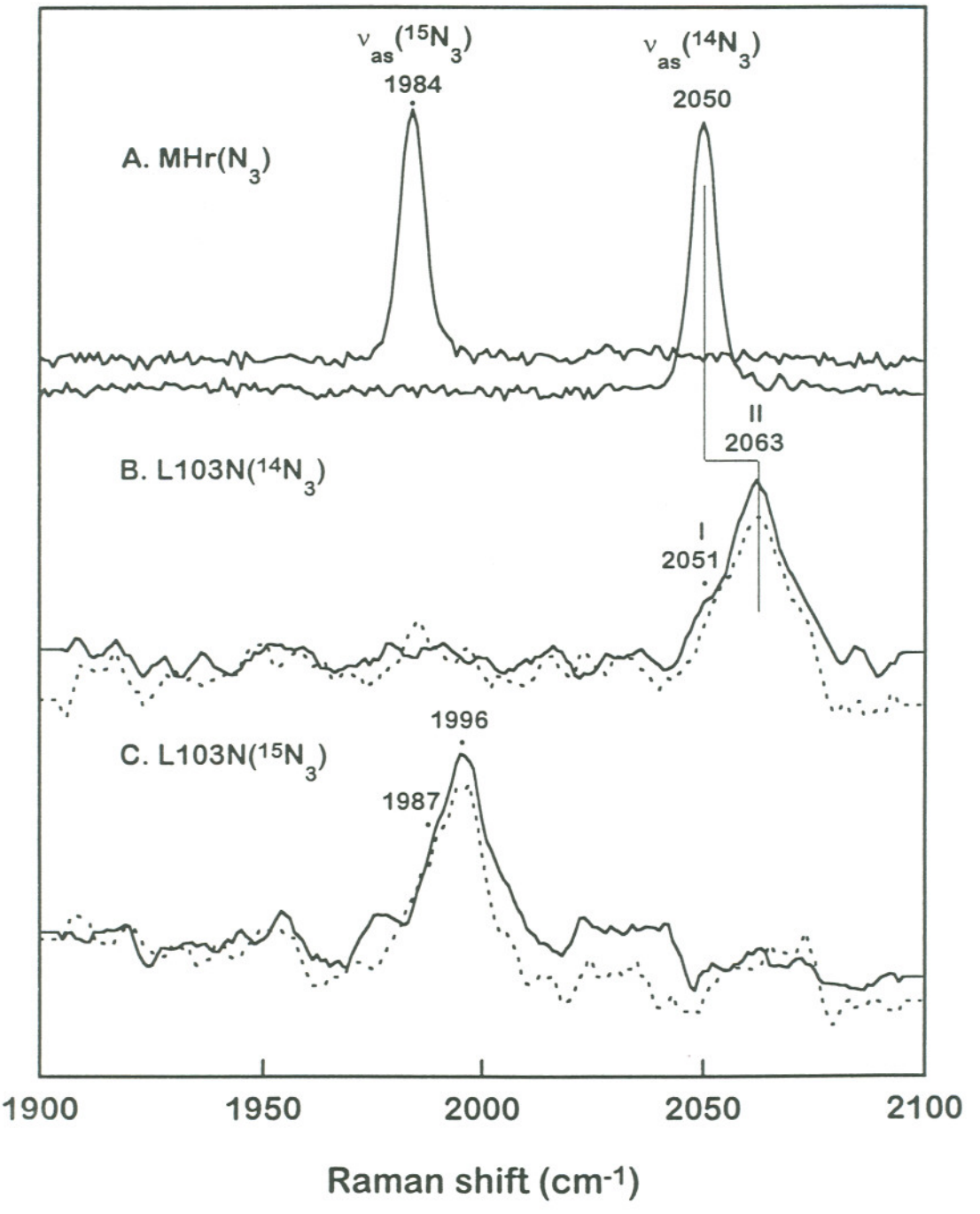

Figure 4.8 Effect of azide on high-frequency Raman spectra of Mhr and L103N mutant. (A) Mhr in 100 mM $Na^{14}N_3$ (____) or $Na^{15}N_3$ (-----) at pH 8.0. (B) L103N mutant in 100 mM $Na^{14}N_3$ in H_2O, pH 8.0 (____) or D_2O, pH reading 8.3 (-----). (C) L103N mutant in 100 mM $Na^{15}N_3$ in H_2O, pH 8.0 (____) or D_2O, pH reading 8.3 (-----). Spectral conditions as in Figure 4.6B, except for an accumulation of 5 scans.

binding. The ν_{as}(NNN) vibration occurs at 2041 cm^{-1} in free azide ion and at 2150 cm^{-1} in hydrazoic acid, with metal-coordinated azides having values closer to that of free azide (Ai et al., 1997; Chapter 3). Thus, the increase in ν_{as}(NNN) frequency for the mode II azide in L103N is actually opposite to what would be predicted for a weakening of the Fe-N bond. Clearly, some other protein electrostatic factors are at play, such as hydrogen bonding of the coordinated azide.

In order to investigate the possibility of H-bonding to azide in the L103N mutant, Raman spectra were obtained in D_2O. As can be seen in Figure 4.8D, exchange has no effect on the frequency of ν_{as}(NNN). Deuterium exchange also has no effect on the ν(Fe-N_3) modes of either Mhr(N_3) or the azide adducts of L103N (data not shown). While this does not lend support for a H-bonded azide structure, it also does not disprove it. Substitution of deuterium for hydrogen in different systems has been shown to cause hydrogen-bond energies to increase, decrease, or stay the same.

Structure of azide and peroxide complexes in L103N mutant

Proposed structures for the two azide binding modes in the L103N mutant are shown in Figure 4.9. In both cases, the azide is directed into the same exogenous-ligand pocket as in the crystal structures of Hr(N_3) (Stenkamp et al., 1984) and Mhr(N_3) (Sheriff et al., 1987). Our proposed coordination geometry for azide mode I is similar to that in Mhr(N_3), thereby explaining the similarity of ν(Fe-N_3) and the Fe-N bond strength (Table 4.2). However, this pocket is less hydrophobic due to the presence of Asn 103 in place of Leu, and possibly an intervening water molecule as observed in the crystal structure of the hydroxy form of L103N (Figure 4.1B). The fact that the azide adduct of L103N has an altered absorption maximum of 429 nm, as well as a 500-fold lower K_{eq} for azide binding (Table 4.2), is most likely due to the electrostatic effects of the polar residues in the azide binding pocket.

Azide mode II is favored by lowering the temperature from 278 K to 15 K. This suggests a conformational change involving the formation of a hydrogen bond. We propose that the intervening water molecule H-bonds to the Fe2-coordinated N of azide (Figure 4.9B). Such an interaction would explain the weakening of the Fe-N

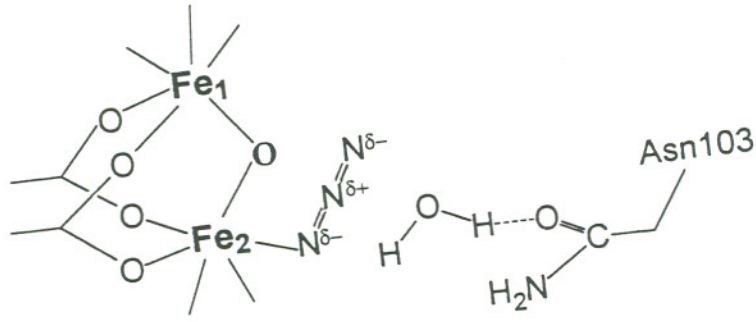

A. Azide Mode I ν(Fe-N3) at 366 cm^{-1}

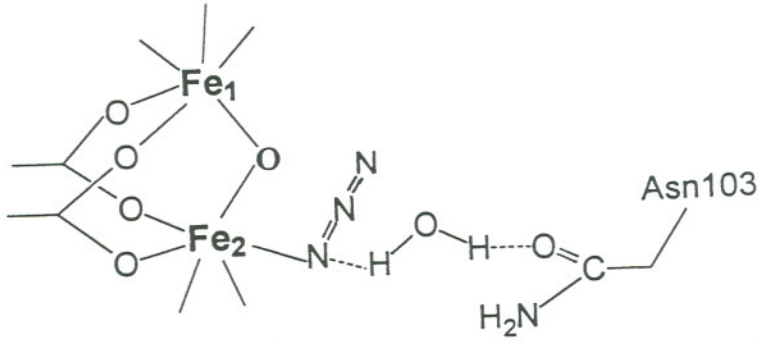

B. Azide Mode II ν(Fe-N3) at 337 cm^{-1}

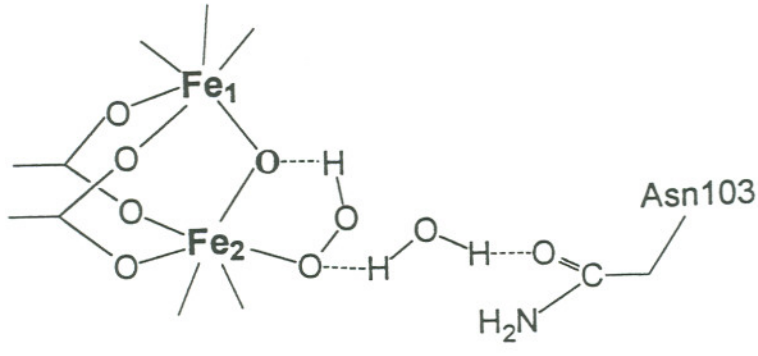

C. Peroxide Complex

Figure 4.9 Proposed structures for the diiron site of the L103N mutant. (A) Mode 1 of the azide adduct (principal form at 278 K). (B) Mode II of the azide adduct (principal form at 15 K). (C) Peroxide complex derived from reaction of O_2 with reduced L103N.

Table 4.2

Properties of Azid Adducts of Mhr and the L103N Mutant

Properties	Mhr (N_3)	L103N(N_3)	
		Mode I	Mode II
Electronic (nm)			
Oxo → Fe(III) CT	325	325	~325
N_3^- → Fe(III) CT	450	429	~429
Resonance Raman (cm^{-1})[a]			
ν_s(Fe-O-Fe)	514	512	512
ν(Fe-N_3)	369	366	337
ν_{as}(NNN)	2051	2051	2063
Binding constants[b]			
K_{eq} (M^{-1})	2.3×10^5	5×10^2	
k_{on} ($M^{-1}s^{-1}$)	6.8	1.1	

[a] RR spectra obtained at 15 K as in Figure 4.6.

[b] From Raner et al., 1997.

bond. It would also explain the increase in frequency for ν_{as}(NNN). In a study of model metal-azide complexes, η^1-terminal azides with M-NNN structures were found to exhibit ν_{as} frequencies of 2039–2062 cm^{-1}, whereas μ-1,1 bridging azides with M_2-NNN structures had higher ν_{as} frequencies of 2065–2075 cm^{-1} (Pate et al., 1989). A hydrogen bond to the Fe-coordinated nitrogen could have an effect similar to the coordination of two metals to the same N and thereby account for the increase in the vibrational frequency of ν_{as}(NNN) in azide mode II of the L103N mutant.

Our proposed azide binding modes in the L103N mutant could serve as a model for the peroxide complex and its mechanism of autooxidation. Lloyd et al. (1998) observed that the oxy form of L103N autooxidizes 10^3-fold faster than wild-type Mhr and proposed that this is due to displacement of the coordinated peroxide by a nearby solvent molecule. We suggest that the peroxide complex of the L103N mutant could have a structure similar to azide mode II (Figure 4.9C). Hydrogen-bonding of the Fe-coordinated oxygen to the intervening water molecule would facilitate cleavage of the Fe-O bond and proton donation to the bound peroxide would promote its release as H_2O_2. The wild-type protein presumably has a slower rate of autooxidation because its hydrophobic pocket restricts solvent access and increases the strength of the metal-ligand bond (Yamashita et al., 1990). Interestingly, conversion of the conserved Leu 103 to a larger hydrophobic residue (L98F mutant in Hr) results an a even lower rate of autooxidation than in wild-type (see Chapter 5). This is most likely due to a further limitation of solvent access to the O_2 binding site.

CHAPTER V

GENERATION OF FERRIC-PHENOLATE AND STABLE MIXED-VALENCE SPECIES IN HEMERYTHRIN BY AROMATIC SUBSTITUTION[1]

Abstract

To investigate the biological function of the hydrophobic residues around the diiron center of hemerythrin (Hr), aromatic substitutions have been studied by electronic, resonance Raman (RR), and EPR spectroscopy. In Hr from *Phascolopsis gouldii*, the dioxygen binding site on the pentacoordinate iron atom is bordered by the hydrophobic side chains of conserved leucines at positions 28 and 98. The L98Y mutant and the phenolate complex of the L98A mutant (L98A-phenol) exhibit absorption bands at 530 and 490 nm, respectively, indicative of phenolate → Fe^{III} charge transfer (CT). This has been verified by RR spectroscopy. With 514-nm excitation, the L98Y mutant exhibits vibrations at 573, 1167, 1297, 1502, and 1603 cm^{-1}, which are characteristic a of ferric phenolate complex. Similarly, the L98A-phenol complex has vibrations at 598, 1158, 1290, and 1586 cm^{-1}. Addition of catechol to the L98A mutant (L98A-catechol) results in a new absorption band at 630 nm, suggestive of catecholate → Fe^{III} CT. With 647-nm excitation, the L98A-catechol complex exhibits vibrations at 614, 1145, 1259, 1286, 1314, 1487, and 1603 cm^{-1}. These vibrational modes do not correspond exactly to the spectrum of either a typical ferric-phenolate complex or a bidentate ferric-catecholate complex. Rather, the absorption and RR data indicate that L98A-catechol contains a monodentate ferric catecholate that does not alter the tribridged structure of the diiron site.

---

[1] This work was performed in collaboration with Dr. Donald M. Kurtz, Jr. And Chris Farmer at University of Georgia, who provided protein samples and EPR spectra.

The L28Y mutant exhibits completely different behavior. Instead of forming a ferric phenolate complex, it displays an EPR signal with $g_x = 1.98$, $g_y = 1.85$, which are characteristic of an antiferromagnetically coupled $Fe^{II}Fe^{III}$ cluster. The L28Y mutant has an absorption band at 657 nm ($\epsilon = 700\ M^{-1}cm^{-1}$) which appears to be due to intervalence charge transfer, and not a ferric phenolate. With 647-nm excitation, the L28Y mutant exhibits resonance-enhanced peaks at 479 and 694 cm^{-1}, which can be assigned to ν_s(Fe-O-Fe) and ν_{as}(Fe-O-Fe), respectively, of the Fe^{II}-O-Fe^{III} cluster. The large intensity ratio of 2.2 for ν_{as}/ν_s implies that the Fe^{II}-O-Fe^{III} cluster has a trapped valence state with inequivalent iron atoms. Addition of azide to the L28Y mutant results in a new absorption maximum at 470 nm characteristic of $N_3^-\rightarrow$Fe(III) CT. With 514-nm excitation, the RR spectrum reveals a new ν(Fe-N_3) at 379 cm^{-1} and an altered ν_s(Fe^{III}-O-Fe^{III}) at 504 cm^{-1}. This indicates that the Fe^{II}-O-Fe^{III} cluster in L28Y mutant can be oxidized to the Fe^{III}-O-Fe^{III} state in the presence of azide and O_2. A similar oxo-bridged, mixed-valence species can be generated by changing Hr residues 45 to 51 from GELRRCT to NAAIEVF (in a region responsible for interactions between subunits), presumably due to the aromatic side chain of F51 being in close proximity to the diiron site. Overall, these studies provide evidence that the introduction of aromatic residues near the O_2-binding site of Hr can result either in iron ligation or in the stabilization of a mixed-valence intermediate.

Introduction

Hemerythrin (Hr) is an oxygen carrying protein found in the blood of a number of marine invertebrate worms. It consists of several identical 13 kDa subunits which reversibly bind oxygen at their diiron sites (Stenkamp, 1994). The crystal structures of Hr from *Themiste dyscrita* in both the deoxy and oxy forms were solved at 2.0-Å resolution, and the coordination environments around the diiron sites were revealed in detail (Holmes et al., 1991). One iron atom (Fe1) is coordinated by His 73, His 77, and His 101, while the other iron (Fe2) is coordinated by His 25 and His 54 (Figure 1.2). The iron atoms are bridged by the bidentate carboxylates of Glu 58 and Asp 106. A third bridge is provided by a hydroxo group in deoxyHr and an

oxo group in oxyHr. The Fe2 of deoxyHr has an open coordination site for binding its physiological exogenous ligand, dioxygen, which results in a diferric peroxide complex (Figures 1.2 and 5.1). The diferric met form of Hr, produced by the dissociation of peroxide, binds other small anionic ligands such as azide and chloride (Freier et al., 1980) (Figures 4.1 and 4.8).

A hydrophobic pocket surrounds the diiron center and apparently functions to stabilize the peroxo complex in oxyHr (Stenkamp, 1994). Thus, the sidechains of Leu 28 and Leu 98 are in close proximity to the coordinated O_2 (Figure 5.1A,B). Upon binding O_2, the μ-OH of deoxyHr transfers its proton to O_2, concomitant with the oxidation of the diferrous to the diferric state and the reduction of dioxygen to a hydroperoxide (Sanders-Loehr, 1989). This hydroperoxide is stabilized by H-bonding to the μ-oxo group (Shiemke et al., 1986), thereby slowing down autooxidation. However, the exact role of the hydrophobic residues in regulating this biological mechanism remains to be determined.

The diiron center in Hr may exist in oxidized Fe^{III}-O-Fe^{III}, reduced Fe^{II}-OH-Fe^{II}, and mixed-valence Fe^{II}-OH-Fe^{III} forms (Sanders-Loehr, 1989). The mixed-valence forms can be produced by one-electron oxidation of deoxyHr, yielding $semimet_O$, or by one-electron reduction of metHr, yielding $semimet_R$ (see Figure 5.12A below). The $semimet_R$ form has a rhombic EPR spectrum, whereas the $semimet_O$ form gives an axial EPR spectrum (Wilkins and Harrington, 1983; McCormick et al., 1989). These two forms can interconvert via a slow conformational change which is believed to involve a change in the localization of the unpaired electron and the coordination of a hydroxide in the exogenous ligand site of $semi\text{-}met_R$ (Pearce et al, 1987; McCormick et al., 1989). Both forms appear to have a hydroxo rather than an oxo group bridging the two iron atoms (DeRose et al., 1993; Thomann et al., 1993). Normally, the mixed-valence forms of Hr are thermodynamically unstable because they disproportionate to the $Fe^{II}Fe^{II}$ and $Fe^{III}Fe^{III}$ states (Babcock et al., 1980). We have found that the introduction of aromatic residues near the diiron center helps to stabilize an oxo-bridged, mixed-valence state in Hr.

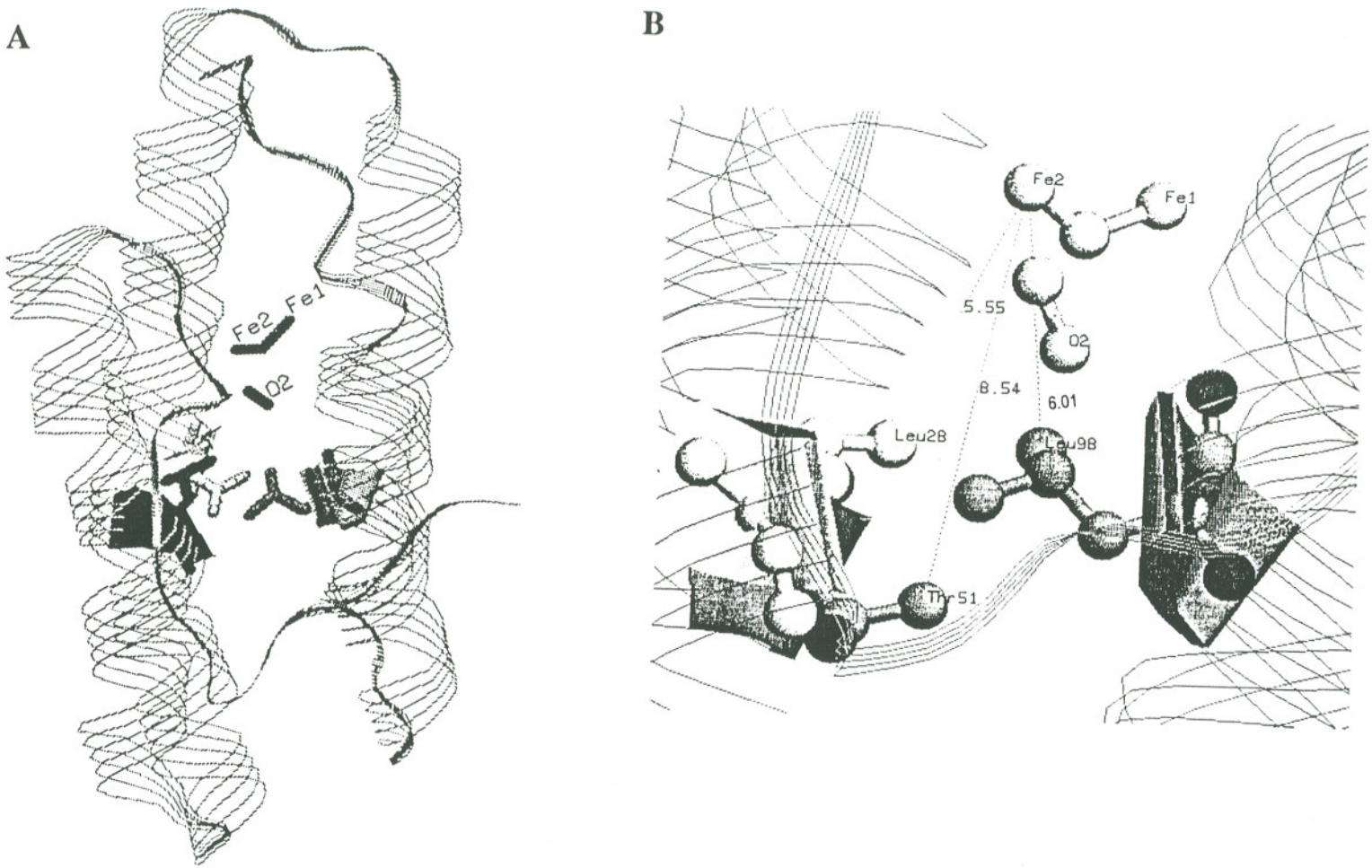

Figure 5.1 (A) Structure of one single subunit of oxyhemerythrin from *Themiste dyscrita*. The three side chains depicted below the bound O_2 (from left to right) are from Leu 28, Thr 51, and Leu 98. (B) Structure of the diiron site of oxyhemerythrin. Distances from Fe2 to the outermost carbon in the sidechain are 5.55 Å for Leu 28, 8.54 Å for Thr 51, and 6.01 Å for Leu 98. Structures adapted from Holmes et al., 1991 (PDB file: 1HMO).

Aromatic substitution in the vicinity of the metal center has provided useful information about the function of other metalloproteins. As discussed in Chapter 1, the hydroxylase component of methane monooxygenase (MMOH) and the R2 protein of ribonucleotide reductase (R2) also contain diiron clusters which are the sites for dioxygen activation. Aromatic substitution has been performed close to the diiron centers of R2 and MMOH, as well as the O_2-binding heme site of myoglobin (Mb). In the R2 protein, the function of the diiron cluster is to produce a tyrosyl radical at position 122 which initiates the catalytic reaction. The Phe 208, which is close to the diiron site, was mutated to Tyr. The resulting Tyr 208 was found to have been hydroxylated to dihydroxyphenylalanine (DOPA) which then became a bidentate catecholate ligand to one of the iron atoms (Åberg et al., 1993; Ormö et al., 1992). In MMOH, both iron sites of the diferric center can bind phenol to form ferric-phenolate complexes (Andersson et al., 1992a). In human Mb, mutation of the His 93 proximal ligand to a tyrosine results in Tyr 93 becoming the proximal heme ligand. The resultant H93Y Mb exhibits catalase activity (dismutation of hydrogen peroxide) (Adachi et al., 1993).

In oxyHr, the Leu 28 and Leu 98 residues in the hydrophobic pocket at the O_2-binding site are 5.6 and 6.0 Å, respectively, from the Fe2 atom (Figure 5.1B). These two residues are largely conserved (either Leu or Ile) in myohemerythrin (MHr) and Hr proteins from many species (Stenkamp, 1994). In an attempt to determine the effect of aromatic substitution, each of these residues has been mutated separately to Tyr. In addition, mutation of Leu 98 to Ala produced a pocket which could accommodate larger exogenous ligands such as phenolate and catecholate. The sidechain of Thr 51 lies within 8.5 Å of the Fe2 atom in oxyHr (Figure 5.1B). Replacement of residues 45 to 51 (GELRRCT) of the B helix with a more hydrophobic sequence (NAAIEVF) places an aromatic sidechain at position 51 and is henceforth referred to as T51F. We have investigated the effect of each of these aromatic substitutions on the structure and function of the diiron cluster in Hr using electronic, resonance Raman, and EPR spectroscopy. We have found that the L98Y mutant of Hr behaves like the H93Y mutant of Mb (Adachi et al., 1993) in allowing tyrosine to become an iron ligand. The L98A mutant of Hr behaves like MMOH

(Andersson et al., 1992a) in permitting the binding of phenol as an exogenous ligand. We found no evidence for the aromatic hydroxylation reaction which had been previously observed in the F208Y mutant of R2 (Ormö et al., 1992). However, both the L28Y and T51F mutants of Hr were found to stabilize novel mixed-valence Fe^{II}-O-Fe^{III} clusters.

Materials and Methods

Protein samples

The wild-type Hr gene from *Phascolopsis gouldii* was inserted into a pT7-7 plasmid and expressed in *Escherichia coli* strain BL21(DE3) in which the gene for the T7 RNA polymerase is under the control of the lac promoter (Kurtz & Farmer). Addition of IPTG resulted in the expression of the Hr gene, with large amounts of apoprotein accumulating as inclusion bodies. After disruption of cells, the insoluble pellet was dissolved in 6 M guanidinium hydrochloride and then flushed with argon. A ferrous ammonium sulfate/β-mercaptoethanol solution was added, and the protein was slowly diluted with anaerobic buffer to lower the guanidinium concentration to $\sim$0.5 M. This procedure caused the protein to solubilize as it refolded around the iron atoms. Large amounts of precipitated protein were removed by centrifugation. The supernatant was concentrated by ultrafiltration and the remaining contaminating proteins were removed by gel filtration. The resulting Hr preparation gave a single band with SDS-PAGE and characteristic UV/vis spectra of the Fe^{III}-O-Fe^{III} site. Samples for RR experiments were $\sim$1.5 mM (in diiron center) in 150 mM Na_2SO_4, 50 mM HEPES (pH 7.5). All mutated Hrs were prepared analogously to the wild-type Hr after appropriate mutation of the gene by PCR techniques.

Spectroscopy

EPR spectra were obtained at the University of Georgia on a Bruker ER-220D spectrometer equipped with an Oxford Instruments model ESR-9 cryostat. The EPR sample was placed in a 4-mm o.d. quartz tube and frozen in liquid N_2 bath.

Electronic absorption spectra were recorded on a Perkin-Elmer Lambda 9 spectrophotometer using concentrated Raman samples in glass capillaries (1.5-1.8 mm path length) (Loehr and Sanders-Loehr, 1993).

Raman spectra were obtained using a custom McPherson 2061/207 spectrograph (0.67 m) with a Princeton Instruments (LN-1100PB) liquid N_2-cooled CCD detector, and Rayleigh scattering was attenuated with a Kaiser Optical holographic super-notch filter. The desired excitation wavelengths were provided by Coherent Innova 90-6 Ar^+ and Innova 302 Kr^+ lasers. Data were collected in a 90°-scattering geometry with the sample capillaries at ~277 K placed in a copper cold finger that was chilled in a metal Dewar filled with an ice/water mixture (Loehr & Sanders-Loehr, 1993). The spectral resolution was 4–6 cm^{-1}. Spectral data were processed using GRAM/386 (Galatic Industries) and Origin (MicroCal) data analysis programs. Absolute frequencies were obtained by calibration with powdered aspirin and are accurate to ± 1 cm^{-1}.

Results

Ferric-phenolate complexes in L98Y and L98A hemerythrin

(A) Electronic spectral evidence. The diferric (met) forms of Hr typically exhibit two bands in the 300 - 400-nm region (Figure 5.2B) that have been assigned as oxo → Fe^{III} charge-transfer transitions (Reem et al., 1989). The mutant proteins (L98Y, L98A, and L98A plus phenol or catechol) also show these two typical oxo → Fe^{III} CT bands at ~325 and 360 nm (Figure 5.2). This indicates that all these proteins have a normal oxo-bridged diferric center.

Interestingly, the L98Y mutant and the L98A-phenol complex exhibit new broad absorptions near 530 and 490 nm, respectively (Figure 5.2A, C). A similar absorption band between 410 and 550 nm has been observed with a number of iron-tyrosinate proteins and ferric phenolate model compounds where it has been assigned to phenolate → Fe^{III} CT (Pyrz et al., 1985). This suggests the formation of ferric-phenolate complexes in the L98 mutants.

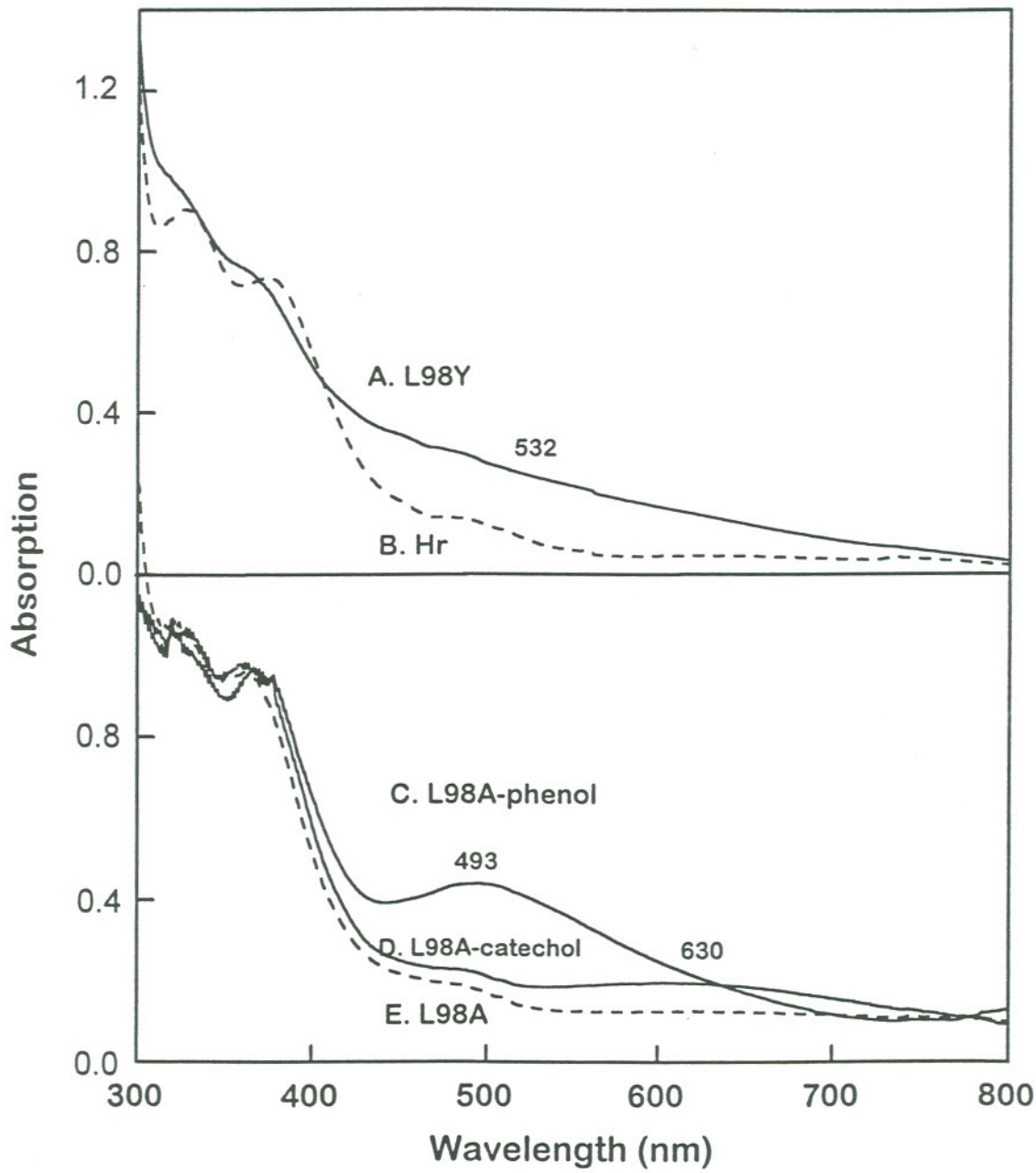

Figure 5.2 Electronic spectra of (A) L98Y metHr, (B) wild-type metHr, (C) phenol adduct of L98A metHr, (D) catechol adduct of L98A metHr, and (E) L98A metHr. These spectra were obtained on the samples subsequently used for Raman spectroscopy in Figure 5.3.

After adding catechol to the L98A mutant, a new absorption band appears at ~630 nm (Figure 5.2D). This absorption band is reminiscent of the catecholate → Fe^{III} CT bands between 690 and 720 nm in the ferric bidentate catecholate complexes formed in tyrosine hydroxylase (Andersson et al., 1988; Andersson et al., 1992b; Michoud-Soret et al., 1995), phenylalanine hydroxylase (Figure 5.5B) (Cox et al., 1988), and the F208Y mutant of R2 (Ormö et al., 1992). However, the 630-nm absorption band in L98A-catechol is blue-shifted by ~70 nm compared to the bidentate catecholate complexes. It is also red-shifted by 100 nm or more relative to the ferric phenolate complexes. Complexation of L98A with *o*-methoxyphenol yields a similar absorption at ~625 nm. Furthermore, an Fe(salen) model compound with monodentate coordination to a protonated catechol has a weak absorption at ~610 nm (Heistand et al., 1982). These results suggest that the binding of catechol to the diiron center in the L98A met Hr is monodentate rather than bidentate, with only one of the catechol hydroxyl groups bound to the iron.

(B) Raman spectral evidence for ferric-phenolate. Studies of iron-tyrosinate proteins and model complexes have identified a set of five intense vibrational modes at ~580, 1170, 1290, 1500, and 1600 cm^{-1} which provide a characteristic fingerprint of ferric complexes with phenol or para-substituted phenols (Table 5.1, top). The L98Y mutant exhibits a similar set of resonance-enhanced Raman modes at 573, 1167, 1297, 1502 and 1603 cm^{-1} (Figures 5.3B, 5.4A). The 573-cm^{-1} peak can be assigned to Fe-OR stretching, the 1297 cm^{-1} peak to C-O stretching, the 1167-cm^{-1} peak to C-H deformation, and the 1502- and 1603-cm^{-1} peaks to C-C stretching in the aromatic ring. Similarly, the L98A-phenol complex exhibits corresponding Raman peaks at 598, 1158, 1290, and 1586 cm^{-1} (Figures 5.3D, 5.4B). None of these vibrational modes are present in the RR spectrum of WT Hr (Figure 5.3A) or L98A (Figure 5.3C, 5.4D). These RR spectra provide definitive proof that Tyr-98 coordinates with Fe in the L98Y mutant and that exogenous phenol coordinates with Fe in the L98A mutant. Since Fe2 has an open coordination site in wild-type metHr, this is the most likely location of the ferric phenolate complex.

Iron-catecholate species have been observed in the DOPA 208 mutant of R2 and in the mononuclear iron sites of tyrosine hydroxylase and phenylalanine

Table 5.1

Resonance Raman Vibrational Modes of Ferric Phenolates and Ferric Catecholates in Proteins and Model Complexes

Samples	Raman Vibrations (cm^{-1})[a]							
	chelate	Fe-O	Fe-O	C-H	C-O	C-C	C-C	C-C
Phenolates								
L98Y Hr[b]		573		1167	1297		1502	1603
L98A Hr-phenol[b]		598		1158	1290			1586
Fe(salen)OPh-4-Me[c]		568		1168	1272		1501	1602
Tyrosine hydroxylase-tyramine (human)[d]		586			1280		1506	1606
Purple phosphatase[e]		575		1168	1285		1503	1603
H87Y Hb Iwate[f]		589			1308		1507	1606
Catecholates								
L98A Hr-catechol[b]			612	1145	1286	1314	1487	1603
L98A Hr-ortho-methoxylphenol[b]			603	1119	1303	1315	1493	1585
Dopa 208 RNR[g]	512	592	619	1143	1263	1319	1475	1569
Tyrosine hydroxylase-catechol (human)[d]	528		619	1150	1257	1314	1466	1566
Tyrosine hydroxylase-catechol (bovine)[h]	527	604	635	1130	1271	1320	1476	
Phenylalanine hydroxylase-catechol[i]	531		621	1151	1257	1313	1470	1568

[a] Assignments are from Cox et al., 1988; Michaud-Soret et al., 1995; Que, 1988. All are stretching modes except chelate ring and C-H deformations. [b] This work. [c] Pyrz et al., 1988. [d] Michaud-Soret et al., 1995. [e] Averill et al., 1987. [f] Hemoglobin, Nagai et al., 1983. [g] F208Y mutant in R2 subunit of ribonucleotide reductase, Ling et al., 1994. [h] Andersson et al., 1988. [i] Cox et al., 1988.

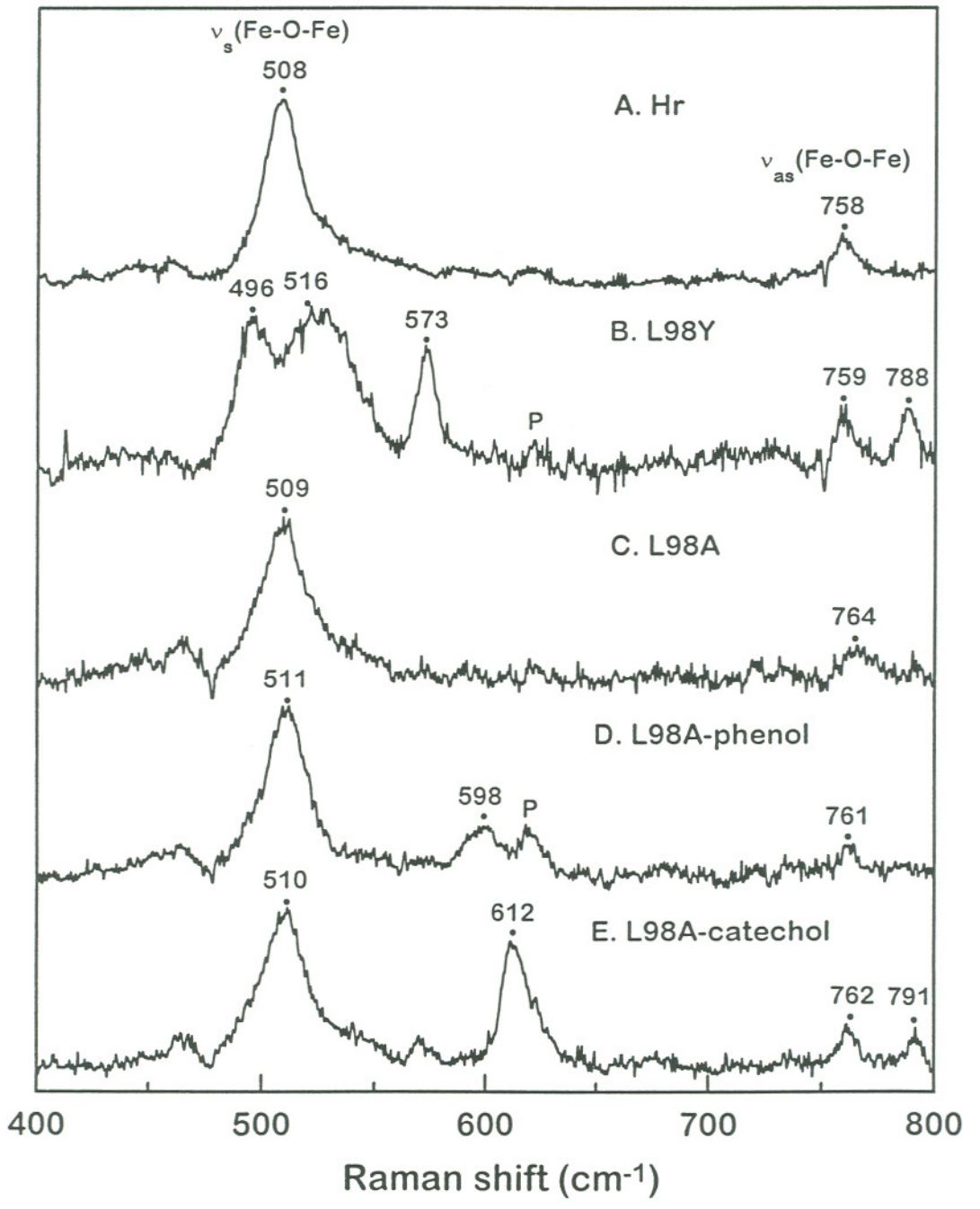

Figure 5.3 Low-frequency Raman spectra of (A) wild-type metHr, (B) L98Y metHr, (C) L98A metHr, (D) L98A metHr plus ~10 mM phenol and (E) L98A metHr plus ~10 mM catechol. The spectra were obtained with 514 nm (20 mW) excitation on samples ~1.5 mM in protein subunits.

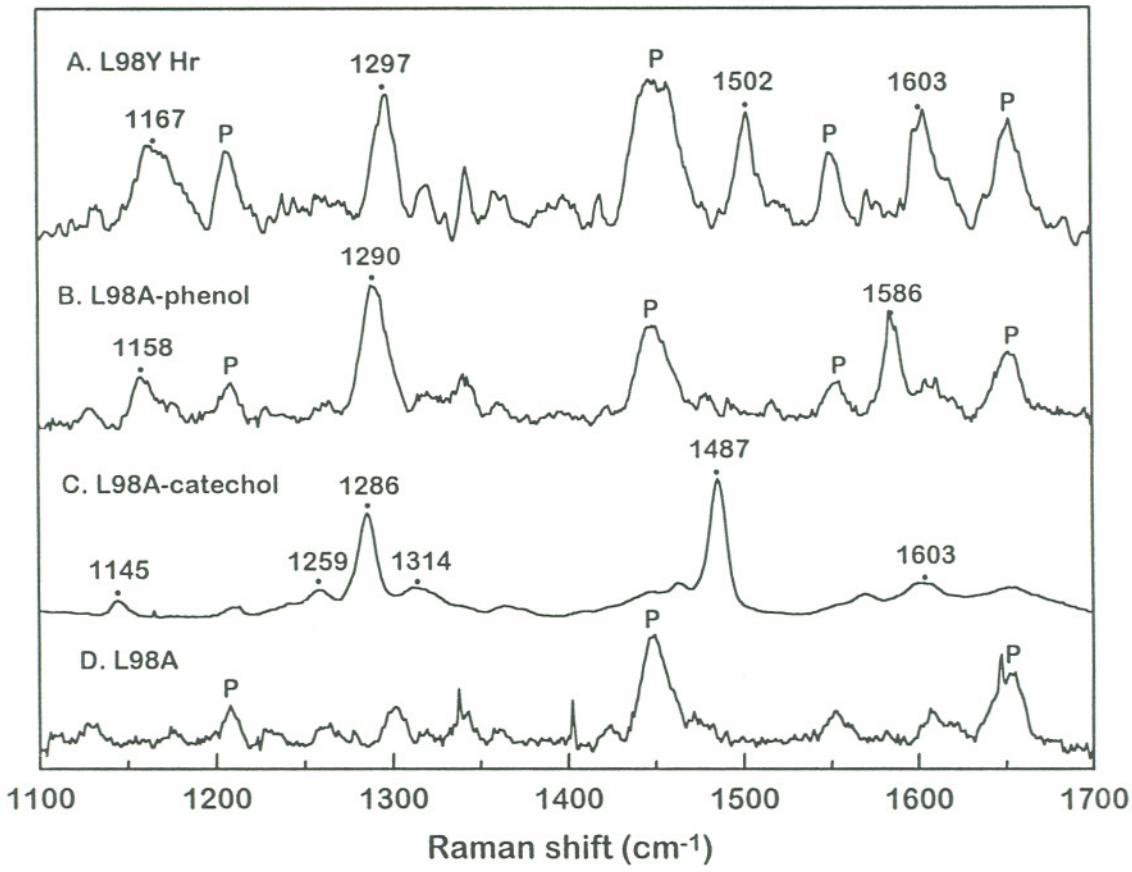

Figure 5.4 High-frequency Raman spectra of (A) L98Y metHr, (B) L98A metHr-phenol, (C) L98A metHr-catechol, and (D) L98A metHr. The samples were as in Figure 5.3; the excitation was at 514 nm (20 mW) for L98Y and L98A-phenol and at 647 nm (30 mW) for L98A and L98A-catechol. P = protein vibrational mode (Lord and Yu, 1970).

hydroxylase, which bind catechol as an exogenous ligand (Table 5.1, bottom). The electronic and RR spectra of these species are typical of model compounds in which the iron is coordinated to both catechol oxygens, and this bidentate coordination has been verified by X-ray crystallography for the DOPA 208 mutant of R2 (Åberg et al., 1993). The RR spectra of these ferric bidentate catecholate complexes exhibit a five-membered ring chelate mode near 520 cm^{-1}, two Fe-OR modes near 590 and 630 cm^{-1}, a C-O stretch near 1270 cm^{-1} and three ring deformation modes near 1320, 1470, and 1570 cm^{-1} (Figure 5.5, bottom, and Table 5.1). The catechol complex of L98A shows similar RR spectral features, particularly the intense peaks at 612 cm^{-1} (Figure 5.3E), 1286, and 1487 cm^{-1} (Figure 5.4C). Probable spectral assignments are given in Table 5.1, based on the work of Pyrz et al. (1988) and Michaud-Soret et al., (1995). However, the RR spectrum of the L98A-catechol complex differs from that of the bidentate catecholates (Figure 5.5) in that it has only one intense peak instead of two to three in the 510-630-cm^{-1} region and only one intense peak instead of two in the 1250-1320-cm^{-1} region. Furthermore, the C-C stretching vibration of L98A-catechol at 1487 cm^{-1} is intermediate between the $\sim$1470-cm^{-1} value for bidentate catecholate and the $\sim$1500-cm^{-1} value for monodentate phenolate (Table 5.1). The RR spectrum of L98A-catechol is actually most similar in peak frequencies and intensities to that of the *o*-methoxyphenol complex of L98A (Table 5.1). Thus, it is likely that catechol binds to L98A in a monodentate fashion.

Further evidence for a monodentate ferric catecholate in L98A comes from the unaltered bridging geometry of the diiron site. The electronic spectrum retains the two iron-oxo bands at $\sim$325 and 360 nm (Figure 5.2D). The RR spectrum exhibits an Fe-O-Fe symmetric stretch at 510 cm^{-1} and an Fe-O-Fe asymmetric stretch at 762 cm^{-1}, which are within 2 and 4 cm^{-1}, respectively, of the values in wild-type metHr (Figure 5.3). This indicates that the L98A-catecholate complex has retained the tribridged diiron structure (Figure 1.2) and makes it unlikely that catechol has replaced any of the histidine or carboxylate ligands. In contrast, in the DOPA 208 mutant of R2, the oxo bridge has been displaced by the bidentate coordination of DOPA to one of the iron atoms (Åberg et al., 1993; Ling et al., 1994). The electronic and RR spectral properties of L98Y-catechol all suggest that the catechol is

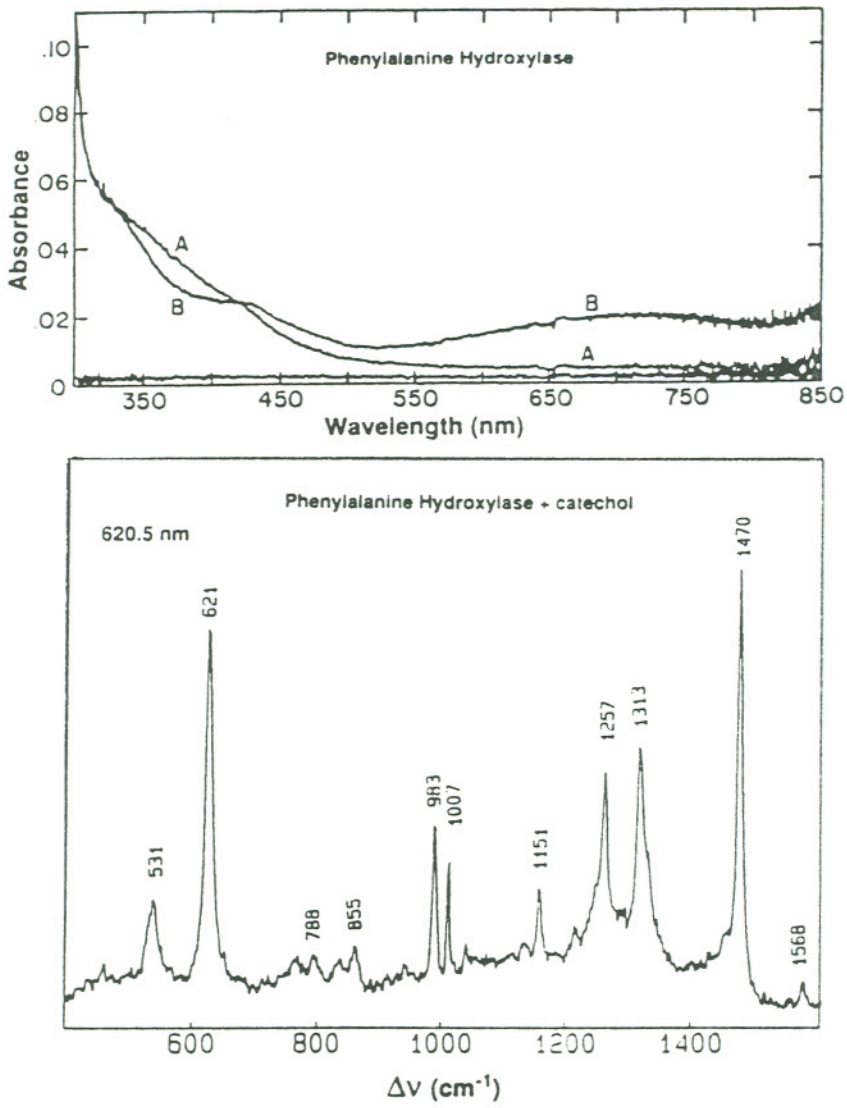

Figure 5.5 Top: Electronic spectra of (A) phenylalanine hydroxylase and (B) catechol complex of phenylalanine hydroxylase. Bottom: RR spectrum of phenylalanine hydroxylase with exogenous catechol. Adapted from Cox et al., 1988.

monodentate, occupying only the exogenous ligand site on Fe2. Thus, Hr appears to have a coordinatively more stable and rigid diiron cluster than that in R2.

Multiple Fe-O-Fe species in L98Y hemerythrin

Wild-type Hr exhibits a single Fe-O-Fe symmetric stretch at 508 cm^{-1} (Figure 5.3A) and a similar feature is observed in the RR spectra of most other forms of Hr (Shiemke et al., 1984; Sanders-Loehr et al., 1989). The L98Y mutant is unusual in that it exhibits two features of similar intensity at 496 and 516 cm^{-1} that appear to represent two different ν_s(Fe-O-Fe) modes (Figure 5.3B). When the excitation wavelength is changed from 514 to 413 nm, the relative intensity of the 496-cm^{-1} feature increases and a new feature due to ν_{as}(Fe-O-Fe) appears at 770 cm^{-1} (Figure 5.6A). These wavelength-dependent changes prove that the two ν_s(Fe-O-Fe) vibrations are associated with different diiron chromophores. The ability of the μ-oxo group of Hr to exchange with solvent oxygen is quite variable. No such exchange is observed for metHr or oxyHr, but oxo-bridge exchange is facilitated in the presence of azide or cyanide (Freier et al., 1980), anions that are known to bind at the exogenous ligand site on Fe2 (Stenkamp, 1994). Incubation of the L98Y metHr in $H_2{}^{18}O$ causes the 516-cm^{-1} mode to undergo a 16-cm^{-1} downshift, whereas the 496-cm^{-1} mode undergoes no isotope shift at all (Figure 5.6B). Since the Tyr-98 residue is expected to have a strong ability to donate electron density to the diiron center and make the oxo bridge more exchangeable, the 516-cm^{-1} mode can be assigned to the tyrosine-ligated species. The greater intensity of the 516-cm^{-1} mode with 514- than 413-nm excitation is consistent with the Fe-O-Fe mode being in resonance with the iron-phenolate chromophore.

Phenolate coordination in the L98A metHr causes a 2-cm^{-1} upshift in ν_s(Fe-O-Fe) (Figure 5.3C, D). This provides additional evidence that the tyrosine-ligated form of the L98Y metHr is associated with ν_s(Fe-O-Fe) at 516 cm^{-1} (an 8-cm^{-1} upshift compared to wild-type) rather than at 496 cm^{-1} (a 12-cm^{-1} downshift). The 516-cm^{-1} mode of the L98Y metHr also undergoes a 4-cm^{-1} downshift in D_2O (Figure 5.6C) that is suggestive of hydrogen bonding of the oxo bridge. Most ligated forms of metHr do not show any such deuterium sensitivity for ν_s(Fe-O-Fe), unless the

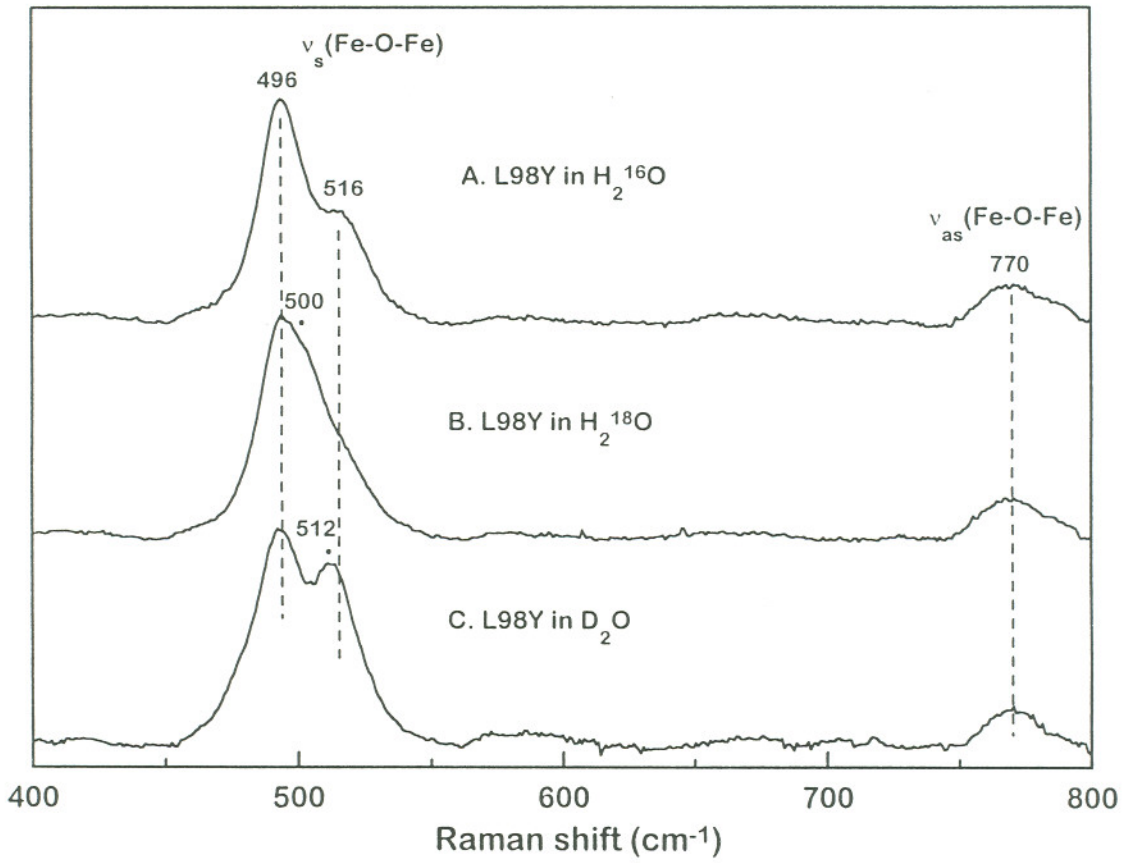

Figure 5.6 Oxygen and deuterium isotope effects on RR spectrum of the L98Y metHr in (A) $H_2{}^{16}O$ buffer, (B) $H_2{}^{18}O$ buffer containing 86 atom % ^{18}O (ICON) and (C) D_2O buffer containing 90 atom % D (Sigma). The samples were incubated in isotopically substituted buffers for 24 hours at ice temperature prior to obtaining RR spectra with 413 nm (20 mW) excitation.

exogenous ligand is protonated and H-bonded to the oxo bridge as in the hydroperoxide of oxyHr and the hydroxide of hydroxometHr (Shiemke et al., 1986). Since it is highly unlikely that the coordinated Y98 would be protonated, the deuterium effect could be due to a hydrogen-bonded water molecule, as has been observed in the crystal structure of metHr at neutral pH (Stenkamp, 1994).

The nature of the species giving rise to the 496-cm^{-1} ν_s(Fe-O-Fe) mode in the L98Y mutant is uncertain. The lack of any oxo-bridge exchange suggests that this species has a 5-coordinate Fe2 or a weak exogenous ligand. The low frequency is suggestive of a hydrogen-bonded Fe-O-Fe moiety, as in oxyHr with ν_s(Fe-O-Fe) at 486 cm^{-1} or hydroxometHr with ν_s(Fe-O-Fe) at 492 cm^{-1} (Shiemke et al., 1996). However, the lack of any frequency shift for the 496-cm^{-1} mode in D_2O (Figure 5.6C), as well as the high frequency of ν_{as}(Fe-O-Fe) (Table 5.2), tends to rule out hydrogen bonding as the cause of the decrease in frequency. Clearly the 496-cm^{-1} form of the L98Y mutant has undergone some alteration that prevents Y98 from coordinating to the diiron site. The resistance of this species to ligand binding is also seen with azide. Addition of 100 mM azide to the L98Y mutant results in the appearance of a new ν_s(Fe-O-Fe) peak at 509 cm^{-1} (Table 5.2), as well as a minor ν_s(Fe-O-Fe) peak at 496 cm^{-1} which finally disappears with 400 mM azide. The 12-cm^{-1} downshift of the ν_s(Fe-O-Fe) peak at 496-cm^{-1} relative to the 508-cm^{-1} value in wild-type Hr, as well as the 12-cm^{-1} upshift of the ν_{as}(Fe-O-Fe) at 770 cm^{-1}, could be due to an increase in Fe-O-Fe angle (Sanders-Loehr et al., 1989). Such behavior has been observed in dibridged sites with only one bridging carboxylate, such as ribonucleotide reductase which exhibits a similarly low value for ν_s(Fe-O-Fe) at 493 cm^{-1} (Table 5.2).

Mixed valence sites in L28Y and T51F hemerythrin

The L28Y and T51F mutants of Hr were expressed as apoprotein in inclusion bodies and reconstituted analagously to wild-type Hr. After solubilization in 6M guanidinium chloride, these mutant proteins were reconstituted by the anaerobic addition of Fe(II) coupled with dilution of the guanidinium concentration to $\sim$0.5 M. The samples were then exposed to air and a blue color appeared in the supernatant.

Table 5.2

Raman Frequencies and Intensities of Fe-O-Fe Vibrational Modes in Proteins and Model Compounds[a]

Samples	ν_s(Fe-O-Fe)	ν_{as}(Fe-O-Fe)	I_{as}/I_s
Mixed-Valence Sites			
L28Y Hr[b]	479	694	2.2
T51F Hr[b]	486	700	2.5
Compound **2**[c]	n.d.	711	»10
Diferric Sites			
Oxy Hr[d]	486	753	0.18
Met Hr[b]	508	758	0.20
Met Hr-azide[d]	507	768	0.27
L28Y Hr-azide[b]	504		
T51F Hr[b]	507	769	0.15
T51F Hr-azide[b]	507		
L98Y Hr, phenolate-coordinated[b]	516		
L98Y Hr, phenolate-free[b]	496	770	0.21
Ribonucleotide reductase[d]	493	756	0.20
Δ^9 Desaturase[e]	519	747	0.29

[a] Frequencies in cm^{-1}. I_{as}/I_s = intensity ratio for ν_{as}(Fe-O-Fe) relative to ν_s(Fe-O-Fe). [b] This work. [c] $[Fe_2O(O_2CCPh_3)_2L_2](BPh_4)$, Figure 5.8 and Cohen et al., 1997. [d] Sanders-Loehr et al., 1989. [e] Fox et al., 1994.

The spectroscopic evidence described below, particularly the S = 1/2 EPR signal, strongly suggests that the blue color is associated with a mixed valence, $Fe^{II}Fe^{III}$ species. These blue forms are quite stable in the presence of O_2 and only undergo oxidation to the diferric state in the presence of azide (see below), ferricyanide alone being ineffective as an oxidant. Reduction of the blue proteins with dithionite is accompanied by considerable protein precipitation and a loss of color. Thus, it has not been possible to selectively titrate the blue species with oxidants or reductants. A related mutant, L98F, is instead oxidized to the oxy or met state during solubilization and reconstitution with Fe(II) and exposure to air or ferricyanide repeatively. Reduction of the L98F mutant with dithionite does lead to the formation of a transient blue species with an electronic spectrum similar to those of the L98Y and T51F mutants, thereby providing evidence for the mixed-valence assignment.

(A) Electronic spectral evidence. The L28Y and T51F mutants of Hr each exhibit a strong absorption at ~650 nm (ϵ = 700 and 1050 $M^{-1}\,cm^{-1}$, respectively) (Figure 5.7, Table 5.3). This absorbance can be ascribed to an intervalence transfer (IT) band of a trapped-valence Fe^{II}-O-Fe^{III} species on the basis of the following evidence. (1) An Fe-phenolate chromophore is ruled out because the Raman spectra of the blue species (see below) do not show any indication of iron-phenolate vibrational modes. (2) The 650-nm absorbance of the L28Y and T51F mutants is considerably more intense than the ligand field bands in the 600-750 nm region of diferric Hr or model complexes which typically have ϵ values $< 100\ M^{-1}\,cm^{-1}$ (Sanders-Loehr et al., 1980). (3) The absorbance is also more intense than the IT bands of the mixed-valence, Fe^{II}-OH-Fe^{III} clusters previously observed in semimet forms of wild-type Hr and a model compound **1** which occur at 900-1350 nm and have ϵ values $< 150\ M^{-1}cm^{-1}$ (Table 5.3). (4) The breadth and intensity of the 650-nm absorption bands in the L28Y and T51F mutants are instead similar to the IT band of the mixed-valence, Fe^{II}-O-Fe^{III} model, compound **2** (Figure 5.8) which occurs at 685 nm (ϵ = 435 $M^{-1}cm^{-1}$) (Cohen et al., 1997). These results suggest that the blue forms of the L28Y and T51F mutants are mixed-valence complexes in which the diiron site is bridged by an oxo rather than a hydroxo moiety.

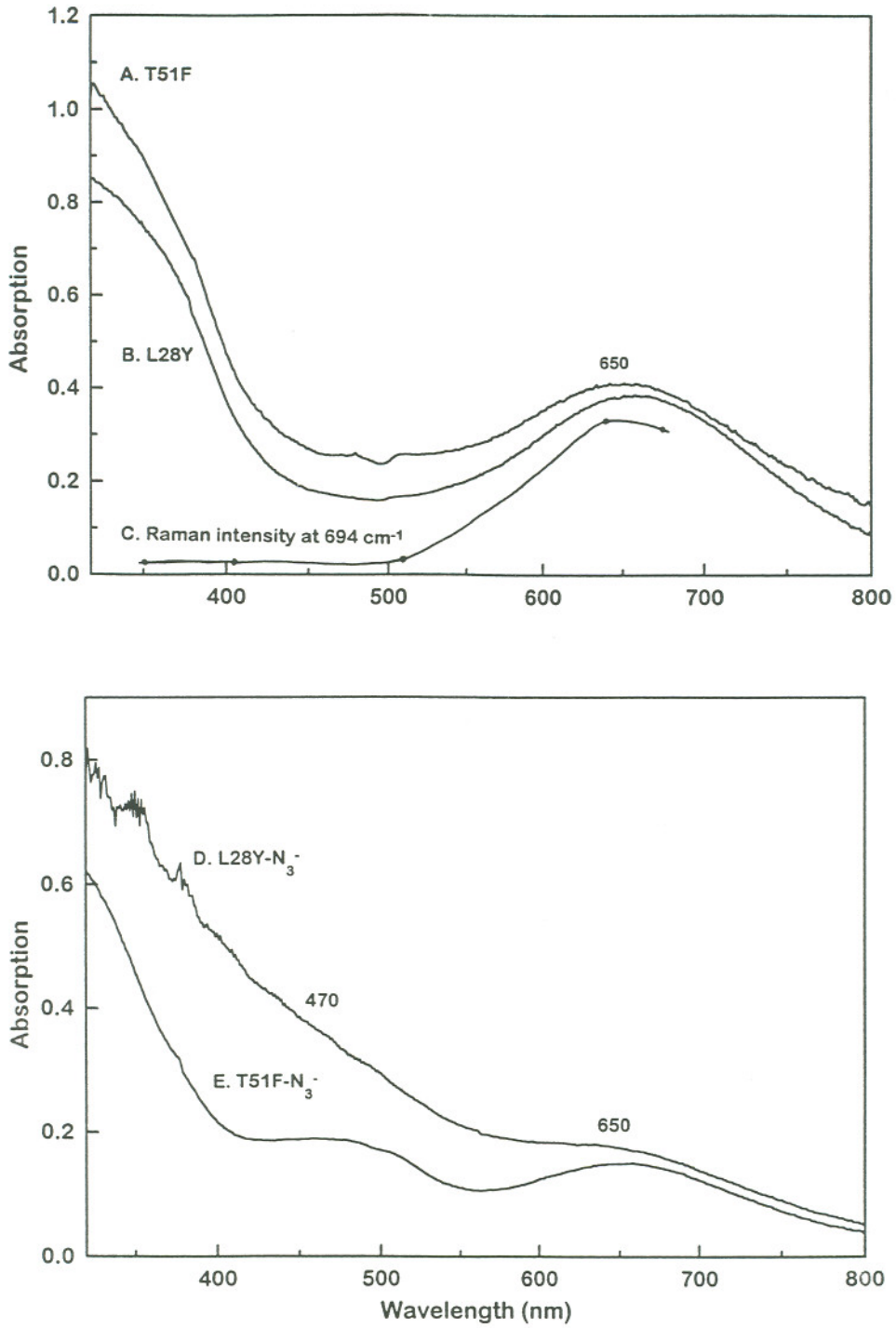

Figure 5.7 Electronic absorption spectra of T51F and L28Y Hrs. (A) As-isolated T51F. (B) As-isolated L28Y. The samples in (A) and (B) were subsequently used for the Raman spectra in Figure 5.9. (C) Excitation profile for 694-cm^{-1} Raman mode of L28Y Hr. Intensity at 694-cm^{-1} was measured relative to intensity of 980-cm^{-1} peak of 0.15 M Na_2SO_4 internal standard and plotted as a function of excitation wavelength. (D) L28Y Hr reacted with 400 mM azide in air. (E) T51F mutant reacted with 50 mM azide in air. The samples in (D) and (E) were derived from azide addition to the samples in (A) and (B) and subsequently used for the Raman

Table 5.3

EPR and Electronic Spectral Properties of Mixed-Valence Diiron Clusters in Proteins and Model Compounds

Samples	EPR				Electronic nm (M^{-1} cm^{-1})
	g_x	g_y	g_z	g_{av}	
Oxo-Bridged					
$Na_4[Fe_2O(EDTA)_2]$[a]	1.95	1.95	1.89	1.93	
RNR mouse[b]	1.94	1.85	1.82	1.87	
Compound **2**[c]	1.93	1.93	1.93	1.93	685 (435)
L28Y Hr[d]	1.98	1.85			656 (700)
T51F Hr[d]	1.96	1.90	1.80	1.88	645 (1280)
Hydroxo-Bridged					
$Semimet_R$ Hr[e]	1.94	1.86	1.65	1.82	1220 (7)
$Semimet_O$ Hr[e]	1.95		1.71		960 (43)
Semimet Hr-azide[e,f]	1.90	1.82	1.50	1.71	1220 (13)
RNR mouse[g]	1.92	1.73	1.60	1.75	
MMO *M. trichosporium*[h]	1.94	1.86	1.75	1.85	
Purple acid phosphatase[i]	1.92	1.77	1.63	1.77	
Compound **1**[j]	1.95	1.52	1.43	1.63	1350 (138)

[a] Davydov et al., 1997b. [b] Davydov et al., 1997a. [c] Cohen et al., 1997, $[Fe_2O(\mu\text{-}O_2CCPh_3)_2\ L_2](BPh_4)$, L as in compound **1**; isotropic EPR signal, Hagen & Payne, personal communication. [d] This work. [e] McCormick et al., 1991. [f] Sanders-Loehr et al., 1980. [g] Ribonucleotide reductase, Atta et al., 1994. [h] Methane monooxygenase, Fox et al., 1988. [i] Davis et al., 1982. [j] Bossek et al., 1995, $[Fe_2OH(\mu\text{-pivalate})_2L_2](ClO_4)_2$, L = 1,4,7-trimethyl-1,4,7-triazacyclononane.

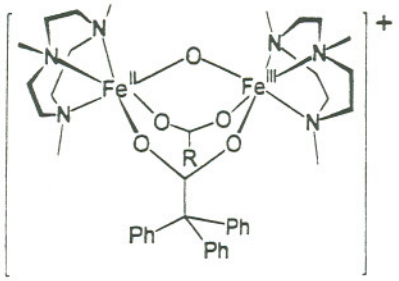

Compound **2**

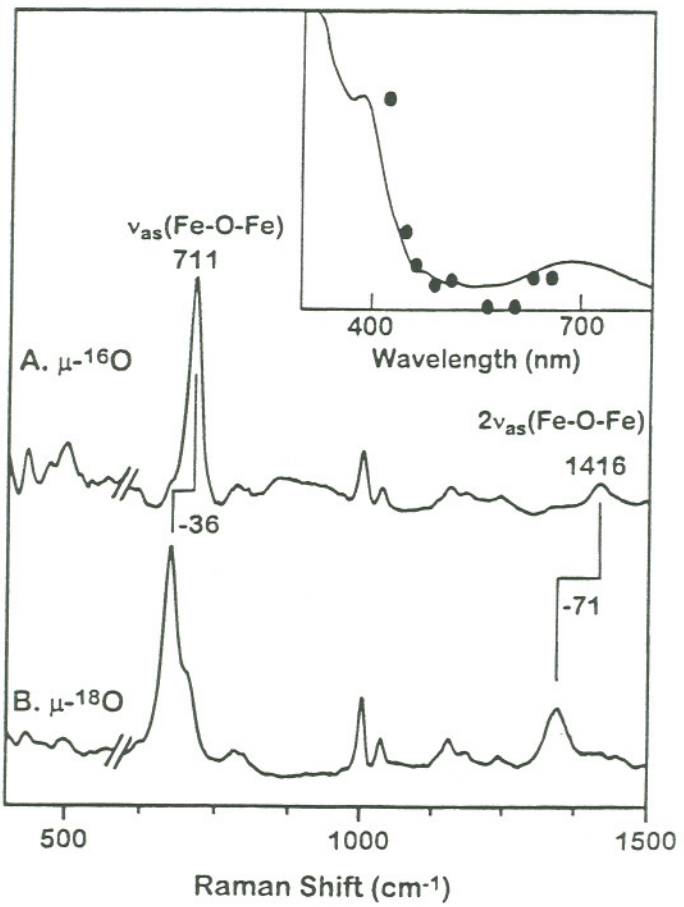

Figure 5.8 Top: Structure of mixed-valence model, compound **2,** $[Fe_2O(\mu\text{-}O_2CCPh_3)_2 L_2](BPh_4)$ where L = 1,4,7-trimethyl-1,4,7-triazacyclononane. Bottom: Raman spectrum of solid compound **2** with (A) ^{16}O and (B) ^{18}O bridge, obtained with 413.1-nm excitation. Inset: Absorption spectrum in CH_2Cl_2 (—) and Raman excitation profile for 711-cm^{-1} mode (•). Adapted from Cohen et al., 1997.

(B) RR Spectral evidence for mixed valence species. Upon excitation within the 650-nm absorption band, the L28Y mutant exhibits a strongly enhanced Raman mode at 694 cm^{-1} with a weaker RR mode at 479 cm^{-1} (Figure 5.9A). These two peaks are the main resonance-enhanced features in the Raman spectrum. Their intensity tracks the 650-nm absorption band, and they are not observed with excitation between 350 and 500 nm (Figure 5.7C). No resonance-enhanced peaks are detected in the 1100-1700 cm^{-1} region where we previously observed iron-phenolate and iron-catecholate vibrations in the L98 mutants (Figure 5.4). This indicates that the Tyr 28 residue (or a modified form) is not involved in binding the diiron site.

For the L28Y mutant, the 479-cm^{-1} peak is within the expected range for ν_s(Fe-O-Fe) in diferric proteins and model compounds (Sanders-Loehr et al., 1989), but it is lower in energy than in any of the diferric forms of Hr (Table 5.2). Similarly, the 694-cm^{-1} peak is significantly below the 750-780-cm^{-1} range for ν_{as}(Fe-O-Fe) in diferric Hrs. Thus, if these features are due to an Fe-O-Fe moiety, they are likely to be indicative of a lower oxidation state. It has not been possible to provide oxygen-isotope evidence for this assignment because the RR spectrum is unaffected by 24-hour incubation in $H_2{}^{18}O$. However, many forms of Hr are resistant to oxo-bridge exchange (Freier et al., 1980). Although oxo-bridge exchange in Hr can be facilitated by cycling through the deoxy state (Shiemke et al, 1984), we have not found conditions for regenerating the blue species from the deoxy state of the L28Y mutant.

Additional support for the mixed-valence assignment in the L28Y mutant comes from the similarity of its RR spectrum to that of the Fe^{II}-O-Fe^{III} model, compound **2**. The RR spectrum of compound **2** is dominated by an intense feature at 711 cm^{-1}, that has been assigned to ν_{as}(Fe-O-Fe) on the basis of its 36-cm^{-1} shift to lower energy with ^{18}O in the bridge and that is strongly enhanced within the 685-nm absorption band (Figure 5.8). The 694-cm^{-1} feature of L98Y mutant is similar to the 711-cm^{-1} feature of compound **2** in frequency, intensity, and excitation behavior and, thus, can also be assigned to the asymmetric stretch of an Fe^{II}-O-Fe^{III} cluster.

The blue-colored T51F mutant has an amazingly similar RR spectrum to that of the L28Y mutant (Figure 5.9B). Excitation within its 650-nm absorption band (Figure 5.7) leads to a Raman spectrum that is dominated by an intense feature at 700

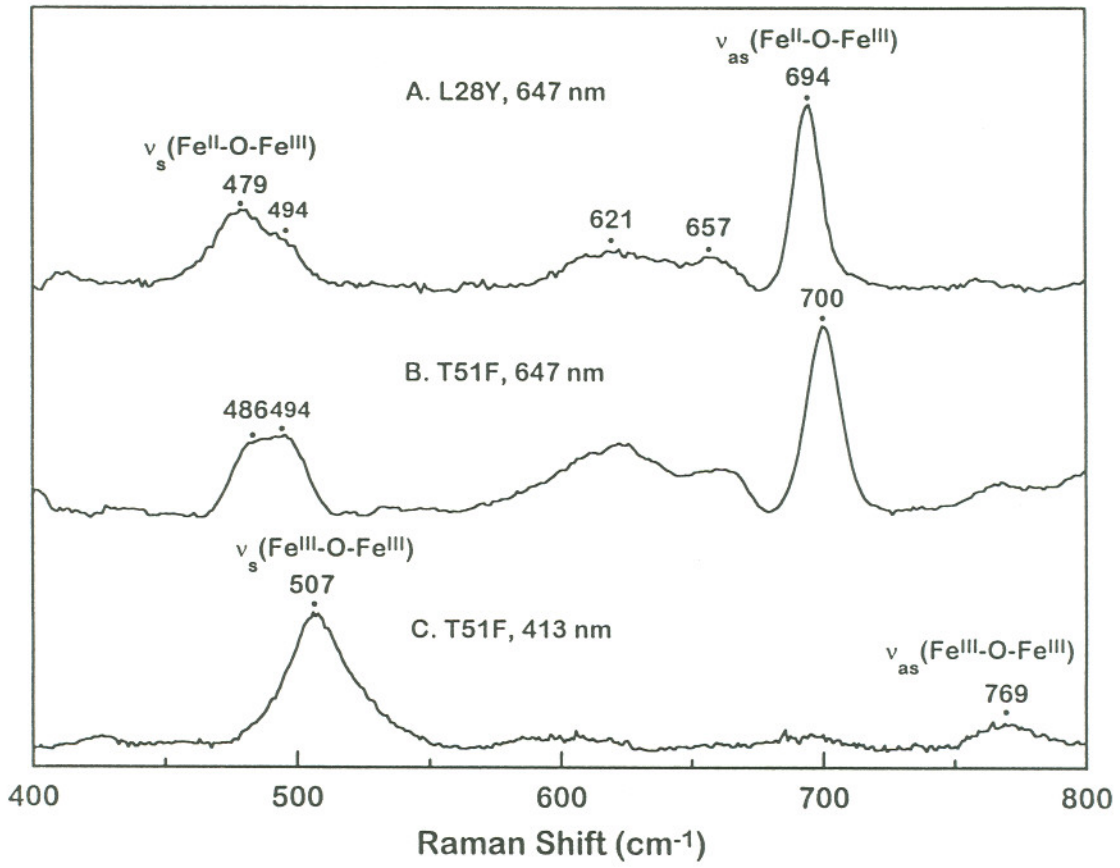

Figure 5.9 Raman spectra of (A) L28Y mutant and (B) T51F mutant obtained with 647-nm excitation (30 mW) and (C) T51F mutant obtained with 413 nm excitation (10 mW).

cm^{-1}, similar to the 694-cm^{-1} mode in the L28Y mutant and the 711-cm^{-1} mode in compound **2** and is similarly assigned to the asymmetric Fe-O-Fe stretch of a mixed valence Fe^{II}-O-Fe^{III} cluster. There are two resonance-enhanced modes at 486 and 494 cm^{-1} in the ν_s(Fe-O-Fe) region. By analogy to the L28Y spectrum (Figure 5.9A), the 486-cm^{-1} feature is most likely associated with the same Fe^{II}-O-Fe^{III} moiety as the 700-cm^{-1} feature. The 494, 621, and 657-cm^{-1} features are actually observed at the same frequencies with both mutants and may correspond to other vibrations of the mixed-valence site (Czernuszewicz et al., 1987). These peaks cannot be associated with a diferric cluster because they are not observed using 413 nm excitation (Figure 5.9C).

The alternative of a hydroxo-bridged cluster has been ruled out for the T51F mutant by the insensitivity of its RR spectrum to incubation of the protein in D_2O. Although the oxo bridge of Hr may fail to exchange with solvent, OH groups at the active site of Hr generally do exchange with D_2O (Shiemke et al., 1984). Furthermore, Raman modes of metal-OH species tend to be much less strongly resonance enhanced, and RR spectra of hydroxo-bridged diiron clusters have yet to be observed. For example, the azide complex of the semimet$_R$ Hr, which is hydroxo-bridged (DeRose et al., 1993), exhibits an Fe-N_3 stretch in its RR spectrum but no feature that can be assigned to an Fe-OH or Fe-OH-Fe moiety (Irwin et al., 1983). Thus, the high intensity of the $\sim$650-nm peak in the absorption spectrum and the high intensity of the $\sim$700-cm^{-1} peak in the RR spectra of the L28Y and T51F mutants are both indicative of oxo- rather than hydroxo-bridged clusters.

Model compounds containing a diamond core structure (two oxo groups bridging between two iron atoms) exhibit an Fe_2O_2 vibrational mode at 660-690 cm^{-1} (Que & Dong, 1996; Que personal communication). This is an alternative possibility for the 694 and 700-cm^{-1} modes in the L28Y and T51F mutants. However, the lack of exchange of the μ-oxo group with solvent oxygen in these Hr mutants makes the addition of a second bridging oxygen atom unlikely.

When the T51F mutant is probed with 413-nm excitation, two new vibrations appear at 507 and 769 cm^{-1} (Figure 5.9C). These two peaks can be assigned to ν_s(Fe-O-Fe) and ν_{as}(Fe-O-Fe), respectively, of an Fe^{III}-O-Fe^{III} cluster (Table 5.2). Thus, the

T51F mutant contains some oxidized diferric cluster in addition to the mixed-valence species. The presence of an oxidized cluster is also apparent from the greater absorbance in the 350-nm region for T51F than L28Y (Figure 5.7). Probing of the L28Y mutant with 413-nm excitation gives no indication of ν_s(Fe-O-Fe) for an oxidized cluster. The residual absorbance at ~360 nm in the L28Y mutant is most likely due to oxo → Fe(III) CT of the Fe^{II}-O-Fe^{III} species. However, the L28Y mutant differs from compound **2** in that excitation within this absorption band does not result in resonance enhancement of vibrations of the Fe^{II}-O-Fe^{III} cluster (Figures 5.7C and 5.8, inset).

The relative intensities of the two Fe-O-Fe stretching vibrations provide an additional useful parameter for characterizing diiron sites. Diferric clusters with similar ligand sets on either iron have a high degree of symmetry. Since the Raman selection rules favor symmetric vibrational modes, the ν_{as}(Fe-O-Fe) is typically much less intense than ν_s(Fe-O-Fe), leading to an intensity ratio (I_{as}/I_s) of 0.3 or less for the Fe^{III}-O-Fe^{III} cluster in proteins and model compounds (Sanders-Loehr et al., 1989). The diferric sites in the Hr mutants all exhibit the low intensity ratios expected for a symmetric structure (Table 5.2). In contrast, diferric clusters with a different ligand set on either iron have a much lower symmetry and can have markedly enhanced intensities for ν_{as}(Fe-O-Fe), resulting in I_{as}/I_s ratios as high as 4.2 (Sanders-Loehr et al., 1989). For the mixed valence cluster of compound **2**, no ν_s(Fe^{II}-O-Fe^{III}) peak was observed (Cohen et al., 1997). The extreme asymmetry of this site, despite the same ligand set on both irons, was attributed to its trapped valence character with very little electron exchange between Fe^{II} and Fe^{III}. The blue forms of the L28Y and T51F mutants have I_{as}/I_s ratios of 2.2 and 2.5, respectively (Table 5.2). It is likely that these blue species also have localized Fe^{II} and Fe^{III} centers, with one Fe atom having more Fe^{III} character and the other Fe atom having more Fe^{II} character.

EPR spectral evidence for mixed-valence species

The L28Y mutant exhibits an EPR spectrum with g_x = 1.98 and g_y = 1.85 (Figure 5.10). The T51F mutant displays similar EPR parameters (Table 5.3). The appearance of an EPR spectrum with the three principal g-values below 2.0 is

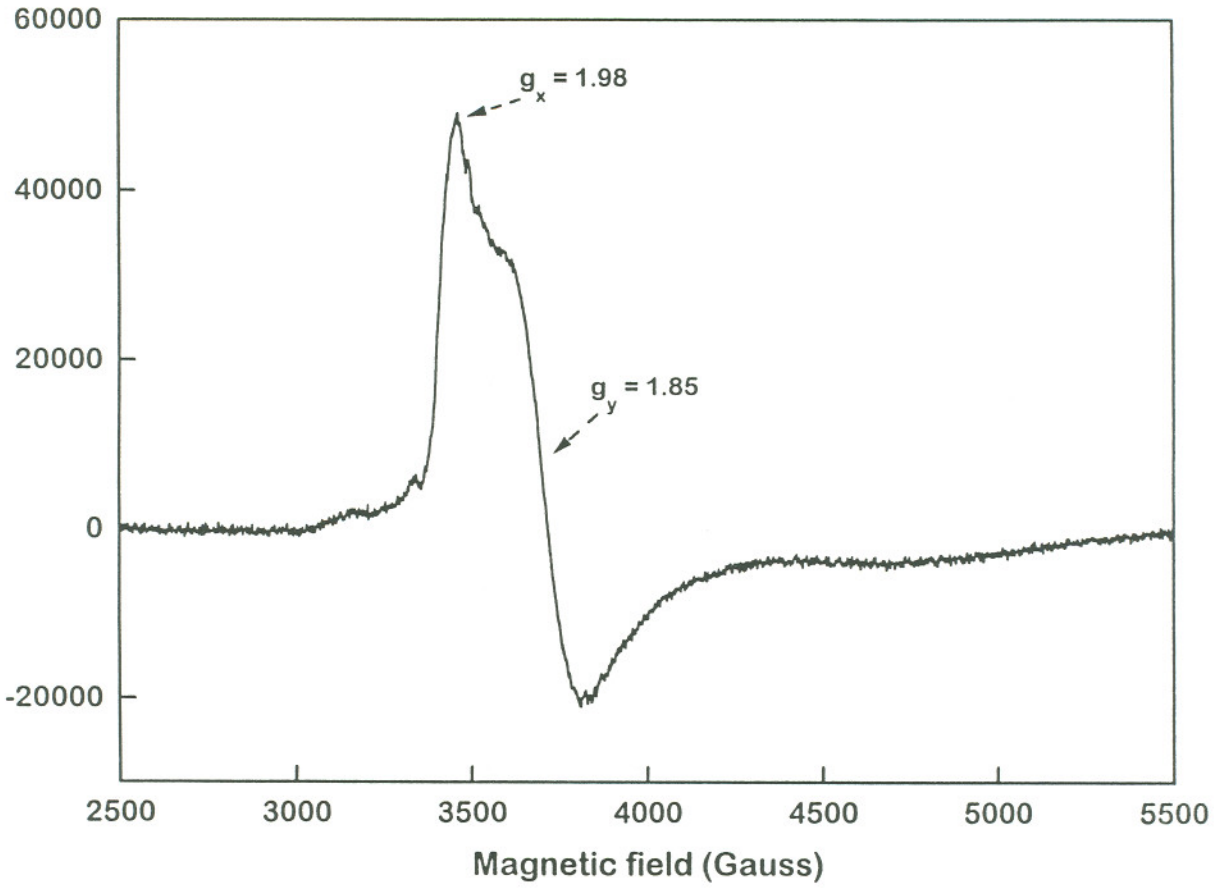

Figure 5.10 EPR spectrum of the L28Y mutant. Spectrum obtained at 6 K with a microwave frequency of 9.587 GHz and a power of 10.1 mW.

characteristic of an S = ½ state from an antiferromag-netically coupled high-spin Fe^{II} (S = 2) and high-spin Fe^{III} (S = 5/2) pair (Sanders-Loehr, 1989; Vincent et al., 1990). Similar EPR spectra have been observed for the mixed-valence $Fe^{II}Fe^{III}$ clusters in Hr, ribonucleotide reductase, methane monooxygenase, and corresponding model compounds (Table 5.3). Thus, the EPR spectra clearly indicate the presence of a mixed-valence cluster in the L28Y and T51F mutants.

EPR parameters have been used to distinguish between oxo- and hydroxo-bridged $Fe^{II}Fe^{III}$ clusters (Davydov et al., 1997). Normally these mixed valence sites are prepared by chemical reduction of the corresponding diferric complex. However, reduction can also be accomplished by γ-irradiation of diferric species at 77 K, with the reduced species being trapped in the frozen state. Using a series of diferric model complexes, it was discovered that the EPR parameters of the mixed-valence species would change if the sample was annealed at temperatures >115 K , due to the conversion from an oxo-bridged complex to a hydroxo-bridged complex (Davydov et al, 1997b). Comparison with a series of mixed-valence protein samples (Davydov et al, 1997a) revealed that the initial (putative) oxo-bridged species had relatively high g values with g_{av} ranging from 1.86-1.96 (e.g., $Fe_2O(EDTA)_2$ complex in Table 5.3). In contrast, the hydroxo-bridged species had a larger spread in the three principal g values with g_{av} ranging from 1.78-1.87. Furthermore, the oxo-bridged species exhibited unbroadened EPR spectra up to 110 K, whereas the hydroxo-bridged species could be observed only below 25 K due to their weaker antiferromagnetic coupling.

The hydroxo-bridged, mixed-valence sites produced by chemical reduction of diferric proteins and model compounds have g_{av} values of 1.63-1.85 (Table 5.3) that are seen only at low temperature (below ~ 30 K), fitting the above hydroxo-bridged classification. In contrast, the oxo-bridged cluster in compound **2** has an isotropic EPR signal at g = 1.93 that can still be observed at 90 K (albeit with markedly reduced intensity), agreeing with the oxo-bridged classification (Hagen & Payne, personal communication). The relatively high values for g_x and g_y in the L28Y and T51F mutants (Table 5.3) also support an oxo-bridged classification. However, the EPR signal disappears by 25 K, suggesting a weaker antiferromagnetic interaction of the diiron cluster in the protein than in the model compounds. Although the latter

behavior is more typical of a hydroxo-bridged system, the weight of the other evidence from electronic and RR spectroscopy (including the lack of a D-isotope effect) favors an oxo-bridged formulation for the blue forms of the L28Y and T51F mutants.

Azide-dependent oxidation of mixed-valence sites

The mixed-valence form of the L28Y mutant is the major species isolated upon reconstitution of apoprotein with Fe(II) and O_2. Remarkably, it remains stable in air, with no evidence of oxidation to the diferric state. The addition of 400 mM azide under anaerobic conditions has no significant effect on the absorption or RR spectrum, indicating that the oxo-bridged, mixed-valence form of L28Y does not bind azide or binds it very weakly. This behavior is different from that of wild-type Hr where the hydroxo-bridged semimet$_R$ form readily binds azide at the mixed-valence diiron site (Irwin et al., 1983). Thus, the mixed-valence form of L28Y has a lower affinity for exogenous ligands, possibly due to Fe2 being trapped in an Fe(II) state (see Figure 5.12A below).

When azide is added to the L28Y mutant in the presence of O_2, new absorption appears at ~470 nm (Figure 5.7D). This broad feature is reminiscent of the $N_3^- \rightarrow Fe^{III}$ CT bands at 440 and 500 nm in the azide complex of metHr (Reem et al., 1989). At the same time, the intensity of the 650-nm IT band has decreased. This suggests that some of the mixed-valence form of the L28Y mutant has been oxidized to the diferric state, with the equilibrium being driven by the formation of an azide complex. Raman spectra provide additional evidence for the change in oxidation state. Excitation within the 470-nm absorption band yields a RR spectrum characteristic of a diferric-azide species (Figure 5.11). Thus, the L28Y-azide complex exhibits a peak at 374 cm^{-1} that can be assigned to ν(Fe-N_3) by analogy to the corresponding mode at 375 cm^{-1} in wild-type metHr-azide (Shiemke et al., 1984) and a peak at 504 cm^{-1} that corresponds to the ν_s(Fe-O-Fe) mode at 507 cm^{-1} in metHr-azide (Table 5.2). The appearance of the met-azide RR modes at 374 and 504 cm^{-1} is accompanied by a decrease in the intensity of the mixed-valence Fe-O-Fe modes at 479 and 694 cm^{-1}, indicating a shift in the equilibrium towards the diferric

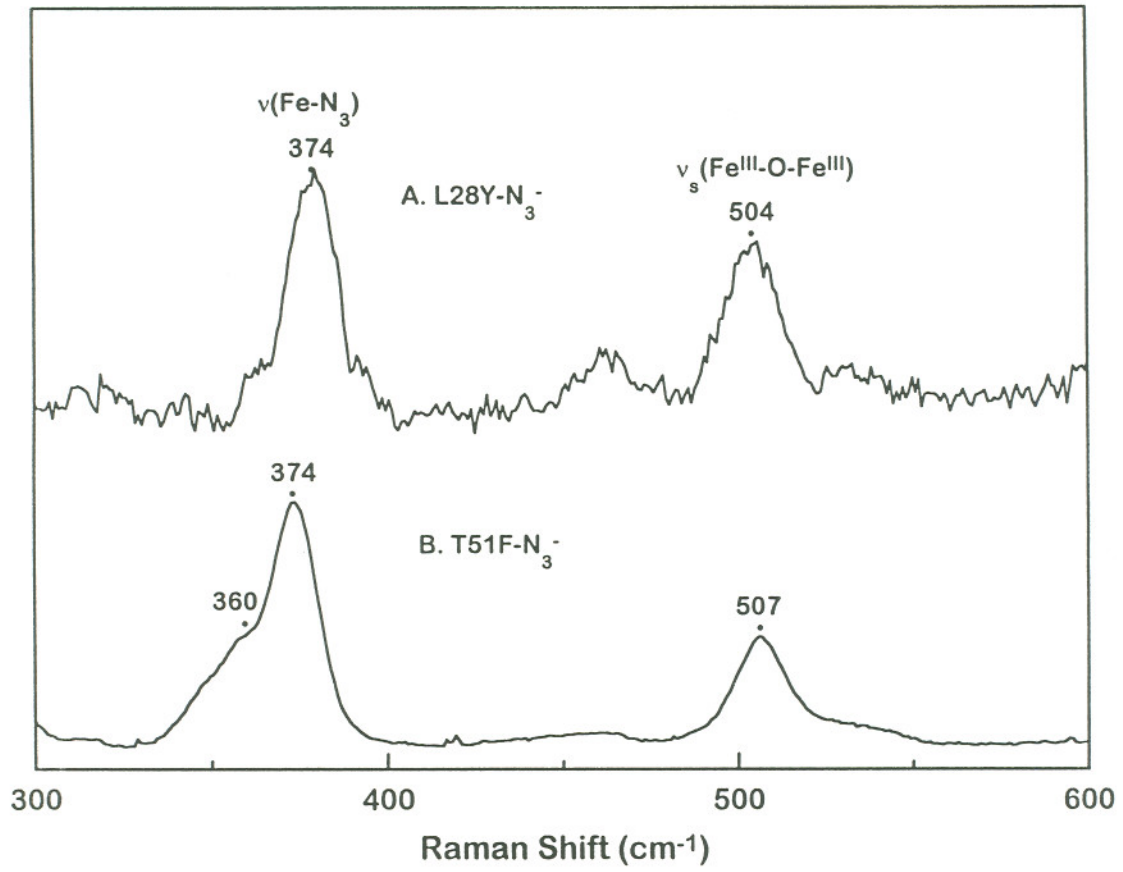

Figure 5.11 Raman spectra of azido complexes of (A) L28Y mutant and (B) T51F mutants obtained with 514 nm excitation (20 mW). Azide concentrations as in Figure 5.7.

state. Nevertheless, even with 400 mM azide, a substantial amount of mixed valence cluster is still present, as indicated by the remaining absorption band at 650 nm and associated RR spectrum.

The T51F mutant exhibits an even more pronounced reaction with O_2 upon addition of azide. The azide complex of the T51F mutant has a more prominent azide → Fe(III) CT band at 470 nm (Figure 5.7E) and more intense ν(Fe-N_3) and ν_s(Fe-O-Fe) modes at 374 cm^{-1} and 507 cm^{-1}, respectively (Figure 5.11B). Furthermore, this oxidation was accomplished at a significantly lower azide concentration of only 50 mM, compared to the 400 mM azide required for oxidation of the L28Y mutant. The T51F mutant had already revealed a significant amount of diferric cluster being present in the mixed-valence preparation (Figure 5.9C). However, additional oxidation in the presence of azide is clearly evident from the reduced absorbance at 650 nm (Figure 5.7E).

The T51F mutant also exhibits a more distinct shoulder at 360 cm^{-1} in its RR spectrum (Figure 5.11B). Although this could be due to ν(Fe-N_3) of an alternative diferric-azide conformation (as in Chapter 4), a more likely possibility is that it represents ν(Fe-N_3) of a mixed-valence azide species. The azide complex of the semimet form of wild-type Hr exhibits an almost identical ν(Fe-N_3) mode at 359 cm^{-1} (Irwin et al., 1983). In both cases, no accompanying Fe-O-Fe vibrations are observed. If the 360-cm^{-1} mode in the T51F mutant is due to a mixed-valence azide complex, then it is likely to have a protonated (hydroxo) bridge as in the semimet forms of wild-type Hr.

Discussion

Oxidation states in mutant hemerythrins

The deoxy form of wild-type Hr can be oxidized in one electron steps under anaerobic conditions, producing a mixed-valence intermediate that is stable in the absence of O_2 (Figure 5.12A). The $semimet_O$ form slowly converts to a $semimet_R$ form in the presence of added anions. Both forms have been shown to be hydroxo-bridged by pulsed EPR spectroscopy (DeRose et al., 1993; Thomann et al., 1993).

A. Wildtype Hr

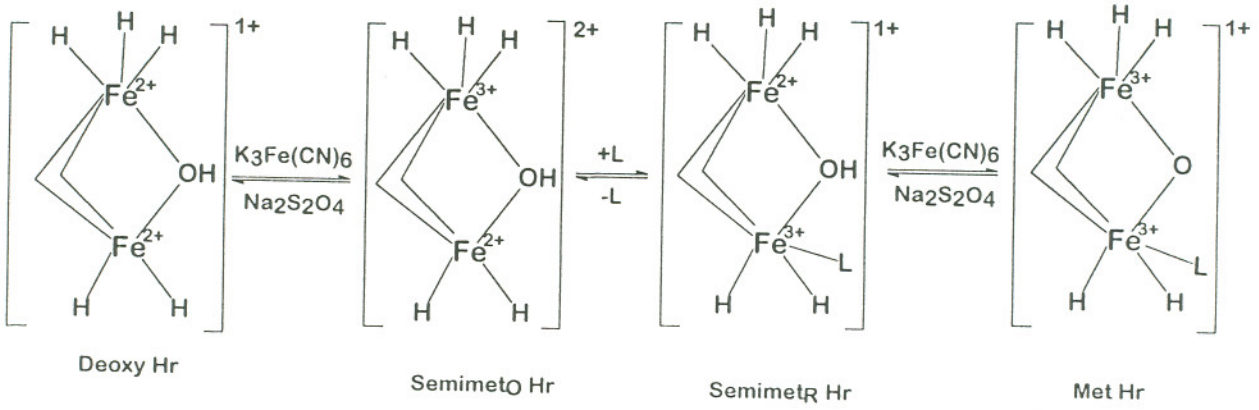

B. L28Y and T51F mutants.

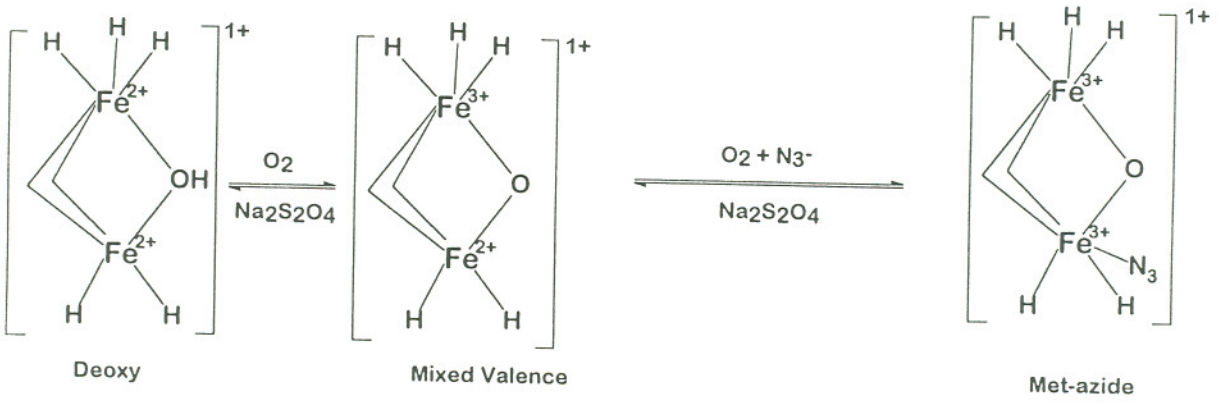

Figure 5.12 Proposed structures of diiron clusters in different oxidation states of (A) wild-type hemerythrin and (B) L28Y and T51F mutants. L = hydroxide ion from solvent or added anion such as azide. The upper iron with three His ligands corresponds to Fe1 and the lower iron with two His ligands and an exogenous ligand site corresponds to Fe2 of Figure 5.1. The structures of the deoxy and met forms of wild-type Hr have been determined by X-ray crystallography (Stenkamp, 1994).

The ferrous state is believed to be localized on Fe2 (lower Fe in Figure 5.12) in the semimet$_O$ form, but switches to Fe1 in the semimet$_R$ form upon the addition of an exogenous ligand to Fe2 (Pearce et al., 1987; McCormick et al., 1989). The latter thus has its Fe2 in the ferric state, similar to metHr. Addition of O_2 to deoxyHr results in the formation of an inner sphere complex at the exogenous ligand site. This is followed by the two-electron reduction of O_2 to peroxide, with no mixed-valence intermediates.

The L28Y and T51F mutants differ from wild-type Hr in that they undergo a one-electron oxidation upon reaction of the deoxy form with O_2 (Figure 5.12B), and this mixed-valence species is stable in the presence of O_2. A further difference from wild-type is that the mixed-valence species is oxo-bridged rather than hydroxo-bridged. This Fe^{II}-O-Fe^{III} cluster in the L28Y and T51F mutants has been definitively identified by electronic, RR, and EPR spectroscopy. Each of these mutants has an additional aromatic residue in the vicinity of the exogenous ligand site on Fe2 (Figure 5.1B). It is likely that the greater hydrophobicity of the diiron site in these mutants favors an oxo-bridged, mixed-valence site with a net charge of +1 (Figure 5.12B) over a hydroxo-bridged structure such as semimet$_O$ with a net charge of +2 (Figure 5.12A). However, since the T51F mutant has multiple amino acid changes, proof of its hydrophobic contribution must await the synthesis of a T51F single mutant.

A similar trend has been observed in the mixed-valence model compounds, **1** and **2**, whose structures have been determined by X-ray crystallography. Compound **1** has its Fe(II) and Fe(III) bridged by two trimethylacetates and a hydroxide, with two neutral trimethyltriazacyclonanes as capping ligands, yielding a net charge of +2 (Bossek et al., 1995). Compound **2** has replaced the bridging trimethylacetates with bulkier triphenylacetates and results in an oxo-bridged product which has a net charge of +1 (Cohen et al., 1997). Presumably, bridge deprotonation occurs in compound **2** because the more hydrophobic environment favors a lower net charge on the cluster. However, both of these mixed-valence compounds are readily oxidized by O_2. Thus, the L28Y and T51F mutants represent the first oxygen-bridged $Fe^{II}Fe^{III}$ species that is stable towards oxidation by O_2. There are other proteins with mixed-valence sites that are stable in the presence of O_2, such as the sulfur-bridged iron clusters in

ferredoxins and the sulfur-bridged Cu_A clusters in cytochrome oxidase and N_2O reductase (Beinert, 1997). The present work suggests that the nonpolar character of the cluster environment in the protein may be important in stabilizing the cluster to oxidation by O_2.

We have demonstrated that oxidation of the mixed-valence site in the L28Y and T51F mutants does occur when azide is added in the presence of O_2. However, the mixed-valence state in the mutants differs from the $semimet_R$ form of wild-type Hr in that it does not form a strong complex with azide. This suggests that the trapped-valence structure in the mutants has the ferrous state localized on Fe2, as in $semimet_O$ (Figure 5.12). Outer sphere oxidation of the mixed-valence L28Y and T51F by O_2 is also consistent with Fe2 being ferrous. Fe(II) at Fe2 in wild-type does react with O_2. The diminished tendency of a ferrous site to react with anions is also seen in deoxyHr which forms weaker complexes with exogenous ligands such as azide (Reem & Solomon, 1987). In the case of the L28Y and T51F mutants, weak binding of azide to the mixed valence site may promote conversion to a state analogous to $semimet_R$ (Figure 5.12A) with azide bound at Fe2, a hydroxo bridge, and the ferrous site switched to Fe1. This species might be more susceptible to outer sphere oxidation by O_2. Such an outer-sphere oxidation process has been demonstrated in the formation of compound **2** (Cohen et al., 1997).

Function of aromatic residues at active site

In wild-type Hr, the side chain carbons of Leu 28 and Leu 98 are in close proximity to the O_2-binding site on Fe2 at distances of 5.5 and 6.0 Å, respectively (Figure 5.1B). However, completely different behavior occurs at these two positions when the leucine is replaced by tyrosine. The L98Y mutation results in the coordination of tyrosine in a portion of the met form. The L28Y mutant shows no evidence of tyrosine coordination to iron in either the mixed-valence state or diferric azide complex, despite the fact that Leu28 is closer than Leu98 to Fe2 in wild-type Hr. Presumably, steric hindrances in the protein prevent the positioning of the phenolate oxygen of Tyr 28 at the correct distance and/or geometry for coordination to Fe2. Instead, introduction of this aromatic group at residue 28 has the effect of

blocking reversible O_2 binding at Fe2 and actually stabilizes a mixed-valence state of the protein. Very similar behavior is observed upon insertion of phenylalanine in the T51F mutant. In contrast, the phenylalanine in the L98F mutant does permit complete oxidation to the met form by O_2, but L98F met Hr also reveals a transient blue mixed-valence species upon reduction. In each of these cases (L28Y, T51F, and L98F), the introduction of an aromatic residue has increased the stability of the mixed-valence state and favored an oxo- over a hydroxo-bridged species.

The L98Y mutant actually exists in two different active-site conformations: with and without an Fe-coordinated phenolate (Figure 5.6). The phenolate-coordinated form exhibits an Fe-O-Fe stretch at 516 cm^{-1}, as well as the RR signature of an Fe-phenolate, and undergoes oxo-bridge exchange with solvent. The phenolate-free from has its Fe-O-Fe stretch at 496 cm^{-1} and is resistant to oxo-bridge exchange, indicating the lack of a ligand in the exogenous-ligand site on Fe2. The deoxy form of the L98Y mutant is still capable of binding O_2 in a reversible fashion, forming the oxyHr hydroperoxide (Farmer et al., 1997). However, the rate of reaction of deoxy L98Y is 380-fold slower than in wild-type Hr. In contrast, deoxy L98F binds O_2 at a rate that is 3-fold faster than that of wild-type. This suggests that the phenol side chain of Tyr 98 is blocking access of O_2 to the exogenous ligand site on Fe2, either with or without coordination to Fe. An Fe^{III}-phenolate is expected to be (thermodynamically) very difficult to reduce whereas, L98Y met Hr can be reduced to deoxy, albeit more slowly than wild-type Hr. This observation argues against coordination of tyrosine to iron in L98Y deoxy Hr (i.e., the form that binds O_2).

The decrease in side-chain size upon conversion of Leu 98 to Ala allows exogenous phenol and catechol to have access to the diiron site. The resulting diferric complexes have only one active site conformation, as judged by the appearance of a single ν_s(Fe-O-Fe) mode in each case (Figure 5.3D, E). Interestingly, the RR data indicate that catechol coordinates to the L98A diferric site in a monodentate fashion, rather than the bidentate mode that has been observed for catecholate complexes of tyrosine hydroxylase and the F208Y mutant of ribonucleotide reductase (Table 5.1). The crystal structure of the F208Y mutant of R2 shows that the Tyr 208 has been oxidized to an endogenous catechol which then

displaces the oxo-bridge from the diiron site in order to form a bidentate ferric catecholate (Åberg et al., 1993). The bridging oxo group in Hr is also in close proximity to the exogenous ligand site (Figure 5.1B). The resistance of the μ-oxo in L98A Hr to displacement by catecholate is reminiscent of the resistance of wild-type Hr to solvent isotope exchange. This is perhaps indicative of greater Fe-μ-O coordination or rigidity of the diiron site in Hr than in R2. The ability of the L98A mutant to bind exogenous phenol and catechol suggests that Leu 98 in wild-type Hr functions in sterically blocking the binding of large organic molecules, as well as in promoting the reversible binding of O_2.

Application to diiron sites in R2 and MMOH

In the F208Y mutant of R2, the Tyr-208 residue is oxidized to dihydroxyphenylalanine (dopa) during the reaction of diferrous R2 with O_2 (Ormö et al., 1992; Åberg et al., 1993; Ling et al., 1994). The Tyr-98 residue in the L98Y mutant of Hr is also located in close proximity to the diiron site, leading to the possibility of a similar oxidation. However, the spectroscopic characteristics of the L98Y metHr are those of an iron phenolate, with no indication of the formation of an iron-catecholate. Thus, if oxidation of the Tyr-98 ring is occurring, it is not leading to an iron-bound product. Furthermore, L98Y oxyHr exhibits absorption and RR spectra very similar to those of wild-type Hr, indicating formation of a stable diferric hydroperoxide in L98Y Hr. Most likely, the difference between the F208Y mutant of R2 and L98Y mutant of Hr is that the diiron site in R2 can break the O-O bond and form a high valent Fe^{IV} intermediate, while in the L98Y mutant the O-O bond remains intact in the hydroperoxide state. This suggests that only a high-valent intermediate can accomplish the types of hydroxylation reactions observed in R2 and in the enzymatic cycle of methane monooxygenase, and that such a high-valent intermediate is inaccessible in Hr.

Rapid freeze-quench experiments with R2 and MMOH have led to the trapping of several high-valent intermediates. R2 forms intermediate **X** at the $Fe^{III}Fe^{IV}$ oxidation level which has the power to oxidize Tyr 122 to a free radical (Tong et al., 1996; Sturgeon et al., 1996), while MMOH forms intermediate **Q** at the $Fe^{IV}Fe^{IV}$

level which has the power to insert an activated oxygen into methane (Lee et al., 1993). Both MMOH and R2 have a hydrophobic pocket surrounding the diiron center and composed of varying residues (Holmes et al., 1991; Nordlund & Eklund, 1993; Rosenzweig et al., 1995). It is possible that R2 and MMOH use their different hydrophobic environments to stabilize different intermediates **X** and **Q**, respectively, and thereby regulate the different reaction abilities of their diiron clusters. The present work has shown that changing a single hydrophobic residue in Hr from Leu 28 to Tyr 28 results in the stabilization of a completely different oxidation state: $Fe^{III}Fe^{III}$ with Leu 28 and $Fe^{II}Fe^{III}$ state with Tyr 28. Thus, the nature of the individual residues in a hydrophobic pocket can play a critical role in determining the intermediates in a reaction pathway.

CHAPTER VI
CONCLUSIONS AND FUTURE DIRECTIONS

As described in Chapter I, previous studies using resonance Raman spectroscopy have provided unique information on the structure of the ligand binding sites and on the chemistry of the diiron-oxo centers of hemerythrin (Hr) and the R2 subunit of ribonucleotide reductase (R2). In this thesis, we have extended the study to another diiron-oxo enzyme, stearoyl Δ^9 desaturase (Δ9D), and to mutants of myohemerythrin (Mhr) and Hr. In this Chapter, I will briefly summarize our new contributions to the diiron-oxo proteins, and conclude with suggestions for future research directions.

Conclusions

Comparison of diiron-oxo sites

Diiron-oxo centers are currently receiving much attention in bioinorganic chemistry and research on proteins and model systems is vigorous and expanding rapidly (Kurtz, 1997). Recent studies on diiron-oxo proteins including Hr, Mhr, R2, methane monooxygenase (MMOH), and Δ9D have been reviewed in Chapter I. All of these proteins share a common motif of a four-helix bundle surrounding a diiron-oxo core, and they use these diiron sites to react with O_2 as part of their functional processes. In Chapter II, we classified these diiron-oxo proteins into two different, evolutionarily unrelated classes. The class I diiron-oxo proteins include Hr and Mhr, whereas class II diiron-oxo proteins include R2, MMOH, and Δ9D.

The two classes of diiron-oxo proteins differ in their functions, structures, and amino acid sequences. Thus, Hr and Mhr are reversible O_2 transport proteins in certain marine invertebrates, whereas R2, MMOH, and Δ9D are enzymes that

activate O_2 to form, respectively, a tyrosyl radical necessary for the reduction ribonucleotides, an intermediate that hydroxylates hydrocarbons, and an oxidant that inserts a 9,10 *cis* double bond into a fatty acid. In Hr and Mhr, the iron···iron axis is oriented perpendicular to the major axis of the four helix bundle, but in R2, MMOH, and Δ9D, the diiron axis is parallel to the helix-bundle axis. In Hr and Mhr, the diiron-oxo core has a histidine-rich protein ligand environment: One iron is coordinated by three, and the second iron by two His ligands. In contrast, the diiron-oxo cores of R2, MMOH, and Δ9D have a carboxylate-rich (Glu and Asp) coordination environment, and, in addition, each iron atom has only a single His ligand, each provided by one of the two conserved EX_2H sequence motifs. This amino acid sequence motif is lacking in the hemerythrins.

In the fully reduced $[Fe(II)]_2$ state of Hr, only one iron, Fe2, is five-coordinate and, hence, has an open ligand site at for end-on O_2 coordination. Upon oxidation to the μ-oxo, di-μ-carboxylato-bridged diiron(III) state, this core structure becomes very rigid. This contrasts with the diiron(II) states of R2, MMOH, and Δ9D where open or labile coordination sites exist on both iron atoms, and, upon oxidation to the respective diiron(III) states, their cores show much greater coordination flexibility. These structural differences between the two classes of diiron-oxo proteins presumably determine their different reactivities.

Identification of a diiron-oxo cluster

In Chapter II, we characterized the structure of the diiron-oxo site in Δ9D. Generally speaking, oxo-bridged diiron(III) complexes exhibit enhanced Fe–O–Fe stretching vibrations in their resonance Raman spectra upon excitation into their oxo → Fe(III) charge transfer (CT) bands (Sanders-Loehr et al., 1989). Δ9D displays an absorption band in the 300-370-nm region with an ϵ_{340} value of 8400 $M^{-1}cm^{-1}$, which was assigned to oxo → Fe^{3+} CT based on its excitation profile. With 350-nm excitation, we have detected a ν_s(Fe–O–Fe) peak at 519 cm^{-1} and a ν_{as}(Fe–O–Fe) peak at 747 cm^{-1}. When the enzyme is prepared in $H_2{}^{18}O$ solvent, these two peaks have isotope shifts of -18 and -34 cm^{-1}, respectively. Thus, electronic and resonance Raman spectroscopy, together with earlier Mössbauer spectroscopic studies (Fox et

al., 1993), clearly identified an oxo-bridged diiron core structure in Δ9D. From the positions of ν_s(Fe–O–Fe) and ν_{as}(Fe–O–Fe), and their ^{18}O-dependent shifts, we calculated an Fe–O–Fe angle of $\sim 123^\circ$, suggesting that the diiron-oxo cluster in Δ9D is triply bridged in the diferric state. From the results of these studies and the amino acid sequence of the enzyme, a structure for the diiron-oxo site has been proposed (Figure 2.10).

The oxo bridge in R2 and Δ9D is more accessible to solvent than that in Hr. Earlier resonance Raman studies showed that the oxo bridge in R2 can exchange with $H_2{}^{18}O$ water ($t_{1/2} \sim 15$ minutes; Sjöberg et al., 1982), but that the source of the oxo-bridge oxygen atom in R2 is from the O_2 molecule (Ling et al., 1994). In Chapter II, we found that the oxo bridge in Δ9D also exchanges with $H_2{}^{18}O$ water ($t_{1/2} \sim 7$ minutes). However, the source of the oxo-bridge O-atom in Δ9D is less clear-cut. When the reaction between diferrous Δ9D with $^{18}O_2$ was quenched after 3 minutes, the oxo-bridge oxygen was found to be ^{16}O from water. Even if the origin of the oxo-bridge atom is from the gaseous O_2 as in R2, then a plausible explanation for the rapid exchange is that the high-valent intermediate of Δ9D undergoes more facile exchange than the diferric form. This could be because Fe(IV) atoms are more susceptible to nucleophilic attack by solvent, leading to Fe-μO bond breakage and bridge exchange.. In contrast, the oxo bridge in Hr cannot be exchanged with solvent water by simple incubation. Only after the diiron site was reduced to diferrous state, did the resulting hydroxo bridge of deoxyHr exchange with $H_2{}^{18}O$ at a slow rate (Shiemke et al., 1984).

Exogenous ligand binding to the diiron-oxo site

When a class II diiron-oxo protein in its reduced, diiron(II) state reacts with O_2, a diferric-peroxo intermediate (**P**) is formed. This intermediate **P** has been proposed as the first common intermediate for class II diiron-oxo proteins (Que & Dong, 1996). However, its exact structure still remains unclear. In Chapter III, we studied azide binding of Δ9D, and provided a model structure for intermediate **P**. Resonance Raman spectroscopic experiments demonstrated the existence of two different adducts: an η^1 (end-on) structure at pH 7-8 ($^{14}N_3^-$ asymmetric stretch at 2073

cm^{-1}, resolved into two bands with $^{15}N^{14}N_2^-$), and a μ-1,3 bridging structure at pH < 7 ($^{14}N_3^-$ asymmetric stretch at 2100 cm^{-1}, shifted as a single band with $^{15}N^{14}N_2^-$). Both adducts also exhibit an Fe–N_3 stretching mode at ~380 cm^{-1}, but no accompanying Fe–O–Fe stretching mode, presumably due either to protonation or loss of the oxo bridge. The ability of the Δ9D core to form a μ-1,3 bridging azide is considered to be supporting evidence for a μ-1,2 bridging peroxide as a possible structure for **P** (Figures 3.8, 3.10). Studies of the ferrous sites in R2 showed that each iron can bind one molecule of azide (Pulver et al., 1995) or NO (Haskin et al., 1995). The μ-1,2 bridging diferric peroxide model of **P** is also consistent with Mössbauer data that suggest that peroxide binds to the diferric center in a symmetric manner (Liu et al., 1994).

Recently, an azide adduct of an oxo-bridged diferric model compound containing an end-on, terminal azide was reported (Mizoguchi & Lippard, 1997). This complex has a $\nu_{as}(N_3)$ mode at 2043 cm^{-1} in its IR spectrum which increases in breadth with $^{15}N^{14}N_2$, but fails to resolve into two peaks. This result is contradictory to the behavior of six other terminal metal-azide complexes where splittings of 6-12 cm^{-1} have been observed (Table 3.1). The lack of splitting for a known end-on complex places some doubt on our assignment of the 2100-cm^{-1} peak in Δ9D to a μ-1,3 bridging azide (Chapter 3). Our assignment was based on the lack of any isotope splitting and is further supported by the samples having identical peak widths with ^{14}N and ^{15}N, with no indication of line broadening in the $^{15}N^{14}N_2$ mixed isotope.

In contrast, the peroxide in oxy-Hr binds to only the Fe2 site in an end-on binding mode (Stenkamp, 1994). These different binding modes between class I and II proteins may correspond to their different functional properties. The class II proteins (Δ9D and R2) need to break the O–O bond to generate high-valent intermediates (**Q** or **X**) for catalysis, whereas Hr must maintain and protect the O–O bond during O_2 transport. We proposed that the O–O bond of the μ-1,2 bridged peroxo group in Δ9D undergoes homolysis due to electron donation from both Fe atoms (Figure 3.10). In heme-containing peroxidases and monooxygenases, a different mechanism involving heterolysis of the O–O bond has been presented: the Fe–O bond is strengthened by a "push" from the proximal axial ligand and the O–O

bond is weakened by a "pull" on the outer O atom by hydrogen bond donors in the distal pocket (Poulos 1987; Gerber & Sligar, 1992).

Functional roles of the hydrophobic residues

As described in Chapter I, hydrophobic residues have been found around the diiron-oxo site in all of the diiron-oxo proteins. However, their functional roles are not understood. Recently, the L103N mutant of Mhr from *Themiste zostericola,* and the L28Y, T51F (the sequence ...GELRRCT... was mutated to ...NAAIEVF..., respectively), L98Y, and L98A mutants of Hr from *Phascolopsis gouldii* have been expressed and purified. The Leu 103 residue in Mhr from *T. zostericola* has the analogous position to the Leu 98 residue in Hr from *P. gouldii*. Both the Leu 98 and Leu28 residues in oxy-Hr are in van der Waals' contact with bound O_2 as seen in the X-ray crystal structure (Figure 5.1). In Chapters IV and V, we investigated the effects of these mutations on the structures of the diiron-oxo site and their ligand binding properties.

As described in Chapter IV, the Leu 103 residue of Mhr was mutated to a hydrophilic residue of similar size: Asn. This L103N mutant exhibits a ν_s(Fe–O–Fe) peak at 514 cm^{-1} and a ν_{as}(Fe–O–Fe) peak at 760 cm^{-1}, respectively. In D_2O buffer, the ν_s(Fe–O–Fe) peak of L103N mutant displays Fermi resonance coupling with δ(Fe–O–D), and splits into two peaks at 506 and 526 cm^{-1}. In contrast, the ν_{as}(Fe–O–Fe) peak has no D-effect. Combining the spectroscopic data with the crystal structure, we concluded that the Fe2 site of L103N Mhr is coordinated by a hydroxide ligand. Exposure of deoxy L103N Mhr to O_2 resulted in oxy formation, followed by rapid autooxidation that is $\sim 10^3$ faster than that of the wild-type oxy-Mhr (Lloyd et al., 1998). As a substitute for O_2, we used azide as a probe to study ligand binding. The L103N mutant can bind azide in two modes with ν(Fe–N_3) peaks at 337 and 366 cm^{-1}, respectively. Compared with wild-type azido-Mhr, the bond between Fe2 and azide is significantly weakened, and the azide binding constant decreases $\sim$500 times (Raner et al., 1997). We believe this is due to the H-bonding interaction of azide with water and the amide of Asn 103 (Figure 4.9). These results clearly indicate that the methyl groups of Leu 103 provide a hydrophobic environment which orients and

enhances exogenous ligand binding to the Fe2 site by restricting the access of water molecules.

The L98Y mutant of Hr forms a ferric phenolate complex. This mutant has an absorption band at 530 nm due to phenolate → Fe(III) charge transfer. With 514-nm excitation, the Raman spectrum has vibrational frequencies at 573, 1167, 1502, and 1603 cm^{-1}. The deoxy form of the L98Y mutant can still react with O_2 to form oxyHr. However, the rate of O_2 binding is 380-fold slower than in wild-type, indicating that the phenolate moiety sterically blocks O_2 access. Furthermore, the rate of autooxidation of both L98Y and L98F mutants is slower than in wild-type (Farmer et al., 1997). This shows that the replacement of Leu by bulkier hydrophobic residues causes enhancement of O_2 binding by further restricting the access of water molecules.

In contrast, the L28Y mutant of Hr contains an oxo-bridged mixed-valence species (Fe^{II}–O–Fe^{III}). It displays an antiferromagnetically coupled $Fe^{II}Fe^{III}$ EPR signal, and an intervalence charge transfer band at 657 nm. With 647-nm excitation, the L28Y mutant exhibits a ν_s(Fe^{II}–O–Fe^{III}) peak at 479 cm^{-1} and an anomalously intense ν_{as}(Fe^{II}–O–Fe^{III}) peak at 694 cm^{-1}. The T51F mutant also exhibits similar spectroscopic properties. These results indicate that the mixed-valence state of the diiron-oxo cluster can be stabilized simply by adding bulkier hydrophobic residues around the diiron-oxo site (Figure 5.12). Such differences in hydrophobic residues could be important in stabilizing the different oxidation states for catalytic intermediates: diferryl ($Fe^{IV}Fe^{IV}$) in compound **Q** of MMOH versus mixed valence ($Fe^{III}Fe^{IV}$) in compound **X** of R2.

Overall, our studies demonstrated that the Leu 98 residue in Hr (or Leu 103 in Mhr) has a different functional role from the Leu28 residue. The Leu 98 residue controls exogenous ligand binding, while the Leu28 residue helps to maintain the oxidation state of the diiron-oxo cluster.

Future Directions

From the experiments described above, we see that resonance Raman spectroscopy is highly suitable both for identifying the nature of the diiron-oxo center and for following ligand binding to the metal center. However, many challenging projects remain. For example, several intermediates such as **P**, **Q**, and **X** of diiron-oxo proteins (Figure 1.6) have been trapped through rapid freeze-quench methods and studied by EPR and Mössbauer spectroscopy. Yet, no successful resonance Raman spectroscopic data on these intermediates have been obtained.

Intermediates

Judging from their absorption spectra, intermediates **P** and **Q** would be good candidates for resonance Raman experiments. Intermediate **P** has a strong absorption band near 600 nm (λ_{max} 625 nm, ϵ 1500 $M^{-1}cm^{-1}$) which may be due to peroxide → Fe(III) charge transfer (Liu et al., 1995). Intermediate **Q** exhibits absorption bands at 330 and 430 nm with $\epsilon \approx 7500\ M^{-1}cm^{-1}$ (Lee et al., 1993). The intermediate **X** of R2 was also reported to have an absorption band at ~360 nm (Tong et al., 1996). If we could obtain resonance Raman spectra, intermediate **P** would be expected to have a ν(O–O) in the 750-950 cm^{-1} region which could be confirmed by use of $^{18}O_2$. The binding mode of **P** could be further clarified by using mixed-isotope $^{16}O^{18}O$ gas. The original report of the RR spectrum of compound **P** (Liu et al., 1995) has since been retracted (Liu et al., 1997). If intermediates **Q** and **X** have the diamond-core structure as proposed by Que and Dong (1996), they should have an Fe_2O_2 breathing mode at ~670 cm^{-1} (Sanders-Loehr, 1996).

In order to carry out a successful resonance Raman experiment on these intermediates, we need to figure out how to improve experimental conditions.

1. Increasing the concentration of intermediate. Typically, to get a high-quality spectrum on diferric-oxo proteins, we have used a concentration (in diiron centers) of ~1 mM. How to reach this concentration is a key factor for success. Thus far, all of the intermediates were trapped in liquid nitrogen-cooled isopentane. However, by this quenching method, the concentration of

the sample is significantly decreased. For example, the maximum concentration of intermediate **X** has only reached 300 μM.

2. Changing solvent. In the presence of isopentane, the Raman spectra are dominated by isopentane peaks, and many of these solvent peaks fall at the same frequency as candidate peaks for O–O and Fe–O vibrations (Liu et al., 1995). Hence, only difference spectra can be analyzed for these samples. However, this methodology can easily result in the over-interpretation of small peaks. New approaches would be to consider removing the isopentane solvent, for example, by pumping the frozen sample pellet, or by investigating the use other solvents that would have the correct thermal properties but be free from spectral interference in the regions of interest of the intermediates.

3. Improving the experimental setup. In our experience, low temperature resonance Raman experimental data obtained from samples loaded on a Displex generally give superior signals than those from glass capillaries loaded in a cold-finger immersed in a Dewar. Two major reasons are the elimination of the glass surface of the cell in contact with the scattering sample and, often, an improved scattering surface itself. A major impediment, however, is the loading of the frozen samples onto a pre-chilled Displex surface at $\sim$ 100 K. Because of this difficulty, many of our Raman experiments on intermediates have been carried out on frozen samples contained in EPR tubes that are inserted into the copper cold finger immersed in liquid nitrogen. A possible improvement would be to design a sample holder that could be mounted on the cold Displex while remaining at sufficiently low temperature to prevent reaction. One such possibility is to directly pack the sample onto a sample holder that can be transferred to Displex at low temperature. An idea along these lines has been published (Spiro & Czernuszewicz, 1995). However the EPR tubes offer the possibility of monitoring the integrity of the intermediate to laser irradiation, in cases like compound **X** where it is a paramagnetic species. With compound **Q** of MMOH prepared by John Lipscomb, neither pumping of isopentane, nor direct freezing in liquid N_2, nor ice temperature flow experiments with Gerald Babcock led to any detectable RR signals for

compound **Q** (J. Cohen and J. Sanders-Loehr, personal communication). An alternative possibility is that these intermediates are particularly sensitive to photochemical decomposition upon laser irradiation.

Blue species

The blue mutant species L28Y and T51F of Hr need to be further characterized. First of all, we need to do ^{18}O-bridge exchange experiments to confirm our assignment of the $\nu_s(Fe^{II}–O–Fe^{III})$ and $\nu_{as}(Fe^{II}–O–Fe^{III})$ peaks. One planned approach is to gently denature the purified blue protein in guanidinium chloride allowing the formation of apoprotein by releasing iron. The unfolded protein may be diluted in $H_2{}^{18}O$ or D_2O, to which Fe(II) may be added back anaerobically. Optical and Raman spectra may then be obtained from the blue species that forms upon exposure to O_2. An ^{18}O-isotope effect would be seen on the ν_s and $\nu_{as}(Fe^{II}–O–Fe^{III})$ frequencies. A parallel experiment done in D_2O can prove whether there is an oxo or hydroxo bridge between the two iron atoms. A third approach would be to reconstitute the apoprotein with an iron isotope (^{54}Fe).

NO binding with Δ9D

For further support of our proposed μ-1,2 binding mode of O_2 in intermediate **P**, we suggest investigating the binding of nitric oxide (NO) to diferrous Δ9D. NO has a similar electronic structure to that of O_2. Also similar to O_2, NO reacts with deoxy-Hr to form a bent, end-on structure with the Fe2 site (Nocek et al., 1988). NO also reacts with both Fe(II) atoms in reduced R2 to form a magnetically coupled $\{FeNO\}_2$ center and N_2O (Haskin et al., 1995). Preliminary studies by Dr. Brian Fox have shown that NO can react with the reduced Δ9D to form an iron-nitrosyl complex with a green color. Iron-nitrosyl complexes would be expected to have ν(Fe–NO) and δ(Fe–N–O) peaks in 400-500 cm^{-1} region, and a ν(NO) peak at high frequency ($\sim$1650 cm^{-1}) (Tsubaki & Yu, 1982). We can use ^{15}NO, N^{18}O, and ^{15}N^{18}O isotopes to identify these vibrational peaks. If NO bridges between two iron atoms in a μ-1,2 mode, the ν(NO) peak should have an altered frequency and exhibit no deuterium effect in D_2O buffer. If only the nitrogen atom of NO bridges between the two iron

atoms, we expect to see a ν_s(Fe–N–Fe) mode at higher frequency ($\sim$500 cm^{-1}), whereas the presence of an NO on each Fe should yield a ν_s(Fe–NO) closer to that of the nitric oxide complex of Hr.

LITERATURE CITED

Åberg, A. (1993) Ribonucleotide reductase from *E. coli*. Structural aspects of protein function. Ph.D. Dissertation, Stockholm University, Stockholm.

Åberg, A., Ormö, M., Nordlund, P., and Sjöberg, B.-M. (1993) Autocatalytic generation of dopa in the engineered protein R2 F208Y from *Escherichia coli* ribonucleotide reductase and crystal structure of the dopa-208 protein. *Biochemistry* **32,** 9845–9850.

Adachi, S., Nagano, S., Ishimori, J., Watanabe, Y., Morishima, I., Egawa, T., Kitagawa, T., and Makino, R. (1993) Roles of proximal ligand in heme proteins: replacement of proximal histidine of human myoglobin with cysteine and tyrosine by site-directed mutagenesis as models for P-450, chloroperoxidase, and catalase. *Biochemistry* **32,** 241–252.

Ahmad, S., McCallum, J.D., Shiemke, A.K., Appelman, E.H., Loehr, T.M., and Sanders-Loehr, J. (1988) Raman spectroscopic evidence for side-on binding of peroxide ion to Fe(III)(edta). *Inorg. Chem.* **27,** 2230–2233.

Ai, J., Broadwater, J.A., Loehr, T.M., Sanders-Loehr, J., and Fox, B.G. (1997) Azide adducts of stearoyl-ACP desaturase: a model for μ-1,2 bridging by dioxygen in the binuclear iron active site. *J. Biol. Inorg. Chem.* **2,** 37–45.

Andersson, K.K., Cox, D.D., Que, L., Jr., Flatmark, T., and Haavik, J. (1988) Resonance Raman studies on the blue-green-colored bovine adrenal tyrosine 3-monooxygenase (tyrosine hydroxylase). Evidence that the feedback inhibitors adrenaline and noradrenaline are coordinated to iron. *J. Biol. Chem.* **263,** 18621–18626.

Andersson, K.K., Froland, W.A., Lee. S.-K., and Lipscomb, J.D. (1991) Dioxygen independent oxygenation of hydrocarbons by methane monooxygenase hydroxylase component. *New J. Chem.* **15,** 411–415.

Andersson K.K., Elgren, T.E., Que, L., Jr., and Lipscomb, J.D. (1992a) Accessibility to the active site of methane monooxygenase: the first demonstration of exogenous ligand binding to the diiron cluster. *J. Am. Chem. Soc.* **114,** 8711–8713.

Andersson, K.K., Vassort, C., Brennan, B.A., Que, L., Jr., Haavik, J., Flatmark, T., Gros, F., and Thibault, J. (1992b) Purification and characterization of the blue-

green rat phaeochromocytoma (PC12) tyrosine hydroxylase with a dopamine-Fe(III) complex. Reversal of the endogenous feedback inhibition by phosphorylation of serine-40. *Biochem. J.* **284,** 687–695.

Atta, M., Fontecave, M., Wilkins, P.G., and Dalton, H. (1993) Abduction of iron(III) from the soluble methane monooxygenase hydroxylase and reconstitution of the binuclear site with iron and manganese. *Eur. J. Biochem.* **217,** 217–223.

Atta, M., Andersson, K.K., Ingemarson, R., Thelander, L., and Gräslund, A. (1994) EPR studies of mixed-valent [$Fe^{II}Fe^{III}$] clusters formed in the R2 subunit of ribonucleotide reductase from mouse or herpes simplex virus: mild chemical reduction of the diferric centers. *J. Am. Chem. Soc.* **116,** 6429–6430.

Averill, B.A., Davis, J.C., Burman, S., Zirino, T., Sanders-Loehr, J., Loehr, T.M., Sage, J.T., and Debrunner, P.G. (1987) Spectroscopic and magnetic studies of the purple acid phosphatase from bovine spleen. *J. Am. Chem. Soc.* **109,** 3760–3767.

Beinert, H. (1997) Copper A of cytochrome *c* oxidase, a novel, long-embattled, biological electron-transfer site. *Eur. J. Biochem.* **245,** 521–532.

Bollinger, J.M., Jr., Edmondson, D.E., Huynh, B.H., Filley, J., Norton, J. R., and Stubbe, J. (1991) Mechanism of assembly of the tyrosyl radical-dinuclear iron cluster cofactor of ribonucleotide reductase. *Science* **253,** 292–298.

Bollinger, J.M., Jr., Tong, W.H., Ravi, N., Huynh, B.H., Edmondson, D.E., and Stubbe, J. (1994) Mechanism of assembly of the tyrosyl radical-diiron(III) cofactor of *E. coli* ribonucleotide reductase. 2. Kinetics of the excess Fe^{2+} reaction by optical, EPR, and Mössbauer spectroscopies. *J. Am. Chem. Soc.* **116,** 8015–8023.

Bonomi, F., Kurtz, D.M., Jr., and Cui, X. (1996) Ferroxidase activity of recombinant *Desulfovibrio vulgaris* rubrerythrin. *J. Biol. Inorg. Chem.* **1,** 67–72.

Bossek, U., Hummel, H., Weyhermüller, T., Bill, E., and Wieghardt, K. (1995) The first μ(OH)-bridged model complex for the mixed-valent $Fe^{II}Fe^{III}$ form of hemerythrin, *Angew. Chem. Int. Ed. Engl.* **34,** 2642–2645.

Bradic, A., and Wilkins, R.G. (1983) Slow interconversion of acid and base forms of methemerythrin and some implications for methemerythrin reactivity. *Biochemistry* **22,** 5396–5401.

Brown, C.A., Pavlosky, M.A., Westre, T.E., Zhang, Y., Hedman, B., Hodgson, K.O., and Solomon, E.I. (1995) Spectroscopic and theoretical description of the electronic structure of S = 3/2 iron-nitrosyl complexes and their relation to O_2 activation by non-heme iron enzyme active sites. *J. Am. Chem. Soc.* **117,** 715–732.

Burdi, D., Sturgeon, B.E., Tong, W.H., Stubbe, J., and Hoffman, B.M. (1996) Rapid freeze-quench ENDOR of the radical X intermediate of *Escherichia coli* ribonucleotide reductase using $^{17}O_2$, $H_2{}^{17}O$ and ^2H_2O. *J. Am. Chem. Soc.* **118,** 281–282.

Cahoon, E.B., Shanklin, J., and Ohlrogge, J.B. (1992) Expression of a coriander desaturase results in petroselinic acid production in transgenic tobacco. *Proc. Natl. Acad. Sci. U.S.A.* **89,** 11184–11188.

Cardy, D.L.N., Laidler, V., Salmond, G.P.C., and Murrell, J.C. (1991) Molecular analysis of the methane monooxygenase (MMO) gene cluster of *Methylosinus trichosporium* OB3b. *Mol. Microbiol.* **5,** 335–342.

Carlson, J., Fuchs, J.A., and Messing, J. (1984) Primary structure of the *Escherichia coli* ribonucleoside diphosphate reductase operon. *Proc. Natl. Acad. Sci. U.S.A.* **81,** 4294–4297.

Chaudhuri, P., Oder, K, Wieghardt, K., Nuber, B., and Weiss, J. (1986) Magnetic exchange interactions in some novel μ-azido-bridged copper(II) dimers. Crystal structures of $[L_2Cu_2(\mu\text{-}N_3)(N_3)_2](ClO_4)\cdot H_2O$, $LCu(N_3)_2$, $[L_2Cu_2(\mu\text{-}N_3)_2(ClO_4)_2]$, and $L'Cu(N_3)_2$. *Inorg. Chem.* **25,** 2818–2824.

Clark, P.E., and Webb, J. (1981) Mössbauer spectroscopic studies of hemerythrin from *Phascolosoma lurco*. *Biochemistry* **20,** 4628–4632.

Cohen, J.D., Payne, S., Hagen, K.S., and Sanders-Loehr, J. (1997) Raman evidence for a trapped-valence Fe^{II}-O-Fe^{III} complex formed from an outer-sphere reaction of diiron(II) with dioxygen. *J. Am. Chem. Soc.* **119,** 2960–2961.

Cox, D.D., Benkovic, S.J., Bloom, L.M., Bradley, F.C., Nelson, M.J., Que, L., Jr., and Wallick, D.E. (1988) Catecholate LMCT bands as probes for the active sites of nonheme iron oxygenases, *J. Am. Chem. Soc.* **110,** 2026–2032.

Czernuszewicz, R.S., Sheats, J.E., and Spiro, T.G. (1987) Resonance Raman spectra and excitation profile for $[Fe_2O(O_2CCH_3)_2(HB(pz)_3)_2]$, a hemerythrin analogue, *Inorg. Chem.* **23,** 2063–2067.

Dave, B.C., Czernuszewicz, R.S., Prickril, B.C., and Kurtz, D.M., Jr. (1994) Resonance Raman spectroscopic evidence for the FeS_4 and Fe-O-Fe sites in rubrerythrin from *Desulfovibrio vulgaris*. *Biochemistry* **33,** 3572–3576.

Davis, J.C., and Averill, B.A. (1982) Evidence for a spin-coupled binuclear iron unit at the active site of the purple acid phosphatase from beef spleen. *Proc. Natl. Acad. Sci. U.S.A.* **79,** 4623–4627.

Davydov, R.M., Davydov, A., Ingemarson, R., Thelander, L., Ehrenberg, A., and Gräslund, A. (1997a) EPR study of the mixed-valent diiron sites in mouse and herpes simplex virus ribonucleotide reductase. Effect of the tyrasyl radical on structure and reactivity of the diferric center. *Biochemistry* **116,** 11120–11128.

Davydov, R.M., Ménage, S., Fontecave, M, Gräslund, A., and Ehrenberg, A. (1997b) Mixed-valent μ-oxo-bridged diiron complexes produced by radiolytic reduction at 77 K studied by EPR. *J. Biol. Inorg. Chem.* **2,** 242–255.

Dawson, J.H. (1988) Probing structure-function relations in heme-containing oxygenases and peroxidases. *Science* **240,** 433–439.

Dawson, J.W., Gray, H.B., Hoenig, H.E., Rossman, G.R., Schredder, J.M., and Wang, R.-H. (1972) A magnetic susceptibility study of hemerythrin using an ultrasensitive magnetometer. *Biochemistry* **11,** 461–465.

deMaré, F., Kurtz, D.M., Jr., and Nordlund, P. (1996) The structure of *Desulfovibrio vulgaris* rubrerythrin reveals a unique combination of rubredoxin-like FeS4 and ferritin-like diiron domains, *Nat. Struct. Biol.* **3,** 539–546.

DeRose, V.J., Liu, K.E., Kurtz, D.M., Jr., Hoffman, B.M., and Lippard, S.J. (1993) Proton ENDOR identification of bridging hydroxide ligands in mixed-valent diiron centers of proteins: methane monooxygenase and semimet azidohemerythrin. *J. Am. Chem. Soc.* **115,** 6440–6441.

Dewitt, J.G., Bentsen, J.G., Rosenzweig, A.C., Hedman, B., Green, J., Pilkington, S., Papaefthymiou, G.C., Dalton, H., Hodgson, K.O., and Lippard, S.J. (1991) X-ray absorption, Mössbauer, and EPR studies of the dinuclear iron center in the hydroxylase component of methane monooxygenase. *J. Am. Chem. Soc.* **113,** 9219–9235.

Dibar Ure, M.C., and Flinn, P.A. (1971) *A Technique For Removal of The "Blackness" Distortion Of Mössbauer Spectra*, Vol. 7, Plenum Press, New York.

Dong, Y., Fujii, H., Hendrich, M.P., Leising, R.A., Pan, G., Randall, C.R., Wilkinson, E.C., Zang, Y., Que, L., Jr., Fox, B.G., Kauffmann, K., and Münck, E. (1995a) A high-valent nonheme iron intermediate. Structure and properties of $[Fe_2(m\text{-}O)_2(5\text{-Me-TPA})_2](ClO_4)_3$. *J. Am. Chem. Soc.* **117,** 2778–2792.

Dong, Y., Que, L., Jr., Kauffmann, K., and Münck, E. (1995b) An exchange-coupled complex with localized high-spin Fe^{IV} and Fe^{III} sites of relevance to cluster X of *Escherichia coli* ribonucleotide reductase. *J. Am. Chem. Soc.* **117,** 11377–11378.

Dong, Y., Yan, S., Young, V.G., Jr., and Que, L., Jr. (1996) Crystal structure analysis of a synthetic non-heme diiron-O_2 adduct: insight into the mechanism of oxygen activation. *Angew. Chem. Int. Ed. Engl.* **35,** 618–619.

Duff, L.L., Klippenstein, G.L., Shriver, D.F., and Klotz, I.M. (1981) Multiple conformation at functional site of hemerythrin: evidence from resonance Raman spectra. *Proc. Natl. Acad. Sci. U.S.A.* **78,** 4138–4140.

Dunn, J.B.R., Shriver, D.F., and Klotz, I.M. (1973) Resonance Raman studies of the electronic state of oxygen in hemerythrin. *Proc. Natl. Acad. Sci. U.S.A.* **70,** 2582–2584.

Dunn, J.B.R., Shriver, D.F., and Klotz, I.M. (1975) Resonance Raman studies of hemerythrin-ligand complexes. *J. Am. Chem. Soc.* **14,** 2689–2695.

Elgren, T.E., Hendrich, M.P., and Que, L., Jr. (1993) Azide binding to the diferrous clusters of the R2 protein of ribonucleotide reductase from *Escherichia coli*. *J. Am. Chem. Soc.* **115,** 9291–9292.

Farmer, C.S., Xiong, J., Arastu, S., Phillips, R.S., Ai, J., Sanders-Loehr, J., and Kurtz, D.M., Jr. (1997) Effects of site-directed mutagenesis on the O_2-reactivity of hemerythrin and myohemerythrin. In preparation for submission to *Biochemistry*.

Feig, A.L., and Lippard, S.J. (1994) Reactions of non-heme iron(II) centers with dioxygen in biology and chemistry. *Chem. Rev.* **94,** 759–805.

Filter, W.F., Dunham, W.R., Polichar, R.M., and Sands, R.H. (1978) *Added Precision in ^{57}Fe Mössbauer Spectrometry Of Proteins*, Vol. 1, Academic Press, New York.

Fontecave, M., Nordlund, P., Eklund, H., and Reichard, P. (1992) The redox centers of ribonucleotide reductase of *Escherichia coli*. *Adv. Enzymol. Relat. Areas Mol. Biol.* **65,** 147–183.

Fox, B.G., Surerus, K.K., Münck, E., and Lipscomb, J.D. (1988) Evidence for a μ-oxo-bridged binuclear iron cluster in the hydroxylase component of methane monooxygenase. Mossbauer and EPR studies. *J. Biol. Chem.* **263,** 10553–10556.

Fox, B.G., Froland, W.A., Dege, J., and Lipscomb, J.D. (1989) Methane monooxygenase from *Methylosinus trichosporium* OB3b. Purification and properties of a three-component system with high specific activity from a type II methanotroph. *J. Biol. Chem.* **264,** 10023–10033.

Fox, B.G., Hendrich, M.P., Surerus, K.K., Andersson, K.K., Froland, W.A., Lipscomb, J.D., and Münck, E. (1993a) Mössbauer, EPR, ENDOR studies of the

hydroxylase and reductase components of methane monooxygenase from *Methylosinus trichosporium* OB3b. *J. Am. Chem. Soc.* **115,** 3688–3701.

Fox, B.G., Shanklin, J., Somerville, C., and Münck, E. (1993b) Stearoyl-acyl carrier protein Δ^9 desaturase from *Ricinus communis* is a diiron-oxo protein. *Proc. Natl. Acad. Sci. U.S.A.* **90,** 2486–2490.

Fox, B.G., Shanklin, J., Ai, J., Loehr, T.M., and Sanders-Loehr, J. (1994) Resonance Raman evidence for an Fe-O-Fe center in stearoyl-ACP desaturase. Primary sequence identity with other diiron-oxo proteins. *Biochemistry* **33,** 12776–12786.

Freier, S.M., Duff, L.L., Shriver, D.F., and Klotz, I.M. (1980) Resonance Raman studies and structure of a sulfide complex of methemerythrin. *Arch. Biochem. Biophys.* **205,** 449–463.

Froland, W.F., Andersson, K.K., Lee, S.-K., Liu, Y., and Lipscomb, J.D. (1991) *Applications Of Enzyme Biotechnology* (Kelly, J.W. and Baldwin, T.O., Eds.), Plenum Press, New York, pp. 39–53.

Froland, W.A., Andersson, K.K., Lee, S.-K., Liu, Y., and Lipscomb, J.D. (1992) Methane monooxygenase component B and reductase alter the regioselectivity of the hydroxylase component-catalyzed reactions. A novel role for protein-protein interactions in an oxygenase mechanism. *J. Biol. Chem.* **267,** 17588–17597.

Fulco, A.J. (1974) Metabolic alterations of fatty acids. *Annu. Rev. Biochem.* **43,** 215–241.

Garbett, K., Darnall, D.W., Klotz, I.M., and William, R.J.P. (1969) Spectroscopy and structure of hemerythrin. *Arch. Biochem. Biophys.* **205,** 449–463.

Gerber, N.C., and Sligar, S.G. (1992) Catalytic mechanism of cytochrome P-450: evidence for a distal charge relay. *J. Am. Chem. Soc.* **114,** 8742–8743.

Gerez, C., Gaillard, J., Latour, J.M., and Fontecave, M. (1991) Reduction of the small subunit of ribonucleotide reductase by diimide: Evidence for the formation of the mixed-valence Fe^{II}-Fe^{III} center. *Angew. Chem. Int. Ed. Engl.* **30,** 1135–1136.

Girsch, P., and de Vries, S. (1997) Purification and initial kinetic and spectroscopic characterization of NO reductase from *Paracoccus denitrificans*. *Biochim. Biophys. Acta* **1318,** 202–216.

Gupta, N., Bonomi, F., Kurtz, D.M., Jr., Ravi, N., Wang, D.L., and Huynh, B.H. (1995) Recombinant *Desulfovibrio vulgaris* rubrerythrin. Isolation and characterization of the diiron domain. *Biochemistry* **34,** 3310–3318.

Hagen, K.S., and Payne, S. (1997) Department of Chemistry, University of Emory, Atlanta, GA. Personal communication.

Halfen, J.A., Mahapatra, S., Wilkinson, E.C., Kaderli, S., Young, V.G., Jr., Que, L., Jr., Zuberbühler, A.D., and Tolman, W.B. (1996) Reversible cleavage and formation of the dioxygen O-O bond within a dicopper complex. *Science* **271,** 1397–1400.

Haskin, C.J., Ravi, N., Lynch, J.B., Münck, E., and Que, L., Jr. (1995) Reaction of NO with the reduced R2 protein of ribonucleotide reductase from *Escherichia coli*. *Biochemistry* **34,** 11090–11098.

Heistand, R.H., II, Lauffer, R.B., Fikrig E., and Que, L., Jr. (1982) Catecholate and phenolate iron complexes as models for the dioxygenases. *J. Am. Chem. Soc.* **104,** 2789–2796.

Hendrich, M.P., Münck, E., Fox, B.G., and Lipscomb, J.D. (1990) Integer spin EPR studies of the fully reduced methane monooxygenase hydroxylase component. *J. Am. Chem. Soc.* **112,** 5861–5865.

Hoffman, B.J., Broadwater, J.A., Johnson, P., Harper, J., Fox, B.G., and Kenealy, W.R. (1995) Lactose fed-batch overexpression of recombinant metalloproteins in *Escherichia coli* BL21 (DE3): process control yielding high levels of metal-incorporated, soluble protein. *Protein Expr. Purif.* **6,** 646–654.

Holloway, P.W. (1983) Fatty acid desaturation. In: *The Enzymes*, 3rd Ed. (Boyer, P.D., Ed.), Academic Press, New York, pp. 63–83.

Holmes, M.A., and Stenkamp, R.E. (1991) Structures of met and azidomet hemerythrin at 1.66 Å resolution. *J. Mol. Biol.* **220,** 723–737.

Holmes, M.A., Le Trong, I., Turley, S., Sieker, L.C., and Stenkamp, R. E. (1991) Structures of deoxy and oxy hemerythrin at 2.0 Å resolution. *J. Mol. Biol.* **218,** 583–593.

Irwin, M.J., Duff, L.L., Shriver, D.F., and Klotz, I.M. (1983) Stoichiometric characteristics and resonance Raman spectra of azidosemimethemerythrin. *Arch. Biochem. Biophys.* 224, 473–478.

Jacobsen, R.R., Tyeklar, Z., Farooq, A., Karlin, K.D., Liu, S., and Zubieta, J. (1988) A Cu_2-O_2 complex. Crystal structure and characterization of a reversible dioxygen binding system. *J. Am. Chem. Soc.* **110,** 3690–3692.

Jaworski, J.G., and Stumpf, P.K. (1974) Fat metabolism in higher plants. Properties of a soluble stearyl-acyl carrier protein desaturase from maturing *Carthamus tinctorius*. *Arch. Biochem. Biophys.* **162,** 158–165.

Jung, B., Karlin, K.D., and Zuberbühler, A.D. (1996) Formation and interconversion of end-on and side-on μ-peroxo-dicopper(II) complexes. *J. Am. Chem. Soc.* **118,** 3763–3764.

Kim, C., Dong, Y., and Que, L., Jr. (1997) Modeling nonheme diiron enzymes: hydrocarbon hydroxylation and desaturation by a high-valent Fe_2O_2 diamond core. *J. Am. Chem. Soc.* **119,** 3635–3636.

Kim, K., and Lippard, S.J. (1996) Structure and Mössbauer spectrum of a (m-1,2-peroxo)bis(m-carboxylato)diiron(III) model for the peroxo intermediate in the methane monooxygenase hydroxylase reaction cycle. *J. Am. Chem. Soc.* **118,** 4914–4915.

Kitajima, N., and Moro-oka, Y. (1994) Copper-dioxygen complexes. Inorganic and bioinorganic perspectives. *Chem. Rev.* **94,** 737–757.

Kitajima, N., Fujisawa, K., Fujimoto, C., Moro-oka, Y., Hashimoto, S., Kitagawa, T., Toriumi, K., Tatsumi, K., and Nakamura, A. (1992) A new model for dioxygen binding in hemocyanin. Synthesis, characterization, and molecular structure of the μ-η^2: η^2 peroxo dinuclear copper(II) complexes, $[Cu(HB(3,5\text{-}R_2pz)_3)]_2(O_2)$ (R = I-Pr and Ph). *J. Am. Chem. Soc.* **114,** 1277–1291.

Kitajima, N., Fujisawa, K., Hikichi, S., and Moro-oka, Y. (1993) Formation of (μ-hydroxo)(μ-azide) dinuclear copper complex from μ-η^2: η^2-peroxo complex. *J. Am. Chem. Soc.* **115,** 7874–7875.

Kitajima, N., Tamura, N., Fukui, H., Moro-oka, Y., Mitzutani, Y., Kitagawa, T., Mathur, R., Heerwegh, K., Reed, C.A., Randall, C.R., Que, L., Jr., and Tatsumi, K. (1994) Monomeric carboxylate ferrous complexes as models for the dioxygen binding sites in non-heme iron proteins. The reversible formation and characterization of m-peroxo diferric complexes. *J. Am. Chem. Soc.* **116,** 9071–9085.

Knutzon, D.S., Thompson, G.A., Radke, S.E., Johnson, W.B., Knauf, V.C., and Kridl, J.C. (1992) Modification of Brassica seed oil by antisense expression of a stearoyl-acyl carrier protein desaturase gene. *Proc. Natl. Acad. Sci. U.S.A.* **89,** 2624–2628.

Kurtz, D.M., Jr. (1990) Oxo- and hydroxo-bridged diiron complexes: a chemical perspective on a biological unit. *Chem. Rev.* **90,** 585–606.

Kurtz, D.M., Jr. (1997) Structural similarity and functional diversity in diiron-oxo proteins. *J. Biol. Inorg. Chem.* **2,** 159–167.

Kurtz, D.M., Jr., Shriver, D.F., and Klotz, I.M. (1976) Resonance Raman spectroscopy with unsymmetrically isotopic ligands. Differentiation of possible structures of hemerythrin complexes. *J. Am. Chem. Soc.* **98,** 5033–5035.

Kurtz, D.M., Jr., Shriver, D.F., and Klotz, I.M. (1977) Structural chemistry of hemerythrin. *Coord. Chem. Rev.* **24,** 145–178.

Lee, S.-K., Fox, B.G., Froland, W.F., Lipscomb, J.D., and Münck, E. (1993a) A transient intermediate of the methane monooxygenase catalytic cycle containing an $Fe^{IV}Fe^{IV}$ cluster. *J. Am. Chem. Soc.* **115,** 6450–6451.

Lee, S.-K., Nesheim, J.C., and Lipscomb, J.D. (1993b) Transient intermediates of the methane monooxygenase catalytic cycle. *J. Biol. Chem.* **268,** 21569–21577.

Lindqvist, Y., Huang, W., Schneider, G., and Shanklin, J. (1996) Crystal structure of Δ^9 stearoyl-acyl carrier protein desaturase from castor seed and its relationship to other di-iron proteins. *EMBO J.* **15,** 4081–4092.

Ling, J., Farooq, A., Karlin, K.D., Loehr, T.M., and Sanders-Loehr, J. (1992) Vibrational spectroscopic studies of a hydroxo-bridged dinuclear copper complex, a potential model for multicopper proteins. *Inorg. Chem.* **31,** 2552–2556.

Ling, J., Nestor, L.P., Czernuszewicz, R.S., Spiro, T.G., Fraczkiewicz, R., Sharma, K.D., Loehr, T.M., and Sanders-Loehr, J. (1994a) Common oxygen binding site in hemocyanins from arthropods and mollusks. Evidence from Raman spectroscopy and normal coordinate analysis. *J. Am. Chem. Soc.* **116,** 7682–7691.

Ling, J., Sahlin, M., Sjöberg, B.-M., Loehr, T.M., and Sanders-Loehr, J. (1994b) Dioxygen is the source of the m-oxo bridge in iron ribonucleotide reductase. *J. Biol. Chem.* **269,** 5596–5601.

Lippard, S.J., and Berg, J.M. (1994) *Principles of Bioinorganic Chemistry*, University Science Books, Mill Valley, CA, pp. 283–344.

Lipscomb, J.D. (1994) Biochemistry of the soluble methane monooxygenase. *Annu. Rev. Microbiol.* **48,** 371–399.

Liu, K.E., Wang, D., Huynh, B.H., Edmondson, D.E., Salifoglou, A., and Lippard, S.J. (1994) Spectroscopic detection of intermediates in the reaction of dioxygen with the reduced methane monooxygenase/hydroxylase from *Methylococcus capsulatus* (Bath). *J. Am. Chem. Soc.* **116,** 7465–7466.

Liu, K.E., Valentine, A.M., Qiu, D., Edmondson, D.E., Appelman, E.H., Spiro, T.G., and Lippard, S.J. (1995a) Characterization of a diiron(III) peroxo intermediate

in the reaction cycle of methane monooxygenase hydroxylase from *Methylococcus capsulatus* (Bath). *J. Am. Chem. Soc.* **117,** 4997–4998.

Liu, K.E., Valentine, A.M., Wang, D., Huynh, B.H., Edmondson, D.E., Salifoglou, A., and Lippard, S.J. (1995b) Kinetic and spectroscopic characterization of intermediates and component interactions in reactions of methane monooxygenase from *Methylococcus capsulatus* (Bath). *J. Am. Chem. Soc.* **117,** 10174–10185.

Lloyd, C.R., Eyring, E.M., and Ellis, W.R., Jr. (1995) Uptake and release of O_2 by myohemerythrin. Evidence for different rate-determining steps and a caveat. *J. Am. Chem. Soc.* **117,** 11993–11994.

Lloyd, C.R., Raner, G.M., Dennison, A., Eyring, E.M., and Ellis, W.R., Jr. (1998) Oxymyohemerythrin: discriminating between O_2 release and autooxidation. Submitted to *J. Am. Chem. Soc.*

Loehr, T.M., and Sanders-Loehr, J. (1993) Techniques for obtaining resonance Raman spectra of metalloproteins. *Methods Enzymol.* **226,** 431–470.

Loehr, T.M., and Shiemke, A. K. (1988) Non-heme respiratory proteins. In: Biological Applications of Raman Spectroscopy, Vol. 3, *Resonance Raman Spectra of Hemes and Metalloproteins* (Spiro, T.G., Ed.), John Wiley & Sons, New York, pp. 439–490.

Magnus, K.A., Hazes, B., Ton-That, H., Bonaventura, C., Bonaventura, J., and Hol, W.G. (1994) Crystallographic analysis of oxygenated and deoxygenated states of arthropod hemocyanin shows unusual differences. *Proteins* **19,** 302–309.

Manavalan, P., and Johnson, W.C. (1987) Variable selection method improves the prediction of protein secondary structure from circular dichroism spectra. *Anal. Biochem.* **167,** 76–85.

Maroney, M.J., Kurtz, D.M., Jr., Nocek, J.M., Pearce, L.L., and Que, L., Jr. (1986) ^{1}H NMR probes of the binuclear iron cluster in hemerythrin. *J. Am. Chem. Soc.* **108,** 6871–6879.

Martinis, S.A., Atkins, W.A., Stayton, P.S., and Sligar, S.G. (1989) A conserved residue of cytochrome P-450 is involved in heme-oxygen stability and activation. *J. Am. Chem. Soc.* **111,** 9252–9253.

Martins, L.J., Hill, C.P., and Ellis, W.R., Jr. (1997) Structures of wild-type chloromet and L103N hydroxomet *Themiste zostericola* myohemerythrins at 1.8 Å resolution. *Biochemistry* **36,** 7044–7049.

McCallum, J.D., Shiemke, A.K., and Sanders-Loehr, J. (1984) Hydroxide ion binding to methemerythrin. An investigation by resonance Raman and difference spectroscopy. *Biochemistry* **23,** 2819–2825.

McCormick, J.M., Reem, R.C., and Solomon, E.I. (1991) Chemical and spectroscopic studies of the mixed-valent derivatives of the non-heme iron protein hemerythrin. *J. Am. Chem. Soc.* **113,** 9066–9079.

McKee, V., Dagdigian, J.V., Bau, R., and Reed, C.A. (1981) Copper(II) hemocyanin models. *J. Am. Chem. Soc.* **103,** 7000–7001.

McKee, V., Zvagulis, M., Dagdigian, J.V., Patch, M.G., and Reed, C.A. (1984) Hemocyanin models: synthesis, structure, and magnetic properties of a binucleating copper(II) system. *J. Am. Chem. Soc.* **106,** 4765–4772.

McKeon, T.A., and Stumpf, P.K. (1982) Purification and characterization of the stearoyl-acyl carrier protein desaturase and the acyl-acyl carrier protein thioesterase from maturing seeds of safflower. *J. Biol. Chem.* **257,** 12141–12147.

Menage, S., Brennan, B.A., Juarez-Garcia, C., Münck, E., and Que, L., Jr. (1990) Models for iron-oxo proteins: dioxygen binding to a diferrous complex. *J. Am. Chem. Soc.* **112,** 6423–6425.

Michaud-Soret, I., Andersson, K.K., and Que, L., Jr. (1995) Resonance Raman studies of catecholate and phenolate complexes of recombinant human tyrosine hydroxylase. *Biochemistry* **34,** 5504–5510.

Mizoguchi, T.J., and Lippard, S.J. (1997) (μ-oxo)bis(μ-carboxylato)bis(2,2′-bipyridyl)bis(X)diiron(III) complexes, X = NCS^-, $NCSe^-$, and N_3^-: synthetic models of pseudohalide derivatives of carboxylate-bridged diiron proteins. *Inorg. Chem.* **36,** 4526–4533.

Morris, L.J. (1970) Mechanisms and stereochemistry in fatty acid metabolism. *Biochem. J.* **118,** 681–693.

Murch, B.P., Bradley, F.C., and Que, L., Jr. (1986) A binuclear iron peroxide complex capable of olefin epoxidation. *J. Am. Chem. Soc.* **108,** 5027–5028.

Nagai, J., and Bloch, K. (1966) Enzymatic desaturation of stearyl acyl carrier protein, *J. Biol. Chem.* **241,** 1925–1927.

Nagai, J., and Bloch, K. (1968) Enzymatic desaturation of stearyl acyl carrier protein. *J. Biol. Chem.* **243,** 4626–4633.

Nagai, K., Hayashi, A., Taketa, F., and Kitagawa, T. (1983) Resonance Raman studies of hemoglobins M: evidence for iron-tyrosine charge-transfer interactions in the abnormal subunits of Hb M Boston and Hb M Iwate. *Biochemistry* **22,** 1305–1311.

Nakamoto, K. (1970) *Infrared Spectra of Inorganic and Coordination Compounds*, 2nd ed., Wiley-Interscience, New York.

Nakamoto, K. (1986) *Infrared and Raman Spectra of Inorganic and Coordination Compounds*, John Wiley, New York.

Nesheim, J.C., and Lipscomb, J.D. (1996) Large kinetic isotope effects in methane oxidation catalyzed by methane monooxygenase: evidence for C-H bond cleavage in a reaction cycle intermediate. *Biochemistry* **35,** 10240–10247.

Newman, L.M., and Wackett, L.P. (1995) Purification and characterization of toluene 2-monooxygenase from *Burkholderia cepacia* G4. *Biochemistry* **34,** 14066–14076.

Nishida, I., Beppu, T., Matsuo, T., and Murata, N. (1992) Nucleotide sequence of a cDNA clone encoding a precursor to stearoyl-(acyl-carrier-protein) desaturase from spinach, *Spinacia oleracea*. *Plant Mol. Biol.* **19,** 711–713.

Nocek, J.M., Kurtz, D.M., Jr., Sage, J.T., Xia, Y.M., Debrunner, P., Shiemke, A.K., Sanders-Loehr, J., and Loehr, T.M. (1988) Nitric oxide adducts of the binuclear iron site of hemerythrin: spectroscopy and reactivity. *Biochemistry* **27,** 1014–1024.

Nordlund, P., and Eklund, H. (1993) Structure and function of the *Escherichia coli* ribonucleotide reductase protein R2. *J. Mol. Biol.* **232,** 123–164.

Nordlund, P., and Eklund, H. (1995) Di-iron-carboxylate proteins. *Curr. Opin. Struct. Biol.* **5,** 758–766.

Nordlund, I., Powlowski, J., and Shingler, V. (1990a) Complete nucleotide sequence and polypeptide analysis of multicomponent phenol hydroxylase from *Pseudomonas sp.* strain CF600. *J. Bacteriol.* **172,** 6826–6833.

Nordlund, P., Sjöberg, B.-M., and Eklund, H. (1990b) Three-dimensional structure of the free radical protein of ribonucleotide reductase. *Nature* **345,** 593–598.

Nordlund, P., Dalton, H., and Eklund, H. (1992) The active site structure of methane monooxygenase is closely related to the binuclear iron center of ribonucleotide reductase. *FEBS Lett.* **307,** 257–262.

Nordlund, I., Powlowski, J., Hagström, Å., and Shingler, V. (1993) Conservation of regulatory and structural genes for a multi-component phenol hydroxylase within phenol-catabolizing bacteria that utilize a meta-cleavage pathway. *J. Gen. Microbiol.* **139,** 2695–2703.

Olsen, R.H., Kukor, J.J., and Kaphammer, B. (1994) A novel toluene-3-monooxygenase pathway cloned from *Pseudomonas pickettii* PKO1. *J. Bacteriol.* **176,** 3749–3756.

Ookubo, T., Sugimoto, H., Nagayama, T., Masuda, H., Sato, T., Tanaka, K., Maeda, Y., Okawa, H., Hayashi, Y., Uehara, A., and Suzuki, M. (1996) *cis*-μ-1,2-Peroxo diiron complex: structure and reversible oxygenation. *J. Am. Chem. Soc.* **118,** 701–702.

Ormö, M., deMaré, F., Regnström, K., Åberg, A., Sahlin, M., Ling, J., Loehr, T.M., Sanders-Loehr, J., and Sjöberg, B.-M. (1992) Engineering of the iron site in ribonucleotide reductase to a self-hydroxylating monooxygenase. *J. Biol. Chem.* **267,** 8711–8714.

Pate, J.E., Ross, P.K., Thamann, T.J., Reed, C.A., Karlin, K.D., Sorrell, T.N., and Solomon, E.I. (1989) Spectroscopic studies of the charge-transfer and vibrational features of binuclear copper(II) azide complexes: comparison to the coupled binuclear copper active site in met azide hemocyanin and tyrosinase. *J. Am. Chem. Soc.* **111,** 5198–5209.

Paulsen, K.E., Liu, Y., Fox, B.G., Lipscomb, J.D., Münck, E., and Stankovich, M.T. (1994) Oxidation-reduction potentials of the methane monooxygenase hydroxylase component from *Methylosinus trichosporium* OB3b. *Biochemistry* **33,** 713–722.

Pearce, L.L., Kurtz, D.M., Jr., Xia, Y.-M., and Debrunner, P.G. (1987) Reduction of the binuclear iron site in octameric methemerythrins. Characterization of intermediates and a unifying reaction scheme. *J. Am. Chem. Soc.* **109,** 7286–7290.

Pikus, J.D., Studts, J.M., Achim, C., Kauffmann, K.E., Münck, E., Steffan, R.J., McClay, K., and Fox, B.G. (1996) Recombinant toluene-4-monooxygenase: catalytic and Mössbauer studies of the purified diiron and rieske components of a four-protein complex. *Biochemistry* **35,** 9106–9119.

Poulos, T.L. (1988) Heme enzyme crystal structures. *Adv. Inorg. Biochem.* **7,** 1–36.

Powlowski, J., and Shingler, V. (1990) *In vitro* analysis of polypeptide requirements of multicomponent phenol hydroxylase from *Pseudomonas* sp. strain CF600. *J. Bacteriol.* **172,** 6834–6840.

Presnell, S.R., and Cohen, F.E. (1989) Topological distribution of four-α-helix bundles. *Proc. Natl. Acad. Sci. U.S.A.* **86,** 6592–6596.

Prestley, N.D., Floss, H.G., Froland, W.A., Lipscomb, J.D., Williams, P.G., and Morimoto, H. (1992) Cryptic stereospecificity of methane monooxygenase. *J. Am. Chem. Soc.* **114,** 7561–7562.

Pulver, S., Froland, W.A., Fox, B.G., Lipscomb, J.D., and Solomon, E.I. (1993) Spectroscopic studies of the coupled binuclear non-heme of methane monooxygenase: comparison to deoxy and deoxy-azide hemerythrin. *J. Am. Chem. Soc.* **115,** 12409–12422.

Pulver, S.C., Tong, W.H., Bollinger, J.M., Stubbe, J., and Solomon, E.I. (1995) Circular dichroism and magnetic circular dichrosim studies of the fully reduced binuclear non-heme iron active site in the *Escherichia coli* R2 subunit of ribonucleotide diphosphate reductase. *J. Am. Chem. Soc.* **117,** 12664–12678.

Pyrz, J.W., Roe, A.L., Stern, L.J., and Que, L., Jr. (1985) Model studies of iron-tyrosinate proteins. *J. Am. Chem. Soc.* **107,** 614–620.

Que, L., Jr. (1988) *Biological Applications of Raman Spectroscopy* (Spiro, T.G. Ed.) Vol. III, Wiley, New York, pp. 491–521.

Que, L., Jr., and Dong, Y. (1996) Modeling the oxygen activation chemistry of methane monooxygenase and ribonucleotide reductase. *Acc. Chem. Res.* **29,** 190–196.

Que, L., Jr., and True, A.E. (1990) Dinuclear iron- and manganese-oxo sites in biology. In: *Progress In Inorganic Chemistry: Bioinorganic Chemistry* (Lippard, S. J., Ed.), John Wiley & Sons, New York, pp. 97–200.

Raner, T.G., Martins, L.J., and Ellis, W.R., Jr. (1997) Functional role of Leucine-103 in myohemerythrin. *Biochemistry* **36,** 7037–7043.

Rardin, R.L., Tolman, W.B., and Lippard, S.J. (1991) Monodentate carboxylate complexes and the carboxylate shift: implications for poly-metalloprotein structure and function. *New. J. Chem.* **15,** 417–430.

Ravi, N., Prickril, B.C., Kurtz, D.M. Jr., and Huynh, B.H. (1993) Spectroscopic characterization of ^{57}Fe-reconstituted rubrerythrin, a non-heme iron protein with structural analogies to ribonucleotide reductase. *Biochemistry* **32,** 8487–8491.

Ravi, N, Bollinger, J.M., Jr., Huynh, B.H., Edmondson, D.E., and Stubbe, J. (1994) Mechanism of assembly of the tyrosyl radical-diiron(III) cofactor of *E. coli* ribonucleotide reductase. Mössbauer characterization of the diferric radical precursor. *J. Am. Chem. Soc.* **116,** 8007–8014.

Reem, R.C., and Solomon, E.I. (1987) Spectroscopic studies of the binuclear ferrous active site of deoxyhemerythrin: coordination number and probable bridging ligands for the native and ligand-bound forms. *J. Am. Chem. Soc.* **109,** 1216–1226.

Reem, R.C., McCormick, J.M., Richardson, D.E., Devlin, F.J., Stephens, P.J., Musselman, R.L., and Solomon, E.I. (1989) Spectroscopic studies of the coupled binuclear ferric active site in methemerythrins and oxyhemerythrin: the electronic structure of each iron center and the iron-oxo and iron-peroxide bonds. *J. Am. Chem. Soc.* **111,** 4688–4704.

Reichard, P. (1988) Interactions between deoxyribonuelcotide and DNA synthesis. *Annu. Rev. Biochem.* **57,** 349–374.

Riggs-Gelasco, P.J., Shu, L., Chen, S., Burdi, D., Huynh, B.-H., Que, L., Jr., and Stubbe, J. (1996) EXAFS characterization of intermediate X from the assembly of the dinuclear Fe cluster in *E. coli* ribonucleotide reductase. *Conference on Oxygen Intermediates in Nonheme Metallobiochemistry,* 16B, Minneapolis, MN.

Rosenzweig, A.C., Frederick, C.A., Lippard, S.J., and Nordlund, P. (1993) Crystal structure of a bacterial non-heme iron hydroxylase that catalyzes the biological oxidation of methane. *Nature* **336,** 537–543.

Rosenzweig, A.C., Nordlund, P., Takahara, P.M., Frederick, C.A., and Lippard, S.J. (1995) Geometry of the soluble methane monooxygenase catalytic diiron center in two oxidation states. *Chem. Biol.* **2,** 409–418.

Sahlin, M., Sjöberg, S.-M., Backes, G., Loehr, T.M., and Sanders-Loehr, J. (1990) Activation of the iron-containing B2 protein of ribonucleotide reductase by hydrogen peroxide. *Biochem. Biophys. Res. Commun.* **167,** 813–818.

Sanders-Loehr, J. (1989) Binuclear iron proteins. In: *Iron Carriers and Iron Proteins, Physical Bioinorganic Chemistry Series* (Loehr, T.M., Ed.), VCH Publishers, New York, pp. 373–466.

Sanders-Loehr, J. (1996) Mechanism insights from Raman spectroscopy, in *Symposium on Oxygen Intermediates University of Minnesota.*

Sanders-Loehr, J., and Loehr, T.M. (1979) *Advances In Inorganic Biochemistry* (Eichhorn, G., & Marzilli, L., Eds.), Elsevier, New York, pp. 235–252.

Sanders-Loehr, J., Loehr, T.M., Mauk, A.G., and Gray, H.B. (1980) An electronic spectroscopic study of iron coordination in hemerythrin. *J. Am. Chem. Soc.* **102,** 6992–6996.

Sanders-Loehr, J., Wheeler, W.D., Shiemke, A.K., Averill, B.A., and Loehr, T.M. (1989) Electronic and Raman spectroscopic properties of oxo-bridged dinuclear iron centers in proteins and model compounds. *J. Am. Chem. Soc.* **111,** 8084–8093.

Scarrow, R.C., Maroney, M.J., Palmer, S.M., Que, L., Jr., Roe, A.L., Salowe, S.P., and Stubbe, J. (1987) EXAFS studies of binuclear iron proteins: hemerythrin and ribonucleotide reductase. *J. Am. Chem. Soc.* **109,** 7857–7864.

Shanklin, J., and Somerville, C. (1991) Stearoyl-acyl-carrier-protein desaturase from higher plants is structurally unrelated to the animal and fungal homologs. *Proc. Natl. Acad. Sci. U.S.A.* **88,** 2510–2514.

Shanklin, J., Whittle, E., and Fox, B.G. (1994) Eight histidine residues are catalytically essential in a membrane-associated iron enzyme, stearoyl-CoA desaturase, and are conserved in alkane hydroxylase and xylene monooxygenase. *Biochemistry* **33,** 12787–12794.

Sheriff, S., Hendrickson, W.A., and Smith, J.L. (1987) Structure of myohemerythrin in the azidomet atate at 1.7/1.3 Å resolution. *J. Mol. Biol.* **197,** 273–296.

Shiemke, A.K., Loehr, T.M., and Sanders-Loehr, J. (1984) Resonance Raman study of the m-oxo-bridged binuclear iron center in oxyhemerythrin. *J. Am. Chem. Soc.* **106,** 4951–4956.

Shiemke, A.K., Loehr, T.M., and Sanders-Loehr, J. (1986) Resonance Raman study of oxyhemerythrin and hydroxomethemerythrin. Evidence for hydrogen bonding of ligands to the Fe-O-Fe center. *J. Am. Chem. Soc.* **108,** 4951–4956.

Shu, L., Broadwater, J.A., Fox, B.G., and Que, L., Jr. (1996) Department of Chemistry, University of Minnesota. Unpublished results.

Shu, L., Nesheim, J.C., Kauffmann, K., Münck, E., Lipscomb, J.D., and Que, L., Jr. (1997) An $Fe_2^{IV}O_2$ diamond core structure for the key intermediate Q of methane monooxygenase. *Science* **275,** 515–518.

Sjöberg, B.-M., Loehr, T.M., and Sanders-Loehr, J. (1982) Raman spectral evidence for a m-oxo bridge in the binuclear iron center of ribonucleotide reductase. *Biochemistry* **21,** 96–102.

Sjöberg, B.-M., Sanders-Loehr, J., and Loehr, T.M. (1987) Identification of a hydroxide ligand at the iron center of ribonucleotide reductase by resonance Raman spectroscopy. *Biochemistry* **26,** 4242–4247.

Sorrell, T.N., O'Connor, C.J., Anderson, O.P., and Reibenspies, J.H. (1985) Synthesis and characterization of phenolate-bridged copper dimers with a Cu-Cu

separation of >3.5Å. Models for the active site of oxidized hemocyanin derivatives. *J. Am. Chem. Soc.* **107,** 4199–4206.

Spiro, T.G. (1988) *Biological Applications of Raman Spectroscopy* (Spiro, T.G., Ed.), Vol. 3, John Wiley & Sons, New York.

Spiro, T.G., and Czernuszewicz, R.S. (1995) Resonance Raman spectroscopy of metalloproteins. *Methods Enzymol.* **246,** 416–460.

Stainthorpe, A.C., Lees, V., Salmond, G.P.C., Dalton, H., and Murrell, J.C. (1990) The methane monooxygenase gene cluster of *Methylococcus capsulatus* (Bath). *Gene* **91,** 27–34.

Stenkamp, R.E. (1994) Dioxygen and hemerythrin. *Chem. Rev.* **94,** 715–726.

Stenkamp, R.E., Sieker, L.C., and Jensen, L.H. (1984) Binuclear iron complexes in methemerythrin and azidomethemerythrin at 2.0-Å resolution. *J. Am. Chem. Soc.* **106,** 618–622.

Stenkamp, R.E., Sieker, L.C., Jensen, L.H., McCallum, J.D., and Sanders-Loehr, J. (1985) Active site structure of deoxyhemerythrin and oxyhemerythrin. *Proc. Natl. Acad. Sci. U.S.A.* **82,** 713–716.

Strittmatter, P., Spatz, L., Corcoran, D., Rogers, M.J., Setlow, B., and Redline, R. (1974) Purification and properties of rat liver microsomal stearyl coenzyme A desaturase. *Proc. Natl. Acad. Sci. U.S.A.* **71,** 4565–4569.

Sturgeon, B.E., Burdi, D., Chen, S., Huynh, B.-H., Edmondson, D.E., Stubbe, J., and Hoffman, B.M. (1996) Reconsideration of X, the diiron intermediate formed during cofactorassembly in *E. coli* ribonucleotide reductase. *J. Am. Chem. Soc.* **118,** 7551–7557.

Suzuki, M., Hayakawa, T., Shaw, J. P., Rekik, M., and Harayama, S. (1991) Primary structure of xylene monooxygenase: similarities to and differences from the alkane hydroxylation system. *J. Bacteriol.* **173,** 1690–1695.

Takashi, T., and Cox, J.A. (1991) Primary structure of myohemerythrin from the annelid *Nereis diversicolor*. *FEBS Lett.* **285,** 25–27.

Thomann, H., Bernardo, M., McCormick, J.M., Pulver, S., Andersson, K.K., Lipscomb, J.D., and Solomon, E.I. (1993) Pulsed EPR studies of mixed valent [Fe(II)Fe(III)] forms of hemerythrin and methane monooxygenase: evidence for a hydroxide bridge. *J. Am. Chem. Soc.* **105,** 8881–8882.

Thompson, G.A., Scherer, D.E., Foxall-Van Aken, S., Kenny, J.W., Young, H.L., Shintani, D.K., Kridl, J.C., and Knauf, V.C. (1991) Primary structures of the precursor and mature forms of stearoyl-acyl carrier protein desaturase from safflower embryos and requirement of ferredoxin for enzyme activity. *Proc. Natl. Acad. Sci. U.S.A.* **88,** 2578–2582.

Tong, W.H., Chen, S., Lloyd, S.G., Edmondson, D.E., Huynh, B.H., and Stubbe, J. (1996) Mechanism of assembly of the diferric cluster-tyrosyl radical cofactor of *Escherichia coli* ribonucleotide reductase from the diferrous form of the R2 subunit. *J. Am. Chem. Soc.* **118,** 2107–2108.

Tsubaki, M., and Yu, N.-T. (1982) Resonance Raman investigation of nitric oxide bonding in nitrosylhemoglobin A and myoglobin: detection of bound N-O stretching and Fe-NO stretching vibrations from the hexacoordinated NO-heme complex. *Biochemistry* **21,** 1140–1144.

Turowski, P.N., Armstrong, W.H., Liu, S., Brown, W.N., and Lippard, S.J. (1994) Synthesis and characterization of hydroxo-bridged diiron(III) complexes containing carboxylate or phosphate ester bridges: comparisons to diiron(III) proteins. *Inorg. Chem.* **33,** 636–645.

Van Beilen, J.B., Penninga, D., and Witholt, B. (1992) Topology of the membrane-bound alkane hydroxylase of *Pseudomonas oleovorans*. *J. Biol. Chem.* **267,** 9194–9201.

van de Loo, F.J., Fox, B.G., and Somerville, C. (1993) Unusual fatty acids. In: *Lipid Metabolism in Plants* (Moore, T.E., Ed.), CRC Press, Boca Raton, pp. 91–126.

Veselov, A., and Scholes, C.P. (1996) X-bond ENDOR of the liganding environment from the radical X intermediate of *Escherichia coli* ribonucleotide reductase. *Inorg. Chem.* **35,** 3702–3705.

Vincent, J.B., Olivier-Lilley, G.L., and Averill, B.A. (1990) Proteins containing oxo-bridged dinuclear iron centers: a bioinorganic perspective. *Chem. Rev.* **90,** 1447–1467.

Volbeda, A., and Hol, W.G.J. (1989) Pseudo 2-fold symmetry in the copper-binding domain of arthropodan haemocyanins. Possible implications for the evolution of oxygen transport proteins. *J. Mol. Biol.* **206,** 531–546.

Wallar, B.J., and Lipscomb, J.D. (1996) Dioxygen activation by enzymes containing binuclear non-heme iron clusters. *Chem. Rev.* **96,** 2625–2657.

Wang, D.L., Holz, R.C., David, S.S., Que, L., Jr., and Stankovich, M.T. (1991) Electrochemical properties of the diiron core of uteroferrin and its anion complexes. *Biochemistry* **30,** 8187–8194.

Wieghardt, K., Pohl, K., and Ventur, D. (1985) Reactivity of the [$Fe_2(\mu_2$-O)(μ-acetato)$_2$] unit in methemerythrin model compounds towards N_3^- and NCS^-. *Angew. Chem. Int. Ed. Engl.* **24,** 392–393.

Wilkins, R.G., and Harrington, P.C. (1983) The chemistry of hemerythrin. *Adv. Inorg. Biochem.* **5,** 51–85.

Wing, R.M., and Callahan, K.P. (1969) The characterization of metal-oxygen bridge systems. *Inorg. Chem.* **8,** 871–874.

Woolery, G.L., Powers, L., Winkler, M., Solomon, E.I., and Spiro, T.G. (1984) EXAFS studies of binuclear copper site of oxy-, deoxy-, metaquo-, metfluoro-, and metazido hemocyanin from arthropods and molluscs. *J. Am. Chem. Soc.* **106,** 86–92.

Yamashita, M.M., Wesson, L., Eisenman, G., and Eisenberg, D. (1990) Where metal ions bind in proteins. *Proc. Natl. Acad. Sci. U.S.A.* **87,** 5648–5652.

Yen, K.-M., Karl, M.R., Blatt, L.M., Simon, M.J., Winter, R.B., Fausset, P.R., Lu, H.S., Harcourt, A.A., and Chen, K.K. (1991) Cloning and characterization of a *Pseudomonas mendocina* KR1 gene cluster encoding toluene-4-monooxygenase. *J. Bacteriol.* **173,** 5315–5327.

Zang, Y., Dong, Y., Que, L., Jr., Kauffmann, K., and Münck, E. (1995) The first bis(μ-oxo)diiron(III) complex. Structure and magnetic properties of [$Fe_2(\mu$-O)$_2$(6TLA)$_2$](CLO_4)$_2$. *J. Am. Chem. Soc.* **117,** 1169–1170.

BIOGRAPHICAL NOTE

Jingyuan Ai was born in the small village of Ai-Cun, Feng-Qiu County, He-Nan province of China, on April 15, 1968 (Lunar calendar). He began his education at the age of six. He spent five years in Xi-Zhao-Gang Primary School and three years in Yin-gang United Middle School. He had a wonderful time and wonderful dreams during that time. He then left home and spent three years in First Advanced High School of Feng-Qiu County. He started his college education in the fall of 1985. He obtained his B.S. degree in Chemistry from the Department of Chemistry, Zheng-Zhou University in 1989, and completed his M.S. degree in Physical Chemistry from the Department of Modern Chemistry, University of Science and Technology of China in 1992. He started his Ph.D. studies in the Department of Biochemistry and Molecular Biology at the Oregon Graduate Institute of Science and Technology in the fall of 1992.